ULTRASONIC TRANSMISSION IMAGING

A thesis presented for the degree of

Doctor of Philosophy in Electrical Engineering

in the University of Canterbury,

Christchurch, New Zealand.

by

G.R. DUNLOP B.Sc. B.E.(Hons.) C.Eng. MIEE

1978

TABLE OF CONTENTS

Page

ABSTRACT

The problem of imaging cross sections of opaque bodies by means of ultrasonic transmissions is considered. Images are computed from measurements of ultrasonic propagation delay times through the body section. The grey levels in the image depend on the ultrasonic propagation velocity in the body section.

Conventional ultrasonic pulse-echo imaging is reviewed and its shortcomings are discussed. Ultrasonic transmission measurements are suggested as a way of removing these shortcomings and complementing pulse-echo imaging. The images are obtained by processing ultrasonic propagation time delay measurements in the same manner as X-ray attenuation measurements are processed to produce images in X-ray computed tomography. These X-ray imaging techniques are reviewed in detail.

Multipath ultrasonic propagation complicates the time delay measurements. Measurements on simple objects are used to illustrate the effect of multipath propagation. Propagation time delays are related to phase measurements in a theoretical study of ultrasonic propagation and scattering. The theoretical study of scattering results in an extension to the Rytov approximation. This extended Rytov approximation is shown to produce improved estimates of the phase of scattered radiation.

Numerous problems associated with automatically obtaining ultrasonic time delay measurements are discussed. Images computed from both calculated and measured time delays are presented to illustrate various points. It is suggested how the measurement system could be improved to yield rapid in vivo measurements.

ACKNOWLEDGEMENTS

I am indebted to my supervisor, Professor R.H.T. Bates, for his guidance and encouragement during the course of this work. I also wish to thank Professor W.M. Boerner of the Electrical Engineering Department of the University of Manitoba for his assistance in developing the scattering theories in Chapter 3.

I am grateful to my colleagues, Drs T.M. Peters, P.T. Gough and R.M. Lewitt in the Electrical Engineering Department for many interesting discussions on holography and X-ray computed tomography. The assistance of two technicians in the Electrical Engineering Department, G. Clark and A. Vernon, who fabricated the ultrasonic transducers and scanner gantry, is gratefully acknowledged.

I am also grateful to Dr M.J. McDonnell, previously of the Electrical Engineering Department, and now of Physics and Engineering Laboratory, D.S.I.R., for providing fig. 4.9(b) and to Professor R.F. Myer and Dr F. Thomson of the Mechanical Engineering Department of the University of Auckland for providing figs 5.18 and 5.19(c). I especially wish to thank Mr W.K. Kennedy, Manager of the Hybrid Computing Laboratory of the Department of Electrical Engineering, for his valuable assistance in interfacing equipment to the computer. The assistance of Dr R.G.T. Beetham of Christchurch Women's Hospital, and Dr H.G. Guy of Princess Margaret Hospital is also acknowledged.

I especially wish to thank my wife Elizabeth for patience, encouragement and support for the duration of this work.

I wish to acknowledge the Canterbury Education Board which permitted me to work off a four year Post Primary Teacher's Studentship Bond by working in the Department of Electrical Engineering as a Junior Lecturer.

The financial support of a postgraduate scholarship from the University Grants Committee is gratefully acknowledged.

GLOSSARY

Listed below are those symbols and abbreviations used in this thesis which are not always defined in the immediate context in which they are used.

CRT	cathode ray tube
FFT	fast Fourier transform
$\mathcal{F}\{\ \}$	denotes the Fourier transform
$\mathcal{F}^{-1}\{\ \}$	denotes the inverse Fourier transform
j	$\sqrt{-1}$
k	wavenumber $2\pi/\lambda$
λ	wavelength
S/N	signal to noise ratio
t	time
T	time delay
T_w	acoustic propagation time delay through water
$T(\xi,\phi)$	time delay for acoustic propagation between the transducers when the scanner is at (ξ,ϕ)
τ	equivalent to time
τ_i	acoustic time delay for path i
V(x,y)	acoustic velocity at point (x,y)
V_w	acoustic velocity in water
n	acoustic refractive index V_w/V
(x,y)	cartesian coordinate of a point in the body section
(ξ,η)	cartesian coordinates employed by the scanner - inclined at angle ϕ to (x,y) coordinates
(ξ,ϕ)	polar coordinates used by the scanner
ω	angular frequency (radians/second)
$\omega(x,y)$	the distribution in the body section

$\bar{\omega}_M$	the image of the body section calculated from M projections
M	the number of projections
ϕ_i	angle at which the i^{th} projection is measured = $(i-1)\pi/M$
$\Omega(\alpha,\beta)$	= $\mathcal{F}_{xy}\{\omega(x,y)\}$
$\Lambda(\rho,\phi)$	$\Omega(\alpha,\beta)$ expressed in polar coordinates
$d\eta$	an element of a ray path
f	frequency = $\omega/2\pi$
$f(\xi,\phi)$	X-ray projection
$\tilde{f}(\xi,\phi)$	acoustic time delay projection
$\hat{f}(\xi,\phi)$	the modified projection
*	denotes the complex conjugate
$\circledast$	denotes convolution
ψ	wave function
Ψ	crosscorrelation function
$\delta(t)$	the Dirac delta function
s(t)	the received signal = $p(t) \circledast e(t)$
p(t)	the pulse component of s(t)
e(t)	the ideal received signal
$S(\omega)$	$\mathcal{F}\{s(t)\}$

PREFACE

Conventional X-ray diagnosis has been extended very significantly during the past five years. Excellent pictures of body cross sections are obtained by combining ordinary shadowgraph information received from a large number of angles around the body. This celebrated technique was developed by Hounsfield (1972), and is known as "computer assisted tomography", or simply "computed tomography". The field of X-ray tomography has grown from the first EMI brain scanner released at the end of 1972, to more than 600 brain and body X-ray tomography machines now in use. There are presently more than a dozen different manufacturers constructing X-ray tomography machines and development is very rapid. The methods of, and current research in, computed tomography are reviewed in chapter 2.

During a tomographic X-ray examination, the patient can absorb a radiation dose of as high as 2 rads. The accumulated dosage for repeated or extensive X-ray tomographic examinations can become unacceptably high. Physicians usually argue that the associated morbidity is low and is preferable to the likely mortality caused by an undetected tumour or malignant growth.

The problem of cumulative dosage causing cell damage has not been observed with ultrasonic diagnostic apparatus. Considerable effort has been devoted to the study of ultrasonic cell damage, cavitation and heating in biological specimens. The conclusion drawn from these studies which are reviewed in chapter 1, is that adverse biological effects are not observed at average ultrasonic intensities less than 0.1 W/cm^2. Conventional pulse-echo ultrasonic diagnosis methods are discussed in chapter 1 together with experimental developments in ultrasonic imaging. The diagnostic information can be presented in several different ways, but in all cases it is based on ultrasonic echo returns and hence depends on acoustic impedance mismatches. Conventional ultrasonic diagnostic methods

work well when there is a well defined change of acoustic impedance across a surface and the reflecting surface is almost perpendicular to the probing ultrasonic beam. However, pulse-echo techniques are not suited to examining small or gradual changes of acoustic impedance such as can occur in soft tissue. Changes in both the density and the acoustic velocity contribute to changes in the acoustic impedance. This thesis is concerned with measuring small changes in the acoustic velocity.

Small or gradual changes in the acoustic velocity can be examined by forming a "phase shadowgraph" in which the grey scale represents the acoustic phase in the range of 0 to π. The image is formed in a manner similar to the X-ray shadowgraph. The image also has similarities to those formed by phase contrast and interference light microscopes. The "phase shadowgraph" does not permit the acoustic phase to be determined uniquely if the phase variations are greater than π. A method of uniquely determining the acoustic phase, for variations of many cycles, is developed in chapter 3. Thus an "extended phase shadowgraph" is formed in which the grey scale is proportional to the phase. The theoretical basis relating phase measurements to propagation time delay measurements is established in chapter 3. The acoustic time delay measurements are compared with X-ray attenuation measurements and the basis for ultrasonic transmission tomography is established. Chapter 3 also contains some extensions to approximate scattering theory (c.f. Bates, Boerner and Dunlop 1976, Dunlop, Boerner and Bates 1976).

The equipment and signal processing required to produce acoustic transmission tomograms is described in chapter 4. Several novel solutions to computation and equipment problems are presented in this chapter (c.f. Dunlop 1973, Boys and Dunlop 1978a,b, Dunlop and Boys 1978, Dunlop 1978). The design and construction of broadband ultrasonic transducers is examined in chapter 5. Good agreement is obtained between the theoretical and measured performance of the transducers. The design

ensures that the transducer characteristics are easily reproduced without the need to employ special construction techniques.

The results of tomographic measurements and simulations are contained in chapter 6. Phantoms of various shapes are examined, and the results of in vitro measurements are reported (c.f. Bates and Dunlop 1977). Methods for reducing the measurement time and improving the system performance are outlined in chapter 7.

During the course of this work, the following papers have been prepared for publication:

Dunlop G.R. 1973 Ultrasonic signal processing, presented to the National Electronics Conference NELCON73 at the University of Canterbury, Christchurch, New Zealand.

Bates R.H.T., Boerner W.M. and Dunlop G.R. 1976 An extended Rytov approximation and its significance for remote sensing and inverse scattering, Optics Communications 18 421-423.

Dunlop G.R., Boerner W.M. and Bates R.H.T. 1976 On an extended Rytov approximation and its comparison with the Born approximation, in Digest of Papers, AP-S International Symposium, IEEE catalog no. 76 CH1121-3AP.

Bates R.H.T. and Dunlop G.R. 1977 Inverse scattering and tomography, in Ultrasonics International 1977 (Conference Proceedings), IPC Science and Technology Press, Guildford, England.

Boys J.T. and Dunlop G.R. 1978a Economical stepper motors for speed control applications, submitted to IEE Journal on Electric Power Applications.

Boys J.T. and Dunlop G.R. 1978b Pulse multiplication by four, submitted to IEE Journal on Electronic Circuits and Systems.

Dunlop G.R. and Boys J.T. 1978 A versatile AGC for pulse transmission systems, submitted to Ultrasonics.

Dunlop G.R. 1978 A rapid computation method for improvements to nearest neighbour interpolation, submitted to Journal of Computer Assisted Tomography.

CHAPTER ONE

ULTRASONIC IMAGING METHODS

1.1 HISTORY OF ULTRASOUND

The use of ultrasound for imaging has arisen from the need to visualize the interior of an opaque region when it is difficult, if not impossible to obtain the information by any other means. Some of the more notable developments in ultrasonics are listed in table 1.1. More extensive tables are given by Erikson et al. (1974) and by Wells (1969, Ch.4).

The first practical use of ultrasound by man is generally attributed to Chilowsky and Langevin who devised an underwater signalling system in 1916. Following this, Langevin was employed by the French government to develop a method for detecting submarines. Langevin produced a workable SONAR together with a practical ultrasonic transducer which was patented in France (1918) and Britain (1921). The transducer could be used as a transmitter and as a receiver of ultrasonic waves in water. It was constructed from a mosaic of quartz crystals sandwiched between two steel plates. The basis of the pulse-echo SONAR systems developed during World War II is covered by Langevin's patents. These SONAR systems are the predecessors of most ultrasonic imaging systems in use today. A comprehensive review of the developments in marine ultrasound is given by Hersey (1977).

Sokoloff (1929, 1937) devised a flaw detector which was similar in concept to a radiographer's X-ray shadowgraph. A beam of ultrasound was transmitted through an immersed body, and a receiver detected the emerging energy. The transmitter and receiver were scanned across the body, and at the same time, the intensity of the emerging ultrasound was plotted at a position corresponding to that of the receiver. Interpretation of the "shadowing" is straightforward when only a few large flaws are present.

The therapeutic use of low intensity ultrasound was first reported by Pohlman et al. (1930). Physiotherapists now routinely employ ultrasound to warm an area before massage treatment. The most common use is

for muscular and tendon complaints, and the ultrasonic intensity ranges up to a few watts per square centimetre.

Dussik (1942) is credited with the first attempt to examine the structure of the human body with ultrasound. The fluid filled ventricles in the brain were to be mapped by plotting the attenuation of ultrasound beamed through the skull. This experiment was suggested by Sokoloff some 12 years earlier. It failed because the attenuation and reflections caused by the skull are much greater than the total attenuation through the brain.

At the same time as Dussik was investigating ultrasound transmission, Firestone (1942, 1946) was developing another of Sokoloff's suggestions based on pulse-echo detection of flaws in metals. Firestone also used his pulse-echo flaw detector to examine various bones in the body. A similar system was developed independently by D.O. Spoule in the U.K.

World War II developments in electronics enabled higher frequencies to be used for ultrasonics. The associated shorter wavelengths permitted the development of small highly directional transducers which were suitable for medical imaging systems. Wild (1950), Reid and Wild (1952) and Howry and Bliss (1952) successfully applied high frequency pulse-echo techniques to medical examination of the human body.

During the two decades after 1950, ultrasonic technology developed to the extent that the medical profession accepted it as a useful tool. Investigators examined the heart (Hertz and Elder 1954, Satomaru 1957), the eye (Oksala and Lehtinen 1957, Baum and Greenwood 1958) and the brain (Lindstrom 1954). Ultrasound was also used to visualize the contents of the pregnant uterus (Donald et al. 1958, Kossoff 1963b), to examine blood flow by means of pulse transit time (Kalmus et al. 1954, Haugen et al. 1955, Franklin et al. 1959) and by means of the signal doppler shift (Franklin et al. 1961, Baker 1969, Peronneau and Leger 1969), and to measure the position

of the brain midline which is often off-centre when physical brain damage or tumours exist (c.f. Jeppsson 1961). Lindstrom (1954) employed ultrasound surgically to modify tissue, and others (c.f. Altmann and Waltner 1959, Arslan 1960, Kossoff 1964) have used it to treat Meniere's disease with some success.

Tissue modification by ultrasound led many to question its safety. The results of some of their investigations are summarized in table 1.2. Macintosh and Davey (1970, 1972) reported chromosome damage at radiation levels as low as 8.5 mW/cm^2 for one hour exposure. Later experiments failed to substantiate this claim (c.f. Tremewan 1975). Fry et al. (1970) survey the various cavitation and thermal effects which have been observed to produce lesions in living tissue. Isonification of brain tissue for a long time at moderate power ($10^2 W/cm^2$ for 7 secs) was required to induce lesions thermally. High power, short duration isonification (20 kW/cm^2 for 0.2 msec.) was required to produce lesions by cavitation. Fry et al. also report the results of a survey by Hill (1968) which suggested 10^2 W/cm^2 for 1 μs with a 0.1% duty cycle as the upper limit for commercial diagnostic equipment. (This is several orders of magnitude less than the isonification required to induce observable lesions in the mammalian central nervous system - c.f. Wells 1969). They conclude that since the central nervous system is amongst the most sensitive of adult tissues, (c.f. Dunn and Fry 1971), "there is little likelihood that ultrasound provides a hazard when employed for medical diagnostic purposes".

Measurements of commercial ultrasonic diagnostic machine output intensities have been made by Hill (1968, 1971). These results are shown in fig. 1.1 which also shows the ultrasonic intensity thresholds for tissue damage (c.f. Dunn and Fry 1971). Note that the peak diagnostic intensity is several orders of magnitude less than the intensity required to produce damage.

In a recent symposium (c.f. Hazzard and Litz 1977) on the biological effects of ultrasound, many authors observed cell damage and induced miscarriages (mostly in mice) at quite low intensities. However, in all cases the exposure period was long enough for the ultrasonic dose absorbed to lie near the "embryonic functionally observed threshold" shown in fig. 1.1.

Wells (1969) states that until safety levels have been defined, it is undesirable, either to use greater ultrasonic intensities than those which are currently being employed, or to subject patients to unnecessarily lengthy investigations.

During the past decade, there has been much research into ultrasonic holographic systems (c.f. § 1.5), multiple transducer beam forming for rapid scanning (e.g. Somer 1968, 1971, c.f. § 1.4) and computer processing of the "echo" signal (e.g. McSherry 1972, 1973, 1974). Before these methods can be usefully discussed, it is convenient to review ultrasonic imaging principles. This is done in the next section.

1.2 ULTRASOUND APPLIED TO IMAGING

The fundamentals of ultrasonic pulse-echo imaging are reviewed in this section. Descriptions of the generation, transmission, reflection and detection of ultrasonic pulses are given together with a discussion of image resolution and accuracy.

An ultrasonic pulse-echo diagnostic system is shown diagrammatically in fig. 1.2. A short duration voltage pulse is applied to the ultrasonic transducer, which then produces pressure waves at ultrasonic frequencies (typically 1-15 MHz). The waves radiate away from the transducer as a packet (see for example fig. 5.18 with a duration (typically 2 or 3 cycles) determined by the transducer bandwidth. The centre frequency is determined by the resonance of the piezoelectric element inside the transducer. The wave packet, or ultrasonic pulse, travels into the body

and passes across boundaries between regions of different acoustic impedance. The latter is defined to be the product of density and sound velocity in the region. At each boundary a fraction of the transmitted pulse is reflected back to the transducer as an ultrasonic echo pulse. The transducer receives each ultrasonic echo pulse and generates an electrical signal of typically 4 or 5 cycles in duration. The electrical echo signal is used to deflect vertically the electron beam of a CRT (cathode ray tube). The CRT beam is also deflected horizontally with elapsed time after the pulse transmission. Thus a received echo is displayed at an instant corresponding to twice the time taken for the pulse to travel from the transducer to the boundary (which reflected the echo).

An amplitude or A-scan display on the CRT is formed when the r.f. pulse is rectified and the resulting envelope is used to deflect the CRT beam vertically. The pulse-echo process is repetitive (typically at 1 kHz) and a flicker free echogram is produced.

The amplitude of an ultrasonic echo is proportional to the amplitude of the transmitted pulse. It is also dependent on the attenuation along the path to the particular reflecting boundary, the transmission coefficients of all the boundaries crossed by the path, and the reflection coefficient at the boundary. For a pulse travelling through a region (identified by a subscript 1) incident upon the boundary of another region (identified by a subscript 2) a reflection coefficient A_r and a transmission coefficient A_t can be determined from Snell's Law, and by equating the pressure on both sides of the boundary:

$$A_r = \frac{Z_2 \cos\theta_1 - Z_1 \cos\theta_2}{Z_2 \cos\theta_1 + Z_1 \cos\theta_2} \tag{1.1}$$

$$A_t = \frac{2Z_2 \cos\theta_1}{Z_2 \cos\theta_1 + Z_1 \cos\theta_2} \tag{1.2}$$

Using i to denote either 1 or 2, the pulse in the i^{th} region is inclined at θ_i to the normal at the boundary, and Z_i is the acoustic impedance in region i.

In general, the further a reflector is from the transducer, the weaker the echo because of the spreading of the pulse, as it propagates. The transducer produces a "beam" of ultrasound (c.f. fig. 5.18). Boundaries or scatterers outside this beam do not cause sensible echoes. Those within the beam reflect echoes which can be received by the transducer.

Most diagnostic systems use a time varying receiver gain in an attempt to equalize the amplitudes of near and distant echoes. Exact compensation for echo amplitude reduction by beam spreading can be obtained with time variable gain. For a particular probed region, an approximate correction can be made for the acoustic attenuation. However, boundary transmission and reflection effects are only approximately known for a given region (or patient), and only a crude correction can be made. In some apparatus, the gain-time profile is set manually, or by punched cards, so as to give the best overall performance for a probed region.

If the ultrasonic velocity does not vary greatly within the probed region, the time at which an echo is detected is approximately proportional to the distance of the reflector from the transducer. An average value for the ultrasonic velocity can then be assigned to the region. Interpretation of an echogram for a narrow beam of ultrasound is the same as that of a needle biopsy.

The resolution and accuracy of an ultrasonic imaging system is now discussed in terms of an ideal point scatterer. Such a scatterer can only be accurately located in a uniform medium by using a very narrow beam. Unfortunately, the finite beam width of any practical transducer considerably reduces the azimuthal resolution. Thus echoes from a point target

are observed over a range of angles. A focussed transducer improves the azimuthal resolution, but reduces the depth of field, i.e. the azimuthal resolution is improved within a zone containing the focal point, but is worse outside this focal zone. Diffraction limited azimuthal resolution is determined from the Rayleigh criterion (c.f. Born and Wolf 1970, pp 435 ff). A spherically focussed transducer of radius r operating at a wavelength λ in a medium can produce a focussed beam of diameter a at the focal distance L, where

$$a = 1.22\,\lambda L/r \tag{1.3}$$

A compromise is necessary between the azimuthal resolution and the depth of field which is chosen to produce the required penetration in the probed region. Kossoff et al. (1968) relate the theoretical beamwidth at different axial distances x from the transducer, to the above parameters:

$$a_x = \frac{.48r[L-x]}{L\,\sin\{(\pi r^2/2\lambda)([L-x]/Lx)\}} \tag{1.4}$$

They find that a weakly focussed transducer can give a reasonable depth of field without too much degradation of the azimuthal resolution. For example, at 2 MHz in water, a 4 cm radius transducer strongly focussed at 20 cm, has an azimuthal resolution of 0.46 cm, whereas a weakly focussed transducer of 1.75 cm radius has a resolution of better than 1.2 cm between 20 and 30 cm. Kossoff (1963b) investigated the use of a water bath scanner. The average water path distance between the patient and the transducer is chosen so that the focal zone is coincident with the region to be examined. For example for 10 cm of patient penetration, a water path of 20 cm would be required for the weakly focussed transducer discussed above.

The limited dynamic ranges of CRT displays cause additional complications. The amplitudes of the echoes have to be compressed so that all echoes can be displayed. Thus there is a reduction in the relative echo amplitudes between point scatterers in the centre of the beam and at the edges of the beam. Thus the beamwidth is effectively wider than before the application of pulse amplitude compression. This further reduces the azimuthal resolution.

Changes in the ultrasonic velocity along the pulse propagation path cause refraction. Refraction of the pulse and echoes produces erroneous angle measurements for the scatterer. Multiple reflections can produce large azimuthal errors, and such echo signals are generally referred to as artefacts.

The variations in acoustic velocity cause range errors as well as azimuthal errors. A single point scatterer probed by a narrow beam from different directions is imaged as being at different points. For a finite beam width, many different arcs would replace the points. Range accuracy is crucial for good imaging and it is fortunate that soft tissue exhibits only a small range of acoustic velocity (~6%).

The range resolution is limited by the duration of the echo pulse. For wide bandwidth transducers, the resolution limit can approach one wavelength, e.g. at 1.5 MHz the approximate resolution limit is 1 mm in water or 4 mm in aluminium. There is a compromise between the choice of the bandwidth and the centre frequency. A high centre frequency results in too much signal attenuation. At a lower centre frequency, a low Q transducer is required to give the same bandwidth and sensitivity is traded for bandwidth. Inclined reflecting boundaries produce echoes of long duration from all but the narrowest of beams. A large isonified scattering area produces echoes over a range of distances and the boundary is poorly defined. A large aperture technique is the best method of alleviating the inclined boundary problem (c.f. Maginness 1972).

The inclined boundaries are much easier to visualize in 3-D images. Robinson (1972a,b) describes a method for constructing a 3-D ultrasound image from a series of adjacent 2-D images.

Much research is being devoted to improving azimuth and range resolution. The azimuth and range accuracy can only be improved by computational corrections which require a knowledge of the acoustic velocity distribution throughout the imaged region. Methods of obtaining such velocity distributions are the main concern of this thesis.

1.3 MEDICAL IMAGING SYSTEMS IN CURRENT USE

The principles of operation of all CRT display methods commonly used in ultrasonic diagnostic systems were developed during World War II for RADAR displays. The standard text on the subject (Reintjes 1952) lists 15 methods of CRT data display. Of these 15 methods only 3 are commonly used in ultrasonics. They are the A-scan, the brightness or B-scan, and the motion or M-scan (also known as the time-motion or T-M scan).

The A-scan is discussed in the preceding section. Its advantages are that it is cheap, simple and portable. Its disadvantage is that the output can vary markedly with only small changes in transducer orientation and positions. Thus a skilled operator is required to relate the transducer position and the echogram to the physiology. The A-scan is used in cardiovascular work (Segal et al. 1966, Feigenbam et al. 1967, Miller et al. 1967) for measuring muscle, valve and blood flow velocities from the Doppler shifts of the echo frequencies (Franklin et al. 1961, Baker 1969, Peronneau and Leger 1969). It is also used to align the ultrasonic beam within the heart before displaying information in the M-mode.

Another common use of A-scan displays is in neurology, especially for localization of the brain mid-line (c.f. Jeppson 1961), which vertically divides the two hemispheres (it can be moved laterally by

tumours or injury). Shifts of 2 or 3 mm are normal and are easily measured, even in a moving ambulance. This can expedite treatment for accident victims admitted to hospital casualty wards. The most accurate method of mid-line localization was suggested by Gordon (1959). It employs two transducers placed on opposite sides of the skull. The transducers and display are time shared so that the mid-line shift is measured as half of the distance between the two displayed mid-lines. Transmission breakthrough on the inoperative transducer produces an artefact at the midpoint of the echogram. This artefact interferes with the midline echo, but it can be eliminated by using the electronics and switching circuitry described by Robinson and Kossoff (1966).

Large echoes displayed by the A-scan correspond to the interfaces between various organs. Between the large echoes are many small echoes caused by small impedance changes within an organ. These give an indication of the inhomogeneity of the organ. The small echoes are routinely used to differentiate between solid masses and echo-free cystic regions which are transonic (transparent to sound). For example, a "normal" liver produces considerable echo information which can be quite variable. Despite this variability and different liver sizes, An et al. (1962) achieved success rates of as high as 94% in liver disease diagnosis.

Ultrasonic eye examinations have been used to locate foreign bodies and detached retinas, and to accurately measure (±.1 mm) the axial length of the eye (c.f. Coleman and Carlin 1967). Ultrasonic frequencies of the order of 15 MHz are typically used in opthalmology for which many special probes have been developed. Multiple reflections cause difficulties and most eye examination techniques use a standoff water delay probe in which the multiple echo transducer-eye-transducer-eye-transducer path is longer than the path to and from the farthest point in the eye. The water bath also facilitates the use of a mechanized transducer movement.

The B-scan technique is employed to form a two-dimensional image of a body cross section. The image is formed by constraining the transducer to move and rotate in a single plane. An image of the acoustic impedance changes in this plane is produced on a CRT display. The A-scan information is used to intensity modulate the CRT beam as it is deflected along a straight line. The position of the line on the CRT corresponds to the position of the ultrasonic beam in the imaged plane. The CRT spot starts from a position corresponding to that of the transducer and is deflected along the line at half the rate at which the transmitted pulse propagates. Thus a received echo causes a bright spot to appear on the screen at a position corresponding to the position of the reflector which gives rise to the echo. It is possible to trace out the outline of an organ on the CRT by moving the transducer and probing the organ from many different directions. Such an image is called a compound B-scan.

The A-scan display has an average dynamic range of about 40 dB, whereas a conventional CRT has a brightness range of 20 dB and a storage CRT has a brightness range of less than 10 dB. Thus the B-scan display requires some form of signal compression before the echo amplitudes can be used for brightness modulation. All signal compression schemes produce a degradation in azimuthal resolution.

A sector scan is a B-scan produced by a transducer placed at a single station and slowly rotated to probe the imaged section. These scans are commonly used in ophthalmology and in cardiovascular work. For the repetitive dynamics of the heart, motion can be approximately "frozen" by triggering the ultrasonic pulse at the same point in successive cardiac cycles. The time required to obtain such a frozen image is quite long. Images of the beating heart can be obtained at upwards of 20 images per second by employing high pulse repetition frequencies (up to 5 kHz) and rapid beam orientation. Some of the latest sector scanning systems use electronic beam forming, but this is a relatively new development and is

discussed separately in section 1.5. High speed mechanical scanners often employ several time shared transducers which probe adjacent subsectors. Rotation of the transducer assembly through the subsector angle allows the whole sector to be scanned. Automated scans produce an even spacing of the beam lines on the display which gives a uniform image quality with distance from the transducer. A linear scan for which the orientation of the transducer is fixed produces a uniform quality throughout the image. When the transducer is moved and orientated manually, the image quality tends to be quite uneven. A region of special interest may be probed many times more often than other regions, and this may result in a small area of the CRT phosphor being subjected to high electron beam currents. The observed size of the CRT spot becomes larger and produces a phenomenon known as "blooming", which is particularly noticeable in storage CRT's, but which can also occur on photographic films.

A compound scan is produced when several sector scans taken at different transducer positions are combined. Most of the hand held contact scanners used in obstetrics, abdominal examinations and in neurological imaging yield compound scans. They increase the likelihood of detecting echoes from interface planes which are perpendicular to the cross section plane. Compound scans in which the transducer stations are on arcs or straight lines are often used in eye or breast examinations but require a water bath for satisfactory operation.

The advantages of water bath scanners are four fold. Firstly, there is an improvement in the azimuthal resolution when the imaged region is completely within the focal zone of the transducer (c.f. Kossoff et al. 1968). Secondly, multiple reflections from the transducer are avoided if the transducer-body distance is greater than the imaged depth within the body (c.f. Leary 1967). Thirdly, water provides excellent ultrasonic coupling to human tissue, and finally, an automated scan can be employed. The automation allows the physician to concentrate on the detailed inter-

pretation of the results while the examination is conducted by a technician.

However, a skilled physician operating a manual scanner can achieve results superior to those obtained by an automated scanner. A physician can allow for differences in patient physiology noticed during a scan and repeat the scan in a more appropriate plane to image the desired features. This is especially true in obstetrics where a foetus may have any orientation within the womb. The physician may even have to "pursue" a particularly active foetus. The biparietal diameter is the most common foetal measurement. It is used to estimate a birth date.

Much effort has been devoted to increasing the dynamic range of B-scan images. Kossoff (1972, 1974) employed a good non-storage display CRT and recorded the grey scale tomograph with a 35 mm camera. Kossoff's results were obtained from obstetric and breast examinations while Taylor et al. (1973) used the grey scale for liver analysis. With the grey scale imaging technique, detail within organs is visible and can aid the identification of tumours, moles, cysts and calcification. It is also useful for placenta localization before withdrawing the amniotic fluid to be tested for foetal abnormalities. Special hollow transducers are made for this purpose.

M-mode display systems image the movements of organ interfaces with time. The interface movements are visible in the A-scan display but the exact sequence of movement is difficult to envisage from the echogram. To visualize these movements, the echo amplitude is used to intensity modulate the electron beam current of a storage CRT. The vertical beam deflection is proportional to the penetration of the ultrasonic pulse into the body. After each ultrasonic pulse, the horizontal position is incremented slightly to give a slow horizontal time base. Thus the periodic movement of a reflector in the ultrasonic beam is imaged as a wavy horizontal line. Movements at right angles to the beam are not detected. This type of display is particularly useful in cardiology for

examining the cyclic movements of the various heart components. Movements of the mitral valve and aortic wall can indicate abnormal functioning conditions. The velocity component of a moving part can be determined from the slope of the M-mode display. This can also be determined from the doppler frequency shift in the appropriate range gated echo. Excellent reviews of heart function examination techniques are given by Gottlieb et al. (1975) and by Ferrer et al. (1975).

One other form of CRT display is based on deflection modulation. It is particularly suitable for linear scans or sector scans. A storage CRT beam is deflected as it would be for a B-scan, but the beam writes continuously. The echo amplitude signal is used to deflect the beam from the straight line motion. Detected echoes are then represented as small deflections of the CRT trace which is scanned in synchronism with the transducer as it scans the region (c.f. Fry et al. 1968, Kossoff 1974).

1.4 IMPROVEMENTS TO CONVENTIONAL SYSTEMS

Many experimental ultrasonic imaging systems are being investigated and some have been manufactured commercially (c.f. Utsunomiya 1977). Discussion of these is divided here into two parts. The systems which improve the display, resolution and accuracy of conventional pulse-echo systems are discussed in this section. In the next section, some unconventional imaging systems are described.

In conventional systems, display problems arise because the dynamic range of useful ultrasonic echoes is greater than 100 dB. The receiving system usually compresses this range to 40 dB, which is adequate for A-scan displays. The various receiver characteristic design compromises, necessitated by the uncertain tissue-ultrasound interactions, are reviewed by Wells (1974). The grey scale intensity display used for B-scan imaging is limited to a dynamic range of 26 dB since only 10 shades of

grey can be discerned by the human eye. Yokoi and Ito (1972a,b) converted the echo amplitude directly to a colour B-mode display, whereas Baum (1973) obtained a grey scale image which was subsequently converted to a colour image. The system described by Baum incorporates 12 colours to obtain a 36 dB dynamic range and it has proved useful for breast lesion detection. Liebesny and Lele (1973) and Kossoff (1974) have also used colour to enhance B-scan images. The use of colour images is also quite common in X-ray axial tomograph machines, which display cross sectional images on a CRT (c.f. Ledley 1976).

The use of a computer to prepare B-scan tomographs for image planes other than those measured is discussed by Robinson (1972a,b). A set of parallel tomographs (B-scan images) is measured and stored in a computer. An image plane inclined to the measured set intersects each measured image plane on a line. The desired image is formed by interpolation between the measured values on the lines of intersection. Thus an automated measurement system can be utilized by a technician to obtain results from which a physician can later examine any desired plane within the original isonified volume.

Improved azimuthal resolution can be obtained with an acoustic lens. A variable focus lens is implemented electronically with signal phase shifters or time delays. A prefocussed transducer can be focussed over an extended axial range when the transducer disc is partitioned into a set of concentric rings or annuli to form an annular array. An echo signal originating on the axis of an annular transducer arrives at all points on the annulus at the same instant. Thus an annular transducer is focussed at all points along its axis. The signal from each annulus of the annular array is delayed (or phase shifted) and then summed with the delayed signals from the remaining annuli in the array. The variable focus is obtained by selecting the appropriate time delay for the signal from each annulus in the annular array.

The focus of the annular array is varied so that the focal point is at a reflecting boundary when the echo is received from that boundary. The beam of the transducer is changed with time to produce the effect of a very narrow ultrasonic beam over an extended range. Changing the beam pattern with time is known as real-time beam forming.

Ueda et al. (1976) employ electronic signal processing to generate the required phase shifts for the echoes received at the annuli. Their method relies on discrete values of phase shift and hence is equivalent to the sampled echo signal methods. The sampling methods employ quantized delays and hence produce discrete foci. A small amount of defocussing is required to increase the depth of field so that adjacent focal regions are overlapped (c.f. Miller et al. 1974).

Robinson (1974) varies the focus continuously, rather than in steps. Thus strong focussing and good azimuthal resolution is obtained while avoiding the associated depth of field problem. A multisection network containing voltage dependent capacitive elements is employed to obtain a continuously variable phase shift for the signal from each annulus. The variable phase shift networks are difficult to set up and control. Thus, although the continuous focus method provides the best possible azimuthal resolution, the discrete foci method is usually employed because of its simplicity and stability.

The annular phased array is also used to transmit ultrasound as well as receive it. The focus of the transmitted beam cannot be varied during a single pulsed transmission because of the causal relationship between the focus and the time delays for each annulus. The central disc or the outer ring of the annular array can be used for transmission. However, reduced sidelobes (undesirable off-axis beams) are obtained when all annuli of the array are used and the array is shaded (i.e. a different excitation is applied to each annulus - this is the same principle as "illumination tapering" in antenna engineering, or apodisation in optics.) If too many transmission foci are used, a large number of transmissions

are required to examine the impedance discontinuities in the beam of the transducer. This takes a long time since the high resolution obtained by strong focussing is associated with a small depth of field. Also, the high transmitted intensities at the focus of a highly focussed transducer may cause tissue damage (c.f. Lele 1967). Several annular phased arrays in a mechanical water bath scanner can be used to form compound B-scans. Robinson (1972b) and Kossoff (1973) describe a wide aperture array which has many annular phased arrays arranged on an arc. This scheme increases the probability of detection for specular reflections from interfaces in the cross section plane, and also reduces the speckle (discussed later in this section) in the image.

The annular phased array is relatively simple but is usually employed in a water bath. A more complex surface contact scanner for sector B-scans has been described by Somer (1968, 1971). He produced a linear phased array from a segmented ultrasonic transducer and generated a sector scan by real-time beam forming. The system reported by Doornbos and Somer (1972) utilized a single control voltage to determine the beam direction for both transmission and reception. This eliminated the need for mechanical rotation of the transducer. The beam focus was not varied electronically. Their first system scanned a 90° sector along 32 or 128 directions at sector repetition rates of 30 or 8 times per second respectively. In the second prototype (c.f. Somer 1973), the option of a 30° or 90° sector was included with the 30° sector able to be positioned anywhere within the 90° sector.

Azimuthal scanning is combined with improved azimuthal resolution in a system developed by Thurston and Von Ramm (1973). In their system, the sector size and the number of directions to be probed within the sector is variable. A PDP11-20 digital computer calculates the sets the signal delays for each element of a linear phased array to achieve real-time beam steering and focussing.

The CRT beam deflection voltages for the sector scan display are also set up by the computer. The transducer (24 mm x 14 mm operating at 1.8 MHz and divided into 16 elements) is manually aligned to image the plane defined by the zenith beam which is weakly focussed over an extended zone. Focussing of the transmitted ultrasound is achieved in the near field of the transducer at distances of 6, 4, 8, 5 and 10 cm. This focussing sequence is claimed to reduce coherent image speckle (Von Ramm and Thurston 1976). Coherent image speckle is discussed later in this section. The depth of field required to overlap the focal zones is achieved with aspheric focussing. The echoes are received from 10 adjacent focal zones which are individually selected by means of the switched time delay associated with each transducer element. The time delay can be varied in 63 steps of 0.125 μs to give delays from 0 to 7.875 μs. Each tapped delay line is preceded by a logarithmic amplifier and a preamplifier. The delayed outputs from the 16 channels are summed and detected to give a signal for intensity modulation of the sector scan display.

The system can examine up to 256 directions within a 60^{o} sector at 20 sectors per second. Maximum range is 15 cm with a 1.5 mm resolution. The azimuthal resolution varies from 2 mm at close range to 4 mm at maximum range. The display parameters are easily changed by means of the computer keyboard and the system has proven useful for cardiac work (c.f. Kosslo, Von Ramm and Thurston 1976). Similar systems are now under manufacture.

A novel feature of Thurston's scanner is the addition of the received signals after logarithmic compression. The signal processing is equivalent to multiplying the received signals and then applying logarithmic signal compression. This method of nonlinear signal processing was first described by Lobdell (1968) who claimed several advantages for the method. Firstly, the signal range is compressed thus reducing specular reflection effects. Secondly, the overall S/N (signal to noise ratio) is

increased as the signals have higher amplitudes in the delay lines and are not as adversely affected by switching transients. Finally, the multiplicative process improves the image resolution by reducing the azimuthal sidelobes and giving an increased depth of field.

Eggleton and Johnston (1974) compare mechanically scanned pulse-echo imaging systems with phased array systems. After discussing and comparing various system parameters, they state that ultrasonic beam sidelobe levels are higher for the phased array transducer systems than for conventional transducers. They also claim that logarithmic signal compression increases this performance differential. Fortunately, most phased array systems use shaded arrays and nonlinear signal processing to obtain performance superior to that of conventional single transducer systems.

The echo signal detection of a phased array is improved with the crossed array type of transducer suggested by Kossoff (1973). A linear phased array would be employed for both transmission and reception, whilst a narrow orthogonal array would focus on reception only. Echoes reflected out of the cross section plane are more likely to be detected by the larger receiving aperture. Also, the zenith angle resolution is better than that of the simple linear phased array.

A large aperture technique is used by Maginness (1970) who utilized a two-dimensional array of transducers to measure the ultrasonic field scattered from a volume. The echo data from each small transducer is digitized and stored in a digital computer. The echoes originating from a chosen tomograph plane are digitally processed and an image of the scatterers in that plane is printed out.

Fraser et al. (1974) constructed a linear phased array which is focussed to a line for transmission. Another linear array at right angles to the transmitting array is focussed to a line which intersects the transmission focal line orthogonally. Thus a single volume element is

examined at the common focal point of the two orthgonal linear phased arrays. The phase shifts for each element of the phased arrays are obtained by ingenious signal processing techniques which involve processing linearly swept frequency signals with transversal filters. The system is capable of real-time imaging at up to 60 images (frames) per second for both echo and transmission imaging.

The advantage of a mutually perpendicular phased array is that the imaging resolution obtained is equal to the resolution obtained by a full aperture. This rather unexpected result is discussed in detail by Toraldo di Francia (1969) and by Gori and Guattari (1971). The practical utility of employing only a small number of receivers to synthesize a full aperture is that hardware requirements can be traded off against the computation required. The number of receiver elements determines, to a large extent, the amount of computation required to synthesize a particular beam pattern (c.f. Vilkomerson 1974).

Vilkomerson (1974) utilized a "thin" annular aperture to obtain diffraction limited resolution in acoustic imaging. The theory is the same as for the annular radio telescope (c.f. Carter and Wild 1964, Wild 1965). However, the acoustic imaging system uses coherent isonification and hence the image contains speckle ("noise" which looks like speckling on top of the image). In a later paper, Vilkomerson and Hurley (1975) discuss rapid computation methods (based on the FFT) for imaging with annular arrays. Another study by Macovski and Norton (1975) examined the use of an annular array for isonifying an image plane, and a linear phased array for receiving the acoustic echo signals. This particular combination is claimed to have highly desirable beam characteristics and to be suitable for a high-resolution B-scan imaging system.

The problem of spurious detail in acoustic images is discussed by Korpel et al. (1974). Objectionable spurious image detail is often present when isonification with a high level of temporal and spatial

coherence is used to obtain echoes from an object being examined. The sound field distribution close to the ultrasonic transducer also contributes to the undesirable detail. In addition interference caused by out of focus structures in the object produces Talbot images (c.f. Talbot 1836) which are largely eliminated by using short duration ultrasonic pulses for isonification. However, in some imaging methods, such as the liquid surface holographic methods discussed in section 1.5, the acoustic detector has a long response time and long duration bursts of ultrasound are required to obtain a reasonable response. Under these circumstances, diffuse illumination improves the image quality, but the improvement is limited by an apparently random interference pattern called speckle. In optical images of objects diffusely illuminated by laser light, the speckle detail size is of the order of the optical resolution which is much smaller than the structures of interest (c.f. Goodman 1975). Hence speckle need not be too objectionable for optical work. However, at the wavelengths employed for ultrasonic diagnosis, speckle can be quite objectionable.

Burckhardt (1978) has analysed the effect of many small (fractional wavelength) scatterers within a resolution cell of an ultrasonic scanning system. The random phases of the scattered ultrasound causes both constructive and destructive interference which gives rise to bright and dark detail in the speckle patterns. The speckle is easily seen in modern sector or linear scan systems with a grey scale image display. It is less obvious in compound B-scan displays or storage CRT displays. Although the speckle appears random, it is identical for sequential images obtained under exactly the same conditions. Hence, it is most objectionable in real-time linear and sector scanning systems. Korpel et al. (1974) show that a 10% change of frequency during isonification is sufficient to eliminate most spurious images, including speckle.

When the ratio of echo amplitude to speckle amplitude is calculated for an A-scan, Burckhardt obtains a ratio of 1.91 which compares favourably with experimental measurements of 2.0±.5. The echo signal to speckle amplitude is increased by employing a compound B-scan. The speckle pattern changes when the transducer is shifted, but the echo structures remain almost stationary. Thus the echo to speckle amplitude ratio is increased by image averaging, i.e. by the square root of the number of times each resolution element is isonified from a different direction. The improvement is almost as great if only the largest amplitude echo from a scattering volume is stored and displayed for the compound B-scan. Burckhardt proves that the transducer must be moved by at least half its width to obtain independent speckle patterns. Thus the improvement due to image averaging is limited.

Axial resolution is improved by minimizing the effects of the ultrasonic transducer response. An echo return is then represented as an impulse signal which has a high temporal resolution. Robinson (1966, 1967) developed numerical methods to eliminate the transducer response from seismic measurements. He defines two types of filters: dereverberation filters, and inverse transduction response filters. The dereverberation filters suppress multiple echo artefacts such as can occur in water bath scanners when the transducer-body separation is less than the required penetration into the body. The inverse transduction filter attempts to eliminate the effects of the finite time response of the transducers. The electrical echo signal is the convolution of two transducer responses with the transmitted impulse. Thus, the inverse transduction filter is also known as a deconvolution filter. McSherry (1972, 1973, 1974) has employed Robinson's Z-transform technique to design such digital filters. These were applied to ultrasonic cardiac M-scans, although not in real time. McSherry has also tried the technique on equidistant echoes

in adjacent beam positions of a sector scan. She significantly improved the angular resolution by this method.

If a received ultrasonic echo waveform is denoted by e(t), then ideally

$$e(t) = r(x)\ p(t-x/2V) \tag{1.5}$$

where r(x) is the reflection coefficient at range x, and p(t) is the total transduction impulse response for transmission and reception. The mean acoustic velocity throughout the region is V. Denote the Fourier transform with respect to t by $\mathcal{F}_t\{\ \}$, and define

$$P(\omega) = \mathcal{F}_t\{p(t)\} \tag{1.6}$$

The spectrum of the deconvolved echo waveform e'(t) is:

$$\mathcal{F}_t\{e'(t)\} = E'(\omega) = E(\omega)\left[\frac{P^*(\omega)}{|P(\omega)|^2+|\phi_n(\omega)|^2}\right] \tag{1.7}$$

where the asterisk denotes the complex conjugate, and $|\phi_n(\omega)|^2$ is the power spectrum of the noise which is contaminating the signal. The quantity in the square brackets is known as the Wiener filter. Now

$$E(\omega) = r(x)\ P(\omega)\ \exp(-j\omega x/2V) \tag{1.8}$$

So

$$E'(\omega) = \frac{r(x)\ \exp(-j\omega x/2V)}{1+|\phi_n(\omega)/P(\omega)|^2} \tag{1.9}$$

Thus when

$$|\phi_n(\omega)| \ll |P(\omega)| \tag{1.10}$$

it is seen that

$$e'(t) \approx r(x)\ \delta(t-x/2V) \tag{1.11}$$

For satisfactory operation, the Wiener filter requires a good S/N over a wide bandwidth. In practice, the limited bandwidth of the transduction process can be approximately doubled. The Wiener filter in the frequency domain can also be implemented as a convolution in the time domain. If only a few tens of terms are required for the sampled convolution in the time domain, then a real-time digital Wiener filter may be implemented by means of an analogue shift register device (e.g. a charge-coupled device - c.f. Barbe et al. 1978).

1.5 UNCONVENTIONAL IMAGING SYSTEMS

Conventional ultrasonic imaging systems acquire only one piece of information at any one instant. Real-time image displays are obtained when each piece of information is acquired in a very short time, i.e. high speed serial acquisition of data is used. The parallel acquisition of acoustic information is now possible because of developments in acoustical holography (c.f. Metherell et al. 1969, Metherell and Lamore 1970, Metherell 1971, Hildebrand and Brendon 1972, Wade 1972, Green 1974, Booth 1975). While all pertinent information concerning the acoustic field may be available at one instant, it is often accessed in a serial form. Also, in many experimental systems, equipment complexity is reduced by the serial acquisition of this information.

A real time ultrasonic camera was first proposed by Sokolov (1937). An immersed object is isonified by a continuous ultrasonic beam. Energy scattered by, or passed through the object is focussed by a lens, or formed as a shadow (proximity focussed) on a large piezoelectric plate. The rear surface of the piezoelectric plate is scanned by a primary electron beam in a vacuum. The secondary electron emission from a point on the rear surface of the plate is proportional to the ultrasonic pressure amplitude at the corresponding point on the front face of the plate.

The secondary electron current is used to modulate the intensity of a CRT beam which is scanned synchronously with the primary electron beam. The Sokolov tube, or ultrasonic camera, thus yields a real-time image on the CRT.

A practical system was constructed by Oschepkov et al. (1955). They improved the poor S/N of the system described above by adding an electron multiplier tube to detect the secondary electrons. Also, a large distance is required between the sound source and the object to reduce standing waves and uneven sound intensities in the near field. Multiple reflections in the body and the water bath are reduced by utilizing short time duration (~ 10 μs) isonification. Goldman (1962) developed an aperture plate to store the acoustic intensity values resulting from pulsed isonification so that the electron beam field scan rate could be much longer than the duration of the isonification.

Jacobs (1963) investigated the limitations of the Sokolov tube and developed a phase sensitive system based on an N.T.S.C. colour television receiver (Jacobs 1967, 1968a,b,c). The colour of the image is dependent on the acoustic phase at the camera aperture, and the colour intensity is proportional to the acoustic intensity. The system is especially useful for dark field transmission viewing. A discussion of techniques and results is presented by Jacobs and Peterson (1974).

The mechanical problems associated with large aperture piezoelectric transducers under vacuum on one side are discussed by Du Bois (1970) who formed an acoustic hologram on the front surface of a large aperture Sokolov tube. A photograph of the CRT yielded the hologram which was used to optically reconstruct the acoustic image. The photographic stage prevents real time operation.

Goetz (1970) demonstrated an electro-optical KDP (potassium dihydrogen phosphate) modulator which avoided the photographic step and allowed the real time reconstruction of holograms. The conventional CRT phosphor used in the Sokolov tube display was replaced by a KDP crystal. As with the conventional tube, the hologram is formed by the synchronously scanned electron beam. However, instead of a phosphor glow, the KDP crystal produces an optical phase change which is proportional to the electronically stored intensity of the electron beam. A laser beam is passed through the crystal twice, by reflection at the rear crystal face, and then through a lens to reconstruct the acoustic image, and its conjugate.

The piezoelectric camera plate linearly detects the sound field of the hologram. Thus the acoustic reference beam used to form the hologram can be replaced with an aberrationfree electrical reference. A plane wave reference is generated by multiplying the secondary electron beam current by a frequency which is slightly different from the isonification frequency. The difference frequency is added to a d.c. bias term to form a hologram which yields the image only, and not the conjugate image.

The acoustic images obtained from acoustical holography are usually distorted by irritating magnifications. The transverse magnification M_t is determined by the various object-hologram-image distances, the isonification wavelength λ_s, and the optical reconstruction wavelength λ_o. The longitudinal magnification M_ℓ is given by

$$M_\ell = \frac{\lambda_s}{\lambda_o} M_t^2$$

The hologram dimensions can be photographically scaled by a factor m. Leith, Upatnieks and Haines (1965) showed that if $m = \lambda_o/\lambda_s$ and $M_t = \lambda_o/\lambda_s$, then $M_\ell = M_t$ and both are independent of position. For most acoustic images, $\lambda_s >> \lambda_o$, and a very small hologram is required for $M_\ell = M_t$. The

reconstructed image is so small that it must be viewed with a microscope. Typically, a 30 cm diameter aperture for acoustics gives a 30 μm aperture for optical reconstruction.

El-Sum (1952) has examined the possibility of using these magnifications for microscopy. If a fixed magnification is required, then a real time electro-optical converter can be used to form the image. For real-time holographic imaging with $M_\ell = M_t$, the scale factor is limited by the resolution of the electron beam scanning the KDP crystal. Thus an acoustic frequency of the order of 1 GHz is required for distortion-free real-time imaging. At such a high frequency, attenuation limitations restrict the method to imaging thin specimens. In addition, the sensitivity of the piezoelectric camera plate is greatest when its thickness is half of the acoustic wavelength. Thus the plate must be very thin (~3 μm) and must withstand atmospheric pressure on one side and a vacuum on the other side. It is impractical to construct such a plate, and the camera is replaced by a thin reflecting film (c.f. Gabor, U.S. patent #548939).

A thin reflecting film undergoes a displacement proportional to the amplitude of the ultrasound incident upon it. Korpel and Desmares (1969) proposed the use of a scanning laser beam to examine the displacement of such a film on a solid-gas interface. The laser beam passes twice through a lens above the reflecting surface. The phase modulation of the laser beam is detected by a photo-diode behind a knife edge. The diode current then modulates a CRT beam which is scanned synchronously with the laser beam. Green Macovski and Ramsey (1970) utilized a parallel optical processing scheme to measure the displacements of a thin reflecting film. Their phase contrast imaging system can form the hologram or the image in real time, but the method is not as sensitive as the scanned laser beam method (c.f. Mueller 1971). More recently Mezrich and Vilkomerson (1975) have utilized a thin reflecting film and

a scanning laser readout as the basis of an acoustic phase contrast microscope.

Levitation of a reflecting liquid-gas interface is also used for holographic imaging. Such a phase contrast imaging system was first described by Sokolov (1937) who used a Schlieren system for optical viewing. In the original system, only the sharp edges of the images were visible since the Schlieren viewing system acts as a high pass spatial frequency filter. Lowenthal and Belvaux (1967a,b) found that the low frequency response of a phase contrast imaging system can be improved by the use of an optical Hilbert transform. An explanation of the process is as follows: A lens is used with coherent light to perform the Fourier transform operation (c.f. Goodman 1968). A diaphanous object which causes phase shifts in transmitted light, but has little affect on the transmitted amplitude, is referred to as a "phase object". The phase object is placed in the focal plane of the lens and parallel coherent light is shone through the object and lens. At the other focal plane of the lens, the light intensity variation is dependent on the phase shift of the light through the phase object.

In one-dimension, the phase object is represented as $f(x)$ and its Fourier transform as $F_o(\alpha)$. The spatial frequency spectrum of the radiation emerging from the phase object is

$$F(\alpha) = F_s(\alpha) + F_o(\alpha) \tag{1.12}$$

where $F_s(\alpha)$ is the spectrum of the illumination source. In the phase contrast method, $F_s(\alpha)$ is attenuated and phase shifted by $\frac{\pi}{2}$ with respect to $F_o(\alpha)$. In the dark field method, $F_s(\alpha)$ is blocked out (filtered). The low spatial frequency components of $F_o(\alpha)$ are also filtered so that the low frequency components of the phase object are imperfectly seen, i.e. the system acts as a high pass filter.

The Hilbert transform is implemented optically as a Fourier transform. Define the Hilbert transform of f(x) as

$$f_H(x) = \frac{1}{\pi}\int_{-\infty}^{\infty} \frac{f(y)}{y-x}\,dy$$

$$= f(x) \circledast (-1/\pi x) \tag{1.13}$$

so that its Fourier transform is

$$F_H(\alpha) = jF(\alpha)\ \mathrm{sgn}(\alpha) \tag{1.14}$$

The $\mathrm{sgn}(\alpha)$ function is realized as a π phase shift over half the filter plane. In two dimensions, two diagonally opposite quadrants of the filter plane introduce phase shifts of π. The advantages of the Hilbert transform processing are illustrated by considering the effect on a single spatial frequency of period b. Define

$$f(x) = \exp ja\cos(2\pi x/b) \tag{1.15}$$

where a is small for a diaphanous object.

$$f_H(x) \approx ja\sin(2\pi x/b) + \frac{1}{\pi}\ln\left|\frac{x-D/2}{x+D/2}\right| \tag{1.16}$$

The second term shows a concentration of light near the edge of the imaged object at $|x| = D/2$ where D is the extent of the object. The first term shows that the phase variations in the object are transformed into intensity variations in the image.

The effects due to the finite apertures of the optical processing system have not been considered since they are small. The effects of small phase variations in the optical system are severe and make the Hilbert transform difficult to implement. In particular, the reflecting liquid surface employed for acoustic holography must show only the interference patterns. The relatively high acoustic intensities at the liquid

surface cause it to bulge slightly and this introduces extra unwanted phase shift in the optical path.

The high pass spatial frequency characteristic of the phase contrast imaging system is considerably reduced if the image field is modulated onto a high frequency spatial carrier. The optical modulation has characteristics similar to vestigal sideband radio signals. The carrier modulation is produced by an acoustic reference beam interfering with the image field at the liquid surface. The reference beam amplifies the image field since the surface levitation is proportional to the ultrasonic intensity. Thus the image field at intensities as low as 1 mW/cm^2 is shifted up in spatial frequency and is passed through the optical system with relatively little distortion. The reference beam is usually pulsed to prevent streaming (fluid movement caused by sound waves) which causes the liquid surface to bulge. Such bulges cause severe aberrations and blurring of the image.

Mueller (1971) describes three liquid surface imaging methods. These are characterized by the acoustic field at the liquid-gas surface. The Fourier transform hologram method (Mueller and Sheridon 1966) forms the Fourier transform of the image at the liquid surface. Since the reference acoustic wave is rarely perfectly flat or spherical over the whole of the liquid-gas aperture, the reconstructed image is usually severely blurred. With focussed image holography, the ultrasonic image is focussed onto the liquid surface (c.f. Smith and Brendon 1969). The aberrations in the acoustic reference beam then cause less degradation of the optical image. Holosonics Ltd have manufactured a unit for breast examinations based on focussed image acoustic holograms.

A through transmission system for body examinations is reported by Erikson et al. (1975), who indicate that the images obtained using their through-transmission acoustical holography system are not as clear as acoustic B-scan images for the same patients.

The third method is attributed to Green (1971) who utilized a diffraction grating in place of the reference beam. The first order of the diffracted field produced a liquid surface levitation which was proportional to the intensity of the focussed image field rather than the amplitude.

In the methods discussed above, the distribution of the acoustic image field is acquired by parallel, or rapid serial sampling. Provided the distribution of intensity over the image field is not changing with time, it can be serially sampled at a slow rate. The phase and amplitude of the acoustic field can be accurately deduced from quadrature samples (c.f. Linden 1959). The data values can be used to intensity modulate a scanned light source which forms a hologram on a photoplate. Alternatively, the image may be reconstructed computationally. The imaging aperture may be sampled by an array of transducers, or else by a moving ultrasonic transducer (c.f. Hildebrand and Haines 1969). A scanned acoustic imaging system which is similar to side-looking radars has been described by Smith and Brendon (1968). The transmitting and receiving transducers are scanned together so as to yield a hologram which appears to have been formed by acoustic radiation at twice the frequency. Hence the resolution is doubled. Kock (1970) extended the technique to include pulse echo ranging.

Hildebrand and Haines (1969) examined the possibility of moving the transmitter and receiver independently, but the formation of the hologram became complex. A stationary crossed array of transducers was proposed by Wells (1970). More general schemes have also been proposed by Kreuzer and Vogel (1969) and by Marom et al. (1971).

The systems discussed so far have been based on imaging acoustic fields in a plane aperture. Korpel (1966, 1968) has described an acousto-optical volume interaction in which the amplitude and phase of a

sound beam are modulated onto laser light passed through the sound beam. The image of the sound distribution is obtained from the laser beam by optical processing. The ultrasound produces periodic changes in the optical refractive index by periodically changing the density of the isonified liquid. The periodic changes act as an optical grating and the laser beam undergoes Bragg diffraction. Korpel's method requires careful alignment of the optical system so that constructive optical interference of the scattered light occurs when the two beams are inclined at particular angles. The windows in the sides of the isonification water tank must be made from optical flats. Quate et al. (1965, 1968) devised a variation on the method by utilizing the acousto-optical interaction in birefringent crystals. The required interaction occurs when the acoustic wavenumber in the crystal is equal to the difference in magnitude between the ordinary and extraordinary optical wavenumbers in the crystal. The interaction is colinear and a high modulation efficiency is obtained over a long interaction length. The emerging beams are orthogonally polarized so the information carrying beam can be separated by polarization filtering. Bragg diffraction imaging is being utilized for ultrasonic microscopy at wavelengths less than 1 μm. Such mechanical observations of biological tissues and living specimens can be compared directly with simultaneous optical observations obtained by the same instrument.

1.6 ULTRASONIC TRANSMISSION IMAGING

One of the early attempts to replace X-rays with ultrasound for diagnostic purposes, formed images from ultrasound transmitted through bodies. Dussik (1942, 1947) ultrasonically irradiated the head and measured the intensity of the sound waves emerging from the opposite side of the head. A two-dimensional grey scale image was obtained by scanning transmitting and receiving transducers over each side of the head. The

image shading is proportional to the received ultrasonic intensity. Dussik claimed that an outline of the ventricles of the brain was evident in these images, and that possibly brain tumours could be located. These results encouraged others (Ballentine et al. 1950) to experiment with a similar apparatus. The apparatus is described by Huetter and Bolt (1951) who concluded that "a preliminary evaluation indicates that the echo-reflection is considerably less promising (than their transmission method) for general ventriculography, mainly because of the small amount of reflection at the interface between tissue and ventricular fluid".

A critical analysis of the transmission experiments was carried out by Güttner, Fielder and Pätzold (1952). They imaged an empty skull filled with water and obtained the same results as other researchers. They concluded that ventriculography was not possible because the attenuation masking effect of the skull is much greater than the attenuation due to the brain.

Despite this critical analysis, Ballentine et al. continued to investigate ultrasonic transmission through the skull, and favourable interpretations of their work were reported by Dussik (1954), and by Herrick and Krusen (1954). However, Ballentine et al. (1954) were less enthusiastic and concluded that parallel developments in radioactive isotope imaging were more promising for brain tumour detection. They did not preclude the use of ultrasonic transmission intensity imaging in other body regions. Greenleaf et al. (1974) formed acoustic transmission absorption images, but later Duck (1975) reported that results for even soft tissue were unsatisfactory. These conclusions support the findings of preliminary work for this thesis which showed that the major contribution to the acoustic transmission attenuation is due to reflections at the acoustic impedance boundaries between organs, especially at low ultrasonic frequencies (1-5 MHz). At higher frequencies, the attenuation

due to the tissue is more pronounced but transmission intensity imaging is still inaccurate because of acoustic reflections at tissue boundaries. The only acoustic transmission parameter that is unaffected by the reflections at tissue boundaries is the time taken for an acoustic pulse to propagate from the transmitter through the body to the receiver. This propagation time delay T is dependent only on the acoustic velocity V of the regions through which acoustic pulse travels:

$$T = \int_{\substack{\text{propagation} \\ \text{path}}} \frac{d\eta'}{V} \qquad (1.17)$$

where an element of the acoustic propagation path is represented by $d\eta'$.

Rich et al. (1966) measured the ultrasonic propagation time for transmission through samples of bone immersed in water. They scanned two opposing transducers across the region containing the bone, and at the same time, plotted the propagation time delay as a function of transducer position. This record is termed a "time delay projection" (analogous to the X-ray projections discussed in chapter 2). The calcium content of the bone (determined from chemical analysis) was found to correlate reasonably well with the area under the time delay projection.

Heyser and Le Croisette (1974) produced two-dimensional images in which the shading was proportional to the ultrasonic propagation time delay through the body. These ultrasonic time delay shadowgraphs (c.f. X-ray intensity shadowgraphs) were generated by mechanically scanning the transmitting and receiving transducer across the body in a raster fashion. The time measurement was accomplished by using swept frequency acoustic transmissions in the manner discussed in section 4.4 of this thesis.

Researchers at the Mayo Institute approached the time delay measurement problem directly: Johnson et al. (1975) and Greenleaf et al. (1975) employed a computer controlled transient recorder (Biomation 8100 model) to digitize the received signal. The computer was then used to determine the arrival time of the acoustic pulse.

Another approach was taken by Glover and Sharp (1977) who used a high gain preamplifier which saturates when a pulse is received. The time taken for the preamplifier output to exceed a threshold level is measured to determine the propagation time delay. Both they and the Mayo group use the expression "time of flight profile" to describe time delay measurements as a function of position. However, the term "time delay projection", coined earlier by Rich et al. (1966), is employed throughout this thesis.

1.7 ULTRASONIC TRANSMISSION TOMOGRAPHY

When X-rays are used for diagnostic purposes, regions of quite different density, such as bones and tissue, are easily differentiated. However, the differences between various tissue types are much more difficult to discern. This is especially true for X-ray examinations of the breast where a radiation dose of up to one Rad may be necessary to produce clearly discernible differences in the shadowgraph. X-ray imaging in the form of computerized axial tomography (discussed in chapter 2) delineates between many types of tissue and tumour but the patient radiation dosage is of the order of a few Rads.

Ultrasonic diagnostic imaging does not appear to cause damage at the intensity levels used in current clinical practice. Exposure to X-rays at any intensity level is associated with a finite probability of cell damage (and cancer) whereas ultrasonic damage has (so far) been found only above a threshold in excess of diagnostic intensities (c.f. many of the papers in the symposium edited by Hazzard and Litz, 1977). Thus ultrasonic diagnosis is to be preferred to X-ray examination.

Ultrasonic images are degraded by refraction and range errors because the acoustic velocity is different in various regions of the body. In addition, if the body region examined does not exhibit sharp changes in acoustic impedance (i.e., the region may be homogeneous or

diaphanous) then the amplitude of the echo pulse is very small and the transmitted intensity is increased to produce detectable echo signals. The intensity must be limited to well below the levels at which acoustic damage occurs in the body. Thus examination of diaphanous body regions is best performed using acoustic transmissions which can be much less intense (c.f. fig. 1.1). The acoustic propagation time delay was shown (in section 1.6) to be similar to X-ray intensity measurements in as much that the former is independent of reflections (or echoes) at the various body interfaces intersected by the ultrasonic beams. The possibility of processing ultrasonic time delay measurements in a manner similar to X-ray computed tomography is examined in this thesis.

1918	Sonar	Langevin
1929-1944	Real time ultrasonic imaging	Sokolov, Pohlman
1942	Pulse-echo non-destructive testing	Firestone
1942-1950	Ultrasonic transmission imaging in tissue	Dussik, Hueter, Ballentine
1950-1952	Pulse-echo medical imaging	Wild, Reid, Howry, Bliss
1950-1969	Medical scanning	Howry, Wild, Kikuchi, Wagai, McKinney
1954-1957	Heart imaging	Hertz, Edler, Satomura
1958-1965	Obstetrics and gynaecology	Donald, Kossoff, Wagai
1956-1965	The eye	Baum, Greenwood, Oksala, Ossoinig, Oksala
1964-1968	Medical imaging with the Sokolov tube	Jacobs
1965-1969	Acoustical Holography	Mueller, Metherell, Smith, Brendon
1967	Time delay spectrometry	Heyser.

Table 1.1 A tabulated history of notable developments in ultrasonic imaging.

Ultrasonic Frequency Irradiation					
Intensity W/cm^2	Mhz	Time min.	Biological effect investigated	Result	Reference
<1050	2.7	~.1	Brain damage	+	Basauri and Lele (1962)
1000	1	.5	Permeability changes in frog muscle	+	Hughes et al. (1963)
~400	.6-2.7	~.1	Nerve block	+	Lele (1963)
7-120	1-3	~.3	Nervous conduction changes	+	Takagi et al. (1960)
60	1	~.5	Non-thermal liver damage	+	Curtis (1965)
30-40	1	<.7	Nerve block	+	Fry et al. (1950)
30	1	<8	DNA degradation	+	Hawley et al. (1963)
~25	3	2	Non-thermal damage in Daphnia	+	Wells (1968)
20	3	10	Permeability changes in the inner air	+	James et al. (1963)
~10	.3	1-2	Mortality in Spirogyra	+	Wood and Loomis (1927)
.4-4	.8	.1-20	Abnormalities in the development of Drosophila	+	Fritz-Niggli and Böni (1950)
~2	.8	<10	Nerve block	+	Herrick (1953)
<1.5	1-3	~10	Damage in physiotherapy	-	Patrick (1966)
.1-1	3.6	~5	Tissue regeneration rate	+	Pond and Dyson (1967)
~.05	15	15-30	Brain damage	-	French et al. (1951)
~.01	2.25	~20	Genetic and other damage in mice	-	Smyth (1966)
.0082	2	60	Chromosome damage	*	Macintosh and Davey (1970, 1972)
~.005	~2	-	Abnormalities in the development of rabbits	-	Holmes and Howry (1963)
~.0015	2.5	60	Brain damage in young kittens	-	Donald et al. (1958)
~.0015	~2	1440	Abnormalities in the development of frogs and perch	-	Andrew (1964)
~.001	2	30-90	Brain damage	-	Garg and Taylor (1967)

* A positive result was claimed but later withdrawn after contrary results by others (Buchton and Baker (1972), Coakley et al. (1972) and Brock et al. (1973).

Table 1.2 Results of biological experiments involving ultrasonic isonification.

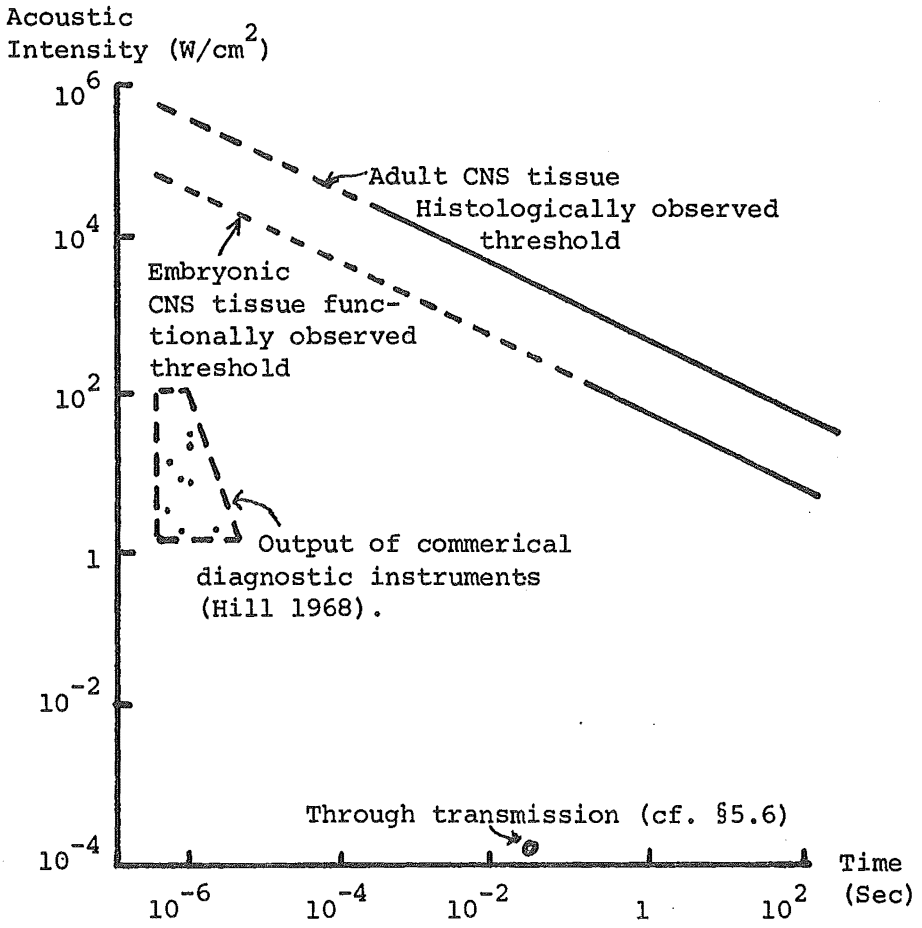

Fig. 1.1 Ultrasound damage thresholds (c.f. Dunn and Fry 1971)

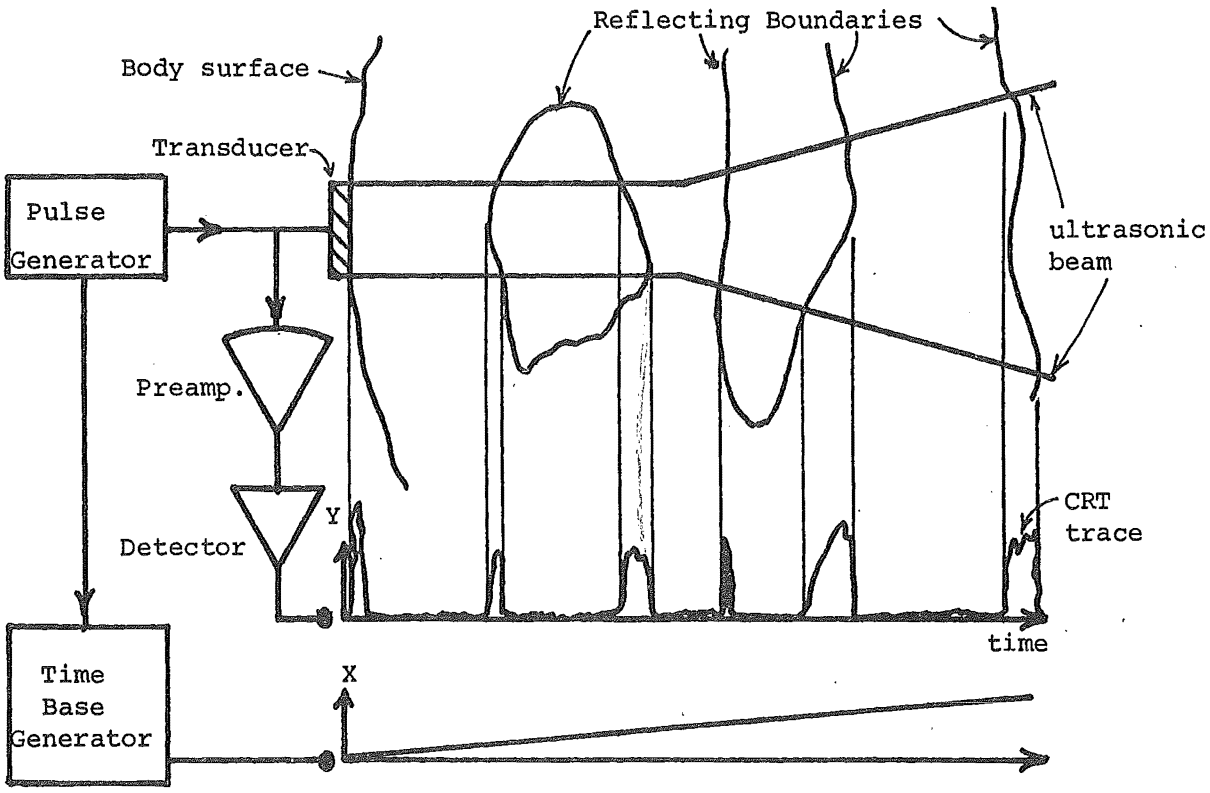

Fig. 1.2 Schematic of pulse-echo A-scan operation.

CHAPTER TWO

MEDICAL X-RAY IMAGING

2.1 BODY SECTION IMAGING METHODS

The medical diagnostic use of X-rays (or Röntgen rays) has developed since the photographic detection of this penetrating radiation by Röntgen in 1890 (reported 1895). The shadowgraphs used by physicians depict three-dimensional anatomical structures as two-dimensional photographs. The anatomy traversed by a single X-ray determines the intensity of the ray at a point in the photographic film. The density or "blackness" of the developed film at that point is dependent on the integral of the incremental X-ray attenuation along the X-ray path to that point. Thus integration with respect to one dimension enables three-dimensional data to be viewed pictorially in two dimensions.

A number of methods have been employed for the unambiguous display of three-dimensional information. Baum and Greenwood (1961) produced a set of two-dimensional transparencies from a set of adjacent parallel sections. The transparencies were stacked side by side to build up an image of the volume. Robinson (1972a,b) digitized the information on such a set of transparencies and then used a computer to calculate and display the density distribution in a chosen plane (c.f. section 1.4). The image plane can be manipulated to display some physiological detail which can be viewed directly rather than through interposed opacities present on the transparencies.

Another method known as tomosynthesis (Grant 1972) utilizes about 20 shadowgraphs taken at even angular spacings around the volume to be imaged. Each shadowgraph is placed around the edge of a cylinder in a position corresponding to that in which it was exposed. A light source is placed behind each shadowgraph so that the light passes through the shadowgraph to converge at the position of the X-ray source used to form the shadowgraph. Thus the information on the shadowgraph is "back projected" along the paths of the X-rays. When all the shadowgraphs are back projected at the same time, a real image is formed inside the

cylindrical volume. Plane images are viewed by positioning an opaque screen in the desired plane of the image. The image is not blurred in directions parallel to the axis of the cylinder but it is blurred in the planes perpendicular to the axis. An image at any point in a plane can be regarded as the superposition of the shadowgraph densities produced by all the X-rays which passed through the corresponding point in the body. As the number of shadowgraphs becomes very large, the imaged point is spread as 1/r. This is explained in detail in section 2.2, where the blurring of a "layergram" is examined.

Holographic methods for storing three-dimensional radiological information require a coherent X-ray source which has yet to be developed. However, a number of X-ray shadowgraphs have been holographically superimposed at optical wavelengths to yield a "pseudo-hologram" (c.f. Redman et al. 1968, Groh and Kock 1970). The pseudo-holograms form real and virtual images when coherently illuminated, but they exhibit discontinuous perspective, i.e. parallax changes occur in quantized steps.

Stereo presentation of two appropriately angled shadowgraphs has been used for three-dimensional imaging but it lacks flexibility since the image does not exhibit parallax. Real-time stereo viewing alleviates this problem since the patient is positioned to obtain the best view of the physiology being examined. Stauffer et al. (1962) utilized two X-ray-television fluoroscopy systems appropriately aligned to yield such real time stereo views. The stereo views are stored on video tape for later comparisons..

Many early X-ray researchers (c.f. Etter 1965, Ch.2) unsuccessfully attempted to focus X-rays in order to sharply image only a single plane in the patient. Movement of the X-ray source and X-ray plane relative to the patient can be used for this purpose. The contributions to the shadowgraph of planes other than the "focussed" plane are blurred.

Appropriate motions can simulate the action of a lens and thus produce an X-ray tomograph.

2.2 BLURRED TOMOGRAPHY

Image blurring methods for simulating the action of a lens are discussed in the next two sub-sections. The first sub-section is concerned with longitudinal tomography (which is used to image sections lengthwise in the body), and the second sub-section describes transverse tomography (in which transversal body cross sections are imaged). A mathematical description of transverse tomography is developed in the third sub-section.

2.2.1 Longitudinal Tomography

Three basic types of motion are employed to enhance a particular focal image plane in a shadowgraph while blurring other unwanted image planes. These are one-dimensional linear blur, two-dimensional blur, and magnification blur.

Linear blur is included in a patent by Bocage (1922). Bocage's scheme A (c.f. Peters 1973) is shown diagramatically in fig. 2.1. Referring to fig. 2.1(a), the X-ray source in position 1 projects points A and B in the focal plane onto points A_{I1} and B_{I1} on the X-ray plate. Points C and D in another plane, parallel to both the focal plane and the X-ray plane, are projected to C_{I1} and D_{I1} respectively. When the X-ray source is moved to position 2, as shown in fig. 2.1(b), the X-ray plate is moved in the opposite direction so that the image of A remains fixed, i.e. A_{I2} is superimposed on A_{I1} in the shadowgraph formed on the X-ray plate. If the X-ray source moves in a plane which is parallel to the focal plane and the X-ray plate, then the image of B also remains fixed in the shadowgraph, while C and D are imaged separately at C_{I2} and D_{I2}. As the X-ray source and the detector are moved linearly from position 1 to

position 2, C_{I1} moves linearly to C_{I2} in the shadowgraph. The image of C is linearly blurred, but points in the focal plane (such as A and B) are not blurred. The further a point is from the focal plane, the more pronounced is the blurring. Since the X-ray source and plate move in one dimension, such a scheme is termed one-dimensional linear blur.

Two-dimensional blur is obtained by the successive application of one-dimensional blurs. e.g. if the X-ray tube describes an arc in the source plane, then the arc can be considered as a series of linear sections. The X-ray plate describes the opposite motion. Bocage's scheme B (c.f. Peters 1973) outlines two-dimensional blurring in which the X-ray source and X-ray plate move in either circles, crosses or spirals.

The principles of magnification blur are illustrated in fig. 2.2. With the X-ray source and detector in position 1, points A and B in the imaged plane appear as A_{I1} and B_{I1} in the shadowgraph. When the source and detector are moved to position 2, A_{I1} and A_{I2} are superimposed as are B_{I1} and B_{I2}. Points out of focus such as C and D, move from C_{I1} and D_{I1} to C_{I2} and D_{I2} during the movement from position 1 to position 2. The distance A_{I1}-B_{I1} is equal to A_{I2}-B_{I2} whereas C_{I1}-D_{I1} is not equal to C_{I2}-D_{I2}. Thus, an out of focus plane undergoes a change of magnification which blurs its details in the shadowgraph. Points along the line 0-0' are not blurred.

In Bocage's method C (c.f. Peters 1973), shown diagramatically in fig. 2.3, the X-ray source and X-ray plate are attached to each end of an arm and are maintained in a fixed orientation by constrained pendulums. The apparatus arm is pivoted in the focussed plane and produces a linear blur as well as magnification blur.

One problem with Bocage's schemes is that the X-ray beam is always directed downwards rather than through the region of interest. Thus the X-ray dosage absorbed by the patient is higher than necessary. The X-ray beam pattern also spatially modulates the blur function of the various

out of focus planes. This effect is readily envisaged by considering the effect of using a narrow X-ray beam in Bocage's scheme A (shown in fig. 2.1). The effects of the downward directed beam were removed by Ziedses des Plantes (1932, 1971) and Grossmann (1935) who directed the X-ray beam into the region of interest throughout the blurring motion.

Ziedses des Plantes' apparatus prescribed two-dimensional blurring motions and was described as a 'planigraphic' apparatus by the inventor who developed it in 1921. The apparatus is the same as Bocage's scheme B but the X-ray tube is always directed at the X-ray plate. This is illustrated in fig. 2.1.

Grossmann's apparatus is based on Bocage's scheme C with the X-ray tube fixed firmly to the pivoting arm rather than directed downwards. Grossmann's method (included in fig. 2.3) has been widely used, and the word 'tomography', coined by Grossmann, is now used for all methods of body-section imaging. The shadowgraph (or shadowgram) produced by the apparatus is called a tomograph (or tomogram).

Vallebona (1930) produced the first practical medical technique in which the X-ray source and plate remain stationary while the patient is rotated about an axis. Unfortunately, the only portion of the patient in focus for the whole movement lies along the axis of rotation, i.e. only a line is clearly imaged. A modification was later published in which the patient lies still and the X-ray source and plate are rigidly attached to opposite ends of a pivoting arm. The apparatus is similar to Grossmann's (c.f. fig. 2.3) but has the X-ray plane fixed to the arm rather than constrained in a horizontal position.

Andrews and Starva (1937) mathematically examine the various tomographic schemes with respect to the desired image and the degree of blurring from the undesired images. They conclude that Grossmann's apparatus gives similar results to Ziedses des Plantes' apparatus when the latter is constrained to a linear motion rather than the usual two-dimensional motion. The possibility of pivoting Grossmann's apparatus at a

point rather than on a single axis does not appear to have been examined. Extensive information has been published (c.f. Edholm 1960, Stieve 1972) on the best motions for imaging various parts of the body.

Several parallel body planes can be imaged at the same time of a stack of X-ray plates is used as a detector. As was shown by Andrews and Starva (1937), multi-section radiography is possible for both longitudinal and transverse tomography, provided magnification blurring is not used. The X-ray plates attenuate the X-rays and the plates nearest the body are over exposed while those furthest away are under exposed. Image intensifying screens are used to increase the effective exposure of the lower plates, but these also attenuate the X-rays and a higher radiation dosage is needed. Takahashi (1965) concluded that the best results are obtained by using X-ray plates of different sensitivity at different positions in the stack.

2.2.2 Transverse Tomography

When radio-therapy is used to destroy regions of malignant tissue, it is desirable to accurately locate the tumour. The treatment is planned to minimize the damage to the surrounding healthy tissue. When a transverse body section is imaged by the longitudinal tomographic methods just described, the X-ray beam must traverse the full length of the body. There are two disadvantages associated with this (c.f. Vallebona 1955, Amisano 1955). Firstly, the X-ray dosage must be increased to allow for the increased X-ray attenuation through the body length. Secondly, the whole body contributes to the information on the X-ray plate, and the image of the focal plane is overlaid by many unwanted blurred images. These unwanted images which are superimposed on the desired image are known as Talbot images (after Talbot 1836 who first described them for optical imaging).

Vallebona (1955) reviews the different approaches to transverse tomography during the period 1938 to 1947. The first practical transverse tomographic apparatus was demonstrated by Vallebona (1947), whose method (shown schematically in fig. 2.4) is still in general use although computed axial tomography (described in section 2.4) is replacing it. Refer to fig. 2.4. The X-rays beamed transversally through the body strike the X-ray plate obliquely, rather than nearly perpendicular as in longitudinal tomography. The X-ray plate and patient rotate synchronously about two separate parallel axes. The imaged focal plane and the X-ray plate are both orthogonal to the axes. The two axes and the X-ray source are coplanar, and a straight line between the source and the centre of the X-ray plate also passes through the centre of the focal plane.

The blurring operation is similar to longitudinal tomography since points in the focal plane projected onto the X-ray plate remain invariant during the rotation. Points above and below the focal plane undergo cyclic blur during the rotation. The relative motion between the patient, X-ray plate and source determines the blurring. Hence the simple apparatus shown in fig. 2.4 is modified so that the patient remains stationary while the tube and X-ray plate rotate.

When the angle of declination between the X-ray beam and the axes is zero, the blurred tomograph contains information derived from the focal plane only, and none from the adjacent body regions (c.f. Takahashi 1965). Such an arrangement forms an axial transverse tomographic apparatus and the imaging process is described exactly. A mathematical description is developed in the next subsection.

2.2.3 A Mathematical Description of Axial Transverse Tomography

Practical axial transverse tomographic systems employ a collimated X-ray beam to irradiate a thin body section. The X-rays enter the edge of the X-ray plate and are progressively absorbed as they propagate across the X-ray plate. The progressive absorption produces a non-uniform exposure across the plate. Ideally, a single X-ray (i.e. a very narrow beam) would give rise to a single line of uniform exposure across the X-ray plate. This is actually attained by Peters (1973, 1974a) who replaces the X-ray plate with a light emitting image intensifying screen (c.f. fig. 2.5). The light is collected by a lens system which focuses each point on the screen to a line on the photographic plate. The photographic plate is rotated in synchronism with the body to form a blurred image (termed a 'layergram' by Bates and Peters, 1971). The spreading process used to form the layergram is shown diagramatically in fig. 2.6(a).

The optical density D of a developed photographic (or X-ray) film is

$$D = -\gamma \log_{10} E \tag{2.1}$$

where γ is the slope of the linear part of the Hurter-Driffield curve (i.e. the H and D number) and E is the exposure (c.f. Dainty and Shaw 1974). The exposure is the product of the light (or X-ray) intensity and the exposure time. For the axial transverse tomographic apparatus, the intensity of the X-rays emerging from the body is

$$I = I_0 \exp -\int_{-\infty}^{\infty} \omega(x,y)\, d\eta \tag{2.2}$$

where $\omega(x,y)$ is the X-ray absorption coefficient at point (x,y) in the imaged plane through which the X-rays pass (hereafter called the imaged plane), and $d\eta$ is an element of the X-ray path. Note that $\omega(x,y)$ is zero outside the body. The film density is

$$D \propto \int_{-\infty}^{\infty} \omega(x,y)\, d\eta \tag{2.3}$$

Using a parallel X-ray beam and the geometry shown in fig. 2.7(a), we define the X-ray projection of the imaged plane as

$$f(\xi,\phi) = \int_{-\infty}^{\infty} \omega(x,y)\, d\eta \tag{2.4}$$

where ϕ is the angle of rotation of the body relative to the parallel X-ray beam, and ξ is the distance measured perpendicular to the X-rays and in the plane of the X-rays. Thus the projection $f(\xi,\phi)$ is a measure of the X-ray attenuation along a line parallel to the η axis (at angle ϕ) at a distance ξ from the origin at the centre of rotation (c.f. fig. 2.7a).

The term "back projection" (mentioned in section 2.1) is the process used to form a layergram. This process is now described mathematically. The X-ray projection measurement at (ξ,ϕ) is dependent on the X-ray absorption at points (x,y) in the imaged plane where x and y satisfy

$$\xi = x \cos\phi + y \sin\phi \tag{2.5}$$

The process of assigning $f(\xi,\phi)$ to all points in the image (x,y) satisfying (2.5) is known as back projection. If the values of $f(\xi,\phi)$ assigned to (x,y) are superimposed for all values of ϕ, the result is a layergram $h(x,y)$ given by

$$h(x,y) = \int_{0}^{\pi} f(\xi,\phi)\, d\phi \tag{2.6}$$

where x,y,ξ and ϕ satisfy (2.5) and ϕ is restricted to $[0,\pi)$ since

$$f(\xi,\phi) = f(-\xi,\phi+\pi).$$

The X-ray absorption coefficient $\omega(x,y)$ is expressed in polar coordinates as $\lambda(r,\theta)$, and the layergram $h(x,y)$ is denoted by $g(r,\theta)$ in polar coordinates. The layergram is now considered in terms of the X-ray paths passing through a single point (r,θ) in the imaged plane. The X-ray travelling through (r,θ) is measured at (ξ,ϕ) when

$$\xi = r\cos(\theta-\phi) \tag{2.7}$$

The back projection of $f(\xi,\phi)$ through the point (r,θ) in the image yields the layergram when the variables satisfy (2.7) and the back projections are superimposed for all angles ϕ. Referring to the geometry shown in fig. 2.8, $g(r,\theta)$ and $\lambda(r,\theta)$ are seen to be related by

$$g(r,\theta) = \int_{-\infty}^{\infty}\int_{0}^{\pi} \lambda(r',\theta')\,d\tau\,d\chi \tag{2.8}$$

$$= \int_{0}^{\infty}\int_{0}^{2\pi} \frac{\lambda(r',\theta')|\tau|}{|\tau|}\,d\tau\,d\chi \tag{2.9}$$

The integral (2.9) is now evaluated in cartesian coordinate form:

$$h(x,y) = \int_{-\infty}^{\infty}\int_{-\infty}^{\infty} \omega(x,y)\,[(x-x')^2+(y-y')^2]^{-\frac{1}{2}}\,dx\,dy \tag{2.10}$$

$$= \omega(x,y) \circledast (x^2+y^2)^{-\frac{1}{2}} \tag{2.11}$$

Reverting to polar coordinates, (2.11) yields

$$g(r,\theta) = \lambda(r,\theta) \circledast |r|^{-1} \tag{2.12}$$

It is thus seen that even an ideal layergram (i.e. one that is formed by radiation which passes through only the imaged plane) is highly blurred. Each point in the ideal image $\lambda(r,\theta)$ is spread out by convolution with the point spread function $|r|^{-1}$.

With purely mechanical and photographic imaging apparatus, $h(r,\theta)$ is the best image one can form. However, if sophisticated optical processing is employed - or, better still, a digital computer is used - the ideal image $\lambda(r,\theta)$ can be deconvolved from $g(r,\theta)$, as is discussed in the next section.

2.3 DEBLURRED TOMOGRAPHY

Several of the equations used to construct ideal images from projections were first developed by Radon (1917) for solutions of gravitation problems. Similar equations were also developed by Bracewell (1956) in an attempt to identify microwave emitting regions on the surface of the sun. Cormack (1963, 1964) investigated X-ray projections from 1953 onwards and produced a mathematical method for exact image reconstruction which he applied to several simple phantoms. Processing of X-ray projections was further analysed by Tretiak Eden and Simon (1969) and by Bates and Peters (1971). Finally in 1972, EMI Ltd produced the first X-ray CAT (computer aided tomograph) scanner which was used for radiographic brain scanning (Hounsfield 1972, 1973).

Similar mathematical image reconstruction techniques were developed independently for optics (Rowley 1969, Berry and Gibbs 1970, Juginger and Van Haeringen 1972) and for electron microscopy where the structure of complex molecules can be reconstructed from a series of transmission images taken at regularly spaced angles (de Rosier and Klug 1968, Gordon Bender and Herman 1970, Crowther de Rosier and Klug 1970, Klug and Crowther 1972).

The mathematics of reconstructing the exact tomogram from the blurred tomogram or layergram is most easily approached from the spatial frequency domain:

$$G(\rho,\phi) = \mathcal{F}_{(2)}\{g(r,\theta)\} \tag{2.13}$$

and

$$\Lambda(\rho,\phi) = \mathcal{F}_{(2)}\{\lambda(r,\theta)\} \tag{2.14}$$

where $\mathcal{F}_{(2)}\{\ \}$ represents the two-dimensional Fourier transform.

$$\mathcal{F}_{(2)}\{|r|^{-1}\} = \int_0^{\infty}\int_0^{2\pi} |r|^{-1}\exp[-j2\pi\rho r\cos\theta]\ r\,d\theta\,dr \tag{2.15}$$

$$= \int_0^{\infty} 2\left(\int_0^{\pi} \exp[-j2\pi\rho r\cos\theta]\,d\theta\right)\ dr$$

$$= \int_0^{\infty} 2\pi J_0(2\pi\rho r)\ dr \tag{2.16}$$

$$= |\rho|^{-1} \tag{2.17}$$

Thus (2.12) is rewritten as

$$G(\rho,\phi) = \Lambda(\rho,\phi)\,|\rho|^{-1}$$

or

$$\Lambda(\rho,\phi) = G(\rho,\phi)\,|\rho| \tag{2.18}$$

Thus

$$\lambda(r,\theta) = \mathcal{F}_{(2)}^{-1}\{G(\rho,\phi)\,|\rho|\} \tag{2.19}$$

Bates and Peters (1971) proposed using a coherent optical system and lenses to perform the Fourier transforms required to implement (2.13) and (2.19). Peters (1973, 1974a) presents results obtained by optically deblurring layergrams. The image formation is practically instantaneous, but exceptional photographic finesse is required to produce satisfactory results on an optical bench. Also, the results are limited by the dynamic range of the film on which the layergram and filter transparencies are recorded.

A large dynamic range is possible if the X-ray projections are measured electronically and the values are stored in the memory of a digital computer. The computer can use (2.5) and (2.6) to construct a layergram in which the dynamic range is limited only by the computer word length and the accuracy of the projection measurements. The Fourier transforms required to implement (2.13) and (2.19) can be performed rapidly in a digital computer by means of the FFT (Fast Fourier Transform) algorithm (Cooley and Tukey 1965).

The image levels are normalized:

$$H = \frac{\omega_{tissue} - \omega_{water}}{\omega_{water}} \; 1000$$

where H is the EMI number which is commonly known as the Hounsfield number after the developer of the first (EMI) CAT scanner. Water has a Hounsfield number of 0 while gas is -1000 and the densest bone is about +1000. Image level resolution is usually better than 1 H or 66 dB which is much greater than the 26 dB dynamic range of film. The computer can either compress or window image levels to display small differences such as those between normal brain tissue and tumours. Computer methods usually form the exact tomogram by modifying the projections before back projection rather than by modifying the layergram as in (2.19). This is referred to as the "modified back projection" method.

The manner in which a single projection is modified to contribute to the ideal image is examined analytically by means of the Fourier transform relationships. In the spatial frequency domain, the ideal image can be expressed in polar $\Lambda(\rho,\phi)$ or cartesian $\Omega(\alpha,\beta)$ form:

$$\Omega(\alpha,\beta) = \int_{-\infty}^{\infty}\int \omega(x,y) \exp[-j2\pi(\alpha x+\beta y)]\,dxdy \qquad (2.20)$$

or

$$\Lambda(\rho,\phi) = \int_{-\infty}^{\infty}\int \omega(x,y)\exp[-j2\pi\rho(x\cos\phi+y\sin\phi)]dxdy \qquad (2.21)$$

Changing from the (x,y) axes to (ξ,η) axes yields

$$\Lambda(\rho,\phi) = \int_{-\infty}^{\infty}[\int_{-\infty}^{\infty}\omega(x,y)d\eta]\exp[-j2\pi\rho\xi]d\xi$$

$$= \int_{-\infty}^{\infty} f(\xi,\phi)\exp[-j2\pi\rho\xi]d\xi$$

$$= F(\rho,\phi) \qquad (2.22)$$

Combine (2.21) and (2.22) to yield

$$\omega(x,y) = \int_0^{2\pi}\int_0^{\infty} F(\rho,\phi)\exp[j2\pi\rho(x\cos\phi+y\sin\phi)]|\rho|d\phi d\rho$$

$$= \int_0^{\pi}\{\int_{-\infty}^{\infty}\hat{F}(\rho,\phi)\exp[j2\pi\rho(x\cos\phi+y\sin\phi)]d\rho\}d\phi$$

$$= \int_0^{\pi}\hat{f}(x\cos\phi+y\sin\phi,\phi)d\phi \qquad (2.23)$$

or

$$\lambda(r,\theta) = \int_0^{\pi}\hat{f}(r\cos[\theta-\phi],\phi)d\phi \qquad (2.24)$$

where the modified projection $\hat{f}(\xi,\phi) = \mathcal{F}_{\rho}^{-1}\{\hat{F}(\rho,\phi)\}$ and $\hat{F}(\rho,\phi) = |\rho|F(\rho,\phi)$.

From M discrete projections, measured at angular increments of π/M, one obtains an estimate of the exact cross-section $\bar{\omega}_M$ by summing the modified projections:

$$\bar{\omega}_M(x,y) = \frac{\pi}{M}\sum_{i=1}^{M}\hat{f}(x\cos\phi_i + y\sin\phi_i,\phi_i) \qquad (2.25)$$

The modified projection

$$\hat{f}(\xi,\phi) = \int_{-\infty}^{\infty}|\rho|F(\rho,\phi)\exp[j2\pi\rho\xi]d\xi \qquad (2.26)$$

is also expressed as a convolution in the spatial domain. The transform

of $|\rho|$ is $-1/2\pi^2\xi^2$ (Lighthill 1958, p.43), so

$$\hat{f}(\xi,\phi) = f(\xi,\phi) \circledast -1/2\pi^2\xi^2$$

$$= -\frac{1}{2\pi^2}\int_{-\infty}^{\infty}\frac{f(\xi',\phi)}{(\xi'-\xi)^2}\,d\xi' \tag{2.27}$$

$$= \frac{1}{2\pi^2}\int_{-\infty}^{\infty}\frac{\partial f(\xi',\phi)/\partial\xi'}{(\xi'-\xi)}\,d\xi' \tag{2.28}$$

where (2.27) has been integrated by parts to yield (2.28). Radon (1917) derived (2.24) and (2.28) for the solution of gravitational problems which involved integrals along manifolds. This pair of equations has been examined by Cormack (1973) and by Beattie (1975). Implementation on a digital computer can however, produce accuracy problems which are associated with the pole and the derivative in the integral. These problems are avoided by limiting the spatial frequencies present in the image. Most of the spectral energy is contained below some upper spatial frequency limit ρ_m so that setting $\Lambda(\rho,\phi) = 0$ for all $|\rho| > \rho_m$ has little effect on the image. Then (2.26) becomes

$$\hat{f}(\xi,\phi) = \int_{-\rho_m}^{\rho_m}|\rho|F(\rho,\phi)\exp[j2\pi\rho\xi]\,d\rho$$

$$= f(\rho,\phi) \circledast b(\xi) \tag{2.28}$$

where the spatial filter $b(\xi)$ is defined as

$$b(\xi) = \int_{-\rho_m}^{\rho_m}|\rho|\exp[j2\pi\rho\xi]\,d\rho$$

$$= 2\int_{0}^{\rho_m}\rho\cos(2\pi\rho\xi)\,d\rho$$

$$= \left(\frac{\rho_m}{\pi\xi}\right)\sin(2\pi\rho_m\xi) - \frac{1}{\pi^2\xi^2}\sin^2(\pi\rho_m\xi) \tag{2.29}$$

If the projection $f(\xi,\phi)$ is sampled at 2N+1 points, then

$$f_n(\phi) = f(\xi,\phi)\delta(\xi-n\Delta) \qquad n = 0,\pm1,\ldots,\pm N$$

where $\Delta = \frac{1}{2\rho_m}$ is the sampling interval. Thus

$$b_n = b(n\Delta) = \begin{cases} 1/4\Delta^2 & n = 0 \\ -1/n^2\pi^2\Delta^2 & n \text{ odd} \\ 0 & n \text{ even} \end{cases} \tag{2.30}$$

The spatial filter or convolution kernel method was proposed by Bracewell and Riddle (1967) and various versions of this, such as (2.29) and (2.30), are discussed by Ramachandran and Lakshminarayanan (1971).

The sampling process produces periodicities in the spatial frequency domain so that

$$\mathcal{F}\{b(n\Delta)\} = |\rho-i2\rho_m| \tag{2.31}$$

$$\leq |\rho_m| \qquad i = 0,\pm1,\pm2,\ldots$$

The main problem with image processing by Fourier transforms and digital computers is that the data must be sampled and the Fourier transforms implemented as discrete Fourier series. This gives rise to artefacts in the image which are discussed in detail by Peters (1973) and Mersereau (1976). The artefacts which arise from discrete Fourier synthesis are reviewed by Bergland (1969) who also discusses windowing the data to be transformed. The artefacts introduced by Fourier synthesis can be largely avoided by employing the convolution methods. Noise is reduced by windowing the higher spatial frequencies which are amplified by the $|\rho|$ multiplication in (2.19). A suitable window was developed by Shepp and Logan (1974). They use a sinusoid which closely approximates $|\rho|$ at low frequencies and removes the sharp discontinuities at the odd multiples of

ρ_m (c.f. 2.31). Shepp and Logan define

$$\mathcal{F}\{b(\xi)\} = \frac{2\rho_m}{\pi} \sin|\pi\rho/2\rho_m| \qquad |\rho| < \rho_m \tag{2.32}$$

so that

$$\begin{aligned} b(\xi) &= \int_{-\rho_m}^{\rho_m} \left(\frac{2\rho_m}{\pi}\right) \sin|\pi\rho/2\rho_m| \exp[j2\pi\rho\xi]d\rho \\ &= \frac{4\rho_m}{\pi}\int_0^{\rho_m} \sin(\pi\rho/2\rho_m)\cos(2\pi\rho\xi)d\rho \\ &= \frac{8\rho_m^2[1-4\rho_m\xi\sin(2\pi\rho_m\xi)]}{\pi^2[1-16\rho_m^2\xi^2]} \end{aligned} \tag{2.33}$$

The sampled version of (2.33) is

$$b_n = -2/\pi^2\Delta^2(4n^2-1) \quad \forall\ n \tag{2.34}$$

This particular filter gives good results and reduces the effects of measurement noise. It is used extensively in the experimental work reported later in this thesis. The sampled projection

$$f_{n,i} = f(n\Delta,(i-1)\frac{\pi}{m}) \tag{2.35}$$

yields a sampled modified projection

$$\hat{f}_{n,i} = -\frac{2}{\pi^2\Delta^2}\sum_{p=-N}^{N}\frac{f_{p,i}}{4(n-p)^2-1} \tag{2.36}$$

The final image is defined on a matrix grid structure and linear interpolation in ξ is used to find intermediate points between those defined by $\hat{f}_{n,i}$.

Other methods based on iterative reconstruction are reviewed by Brooks and Di Chiro (1976) and Herman and Lent (1976), but these methods are not considered in detail here.

The discussion has been restricted to projections measured with parallel X-rays. Reconstruction methods based on projections measured with diverging X-rays have been developed (Peters 1973, Lakshminarayanan

1975) and are derived rigorously by Herman et al. (1976a) and by Peters and Lewitt (1977). More recent papers on this subject have been published by Weinstein (1978) and Reed et al. (1978). These methods are referred to in the next two sections, but are not derived since they are not used in this thesis.

2.4 COMMERCIAL DEVELOPMENTS IN AXIAL TOMOGRAPHY

The first commercial CAT scanner was produced by EMI Ltd in 1972 (c.f. Hounsfield 1972). This machine was designed as a head scanner and the patient was required to lie still during the 4½ minutes required to measure the projections at 1^{o} intervals. Referring to fig. 2.9(a), a γ-ray or X-ray source has a pencil beam which is directed at a detector and both are moved linearly so that the pencil beam is scanned across the head. The intensity of the rays emerging from the head is measured by a sodium iodide crystal detector at intervals $\xi = n\Delta$ during each scan. The sampled projections are stored in a computer and used to reconstruct a 160 * 160 pixel image. The first iterative reconstruction method required about 20 minutes to compute the image but this was later reduced so that the image was displayed half a minute after the scan was completed.

The problems associated with the first EMI machine are examined in detail to provide the background for subsequent scanner developments.

Any movement by the patient produces streaky artefacts tangential to sharp changes in density in the image. As already mentioned, the first generation of scanners were mechanically complicated, and required more than four minutes for a complete scan. The only way of eliminating streaky movement artefacts is to speed up the scanning so that all measurements are taken while the patient holds his breath, i.e. in less than 20 seconds.

Additional artefacts are associated with the spectral energy distribution of the X-ray beam. Since low energy X-rays are preferentially absorbed, the emerging X-ray beam has its spectral energy distribution shifted to the high energy end. This problem is known as beam hardening and manifests itself in the brain images as a slightly low value of skull bone density and a ring of slightly increased density just inside the skull. The ring was originally mistaken for grey matter but is now recognized as a "pseudo-cortex" artefact (Hounsfield 1976, Gado and Phelps 1975). The original EMI scanner used a water bag to support the head and to limit the dynamic range of the detected output. The water bag also reduces the effect of beam hardening (McCullough et al. 1974) but it is not used in most scanners, which can suffer substantial beam hardening artefacts even in the absence of bone. These effects are minimized by prefiltering the X-ray beam so that only a narrow energy spectrum is used for measurements. Considerable research effort has been directed towards separating the photoelectric absorption and Compton scattering effects so that two tomograms of the same body section can be reconstructed at two different X-ray energies (Alvarez and Macovski 1975, Macovski et al. 1975).

Another artefact is "overshoot" or "Gibbs phenomena" at sharp density discontinuities in the image. This is reduced by windowing the spatial frequencies before deriving the convolution kernel or spatial filter which is described at the end of section 2.3. The choice of the convolution kernel used for modified back projection reconstruction has been discussed in detail by Shepp and Logan (1974) who suggested the sinusoidal window now used in many CAT scanners. Gibbs phenomena are expected in analytic reconstructions, but they are also observed in the early EMI brain scanner outputs which are based on iterative reconstruction. Special purpose hardware can reduce the time for "modified back projection" reconstructions and it is widely used on the newer axial tomograph scanning systems.

Other machines are not discussed in detail here but their characteristics are listed in table 2.1. The first generation of machines used a single source and detector configuration which required a slow two-movement scan. However, they were capable of measuring two sections at once and used a separate detector for each section.

The second generation of scanners (based on the principle illustrated in fig. 2.9(b)) use several detectors to measure several X-ray paths at different angles. Thus several projections are measured with one linear scan. These machines still use two movements but the angular increment is slightly larger than the total angle measured by the detectors and thus fewer angular steps are required. Scanning speeds ranged from two minutes to 10 seconds and on the fastest machines, special purpose hardware produces 512 by 512 pixel images within 10 seconds after the scanner stops.

The third generation machines use a wide fan shaped X-ray beam to irradiate the whole body section at once and multiple detectors measure the projections. The principle of operation of these machines is illustrated diagramatically in fig. 2.9(c). A single rotary motion around the patient reduces the scan time to as little as two seconds. Reconstruction with the fan beam geometry is more complicated since the data is often arranged into isoangle projections (i.e. projections formed from X-rays at a single angle) before proceeding with the modified back projection reconstruction. Alternatively, special convolution kernels and modified back projections can be used for fan beam reconstructions (Peters 1973, 1974a,b, Pang and Genna 1975, Herman et al. 1976a, Peters and Lewitt 1977)

A fourth generation of scanner is shown in fig. 2.9(d). It employs a ring of X-ray detectors and moves the X-ray source around the patient. The source is located inside the ring of detectors. The main advantage over the third generation scanners is that the rotating mass is less and scan speeds can be increased. The complication of rotating many

detectors and their associated electronics is also avoided.

Another type of machine has been proposed by Ritman, Sturm and Wood (1976) and incorporates an array of 28 X-ray tubes and 28 fluorescent image detectors. Such a machine is expensive but eliminates all mechanical movement which permits high speed imaging. The hardware system is capable of measuring 60 complete sets of projections each second (c.f. Gilbert et al. 1976a,b).

2.5 CURRENT RESEARCH IN COMPUTED TOMOGRAPHY

An enormous amount of interest in computed tomography was created by the first commercial release of a medical CAT scanner in 1972. This interest has led to the production of a specialist journal, the "Journal of Computer Assisted Tomography - Computed Tomography", many specialist workshops and several special issues of journals (e.g. Computers in Medicine and Biology 6 (4) 1976). Besides the commercial pressure to design and sell CAT scanners, there has also been a great deal of theoretical work devoted to measurement methods and to image reconstruction procedures.

Herman and Lent (1976) review iterative reconstruction methods and various optimization criteria in order to list six ART-type methods (ART for Algebraic Reconstruction Technique after Gordon, Bender and Herman 1970), and three SIRT-type methods (SIRT for Simultaneous Iterative Reconstruction Technique after Gilbert 1972). They also report convergence results for various algorithms and state that computation speeds for the convolution methods are from two to ten times faster than for ART methods which in turn are faster than SIRT methods by a similar factor. The computation times for all methods are reduced by the use of special purpose hardware. In particular, the implementation of the convolution hardware is straightforward. Herman and Lent also list "tricks" which are used to improve the performance of the iterative methods. They also point out

that similar "tricks" are involved in choosing an "appropriate" convolution kernel or spatial filter so that data preprocessing is performed during the convolution (c.f. Hurwitz 1975). They conclude that iterative methods are best suited to underdetermined images (too little data), since they produce the best fit for the available data; and that convolution (modified back projection) methods are well suited to overdetermined images since interpolation and data errors are reduced.

Brooks and DiChiro (1976) make similar claims for the two methods, but their calculation of the amount of data required to form an image is half that required by Smith, Peters and Bates (1973). There have been claims that the ART and back projection methods are the same, but Herman and Lent (1976) show that the methods are not equivalent for either discrete or continuous measurement of the projections.

An advantage of the modified back projection method is that a portion of the image can be computed without forming the remainder of the image. The entire projection is filtered to yield the modified projection, and a limited portion of this is back projected into the region of interest. Herman et al. (1976a) use fine sampling of the projection for the region of interest, and coarse sampling of the projection of the remainder of the body.

Horn (1978) presents images reconstructed from projections which are sampled at random intervals. The results show that images of similar quality require approximately twice as many uniformly spaced samples of the projections. The computational savings of such a random sampling scheme appear small. However, the measurement time could be reduced or else the amount of measurement hardware halved.

The problem of reconstructing a region within a body from X-ray projections of only that region is defined by Bates et al. (1975) as image reconstruction from incomplete projections. The sections missing from the

projections are due to shading of the X-ray beam in order to reduce the radiation dosage to sensitive areas of the patient. In the first of a series of four papers, Lewitt and Bates (1978a) set up the definitions and notation for incomplete projections, and then show theoretically how these affect the computed image. In the second paper in the series, Lewitt Bates and Peters (1978) examine the effect of sampling the image and the projections, and of measuring the projections at a finite number of angles. Expressions are developed to relate the effects of various data interpolation methods for radial interpolation between sample points on a projection, and angular interpolation between projections. They show that linear interpolation in angle is, for the back projection method, equivalent to image rotation and superposition (the contribution of the author - G.R.D. - is acknowledged for this aspect of the paper). For example, if the number of projections to be used for modified back projection reconstruction is doubled by linear angular interpolation, then the resulting image could also be obtained by the superposition of three images. The first image is that derived by modified back projection reconstruction from the measured set of projections, but the amplitude is halved. The second image is the same as the first, but it is rotated about the rotation centre by half of the angular increment between the measured projections, and the amplitude is halved yet again. The third image to be superimposed is the same as the second except that the rotation is in the opposite sense. Brooks and Weiss (1976) discuss linear radial and angular interpolation which they describe, in two-dimensions, as "trapezoidal" interpolation. The equivalence of linear angle interpolation and rotated image superposition does not appear to have been noticed by Brooks and Weiss. Computational savings make the latter method preferable.

The third and fourth papers by Lewitt and Bates (1978b,c) examine methods of augmenting incomplete projections and present theoretical and computational studies. Hollow projections, which have gaps in the central region, can be reconstructed to form useful images by smoothly filling in the gaps in the projection. Accurate reconstructions are based on consistency conditions, but these involve a great deal of extra computation. When the missing portion of the projection is small compared to the total extent of the projection, simple smooth continuation of the measured projections yields good results. Preprocessing the projections is computationally efficient. Truncated projections in which the end portions of the projection are not measured (or irradiated) yield useful reconstructions when the measured projections are smoothly extrapolated to zero. Very good images are obtained when some a priori information about the missing data is available. For example, excellent images result when the body outline is known, and an estimate, or low resolution measure, of the missing data is available. Earlier work on the subject of incomplete projections is described by Oppenheim (1975), Bracewell and Wernecke (1975) and Bates et al. (1975).

The theoretical studies of computed tomography benefit from, and also contribute to, studies in other disciplines. A recent thesis by Lewitt (1977) examines electron microscopy, X-ray crystallography and computed tomography as part of a general theoretical study on imaging which results in contributions to all these fields. Another thesis by Das (1977) relates inverse scattering (for radar target identification) to image reconstructions from projections. He extends, via the Radon transform, the application of computed tomography techniques to echo-location target identification, and in doing so contributes to the unity of both disciplines. The work is reported in two papers by Das and Boerner (1976, 1978).

The formation of images in planes inclined to measured parallel sets of tomographs was discussed in section 1.4 with respect to ultrasonics (c.f. Robinson 1972a,b). Peters (1975) performs similar computations for X-ray tomography when many adjacent body sections are imaged. The process is particularly useful for radiotherapy treatment planning where several views of a tumour (to be destructively irradiated) are required. Since all the X-ray absorption coefficients for the body regions in the vicinity of the tumour are already stored in the computer, it is possible to compute a radiation treatment course which maximizes the destructive dose delivered to the tumour and minizes the dose absorbed by the surrounding tissue. Allowance is made for the radiation sensitivity of the various healthy tissues irradiated during radiotherapy. Such treatment planning schemes are discussed by Rogers (1975), Pistema (1975) and Chernak et al. (1975).

Finally, measurement and reconstruction speeds are being increased so that real-time images can be measured. High speed is required for cardiac and circulation function studies. Real-time X-ray shadowgraphs are obtained with combined fluoroscope-television systems. Workers at the Mayo institute (see description at the end of section 2.4) have used 28 of these systems together with high-speed data acquisition hardware to obtain real-time volume projection measurements of the beating heart. The images are computed at a slower rate. Ultrasonic pulse-echo tomography utilizing analog signal processing and display techniques does seem to enjoy a considerable speed advantage when imaging moving structures such as the heart. However, CAT measurement and computation times have been reduced by 99.3% (5 mins to 2 secs) during the past five years. It is improbable that similar decreases will occur during the next five years, but there will undoubtedly be some reductions in operation times.

2.6 DISCUSSION

Computed tomography produces excellent images of cross sections. However, conventional X-ray shadowgraphs superimpose the information from many cross sections. Thus for the routine screening of patients (such as with a mobile chest X-ray unit), the shadowgraph is preferred. However, the shadowgraph cannot always yield the detailed information required before radiation therapy or surgery. This is especially true for neurology which is why the first tomograph machines were employed for brain examinations.

The skull bone is the most notable feature of head shadowgraphs. The X-ray absorption of the dense skull bone masks many of the small absorption changes contributed by the brain. The small absorption changes are enhanced when an X-ray contrast material (usually an iodine compound) is introduced into the blood supply of the brain. In particular, lesions which disrupt the blood flow in the brain are easier to diagnose. Contrast of the ventricular spaces is enhanced when a gas is introduced into the brain. Other brain imaging techniques utilize radioactive isotopes which are injected into the blood supply. Tumours absorb an amount of the isotope which is different from the amount absorbed by the normal brain tissue. A blurred image of the tumour is obtained with a gamma ray camera. Alternatively, an emission CAT scanner could be utilized to obtain a deblurred image of the tumour. A discussion of emission CAT scanners is contained in a review by Brooks and DiChiro (1976).

When foreign matter is introduced into the brain, the patient usually spends several days in hospital. Non-invasive CAT scans can be performed in less than 15 minutes. Thus a patient can be examined at an outpatient clinic. CAT scanner purchases are often justified by purely neurological requirements. Many scanners are capable of imaging the whole body. They can also be used for automatic radiotherapy planning.

The cross section which is examined by a CAT scanner is exposed to X-ray radiation with a typical dose of about 2 Rads. When a detailed image of the brain volume is constructed from many parallel tomograph images, the brain receives about the same radiation dose as would be received during a normal skull X-ray shadowgraph examination. Some body regions are particularly susceptible to X-ray exposure, e.g. the foetus. Where possible, ultrasonics should replace X-rays for imaging these regions.

Acoustic transmission imaging is best suited to nearly homogeneous regions. The possibility of combining acoustic transmissions and X-ray tomography processing is examined in the next chapter.

COMPANY	MODEL	APPLIC-ATION	DETECTORS PER SLICE	WATER BAG	ANGULAR MOTION	MATRIX SIZE	PIXEL SIZE (mm)	SCAN TIME	ADDITIONAL PROCESSING TIME
			I. One detector - two motions						
EMI	MARK I,CT1000	Head	1 NaI	Yes	180/225° in 1° steps	160	1.5	4.5 min	30s
Pfizer	ACTA 0100,0200	Body	1 CaF_2	No	180° in 1 or 2° steps	160/320	1.5	4.5 min	0
			II. Multidetectors - two motions						
Siemens	Siretom II	Head	4 CaF_2	No	180° in 1.35° steps	256	1	1.3 min	0
Ohio Nuclear	Δ-Scan 25	Head	7 BGO	No	196° in 7° steps	256	1	1/3 min	0
EMI	CT1010	Head	8 NaI	No	180/225° in 3° steps	320	0.75	1/4.5 min	90s
Ohio Nuclear	Δ-Scan 50 Fast	Body	12 BGO	No	180° in 12° steps	256	1/1.7	18s	15s
Syntex	60	Body	12 NaI	Opt.	180° in 12° steps	256	1/1.5	1 min	2.5 min
EMI	CT5000,5005	Body	30 NaI	No	180° in 10° steps	320	0.75/1/1.25	20s	3.3 min
Pfizer	ACTA 0200 FS	Body	30 CaF_2	No	180°/280° in 20° steps	160/256/320	1/1.5	21s	5s
Philips	Tomoscan	Body	30 BGO	No	180/225° in 10° steps	256	1/1.6/2	27s	10s
Elscint	Scanex	Body	60 BGO	No	180° in 30° steps	256/512	0.5/2	10s	10s
			III. Multidetectors - one motion (rotation)						
Artronix	1110	Head	128 Xe	Yes	360° continuous	256	1	9s	1.5 min
Picker	Synerview	Body	60 CaF_2	No	720° continuous	240	1/2	18/30s	30s
Searle	Photrax	Body	252 Xe	No	360° continuous	256	0.5/1/2	5/10/20s	40s
Varian		Body	300 Xe-Kr	No	360° continuous	256	1.9	3s	2 min
General Electric	CT/T	Body	320 Xe	No	360° continuous	320	1.3	5s	3.3 min
Artronix	1120	Body	512 Xe	No	360° continuous	512	1	5s	3 min
Am. Sci. & Eng.		Body	600 BGO	No	495° continuous	512	0.5/1	5/10/20s	1 min
			IV. Stationary detectors - rotating source						
EMI	7000	Body	1100	No	360° continuous	512		3s	
Ohio-Nuclear	Δ-2020	Body	720 Xe	No	360° continuous	512	~1 mm	2/4/8/11s	30s
Am. Sci. & Eng.		Body	Xe	No	360° continuous	512			45s
Pfizer	ACTA-II	Body	Xe	No	360° continuous	512		2s	5s

Table 2.1 Commercial X-ray computed tomography machines.

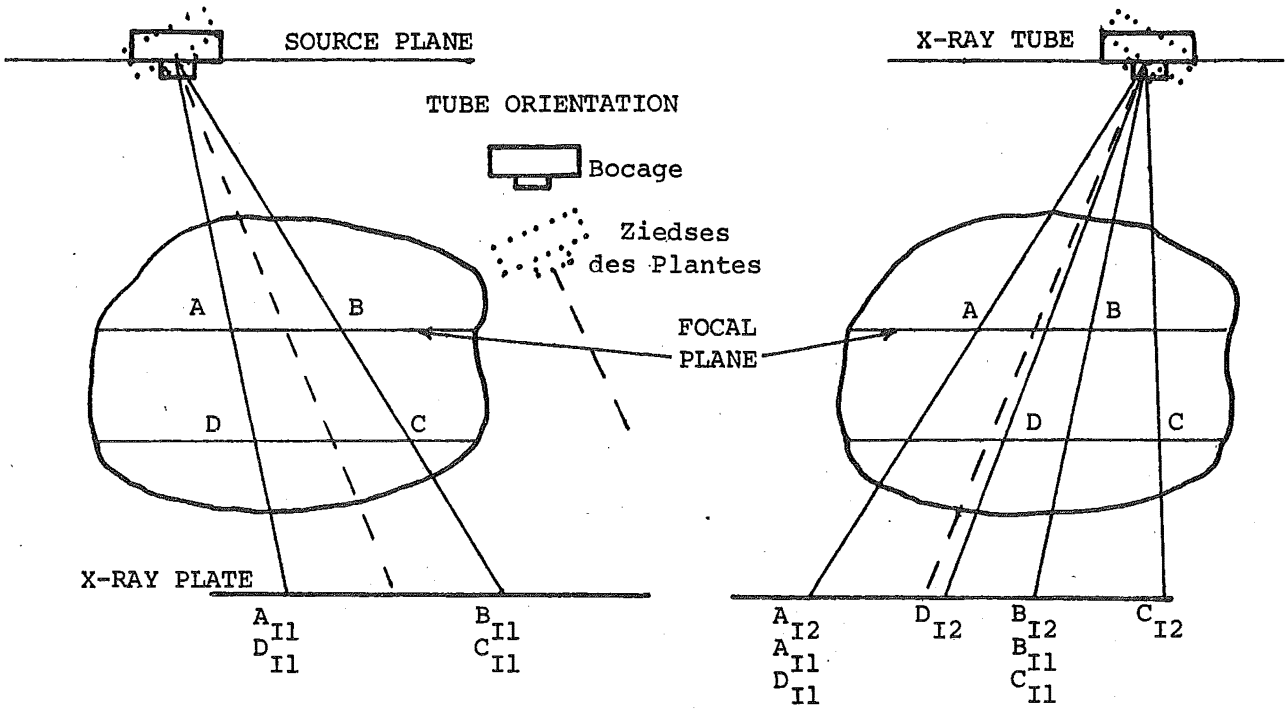

Fig. 2.1 Illustration for linear blur. Focal plane AB.

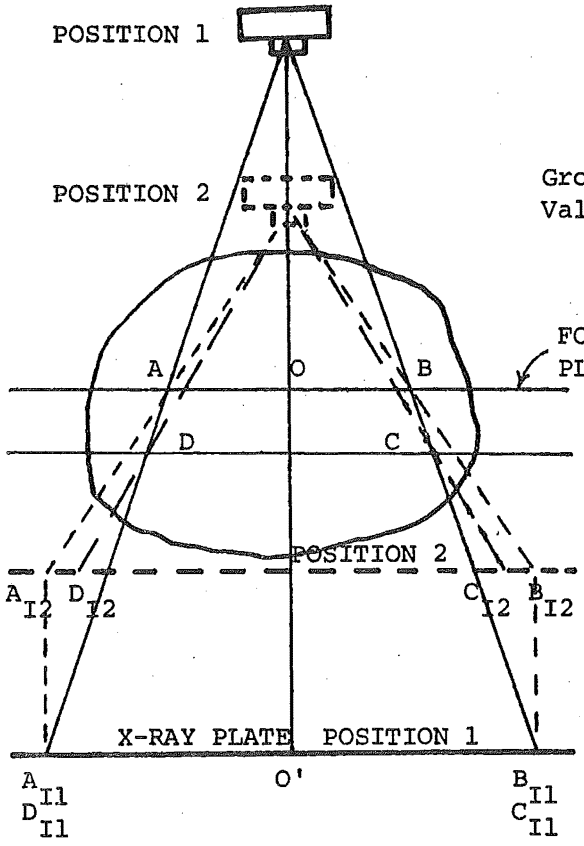

Fig. 2.2 Magnification blur, two imaging positions shown.

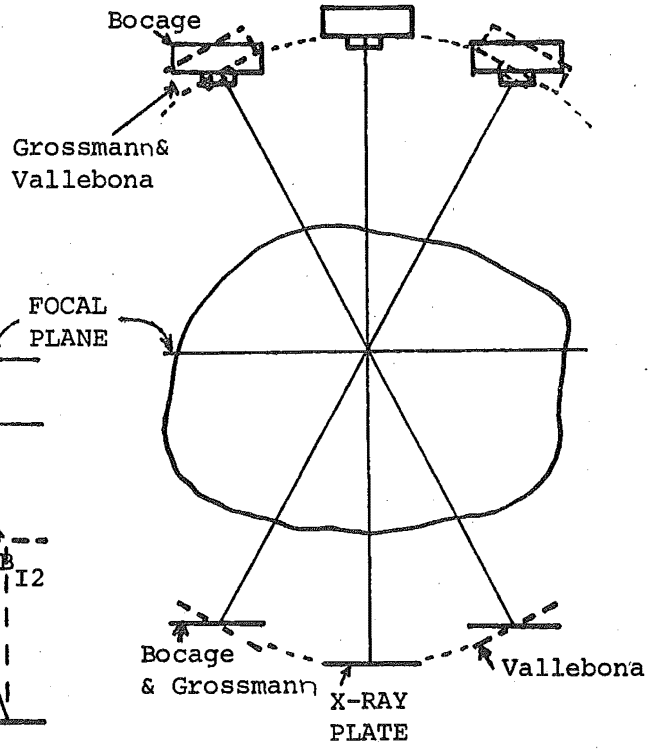

Fig. 2.3 Pivoted rotational blurring systems.

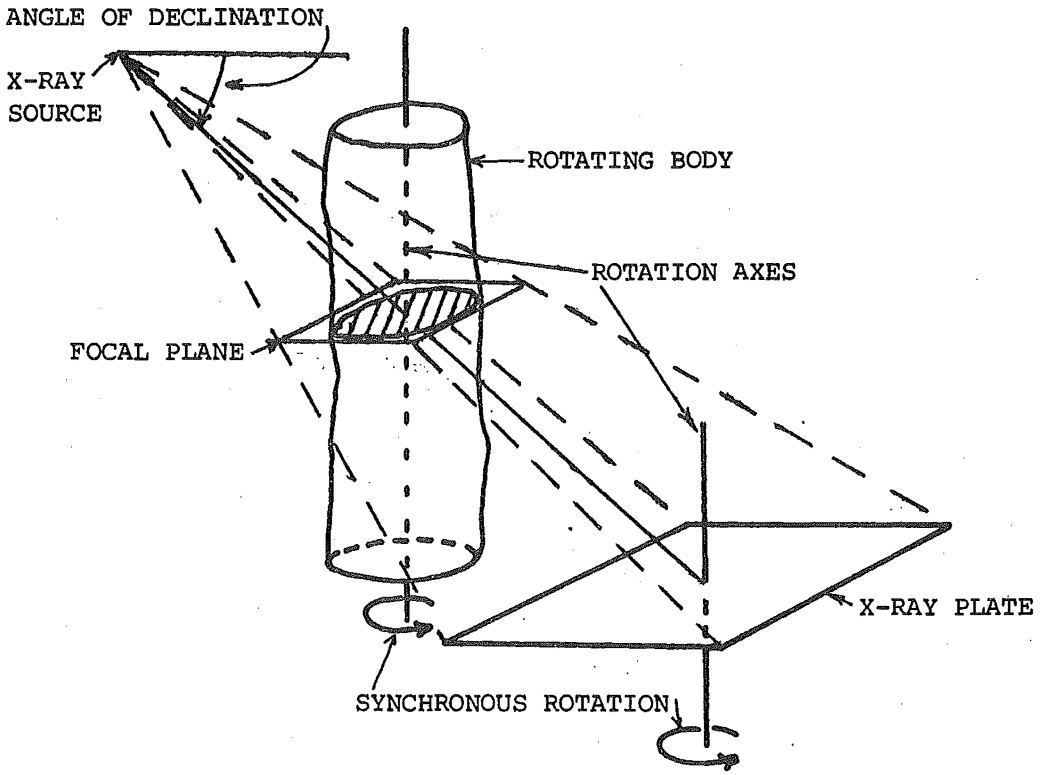

Fig. 2.4 Transverse tomography. Points out of the focal plane are blurred.

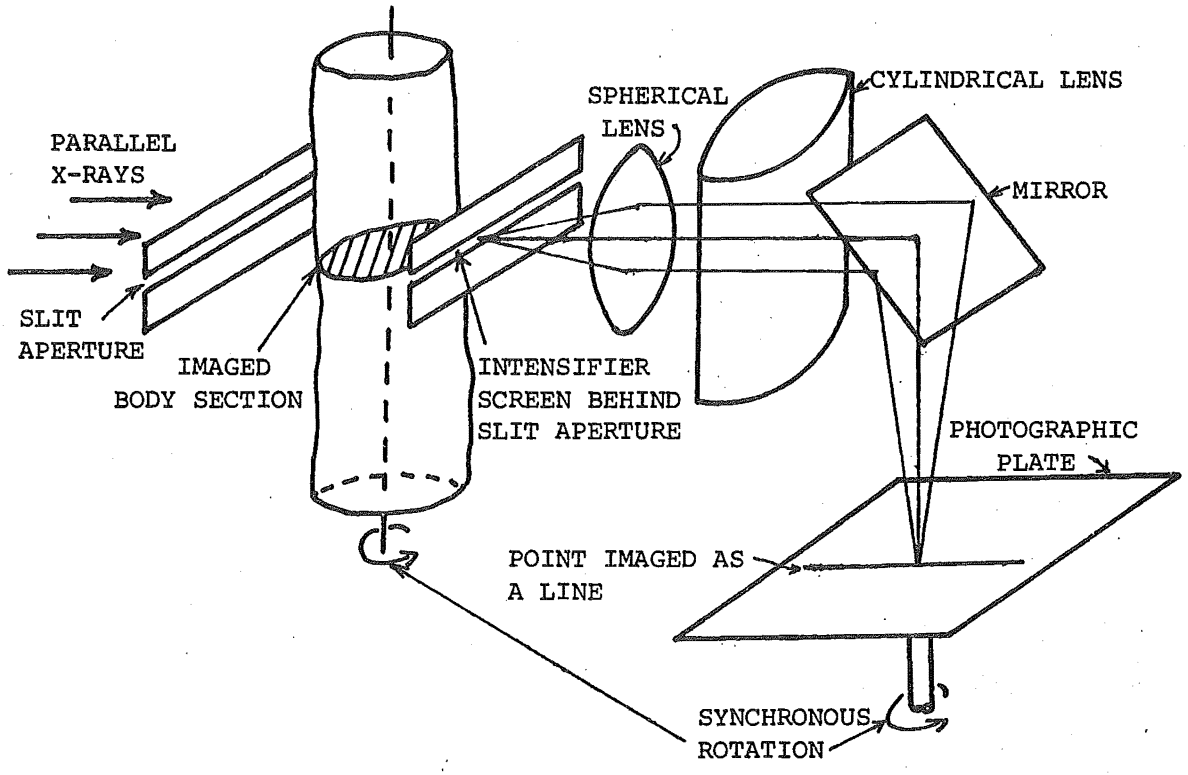

Fig. 2.5 The axial transverse tomograph designed by Peters (1973, 1974a). The X-ray intensity at a point is imaged as a line on the plate.

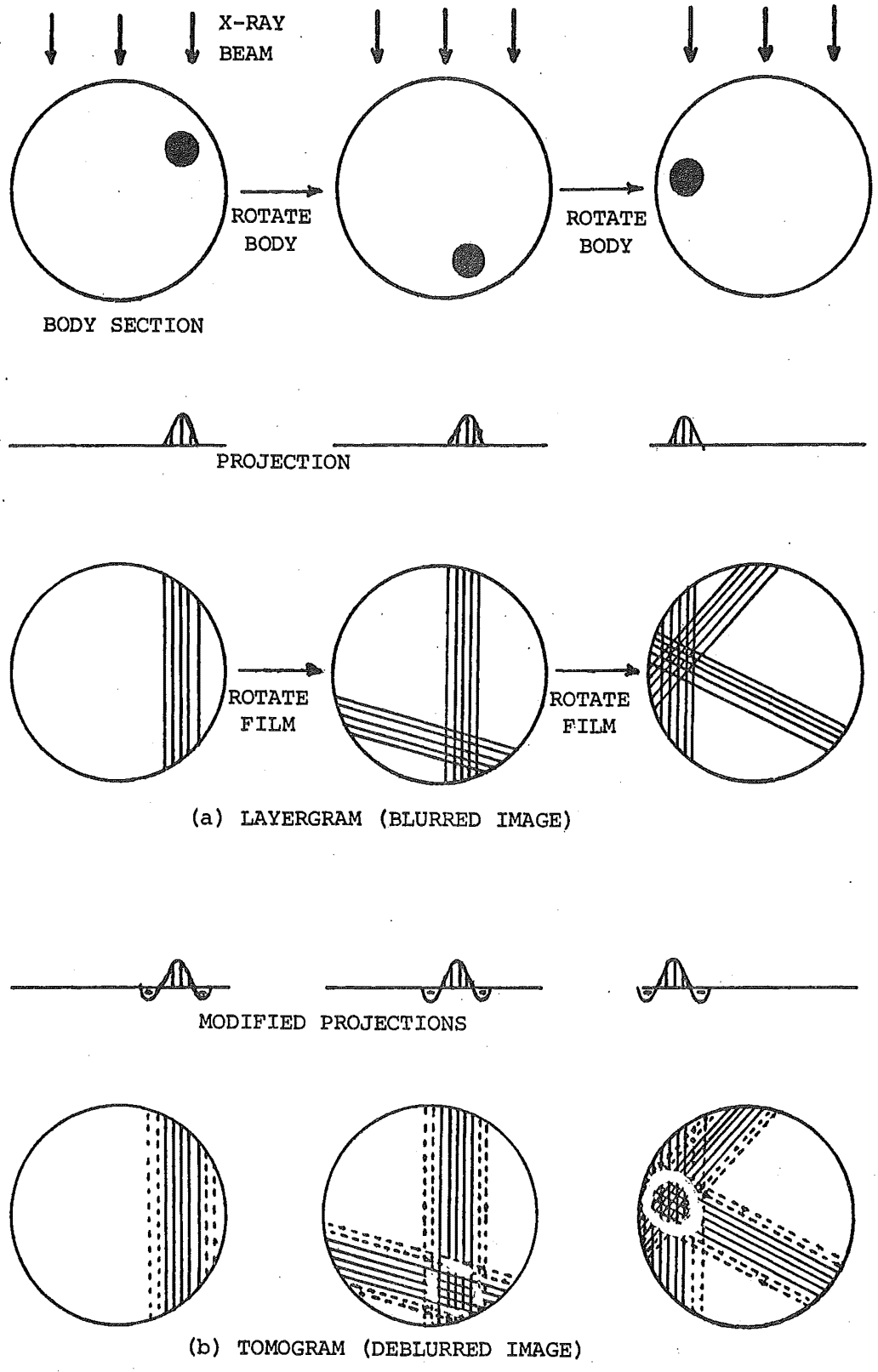

Fig. 2.6 Transverse axial tomograph formation illustrating the formation of the layergram (or blurred image) and of the tomogram (or deblurred image).

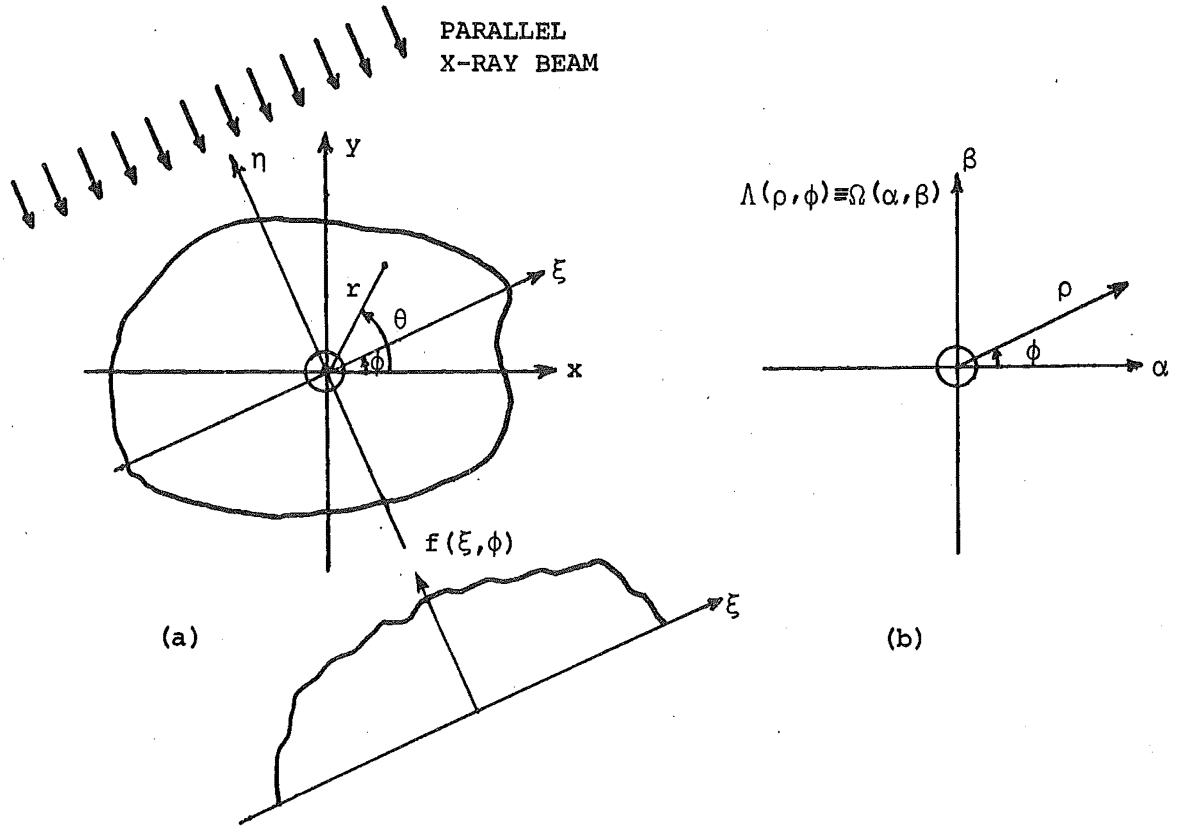

Fig. 2.7 Geometry for development of the mathematics.
(a) Image domain, axes (x,y) and (η,ξ) inclined at φ.
(b) Spatial frequency (or transform) domain.

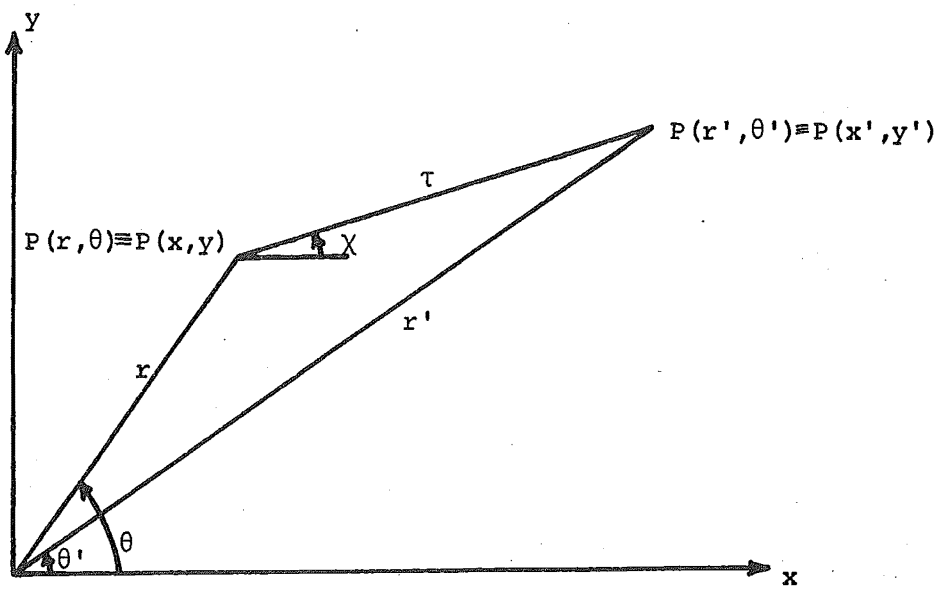

Fig. 2.8 Geometry for computing the layergram from the cross section.

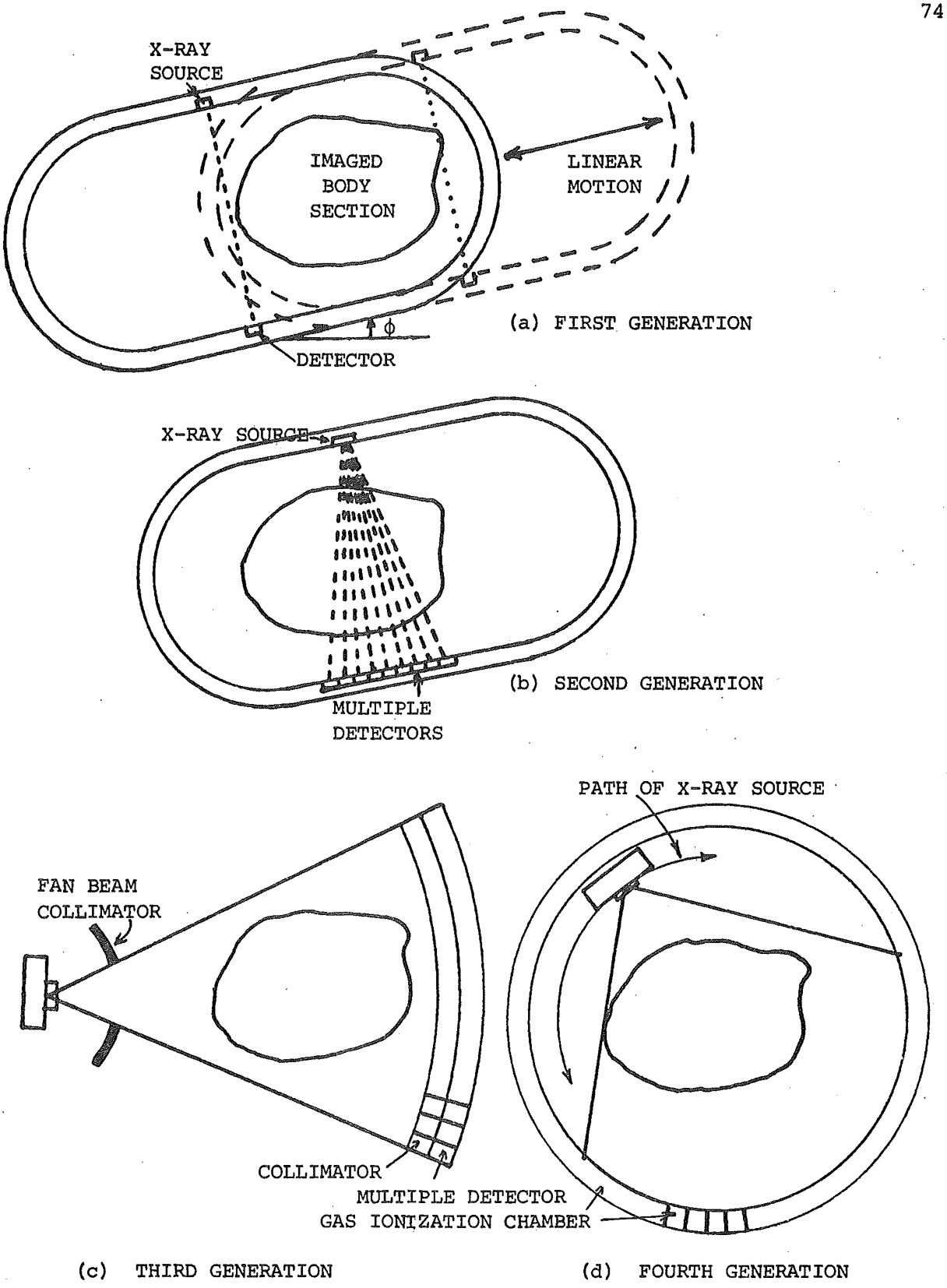

Fig. 2.9 X-ray scanner systems for transverse axial tomography:

(a) incremental rotation and a linear scan for each projection.

(b) large incremental rotations and several projections per scan.

(c) rotation only of X-ray source and detectors.

(d) rotation of X-ray source only.

CHAPTER THREE

ULTRASONIC TRANSMISSION IMAGING

3.1 ULTRASOUND TRANSMISSION TOMOGRAPHY

The great clarity of images obtained with computed tomography (c.f. Digest of Technical Papers, Topical Meeting on Image Processing 1975, Brooks and Di Chiro 1976, Horn 1978) represents a considerable improvement in medical diagnostic technique. Many imaging devices have been constructed (c.f. table 2.1) and all derive from the simple genotype illustrated in fig. 3.1. A transmitter and receiver of radiation, A and B respectively, are moved along the dashed lines XX' and YY', in the scanning plane. The scanning space is circumscribed by a circle centred on O for which XX' and YY' are tangential. The X-ray absorption along the path AB is measured as a function of the angle ϕ and the radial position ξ for equal increments of ϕ. Much study has been devoted to transforming such observed data into high quality images (c.f. Chapter 2).

Prolonged exposure to X-rays is harmful. The use of ultrasound for medical diagnosis is not harmful (c.f. section 1.1, Hazzard and Litz 1977) and its use, as a substitute for X-rays, should be actively investigated (c.f. Pringot et al. 1977). Most existing ultrasonic tomographic apparatus is of the reflection type based on simple sonar-type signal processing (c.f. section 1.2). However, reflection tomography is relatively insensitive to small or gradual changes in acoustic impedance. The equivalent problem in optics was solved with the phase contrast and interference microscopes (c.f. Burnett et al. 1958) in which optical transmissions are used to display small changes in the optical refractive index. Acoustic transmission devices, as developed by Mueller and Sheridon (1966), employ coherent image processing of the kind used in optics (c.f. Goodman 1968). The major disadvantage of these devices is the integration time of the acoustic detector. A high degree of immobility is required in the body and apparatus, unless high acoustic intensities are used to give a rapidly detectable response.

When radiation travels through the image plane in straight lines (as do X-rays), the information processing is straightforward. Unfortunately, acoustic radiation is best described by the conventional wave equation. This means that the information processing associated with acoustic transmission tomography is extremely complicated. In most media, the acoustic propagation is satisfactorily described in terms of rays (c.f. Mawardi 1970). However, the rays are curved, and the necessary tomographic data processing remains very complicated (c.f. Sections 3.2 and 3.4). The curvature of the ultrasonic ray paths is ignored in conventional pulse-echo ultrasonic tomography. However, Johnson et al. (1975) employed acoustic ray tracing to compute corrections to measured acoustic time delay data. They hoped to employ perturbation methods to remove the effects of acoustic refraction from their tomographs.

Despite refraction, interesting "acoustic shadowgraphs" have been produced by Heyser and Le Croissette (1974), and by Glover and Sharp (1977). The shading in these acoustic shadowgraphs depends on the acoustic propagation time delay along an acoustic ray (c.f. X-ray attenuation along an X-ray). For bodies containing only small changes of velocity (i.e. diaphanous bodies or tenuous media) the acoustic ray paths approach straight lines. The detail in such bodies may be resolved by employing acoustic transmissions and using the information processing applicable to X-rays. By this means, the principle of the phase-contrast microscope is invoked unencumbered by coherent image processing. Similar suggestions were made by Rowley (1969), and by Junginger and Van Haeringen (1972) for processing holographic interferograms, but these authors have overlooked the relevance of a large body of directly applicable theory existing for other disciplines.

Finally, when the study reported in this thesis began, there was a lack of experimental and/or computational results for estimating the maximum acoustic velocity variation permissible for the simple X-ray type

processing to be used. In the next section, the acoustic pressure wave equation is derived for propagation through inhomogeneous media. The standard form of the wave equation is then derived and the eikonal equation developed. The measured and computed time delays for propagation through an aluminium cylinder are investigated in section 3.3. In section 3.4, the Born and Rytov approximate theories of wave propagation are examined. An improved version of the Rytov approximation is derived to yield an accurate form for the phase variation (and hence time delay) of ultrasonic waves. The penultimate section discusses existing phase-contrast methods used to image diaphanous objects, and some conclusions are presented in the final section.

3.2 EIKONAL SOLUTIONS FOR ACOUSTIC PROPAGATION

The mathematical description of sound waves propagating through an inhomogeneous medium is, in general, very complicated. In this section, the standard form of the wave equation is derived to yield a function proportional to the acoustic pressure variation. The eikonal equation is then developed. The various assumptions used are emphasized as they occur.

3.2.1 The Wave Equation for Inhomogeneous Media

Consideration of the physics of a small element of a medium through which an acoustic wave is propagating yields two useful equations (c.f. Skudrzyk 1971). These are Euler's equation for irrotational flow, i.e.

$$\frac{\partial \bar{v}}{\partial t} = -\frac{\nabla P}{\rho_D}, \tag{3.1}$$

and the equation of continuity for the medium:

$$\nabla . \bar{v} = -\frac{1}{\rho_D V^2} \frac{\partial P}{\partial t} \tag{3.2}$$

where $\bar{v}$ is the velocity of the infinitesimal volume element (the particle velocity in a solid), V is the velocity of the sound wave, ρ_D is the density of the medium, and P is the pressure. Manipulating (3.1) and (3.2) yields

$$\frac{\partial}{\partial t}(\nabla.\bar{v}) = -\nabla.(\frac{\nabla P}{\rho_D}) \tag{3.3}$$

and

$$\frac{\partial}{\partial t}(\nabla.\bar{v}) = -\frac{\partial}{\partial t}(\frac{1}{\rho_D V^2}\frac{\partial P}{\partial t}) \tag{3.4}$$

which combine to give

$$\nabla.(\frac{\nabla P}{\rho_D}) = \frac{\partial}{\partial t}(\frac{1}{\rho_D V^2}\frac{\partial P}{\partial t}) \tag{3.5}$$

Note that the bulk modulus (which is equal to $\rho_D V^2$) is time invariant for small signals, and that $\frac{\nabla\rho_D}{\rho_D}$ is the same as $\nabla \ln|\rho_D|$. Thus (3.5) becomes

$$\nabla.(\frac{\nabla P}{\rho_D}) = \nabla(\frac{1}{\rho_D}).\nabla P + \frac{1}{\rho_D}\nabla^2 P$$

$$= \frac{1}{\rho_D V^2}\frac{\partial^2 P}{\partial t^2}$$

which is rearranged to yield the pressure wave equation for an inhomogeneous medium

$$\nabla^2 P - \frac{1}{V^2}\frac{\partial^2 P}{\partial t^2} = (\frac{\nabla\rho_D}{\rho_D}) \cdot \nabla P \tag{3.6}$$

Harmonic analysis at frequency ω is utilized to effect further simplification:

$$P(\bar{r},t) = P(\bar{r})\exp[j\omega t] \tag{3.7}$$

and a wave function ψ is defined:

$$\psi = P\,\rho_D^{-\alpha} \tag{3.8}$$

The spatial derivatives of P are then:

$$\nabla P = \rho_D^{\alpha}\nabla\psi + \alpha\rho_D^{\alpha-1}\psi\nabla\rho_D$$

and

$$\nabla^2 P = \rho_D^{\alpha}\nabla^2\psi + 2\alpha\rho_D^{\alpha-1}\nabla\rho_D\cdot\nabla\psi + \alpha(\alpha-1)\rho_D^{\alpha-2}\psi(\nabla\rho_D)^2 + \alpha\rho_D^{\alpha-1}\psi\nabla^2\rho_D$$

The above relationships are used to reduce (3.6) to a more amenable form:

$$\nabla^2\psi + [(\frac{\omega}{V})^2 + \alpha(\alpha-2)(\frac{\nabla\rho_D}{\rho_D})^2 + \alpha\frac{\nabla^2\rho_D}{\rho_D}]\psi = [1-2\alpha](\frac{\nabla\rho_D}{\rho_D})\cdot\nabla\psi \tag{3.9}$$

The term on the right hand side is eliminated by choosing α to be $\frac{1}{2}$. The wavefunction ψ is then

$$\psi = P\,\rho_D^{-\frac{1}{2}}$$

and the wave equation is

$$\nabla^2\psi + [(\frac{\omega}{V})^2 - 3(\frac{\nabla\rho_D}{2\rho_D})^2 + (\frac{\nabla^2\rho_D}{2\rho_D})]\psi = 0 \tag{3.10}$$

The wavenumber in water is defined as

$$k = \omega/V_w$$

where V_w is the acoustic velocity in water. The acoustic refractive index n of the medium relative to water is

$$n = V_w/V$$

Thus (3.10) can be rewritten as

$$\nabla^2\psi + k^2[n^2 - 3(\frac{\nabla\rho_D}{2\rho_D k})^2 + (\frac{\nabla^2\rho_D}{2\rho_D k^2})]\psi = 0 \tag{3.11}$$

The various approximations required to reduce (3.11) to the eikonal form are examined in the following subsections.

3.2.2 The Picht-Bruns Approximation

The Picht-Bruns approximation applies when the spatial change of refractive index per unit wavelength is small, i.e.

$$[n^2 - 3(\frac{\nabla\rho_D}{2\rho_D k})^2 + \frac{\nabla^2\rho_D}{2\rho_D k^2}]^{\frac{1}{2}} \approx n \sim 1$$

Thus (3.11) reduces to

$$\nabla^2\psi + k^2n^2\psi = 0 \tag{3.12}$$

The standard form of the wave equation (3.12) is obtained by assuming that there are only small or gradual changes in the density of the medium, and that the velocity does not vary greatly in the medium. It is under precisely these conditions that pulse-echo imaging is poor and transmission imaging shows greatest promise.

We now examine (3.12) to obtain expressions relating to phase shifts (and hence time delays). The method of small perturbations is applied to ψ:

$$\psi = \psi_0(\bar{r}) \exp[-jkL(\bar{r})] \tag{3.13}$$

where $kL(\bar{r})$ is the small additional phase change introduced by changes in the medium. Substitution into (3.12):

$$\nabla^2\psi_0 - 2jk\nabla\psi_0\cdot\nabla L - [(k\nabla L)^2 + jk\nabla^2 L]\psi_0 + n^2k^2\psi_0 = 0 \tag{3.14}$$

Equating the real and imaginary parts of (3.14) yields

$$\nabla^2\psi_0 - (k\nabla L)^2\psi_0 + n^2k^2\psi_0 = 0$$

or

$$(\nabla L)^2 - \frac{\nabla^2 \psi_0}{k^2 \psi_0} = n^2 \tag{3.15}$$

and

$$\nabla^2 L + 2\nabla L . \nabla \psi_0 = 0 \tag{3.16}$$

Solution of (3.15) for $L(\bar{r})$ yields the wavefronts, (i.e. $L(\bar{r})$ = constant is an equiphase surface or wavefront), but (3.16) is not sufficient to determine ψ_0, even when $L(\bar{r})$ is known.

3.2.3 The Eikonal or High Frequency Approximation

At high frequencies, ω and k become very large and (3.15) reduces to

$$(\nabla L)^2 = n^2$$

or

$$|\nabla L| = n \tag{3.17}$$

which is the eikonal equation. Note that rays perpendicular to the wavefronts are described by

$$\nabla L = \hat{a}_n \, n \tag{3.18}$$

where $\hat{a}_n$ is the unit vector normal to the wavefront. This approach is the basis of the ray methods used in geometrical optics. Thus Fermat's principle (for geometrical optics) is invoked for acoustic propagation. Under almost all conditions of physical interest, an acoustic ray travelling from one point to another follows a path such that, compared with nearby paths, the time taken is a minimum.

Although the expressions derived in subsections 3.2.2 and 3.2.3 are only approximate, they have the advantage of simplicity, and serve to bring out the physics of what is being discussed because they apply quite accurately in the situations delineated here. The analogy between the variational principles of geometrical optics (Fermat's principle) and the principle of least action in particle dynamics was used by Hamilton to

develop the geometrical theory of ray optics in a systematic manner (c.f. Goldstein 1953). Mawardi (1970) used the Hamiltonian approach to develop a goemetrical theory of acoustical propagation. The development is complementary to the approach taken in this section (i.e. 3.2).

3.3 DISTORTIONS OF IMAGED SECTIONS

Images computed from ultrasonic time delay projections exhibit distortions which arise from refraction of the ultrasonic beam. Examples of distorted images are presented in chapter 6. In this section, the effect of multiple acoustic ray paths is examined to determine an appropriate method for measuring the propagation time delay. Acoustic ray tracing is used to calculate time delay projections for a test object so that a comparison is possible with the measured time delay projections.

A circularly symmetric test object (or phantom) is chosen because it is characterized completely by a single projection. The time delay measurements reported here were obtained by estimating the acoustic pulse arrival time from an A-scan display (c.f. section 1.2). Thus the measurement of only a single time delay projection limits the tedium for the experimenter. Since the purpose of the measurements is to illustrate the effects of multiple ray paths, it is important that strong refractions occur so that multiple path arrival times are clearly differentiated in the A-scan.

The above requirements for a test object are satisfied by a solid aluminium cylinder immersed in water. The cylinder used was 20.4 cm in diameter and the acoustic velocity in aluminium is 4.26 times that in water. The experimental arrangement shown schematically in fig. 3.2(a) was used to obtain the time delay projection results shown in fig. 3.2(b). Two types of measurement are shown. The first, based on the shortest time delay for acoustic propagation between the two transducers, shows

that the cylinder affects the time delay up to $|\xi|$ = 17 cm, some 7 cm beyond the extent of the cylinder. The second type of measurement is the time delay for the received pulse with the largest ampltiude (i.e. the one which travels by the maximum energy propagation path). The time delay projection for the maximum energy pulse shows that the cylinder has an effect for only 19 cm (c.f. 20.4 cm for the cylinder diameter).

Computations of the time delay projections are now examined so that the differences between the above measurement methods may be discussed. The shortest acoustic propagation time between the two transducers is calculated for ray paths determined by Fermat's principle (c.f. section 3.2.3). Very accurate numerical results are obtained relatively quickly by utilizing the symmetry of the object and using a Fibonacci search technique (c.f. Himmelblau 1972, p.42) to find the ray path. Using this technique, it is possible to evaluate the shortest time for one path out of more than 17000 by computing only 20 of them. The measurement errors associated with the measured minimum time delay encompass the results calculated (c.f. fig. 3.2b). However, in the interval 5 cm < $|\xi|$ < 15 cm, the measured results are consistently higher. This consistent difference is caused by the 2 cm diameter transducer measuring the acoustic field over an area rather than at a point. The calculated time delays are based on acoustic rays between two points representing the transducers. Thus the small consistent error is as expected, so that the two sets of minimum time results can be said to agree well.

Since errors in the computed image are due to acoustic refraction, a non-physical simulation of acoustic propagation along straight ray paths is also shown in fig. 3.2(b). The resulting ideal time delay projection is used to compute an image which is error free. A comparison of the projections in fig. 3.2(b) shows that the ideal projection is closely approximated by the projection which shows the time delays of the largest received acoustic pulse. Thus the time delay projections based on

the arrival time of the largest amplitude acoustic pulse produce less distortion than time delay projections based on minimum time acoustic propagation.

Parts of the body containing regions having a relatively high acoustic velocity (such as bones) cause strong refraction. The resulting time delay projections reconstruct to form a distorted image. It is desirable to minimize the extent of the strong refractions in the projections, and hence in the image. Maximum energy pulse time delay measurements appear to be the most successful in limiting the area of the distortions in the image.

3.4 TENUOUS MEDIA - SOFT TISSUE IMAGING

In a tenuous medium, the acoustic velocity does not vary greatly and the ray paths are almost straight. For soft tissues, the acoustic velocity varies from 1450 m/s for fat to 1585 m/s for muscle (c.f. Wells 1969), a range of ±4%. Refraction effects are therefore quite small. Lederman computed and plotted the acoustic ray paths for a projection of a human female breast containing a malignant lesion with a relatively high acoustic velocity (c.f. Glover and Sharp 1977, fig. 12). These ray paths deviate from straight lines by less than 5^{o}, so that it is reasonable to treat soft tissues as tenuous media.

Refraction of the acoustic waves can be computed from scattering theory. The calculation of scattered fields from a known volume for known incident fields is the subject of direct scattering theory. The problem of estimating the refractive index (or similar property) inside the scattering volume from measurements of the incident and scattered fields is the subject of inverse scattering and remote sensing theory. Wolf (1969) develops an elegant Fourier transform method for recovering the refractive index $n(\bar{r})$ from observations of the scattered field on two planes either side of the scattering volume. Since the Born approximation

is used in Wolf's solution, the isonifying wavelength must be significantly greater than the product of (n-1) and the largest dimension of the scattering region. Iwata and Nagata (1975) develop a similar procedure for recovering the refractive index volume distribution from measurements on a circumscribing sphere. Their solution employs the Rytov approximation which requires $|n-1| \ll 1$ (c.f. Chernov 1967). Consequently, their method is more general than that of Wolf.

Brekhovskikh (1960) shows that the monochromatic wave equation (3.12) applies to optics and electromagnetics as well as to practical acoustic problems. The various approximate solutions to (3.12) are discussed below and an improved Rytov approximation is derived (c.f. Bates, Boerner and Dunlop 1976, Dunlop, Boerner and Bates 1976). The improvement correctly describes the phase variation of the scattered field (the propagation time delay and phase variation are closely related as is shown later).

The total field ψ is partitioned according to

$$\psi = \psi^I + \psi^S \tag{3.19}$$

where ψ^S is the scattered field and ψ^I the incident field which satisfies the free space (n = 1) wave equation everywhere (c.f. Bates and Ng 1972). i.e.

$$\nabla^2\psi^I + k^2\psi^I = 0 \tag{3.20}$$

Combining (3.12), (3.19) and (3.20) we obtain

$$\nabla^2\psi^S + k^2\psi^S = -F_B\psi \tag{3.21}$$

where

$$F_B = k^2(n^2-1) \tag{3.22}$$

The standard Green's function solution (c.f. Jordan and Balmain 1968, p.340) of (3.21) yields the scattered field:

$$\psi^S = \int_{\mathcal{V}} F_B \psi G(R,k)\, d\mathcal{V} \tag{3.23}$$

where $\mathcal{V}$ is the scattering volume and G the Green's function. The Born approximation is

$$|\psi^S| << |\psi^I|,$$

which means that radiation scattered more than once is negligible. Thus (3.23) becomes

$$\psi^S(\bar{r},k) = \int_{\mathcal{V}} F_B(\bar{x})\psi^I(\bar{x})G(|\bar{r}-\bar{x}|,k)\, d\mathcal{V} \tag{3.24}$$

Since all variables other than F_B are known, (3.24) is solved for F_B and the refractive index distribution obtained.

The fields are defined slightly differently for the Rytov approximation:

$$\psi = e^{\gamma}, \quad \psi^I = e^{\gamma^I}, \quad \gamma = \gamma^I + \tilde{\gamma} \tag{3.25}$$

$$\tilde{\psi} = \tilde{\gamma}\, \psi^I \tag{3.26}$$

$$\psi^S = (\exp[\tilde{\psi}/\psi^I]-1)\psi^I \tag{3.27}$$

These relationships are substituted into the monochromatic wave equation (3.12) and manipulated to yield

$$\nabla^2\tilde{\gamma} + (2\nabla\gamma^I+\nabla\tilde{\gamma}).\nabla\tilde{\gamma} + F_B = 0 \tag{3.28}$$

The Rytov approximation:

$$|\nabla\gamma^I| >> |\nabla\tilde{\gamma}|$$

is used in (3.28) together with (3.20) to yield

$$(\nabla^2\tilde{\gamma}+2\nabla\gamma^I.\nabla\tilde{\gamma}-F_B)\psi^I + (\nabla^2\psi^I+k^2\psi^I)\tilde{\gamma} = 0$$

or

$$(\psi^I\nabla^2\tilde{\gamma}+2\nabla\tilde{\gamma}.\nabla\psi^I+\tilde{\gamma}\nabla^2\psi^I) + k^2\tilde{\gamma}\psi^I = -F_B\psi^I \tag{3.29}$$

The bracketed term is condensed:

$$\nabla^2(\tilde{\gamma}\psi^I) + k^2\tilde{\gamma}\psi^I = -F_B\psi^I \tag{3.30}$$

Substitute (3.26) into (3.30) , apply the Green's function solution:

$$\tilde{\psi} = \int_V F_B\psi^I G(R,k)\,dV \tag{3.31}$$

The function $\tilde{\psi}$ is related by (3.27) to ψ^S. Thus F_B is recovered as before. Notice that if the Born approximation also holds, then

$$\exp[\tilde{\psi}/\psi^I]-1 \approx \tilde{\psi}/\psi^I$$

and from (3.27)

$$\psi^S \approx \tilde{\psi}$$

Hence (3.23) is equivalent to (3.31) for $|\psi^S| << |\psi^I|$.

Bates, Boerner and Dunlop (1976) derive an improvement to the Rytov approximation by utilizing the W.K.B. solution of the wave equation (c.f. Felsen and Marcuvitz 1973) for cases where refraction predominates over reflection. Soft tissue imaging is such a case. The W.K.B. solution is:

$$\psi \approx n^{-\frac{1}{2}} \exp[-jk\int_{\tau_0}^{S_\tau} n\,dS_\tau] \tag{3.32}$$

where S_τ is the path along the τ^{th} ray from the source point τ_0. At a point on the ray, the unit vector $\hat{S}_\tau$ defines the direction of the curved ray which characterizes ψ, and $\hat{\tau}$ defines the direction of the straight ray which characterizes ψ^I. Combining (3.25) and (3.32) gives

$$\nabla\tilde{\gamma} = \nabla(\gamma-\gamma^I)$$

$$= \nabla(\ln\psi-\ln\psi^I)$$

$$= \nabla(\ln\{n^{-\frac{1}{2}}\exp[-jk\int_{\tau_0}^{S_\tau} n dS_\tau]\} - \ln\{\exp[-jk\tau]\})$$

therefore

$$\nabla\tilde{\gamma} = jk(\tilde{\tau}-n\hat{S}_\tau) - \nabla n/2n \tag{3.33}$$

and

$$(\nabla\tilde{\gamma})^2 = -k^2(n^2+1-2n\hat{\tau}\cdot\hat{S}_\tau) + (\frac{\nabla n}{2n})^2 - jk(\frac{\nabla n}{n})\cdot(\hat{\tau}-n\hat{S}_\tau) \tag{3.34}$$

Substitution of (3.34) into (3.28) yields

$$\nabla^2\tilde{\gamma} + 2\nabla\tilde{\gamma}\cdot\nabla\gamma^I + k^2[(n^2-1)-(n^2+1-2n\hat{\tau}\cdot\hat{S}_\tau) + (\frac{\nabla n}{2n})^2 - jk(\frac{\nabla n}{n})\cdot(\hat{\tau}-n\hat{S}_\tau)] = 0$$

or

$$\nabla^2\tilde{\gamma} + 2\nabla\tilde{\gamma}.\nabla\gamma^I = -F_{BBD} \tag{3.35}$$

where

$$F_{BBD} = k^2[2(n\hat{\tau}\cdot\hat{S}_\tau-1) + j(\nabla n/nk)\cdot(n\hat{S}_\tau-\hat{\tau}) + (\nabla n/2nk)^2] \tag{3.36}$$

The steps used to form (3.29) and (3.31) are applied to (3.36):

$$\nabla^2\tilde{\psi} + k^2\tilde{\psi} = -F_{BBD}\psi^I \tag{3.37}$$

Hence

$$\tilde{\psi} = \int_V F_{BBD}\psi^I G(R,k)\,dV \tag{3.38}$$

Note that the three terms in F_{BBD} (3.36) have a different dependence on k, and hence may be separated by solving (3.38) for F_{BBD} at three different frequencies. i.e. three sets of measurements.

The ray path dependence of (3.36) does not permit the straight forward solution of (3.38) by spherical harmonic analysis since a knowledge of n is required. However, the approximation $\hat{\tau}.\hat{S}_\tau = 1$ permits a straight forward solution. It is in error by 6% for a 20^o change of ray direction

and only .4% for a 5° change. Using this approximation, we rewrite (3.36) as

$$F_{BBD} = 2k^2\{(n-1)(1+\frac{j}{2k}\frac{\partial \ln[n]}{\partial \tau}) + \frac{1}{8k^2}(\nabla \ln[n])^2\} \tag{3.39}$$

The incremental phase shift Δ is the extra phase shift per unit length in ψ resulting from the presence of the medium (i.e. $n \neq 1$). A time domain derivation of Δ is as follows: the time difference for a pulse to travel a distance x through a constant medium (acoustic velocity V), and a distance x through water only is:

$$\delta t = \frac{x}{V} - \frac{x}{V_w} = \frac{x}{V_w}(n-1)$$

The extra phase change over the distance x due to the presence of the medium is

$$x\Delta = 2\pi f \delta t = 2\pi f \frac{x}{V}(n-1)$$

$$\therefore \quad \Delta = k(n-1) \tag{3.40}$$

The incremental phase shift may also be calculated from scattering theory:

$$\psi/\psi^I = \exp[\gamma-\gamma^I] = \exp[\tilde{\gamma}]$$

From (3.33), we evaluate $\tilde{\gamma}$ along the ray which is close to the direction of the unperturbated wave ψ^I. Thus

$$\nabla\tilde{\gamma} \approx -jk(n-1)\hat{\tau}$$

$$\therefore \quad \tilde{\gamma} \approx -jk\int_0^{\tau}(n-1)d\ell$$

$$\approx -jk(n-1)\ell$$

Hence

$$\psi/\psi^{I} = \exp[-jk(n-1)\ell]$$

Thus the incremental phase shift per unit length is

$$\Delta \approx (n-1)k, \tag{3.41}$$

which is as derived from the intuitive time domain approach. In addition, the extra terms involving ln(n) account at least partially for the ray curvature. In the same situation, the Rytov approximation yields

$$\Delta \approx (n^2-1)k/2 \tag{3.42}$$

which clearly has the wrong phase variation unless n is so close to unity that $(n+1)/2 \approx 1$, i.e. when

$$\Delta \approx (n^2-1)k/2 = (n-1)k(n+1)/2 \approx (n-1)k$$

Keller (1969) uses a perturbation series to represent a single wave travelling through a tenuous medium and shows that a series based on the Rytov approximation converges faster than one based on the Born approximation. The restriction of a single wave is equivalent to the requirement that refraction predominates over reflection. The analysis performed so far indicates an improvement on the Rytov approximation even if the derivatives of n are neglected in (3.39). Therefore a reasonable approximation is

$$F_{BBD} \approx 2k^2(n-1) \tag{3.43}$$

These formulae are now tested and compared for a known scattering object for which an analytic solution is obtained. The two-dimensional case of a circular cylinder of radius b and constant refractive index n is chosen for a plane incident wave (c.f. fig. 3.3) so that:

$$\psi^I = \sum_{m=-\infty}^{\infty} A_m J_m(k\rho) e^{jm\phi} \qquad \rho \geq b \tag{3.44a}$$

$$\psi^S = \sum_{p=-\infty}^{\infty} B_p H_p^{(2)}(k\rho) e^{jp\phi} \qquad \rho \geq b \tag{3.44b}$$

and

$$\psi = \sum_{q=-\infty}^{\infty} C_q J_q(nk\rho) e^{jq\phi} \qquad \rho \leq b \tag{3.44c}$$

The coefficients A_m, B_p and C_q are related by equating the m^{th} harmonic wave and its derivative at the cylindrical boundary. Manipulation yields

$$B_m = -A_m \frac{J_m(kb)nJ_m'(nkb) - J_m'(kb)J_m(nkb)}{H_m^{(2)}(kb)nJ_m'(nkb) - H_m^{(2)'}(kb)J_m(nkb)} \tag{3.45}$$

where $C_m'(x)$ is $\partial C_m(x)/\partial x$.

We now use (3.24) to obtain B_m for the Born approximation. In two dimensions, the Green's function is $-\frac{j}{4} H_0^{(2)}(kR)$, which can be expanded by Graf's addition theorem (c.f. Abramowitz and Stegun, 1965, §9.1.79) to give

$$G(kR) = -j\pi \sum_{\ell=-\infty}^{\infty} H_\ell^{(2)}(k\rho) J_\ell(kr) e^{j\ell(\phi-\theta)} \tag{3.46}$$

for $\rho \geq r$, where R is the distance between the field point $P(\rho,\phi)$ and a point in the scatterer $Q(r,\theta)$. Using (3.44a) and (3.46) in (3.24), we obtain:

$$\psi^S = -\frac{j\pi}{4\pi} F_B \sum_\ell H_\ell^{(2)}(k\rho) e^{j\ell\phi} \sum_m A_m$$

$$\int_{r=0}^{b} \int_{\theta=0}^{2\pi} J_\ell(kr) e^{-j\ell\theta} J_m(kr) e^{jm\theta} r\,d\theta\,dr$$

$$-\frac{jF_B}{4} \sum_m H_m^{(2)}(k\rho) e^{-jm\phi} 2\pi A_m \int_{r=0}^{b} r J_m^2(kr)\,dr$$

$$= -\frac{j\pi F_B}{4} \sum_m H_m^{(2)}(k\rho) e^{-jm\phi} A_m \left(\frac{b}{2}\right) \left[J_m^2(kb) - J_{m-1}(kb) J_{m+1}(kb)\right]$$

where Eq. 11, p.135, Watson (1966) is used to evaluate the integral. The harmonic components are now equated to yield:

$$B_m = -A_m \frac{j\pi b^2}{4} F_B [J_m^2(kb) - J_{m-1}(kb)J_{m+1}(kb)] \tag{3.47}$$

The same approach to this problem is applied to the first term of the improved Rytov formulation (3.43). This yield an equation which is the same as (3.47) but F_{BBD} replaces F_B, and $\tilde{\psi}$ replaces ψ^S in (3.44b).

Some distance from the scattering volume, the far field approximation can be used and $H_m^{(2)}(k\rho)$ can be replaced by an asymptotic expansion as $k\rho \to \infty$:

$$H_m^{(2)}(k\rho) \to \left(\sqrt{\frac{2}{\pi k\rho}}\, e^{-j(k\rho - \frac{\pi}{4})}\right) e^{jm\frac{\pi}{2}} \tag{3.48}$$

This equation is used to normalize the results so that (3.44b) becomes

$$\psi^S_{norm.} = \sum_m B_m e^{jm(\phi + \frac{\pi}{2})} \tag{3.49}$$

Note that in the far field $|\psi^S| << |\psi^I|$ so

$$\psi^S = (\exp[\tilde{\psi}/\psi^I] - 1)\psi^I \simeq \tilde{\psi}$$

Thus the Born and Rytov approximations yield the same results in the far field. Also, the values of B_m calculated for the improved Rytov formulation can be used to calculate ψ^S directly from (3.49) rather than $\tilde{\psi}$.

The values of $|\psi^S_{norm.}|$ have been calculated for several radii, $b = \lambda$, 2λ and 5λ, and for various refractive indices, n = 1.05, 1.1, 1.15, ...,1.5. A representative plot of $|\psi^S_{norm.}|$ is given in fig. 3.4. Also, a plot of the field magnitude error function ψ:

$$\varepsilon = \frac{\left| |\psi^s_{norm.}|_{exact} - |\psi^s_{norm.}|_{approx.} \right|}{|\psi^s_{norm.}|_{exact}} \qquad (3.50)$$

is plotted in fig. 3.5 for various values of the refractive index. Inspection of fig. 3.5 shows that the first term of the improved Rytov approximation gives a scattered far field which is closer to the exact value than the fields calculated from either the Born or Rytov approximations. The phase terms calculated from either the Born or Rytov approximations must be erroneous since the B_m determined from (3.47) have a fixed phase of -j, whereas the exact calculation of B_m from (3.45) has complex Hankel functions determining the phase. The improved Rytov approximation has a complex F_{BBD} as in (3.39), but the additional derivative terms make a difference of less than 2% in the calculated values when $b = \lambda$, and are thus neglected. A plot of the phase of the field scattered from a cylindrical surface of radius 2λ when the cylinder is centred at λ and $b = \lambda$ (c.f. fig. 3.3) is presented in fig. 3.6 for various values of n.

In the near field, the phase calculation based on the Rytov approximation is more accurate than calculations based on the Born approximation. The phase calculated by the improved Rytov approximation is even more accurate.

In conclusion, the improvements to the Rytov approximation contain the correct form of phase variation. Thus procedures used to calculate refractive index distributions can be upgraded by replacing the Born or Rytov approximations with the improved Rytov approximation. In particular, it may be possible to improve on the ray tracing methods applied a posteriori to acoustic time delay reconstructions (c.f. Johnson et al. 1975).

3.5 EXTENDED PHASE CONTRAST MICROSCOPY

The purpose of this section is to examine acoustic imaging systems which produce two-dimensional images dependent on the acoustic velocity in an object. These systems are similar to the optical phase-contrast microscope. They measure and display, over two-dimensions, the relative phase of the ultrasound transmitted through a body. The image produced is similar to an X-ray shadowgram provided the variation in phase is small. As is explained in chapter 2, many shadowgrams measured at positions around a body can be used to compute tomograms or cross sections through the body. This explains the interest in phase measurements for acoustic time delay computed tomography.

The equivalence of time and phase differences is established in section 3.4 (see the derivations leading to 3.40 and 3.41). The acoustic propagation delay can be estimated from phase measurements extended over many cycles. A method of extending phase measurements is developed at the end of this section.

In 1935, Zernike devised a phase-contrast technique for light microscope inspection of optically transparent objects. The technique is based on spatial filtering principles and has the advantage that the observed intensity is linearly proportional to the phase shift introduced by the object, provided that the phase shift is less than one radian (c.f Goodman 1968).

Mezrich and Vilkomerson (1975) constructed an ultrasonic phase contrast imaging system which is based on similar principles to the optical phase-contrast microscope. In the ultrasonic system, the image is formed on a thin (~6 μm) gold plated plastic pellicle which is optically examined by a scanned laser beam. The displacement at any point on the pellicle is nearly equal to that of the fluid particles displaced by the sound wave passing through the pellicle at that point. The equality is maintained for a sound frequency range of .5-10 MHz and for angles of

incidence less than 40°. Movement of the pellicle is detected by using the pellicle as a mirror in one arm of a mechanically stabilized Michelson interferometer. A phase shift of a few tens of degrees at 2.25 MHz is sufficient to produce clear images of thin objects. Reasonably clear images of thick objects (such as calves' livers) are also produced with good contrast. However, with the thick objects, the image intensity is no longer linearly dependent on the phase shift (c.f. Born and Wolf 1970, p.424).

The ultrasonic microscope system developed by Lemons and Quate (1974) is similar to single sideband holographic systems mentioned in section 1.5 provided the microscope is used on its phase-contrast mode. The microscope uses two liquid lenses (focal length .15 mm, f number .75) and operates near 1 GHz (.75 MHz with a 75% bandwidth). Only a small portion (~1 μm) of the object is isonified at any one time. The object is mechanically scanned in a raster fashion and at the same time the image is produced on a synchronously scanned CRT display. The microscope operates in either an ultrasonic amplitude transmission or reflection mode, or in a transmission phase-contrast mode. For phase-contrast imaging, the phase of the signal output from the microscope is compared with the phase of the transmitted signal so that the relative acoustic phase through each isonified point in the object is obtained. Display of this information results in the phase-contrast image. The received signal is mixed with a portion of the signal supplied to the transmitting transducer in order to generate a base band signal which is applied to the intensity modulation circuitry of the CRT display. 'Bright' or 'dark' phase contrast images can be formed by altering the phase shift between the two signal inputs to the mixer. Images of microtomed tissues and cells can be formed with good contrast by using either amplitude or phase contrast microscopy whereas staining procedures are needed for the equivalent optical observation.

If two reference signals in phase quadrature are used to generate two base band outputs f_1 and f_2:

$$f_1(x,y) = A(x,y)\ \sin[\phi(x,y)] \tag{3.51}$$

and

$$f_2(x,y) = A(x,y)\ \cos[\phi(x,y)] \tag{3.52}$$

Then

$$\phi(x,y) = \tan^{-1}[f_1(x,y)/f_2(x,y)] \tag{3.53}$$

The value of ϕ can be assigned to a quadrant in the range $(0,2\pi]$ by considering signs of f_1 and f_2. If f_1 and f_2 have a bias term greater than the largest value of $|A(x,y)|$ added to them, then they can be used to form two holograms from which the total phase can be calculated. Alternatively, if $A(x,y)$ does not vary greatly, f_1 and f_2 can be digitized and stored so that the phase calculation can be performed in a digital computer. A fast elegant technique is to use the digitized words for f_1 and f_2 as an address for a ROM (read only memory) which outputs the phase $(0\text{-}2\pi]$. To ensure that the full dynamic range of the analogue to digital converters is used, an A.G.C. stage may be required to reduce amplitude variations of $A(x,y)$.

A problem occurs when the phase changes by many cycles since the calculated phase is restricted to the range $(0,2\pi]$. This problem, together with its solution, is illustrated diagramatically in fig. 3.7. Phase changes of greater than π are interpreted as an excursion outside the current $(0\text{-}2\pi]$ range and an extra cycle of phase must be added to, or subtracted from, the cycle counter. Thus, the phase measurement is extended beyond the $(0\text{-}2\pi]$ range and an extended phase contrast measurement is made.

The phase measurement system just described is an incremental system and cannot handle sudden changes of phase such as those which can occur in multipath signal interference. This would cause the extended phase cycle counter to lose count and thus cause major errors. A method based on measuring the phase of a modulation envelope would be capable of producing an absolute extended phase measurement. This method is widely used for electromagnetic distance measurements in land surveying and is based on comparing the phase of a received modulation envelope, with the phase of the envelope applied to the transmission (c.f. Clendinning and Oliver 1969). An initial low frequency envelope gives a rough time estimate without ambiguity. Higher frequency modulation envelopes refine the measurement, but suffer from ambiguity with respect to the number of cycles of the envelope function separating the portions which are compared in phase. The phase ambiguity is removed by using the earlier low modulation frequency measurements to extend the phase measurement. The limit is reached when the phase of the actual carrier is used for phase comparison purposes. Thus, very accurate extended phase or time measurements are possible with this method.

3.6 CONCLUSIONS

Ultrasonic propagation through a diaphanous medium is characterized by straight ray paths whereas propagation through strongly inhomogeneous media is characterized by bent rays. The wave equation for propagation through inhomogeneous media is derived in section 3.2 and acoustic ray equations developed. In section 3.3, measured and computed acoustic propagation time delays are compared for an aluminium cylinder immersed in water. The acoustic ray paths are computed by using Fermat's principle and the ultrasonic pulse propatation time delay is calculated for each ray path. Measured time delays for the acoustic pulse which is received first, and for the pulse received with the largest amplitude, agree well

with the computed time delays.

An approximate solution to the direct scattering problem is developed in section 3.4. This solution is obtained by incorporating the WKB solution of the wave equation into the Rytov approximation. The result is an improved Rytov approximation which contains the correct form of phase variation, something which is absent from both the conventional Born and Rytov approximations. The field scattered from a uniform cylinder is computed for the exact solution, and for the Born, Rytov and improved Rytov approximations. The improved Rytov approximation yields superior results at a distance from the scatterer (i.e. in the far field). The computed amplitude of the scattered field is similar for both the ordinary and improved Rytov approximations. However, the accuracy of the phase computed by the improved Rytov approximation is greatly improved (c.f. fig. 3.6).

The changes in phase and propagation times, due to an inhomogeneous medium, are equated in section 3.4. The possibility of employing phase measurements instead of time measurements is examined in section 3.5. A method is developed to extend phase measurements so that they are equivalent to time delay measurements for a single ultrasonic path. For multipath propagation, the measured phase is dependent on the amplitude and phase of the signal propagating by each path.

Multipath acoustic propagation is most important when strong acoustic refraction occurs. The results obtained in section 3.3 show that time delay measurements based on the largest amplitude acoustic pulse yield a projection which most closely approximates the ideal straight X-ray path projection (c.f. fig. 3.2b). Thus measurement of the quantity

$$T_w - T(\xi,\phi) = \int_{-\infty}^{\infty} \left(\frac{1}{V_w} - \frac{1}{V(x,y)}\right) d\eta' \qquad (3.54)$$

(where $d\eta'$ is an element of the ray path by which the largest amplitude pulse propagates) yields the most accurate computed image since the projections measured are those least affected by refraction.

For soft tissue (or diaphanous media), the differences between ray paths is usually very small. The minimum time delay measurements, the largest amplitude pulse time delay measurements, and the extended phase measurements then yield almost the same results. Thus phase measurements have not been pursued further, and only minimum time delay measurements have been used during the preliminary measurement work. A system for measuring the propagation time delay of the largest amplitude acoustic pulse is described in chapter 4. The system is used extensively to obtain many of the results presented in chapter 7.

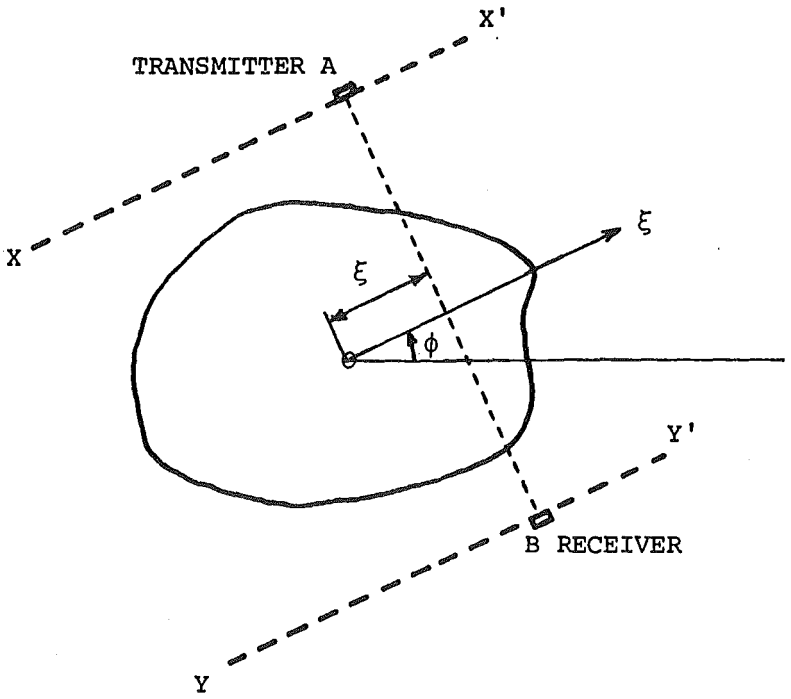

Fig. 3.1 The archetype scanner.

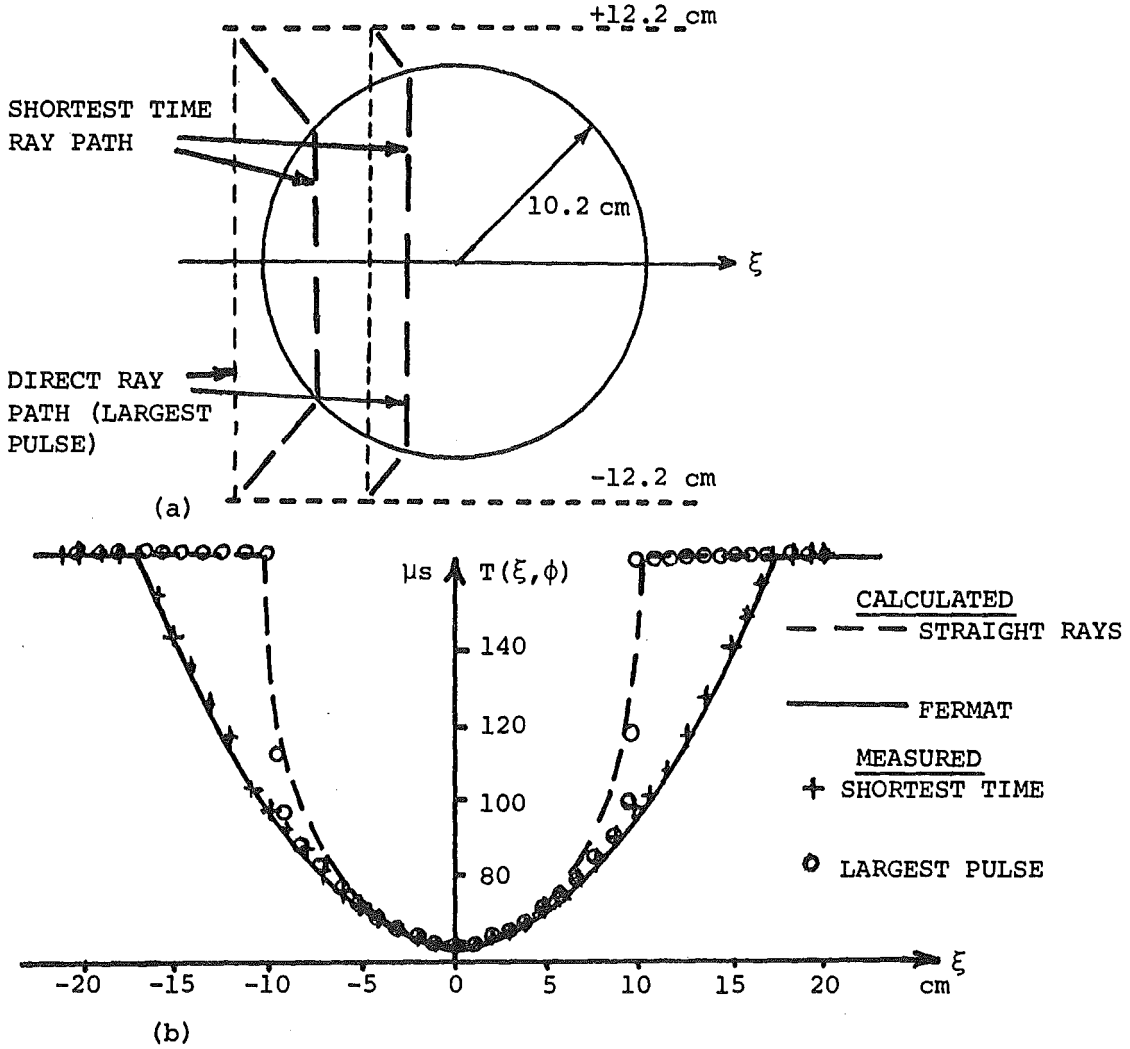

Fig. 3.2 (a) Arrangement for measuring time delays through an aluminium cylinder.

(b) Actual time delay measurements compared with simulated straight and curved ray path times.

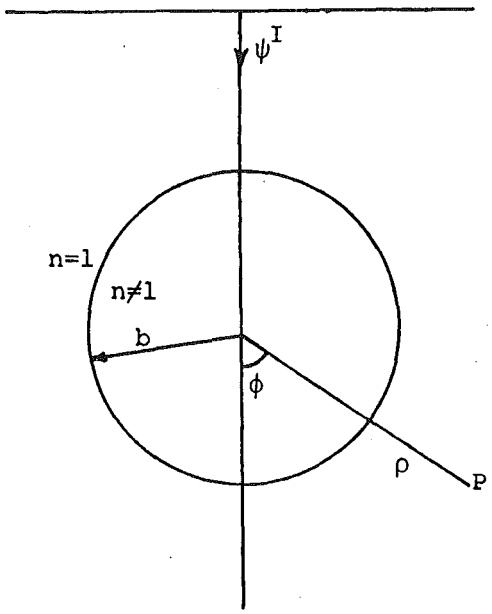

Fig. 3.3 Geometry for the wave incident on the cylindrical scatterer.

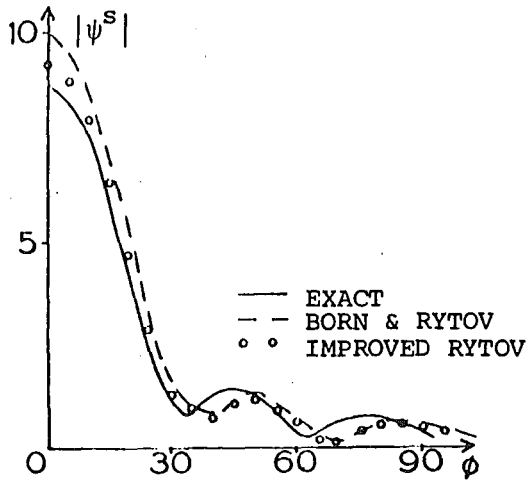

Fig. 3.4 A typical plot of the far field scatter when n = 1.15 and b = λ.

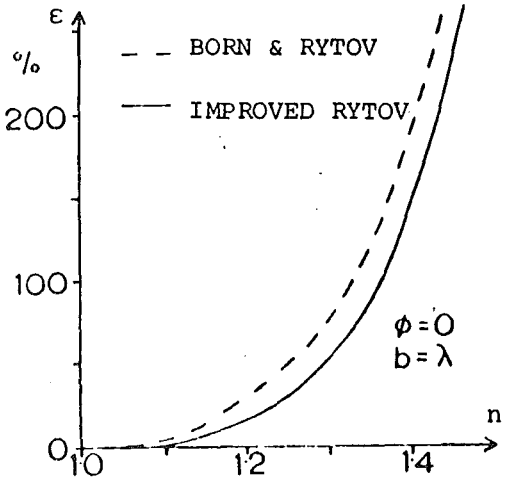

Fig. 3.5 Far field forward scatter error as a function of the refractive index for ϕ = 0 and b = λ.

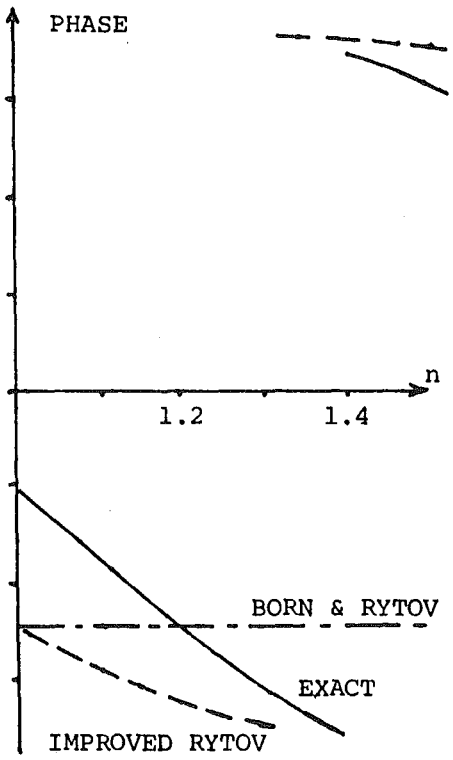

Fig. 3.6 A plot of the phase of the far field forward scatter as a function of n for ϕ = 0 and b = λ.

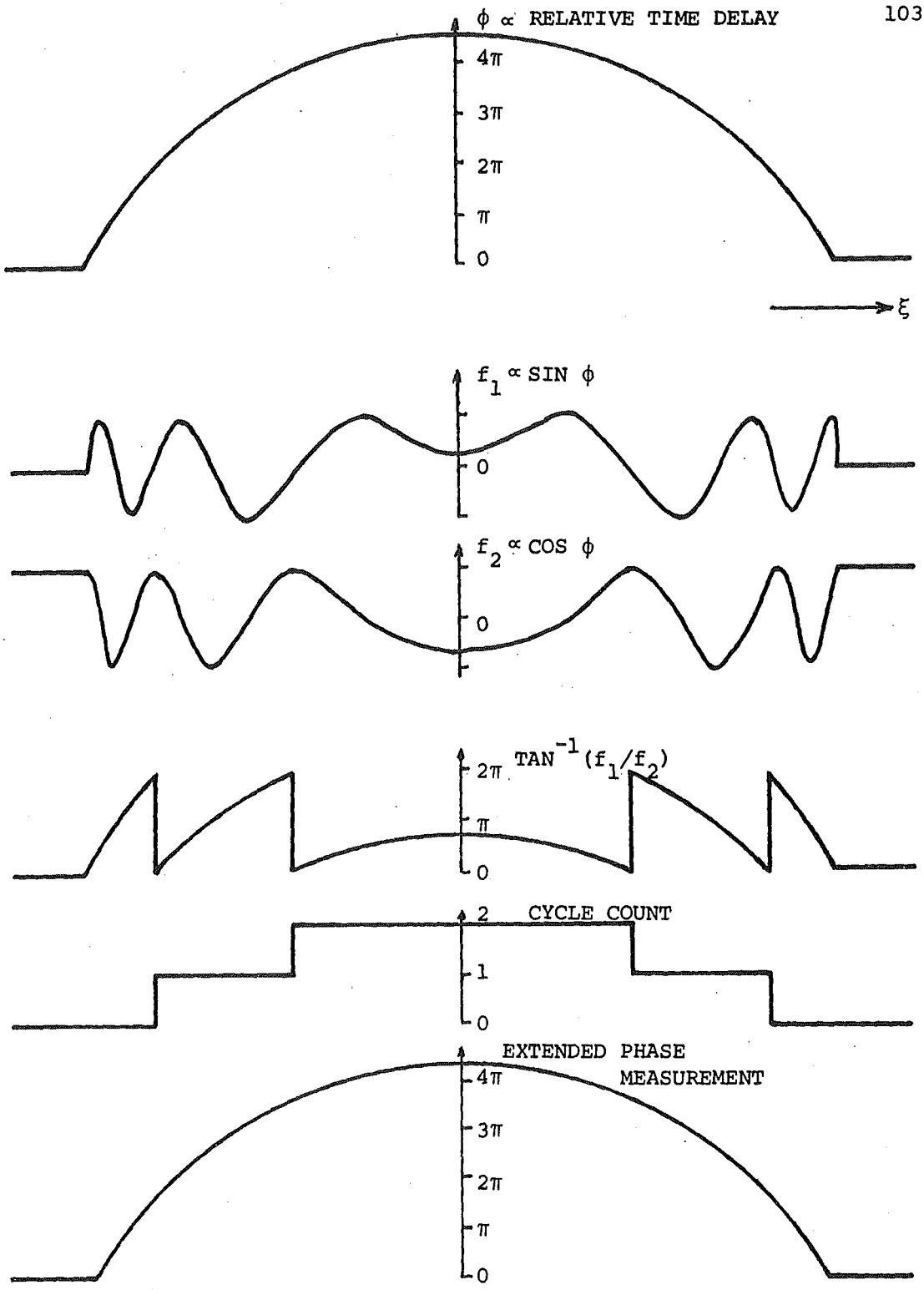

Fig. 3.7 Extended phase measurements using quadrature base band signals f_1 and f_2. A change of 2π in phase is equivalent to a time change equal to the period of the ultrasonic waves.

CHAPTER FOUR

A SIGNAL PROCESSING AND COMPUTER CONTROL SYSTEM

4.1 DESCRIPTION OF THE ULTRASONIC IMAGING SYSTEM

In this section, an ultrasonic transmission imaging system is described. The remainder of this chapter is devoted to examining the components of the system and the associated measurement methods. The purpose of the system is to measure the ultrasonic time delay at positions (ξ,ϕ) so that an acoustic time delay projection measurement based on (3.54) is represented by $\tilde{f}$:

$$\tilde{f}(\xi,\phi) = T_w - T(\xi,\phi) \tag{4.1}$$

The acoustic time delay projection is processed in the same manner as an X-ray projection to yield the quantity $(\frac{1}{V_w} - \frac{1}{V(x,y)})$ at points (x,y) in the image plane, i.e. $\tilde{f}$ replaces f in the process outlined in section 2.3.

A block diagram of the measurement system is shown in fig. 4.1. An E.A.I. 640 digital computer is used to control the measurement system. The computing system (enclosed by the dotted line shown in fig. 4.1) is connected to the scanner and signal processing electronics by 20 m of cabling. The two sets of apparatus are in adjacent rooms.

The digital computer sets the (ξ,ϕ) position, the signal processing gain (via the E.A.I. 590 analog computer) and computes the image from the measured projections. The digital computer is a 16-bit word length machine with integer arithmetic facilities and 16 k words (32 k bytes) of core memory. The limited dynamic range of a 16-bit word length causes accuracy and overflow problems when processing two-dimensional images. The problems are overcome by employing 32-bit floating point arithmetic. Floating point arithmetic is slow when executed on the EAI 640 since only integer arithmetic facilities are installed.

The arrays of data used to represent the projections and the image require many words of memory for storage. Insufficient core memory is available for this purpose so the arrays are stored on a fixed head

magnetic disc. Up to 4 channels are utilized at any one time to transfer the array data between core memory and the disc. The amount of core memory available is also too small to contain the measurement system software. The software is split into blocks, described in section 4.2, and multiphase program execution from disc is employed. At the completion of a measurement session, the 248k bytes of user's disc storage is dumped onto magnetic tape for long term storage.

The methods of measuring time delays are discussed in section 4.3, and matched filtering and signal encoding are discussed in section 4.4. Implementation of the matched filter is discussed in section 4.5 where a non-linear sampling method is also described. The binary data interface (BDI) between the digital computer and the scanner system electronics is described in section 4.6. The initial design of the BDI was produced by the author so it is described in some detail. The digital computer calculates the ξ and ϕ positions as two 12-bit words which are output via the BDI. The numerical control systems set ξ and ϕ according to the two 12-bit control words and they are described in section 4.7. Some innovative work resulting from studies of digital servosystems is reported in section 4.8.

4.2 SOFTWARE ORGANIZATION

The software for the ultrasonic imaging system has been organized as six separate files which are stored on the magnetic disc. The computer memory is time shared and its organisation is shown in fig. 4.2(a). The control file for the Sonic IMAGE system is named SIMAGE. The purpose of SIMAGE is to load into core memory the subroutine files named SIMAG0, SIMAG1, SIMAG2 or SIMAG3, and SIMAG4. The first subroutine in each of these files is named DUMMY so that the files may be loaded and executed sequentially by a single control loop in SIMAGE. The function of each program file is now described in turn.

SIMAGE: This is the control program file for the system software. It contains the subroutines needed to utilize the disc input-output routines resident in the computer system monitor. The first function performed by the control program is to switch off the interrupts from the BDI as these can abort the magnetic disc file loading routines. The program contains the name of the first file to be loaded, SIMAG0, as six ASCII characters stored in an integer name array. After SIMAG0 has been loaded into core memory, subroutine DUMMY is called and the programs contained in SIMAG0 are executed. When control returns to SIMAGE, the loop counter I is incremented (modulo 5) from 0 to 1, and then added to a constant to form a number which is stored in the last element of the file name array. The name array now contains the file name SIMAG1. The loop counter is then tested so that if I = 0 control is returned to the computer system monitor. Otherwise the file in the name array (SIMAGI) is loaded into core memory and the programs contained in it are executed by calling subroutine DUMMY. Thus the control program is ready to be restarted from the system monitor after each imaging run.

SIMAG0: When this file is loaded, constants and data file names are loaded into the common data block area of the core memory so that they can be used by the subroutines contained in the files which are loaded later. The main purpose of SIMAG0 is to obtain the parameters needed to control the scanner, the data collection and the reconstruction programs. The storage CRT screen is used to list the various sense switch options (push button options selected from the digital computer console), and to request various constants such as the number of projections to be measured, and the number of sample points on a projection.

Several modes of operation can be selected by setting the sense switches. The first mode is to measure the time delays and to reconstruct the image. The second mode is to process previously measured time delay

projections contained in a data file and to reconstruct an image from these. The third mode is to calculate time delay projections for rectangular and circular objects, and then to reconstruct an image from these calculated projections.

The data file names loaded into the common data block area may already exist in the disc directory, so a special disc file naming routine tries to locate the file to be named. If the file name is not found on disc, then the file name is free and it is used to name a new data file. If the file name is not free, then the letters A through to Z are successively substituted for the last character of the file name and the positioning process repeated until a free file name is found. This special data file naming routine was written by the author and it is in use as a system file named @MON23.

SIMAG1: This file contains the subroutines needed to move the scanner to the required (ξ,ϕ) positions, and to measure the ultrasonic propagation time delay. A flow chart of the measurement program is given in fig. 4.2(b). The programs, written in FORTRAN IV and assembly language, utilize three different interrupt procedures. Two of the procedures are initiated by the scanner equipment, and the third is associated with trapping the monitor routines for disc file transfers.

The scanner equipment which controls the open loop digital servo systems generates an interrupt if any one (or more) of 11 different logic states indicates an error condition. When a scanner error interrupt occurs, the computer responds by resetting the absolute position of the scanner system. The computer then continues with the measurements. When the scanner has reached the (ξ,ϕ) position demanded by the computer, the interrupt line is used to inform the computer which then initiates the

time delay measurements. The same interrupt line is also used to control the flow of data into the computer memory during the measurements.

Once a projection is measured, the time delay samples are stored in a disc data file. The scanner angle is then incremented for the next projection which is measured by scanning across the projection in the opposite direction to the previous scan. The process continues until the required number of projections is measured. The BDI interrupts are then blocked and the data file is closed.

SIMAG2: The programs in this file make extensive use of the Fast Fourier Transform algorithm (Cooley and Tukey 1965). Some FFT programs written by the author are contained in the system programs as a file named FFT. They are 60% faster (for a 1024 point transform) than the FFT programs supplied by EAI. The Fourier transform $F(\rho,\phi_i)$ of the projection $\tilde{f}(\xi,\phi_i)$ is used to form $\Lambda(\rho,\phi_i)$ as indicated in (2.22). $\Omega(\alpha,\beta)$ is estimated from $\Lambda(\rho,\phi)$ by using linear interpolation in angle and radius to change from polar to rectangular coordinates. A two-dimensional inverse FFT of $\Omega(\alpha,\beta)$ then yields the required image.

Since the sampled projections have only real sample points, the spatial frequency spectrum exhibits Hermitian symmetry and only the positive spectral values are calculated. Also, since the image is purely real, $\Omega(\alpha,\beta)$ also exhibits Hermitian symmetry, and $\Omega(\alpha,\beta)$ is only calculated for non-negative values of β.

The discrete Fourier transform suffers from "leakage" and "picket fence" effects which are associated with the frequencies occurring between the sample frequencies in the discrete spectrum. These effects are discussed in detail by Bergland (1969) and Peters (1973). However, the Fourier method can reconstruct 64 pixel by 64 pixel images in about three minutes on the E.A.I. computer and it is used to form a preliminary

image as soon as a complete set of measurements is obtained. The slower back projection reconstruction process is later used to compute images containing fewer artefacts. This is done by using SIMAG3 in place of SIMAG2.

SIMAG3: This file contains the programs which form the modified back projections $\hat{f}$ from the sampled projections $\tilde{f}$ contained in the data file. Either the Ramachandran-Lakshminarayanan or the Shepp-Logan spatial filter coefficients $b(\xi)$ are calculated and used to form $\hat{f}(\xi)$ from $\tilde{f}(\xi)$ by means of (2.28). Alternatively, the layergram is formed rather than the deblurred image. The use of the Shepp-Logan filter is preferred (see the discussion in section 2.3).

The image is sampled on a cartesian grid and the sample values are stored in a square matrix. The location of a sample value in the matrix corresponds to the position of the sample on the grid. Thus the matrix used to store the samples of the image is termed the "image matrix". The image matrix is often quite large and its storage requirements usually exceed the available core memory. The image matrix is stored on disc and only a few columns of the matrix are retained in core memory at any time. In addition, the modified projections $\hat{f}$ require a large amount of memory, and so only two of these are retained in core memory. The problems caused by the small size of the core memory are overcome by expressing the complete image $\bar{\omega}_M(x,y)$ as a sum of partial images $\omega_i(x,y)$:

$$\bar{\omega}_M(x,y) = \frac{\pi}{M} \sum_{i=1}^{M/2} \omega_i(x,y) \tag{4.2}$$

The number of projections M is even and x and y are restricted to the cartesian grid lines. The partial image is:

$$\omega_i(x,y) = \hat{f}(x \cos \phi_i + y \sin \phi_i, \phi_i)$$

$$+ \hat{f}(-x \sin \phi_i + y \cos \phi_i, \phi_i + \frac{\pi}{2}) \qquad (4.3)$$

The first pair of projections is read from disc storage, modified and back projected to form the first partial image $\omega_1(x,y)$ which is stored in the image matrix. Only a few columns are calculated at a time before they are stored in the image matrix on disc. The process continues until all of the matrix columns are calculated and stored on disc. The image matrix then contains $\omega_1(x,y)$. A second pair of projections is read into the core memory and convolved with the spatial filter coefficients to form a pair of modified projections. The first few columns of the image matrix are then read from disc storage. The first few columns of $\omega_2(x,y)$ are computed and added to the first few columns of the image matrix. These columns of the image matrix are then written into their previous location on the disc. The process of reading, adding to and rewriting the image matrix a few columns at a time continues until the image matrix stored on disc contains the sum of partial images $\omega_1(x,y) + \omega_2(x,y)$. Another pair of projections is read from disc and the process is repeated. This continues until M/2 pairs of projections have been processed and M/2 partial images summed. The complete image $\bar{\omega}_M(x,y)$ is then contained in the image matrix stored on disc.

The values of $(x \cos \phi_i + y \sin \phi_i)$ evaluated in (4.3) rarely correspond to the projection sample points. Various forms of interpolation between the projection sample points are discussed by Lewitt, Bates and Peters (1978). Implementation of a high speed interpolation scheme is discussed by Dunlop (1978).

SIMAG4: The image matrix computed by SIMAG2 or SIMAG3 is stored on disc. The programs in the file SIMAG4 are used to retrieve the image matrix from disc, to process it a few columns at a time, and to display it on the

computer's storage CRT. The image sample values stored in the image matrix are scaled and shifted to lie in the range 0 to 1. The image is then displayed with 0 represented by the "black" level on the CRT and 1 represented by the "white" level. The intermediate values are represented by a "grey scale". After inspecting the image displayed on the CRT, the system operator can select the black and white levels anywhere in the 0 to 1 range so that only a limited image level range is displayed. Alternatively, the picture levels are inverted.

Each value in the image matrix is represented by a square pixel in the image on the CRT. The smallest position increment possible on the storage CRT is .25 mm and the pixel is formed by many bright dots on a .25 mm square grid. Thus a pixel which is 2.5 mm on a side contains 100 such spot positions. Maximum brightness is obtained when only one third of the available spot positions are bright i.e. 33 bright spots would represent brightness level 1 for a 2.5 mm square pixel. The bright spots are positioned within the pixel in a pseudo-random fashion. The number of bright spots determines the "grey level".

The black and white image displayed is also viewed as a perspective image when the appropriate sense switch options are selected. The image displayed in the (x,y) plane is no longer "intensity modulated" to form the black and white image. Instead, the grey level (0 to 1) at sample point (x,y) is allocated to the z coordinate. Thus the image values are represented by the height of a single surface above the x-y plane. Perspective views of such surfaces are used extensively in chapter 6 to present results. To simplify the perspective images, hidden lines are not displayed unless they are specifically selected for display.

4.3 TIME DELAY MEASUREMENTS

The time delay measurement system used by Glover and Sharp (1977) is simple and is capable of measuring the minimum propagation time for an ultrasonic pulse which has travelled by the shortest time ray path. The system employs incoherent signal detection and high signal levels are used to achieve an adequate signal to noise ratio (S/N). However, the system cannot measure the propagation time for the maximum energy ray path when this is different from the minimum time ray path (c.f. section 3.5). Greenleaf et al. (1975) use a high speed transient recorder controlled by a computer to sample the received signal, and then use the computer to calculate the propagation time delay. The samples are taken at 10 ns intervals and the computer is programmed to measure the shortest time delay.

The two time delay measurement systems discussed, both utilize a high voltage pulse (typically up to 800V) to excite the transmitting ultrasonic transducer. Thus both systems achieve signal levels at the receiver output which are sufficient to obtain an adequate S/N, i.e. greater than 20 dB. The incoherent detection system measures the time at which a preset voltage level is exceeded by the received signal. Thus the saturation and dynamic range problems associated with the receiver are avoided. The system based on the transient recorder has over-range and under-range indicators which are used by the control computer to set the gain of the preamplifier in the recorder. Thus the full range of the recorder's ADC is used to give the greatest possible accuracy for the sample measurements.

There are several problems associated with employing high voltages in experimental equipment. The first problem is that the water tank scanner provides an excellent electrocution earth path for anyone working on the scanner or handling the transmitting transducer. Secondly, the

use of high intensity pulses of ultrasound should be avoided until the safety issue is settled definitively. Finally, a failure of the experimental equipment could result in high voltages in the computing system. This would destroy many sections of the computer electronics and cause great inconvenience to the many other researchers using the Computer Laboratory. The above problems are avoided when low voltage transducer drives are employed. However, some form of matched filtering or signal encoding is then required to obtain an adequate S/N.

4.4 MATCHED FILTERING AND SIGNAL ENCODING

It is desirable, for the reasons given in section 4.3, to drive the transmitting transducer with low voltage signals. However, as the voltage of the transmitted signal is reduced, so also is the S/N of the received signal. To improve the S/N of the received signal, signal encoding and matched filtering techniques are employed. Matched filtering is discussed first.

The S/N of the received signal is optimized when a matched filter is implemented (c.f. Dunlop 1973). The received signal s(t) is divided into two parts: the pulse component p(t) which is to be detected, and the noise component n(t) which tends to mask p(t). Thus

$$s(t) = p(t-T) + n(t) \tag{4.4}$$

where the pulse is received a time T after the initial transmission. The matched filter delays the frequency components of p(t) so that the components combine to give the maximum possible output at a time T_1 after the pulse enters the filter. Lathi (1968) derives the impulse response of a matched filter as

$$h(t) = p(T_1-t) \tag{4.5}$$

The output from the matched filter is the convolution of the input signal and the impulse response of the filter:

$$O(t) = \int_{-\infty}^{\infty} s(x)h(t-x)dx \tag{4.6}$$

$$= \int_{-\infty}^{\infty} [p(x-T)+n(x)]p(T_1-t+x)dx$$

$$= \int_{-\infty}^{\infty} p(y)p(T_1+y+T-t)dy + \psi_{np}(t-T_1)$$

$$= \Psi_{pp}(t-T_1-T) + \Psi_{np}(t-T_1) \tag{4.7}$$

where x and y are dummy variables and $\Psi_{np}(t)$ is the cross correlation of signals p(t) and n(t). The matched filter output peaks at $\Psi_{pp}(0)$, i.e. at a time T_1+T which is the time at which the pulse component exits from the matched filter.

The matched filter is usually implemented as a crosscorrelation or transversal filter. A reference signal p(t) is compared with the received signal s(t) to give an output from the crosscorrelation filter:

$$\Psi_{ps}(\tau) = \int_{-\infty}^{\infty} p(t)s(t+\tau)dt \tag{4.8}$$

$$= \int_{-\infty}^{\infty} p(t)[p(t+\tau-T) + n(t+\tau)]dt$$

$$= \Psi_{pp}(\tau-T) + \Psi_{pn}(\tau) \tag{4.9}$$

The arrival time of the pulse component of s(t) occurs at $\tau = T$, the time at which the peak value of Ψ_{pp} occurs. Note that the crosscorrelator does not produce an instantaneous output. The shortest possible time delay for an output is when $\tau = t-T_1$, i.e. at the same time as the matched filter output.

A matched filter detection system was implemented as a cross-correlation on the Electrical Engineering Department's EAI 590 hybrid computer. The computer is used to control the sampling system which is discussed in section 5.5. The signal waveforms shown in figs. 4.3 and 4.5 were obtained by sampling the signal received by a 3 MHz, 5 mm diameter quartz crystal transducer. An identical transmitting quartz crystal was separated from the receiver by a 30 cm water path and was excited by a voltage pulse of -10V and 20 ns duration. The crosscorrelations were performed as convolutions which were evaluated via the FFT algorithm on the digital computer:

$$\Psi_{ps}(\tau) = \mathcal{F}^{-1}\{P(\omega)S(\omega)\} \tag{4.10}$$

$P(\omega)$ and $S(\omega)$, shown in figs 4.4 and 4.6, are the spectra of the reference and received signals respectively. The crosscorrelation $\Psi_{ps}(\tau)$ is shown in fig. 4.7. When the S/N of s(t) is greatly reduced from that shown in fig. 4.5, the matched filter still gives a detectable response as is illustrated in fig. 4.8. Notice that the reference signal p(t) shown in fig. 4.3 peaks at t = 202.900 μs ($\tau \neq 0$) and that the pulse component of the received signal peaks at t = 198.580 μs (c.f. fig. 4.5).

The matched filter has an improved S/N, but the time sidelobes are high and cause signal detection errors when pulses are received at almost the same instant. Superposition of the pulse outputs results in a filter output which may be a maximum at a time intermediate between the individual pulse outputs. Addition or subtraction of the individual pulse outputs depends on the time separation of the pulse components in the received signal.

The probability of erroneous detection is greatly reduced when the reference function is modified to reduce the time sidelobes in the matched filter output. This can be achieved by Wiener filtering (c.f. section 1.4

and Robinson 1967) or by some other optimization technique. In a recent letter, Preis (1977) describes a least-squares method for optimizing filters, while McDonnell (1975) employs Lagrange's undetermined multiplier technique to optimize an optical filter. McDonnell's computer programs were employed for the ultrasonic signal shown in fig. 4.9(a). The filter output, shown in fig. 4.9(b), has greatly reduced time sidelobes.

The S/N of the output of a correlation filter with time sidelobe suppression is lower than that of the matched filter. The output signal contains frequency components within a band which is typically twice the bandwidth of the transducer system. The low amplitude frequency components in the input signal are amplified to increase the bandwidth at the filter output, but at the same time, the noise components are also amplified. Hence the reduction in output S/N.

In order to obtain a S/N similar to that obtained by using a high peak ultrasonic intensity, a transmitted signal with a large time-bandwidth product is required. The average signal energy is similar for the high and low voltage transducer excitation systems. The signal is transmitted over a relatively long time, and when received by a matched filter, the signal is compressed into a relatively short period of time so as to give a reasonable level output with a much increased S/N. This problem has been studied in great detail for RADAR and SONAR remote sensing problems (c.f. Di Franco and Rubin, 1968) and various amplitude and phase encoding procedures have been developed (e.g. Huffman 1962, Huffman 1974). If phase modulation only is used, the signal encoding sequence can be stored in a digital shift register and clocked out as required. Barker codes use the simplest type of phase modulation as they have phase values of 0 or π which can be implemented as signal inversions. Unfortunately, the known Barker codes have a maximum length of 13 bits, and so the encoded signal length is limited unless a more general

type of phase modulation is used. Somaini and Ackroyd (1974) used a numerical minimization procedure to optimize phase coding sequences of up to 100 bits. To test these, a 20 MHz digital shift register containing 256 bits was constructed and various coding sequences tried using ultrasonic transducers with a 3 dB pass band from 1.9 to 3.15 MHz. The received signal was digitized and stored in the computer for decoding and for evaluating the scheme. The shift register was also organized so that it could be used as a 1-bit real-time crosscorrelation detector. The reference signal was programmed as resistor values connecting the 256 output taps of the shift register to either the positive or negative current summing bus. The currents were summed so as to produce an output voltage proportional to the real-time crosscorrelation of the reference signal with the polarity SIGN of the voltage of the received signal $(s(t)/|s(t)|)$. Unfortunately, crosscorrelations carried out in the computer showed that a one-bit correlator failed to give correct detections when the encoded sequence arrived at the receiver via multiple paths. The problem could have been reduced by quantizing the received signal to more levels, but the dynamic range of the signal would then be a problem. A more satisfactory solution for a real-time cross correlator would be to employ a wide dynamic range signal encoder and correlator such as has been developed for modern radar systems. At present, SAW (surface acoustic wave) encoders used in radars operate at frequencies which are too high (typically greater than 40 MHz) for use in medical ultrasonics. The CCD's (charge coupled devices) used for low frequency signal processing run at clock rates up to several MHz. However, experimental CCD's have been run at 100 MHz. So, CCD's are likely to be very useful for filtering ultrasonic signals, in the future.

A hyperbolic phase modulation measurement system was finally implemented with readily available components. The system is shown in diagrammatic form in fig. 4.10. The signal is swept through the ultrasonic

transducer pass band in 25 msecs to give a 31250 (1.25 MHz * 25 msec) time-bandwidth product, i.e. a signal processing gain of nearly 90 dB. The encoding sequence is initiated by an electrical impulse, so the impulse response of the system is

$$h(t) = A \cos\left(\omega_0 t + \tfrac{1}{2}\omega t^2\right) \qquad 0 \leq t \leq T_p \tag{4.11}$$

The frequency sweep period T_p is very much greater than $2\pi/\omega_0$. Thus, the transducers operate under approximately steady state conditions. If the received signal s(t) is composed of the signals which propagate by M paths, which have propagation times $\tau_1, \tau_2, \ldots, \tau_M$, then

$$s(t) = e(t) \circledast h(t) \tag{4.12}$$

where

$$e(t) = \sum_{i=1}^{m} C_i \delta(t-\tau_i) \tag{4.13}$$

thus

$$s(t) = \sum_{i=1}^{m} B_i \cos\left[\omega_0 (t-\tau_i) + \tfrac{1}{2}\dot{\omega}(t-\tau_i)^2\right] \tag{4.14}$$

The signal is composed of a set of overlapping returns which are separated by non-linear processing. The received signal is multiplied by the transmitted signal as in Heyser and Le Croissette's (1974) system, low pass (or band pass) filtered and the resulting base band signal used for spectral analysis. The base band signal q(t) is

$$q(t) = [s(t)h(t)]_{LPF} \tag{4.15}$$

$$= A \sum_{i=1}^{M} D_i \cos(\omega_i t - \phi_i) \tag{4.16}$$

where

$$\omega_i = \dot{\omega}\tau_i$$

$$\phi_i = \omega_0 \tau_i + \tfrac{1}{2}\dot{\omega}\tau_i^2 + \phi_{LPF}$$

$$D_i = B_i \, H_{LPF}(\dot{\omega}\tau_i)$$

$H_{LPF}(\dot{\omega}\tau_i) \angle\phi_{LPF}$ is the transfer function of the low pass filter at frequency $\dot{\omega}\tau_i$. If a pass band filter is used for the low frequencies, then only signals propagating with a time delay within a time window will be unaffected by the filter. For filter limits f_1 and f_2, the time window is $(f_1/\dot{\omega}, f_2/\dot{\omega})$ and the bandwidth sampling theorem is utilized so that the filter/output is sampled at a rate $2(f_2-f_1)$. The spectral components of the base band signal are calculated and the various ultrasonic propagation delays determined:

$$\tau_i = \omega_i/\dot{\omega} \tag{4.17}$$

The implementation and advantages of this method are presented in the next section.

4.5 MATCHED FILTER IMPLEMENTATION, EQUIPMENT TRADE-OFFS AND A NONLINEAR SAMPLING TECHNIQUE

A filter is matched to a particular echo waveform to optimize the S/N of the filtered signal, or else to improve the time resolution of the echo waveform. In both cases, the filtering is carried out in the time domain as shown in fig. 4.11(a), or in the frequency domain as shown in fig. 4.11(b). Filtering to improve the time resolution of a received ultrasonic signal is limited by the S/N throughout the power spectrum of the signal. Where the S/N is not adequate for the time resolution required, the filter is easier to implement via the Z-transform. The poles and zeroes of transducer impulse response p(t) are obtained accurately. The poles and zeroes of the echo signal s(t) are also calculated, but the accuracy is limited by the S/N. The poles and zeroes of the s(t) which due to p(t) are identified, and the remaining poles and zeroes are due to the various propagation paths. These remaining poles

and zeroes are used to reconstruct the "echo" part of the signal e(t), where

$$s(t) = p(t) \circledast e(t) \tag{4.18}$$

The z-transform of p(t) is P(z):

$$P(z) = \mathcal{Z}\{p(iT_s)\} = \sum_{i=0}^{\infty} p_i z^i \tag{4.19}$$

where T_s is the sampling interval and the sampled waveform is denoted by $p_i = p(iT_s)$. In addition,

$$S(z) = \mathcal{Z}\{s(iT_s)\} = \sum_{i=0}^{\infty} s_i z^i \tag{4.20}$$

and

$$E(z) = \mathcal{Z}\{e(iT_s)\} = \sum_{i=0}^{\infty} e_i z^i \tag{4.21}$$

The convolution theorem for z-transforms is applied to (4.18) and yields

$$S(z) = P(z)\, E(z) \tag{4.22}$$

or

$$E(z) = S(z)/P(z) \tag{4.23}$$

The definitions in (4.19) and (4.20) are combined with (4.23):

$$E(z) = \frac{s_0+s_1z+s_2z^2+ \ldots + s_mz^m}{p_0+p_1z+ \ldots +p_nz^n} \qquad n \leq m \tag{4.24}$$

When nT_s is approximately equal to the duration of the transducer response, the digital filter used to implement (4.24) is termed a deconvolution filter or a "spike" filter (c.f. Robinson 1967). When multiply reflected echoes are contained in s(t), then nT_s must be greater than the duration of the reverberation so that a de-reverberation filter is formed. The de-reverberation filter is essential for seismic studies from ships above the continental shelf. The multiple sea bottom - sea surface echo

is usually much stronger than the echoes from the (hopefully) oil bearing structures.

Direct implementation of (4.24) as a digital filter or by polynomial division on a computer requires an adequate S/N. When the S/N is not adequate, the general form of z (i.e. $z = e^{s}$ and $s = \sigma+j\omega$) is used and the poles and zeroes of P(z) are identified in S(z). The remaining poles and zeroes uniquely determine E(z). The computation is time consuming so s is usually restricted: $s = j\omega$. The restricted z-transform is rapidly evaluated as a Fourier transform when the FFT is employed. The choice of $s = j\omega$ reduces the filtering to frequency domain techniques and thus $P(z) = P(\omega)$ must not have any zeroes on, or close to, the imaginary s axis.

The finite bandwidth of the transducer ensures that zeroes will occur in $P(\omega)$ and so conventional Wiener filtering is employed. The continuous time formulation of the optimal filter leads to the Wiener-Hopf integral equation which is very difficult to solve (c.f. Robinson 1967). The integral equation can usually be solved when sampled data is used.

The Wiener filter is usually implemented in the frequency domain, so its use for ultrasonic pulse deconvolution requires the following:

(i) An adequate S/N for the received signal.

(ii) Accurate high speed timing for signal sample and holds.

(iii) High speed analogue to digital converters. (Typically greater than 6 MHz conversion rate).

(iv) High speed memory for the digitized data samples.

(v) A digital computer or signal processor to perform complex multiplication and <u>two</u> FFT's.

It is desirable, for reasons of economy, to relax these requirements and use pulse compression systems, since suitable SAW or CCD matched filter systems are not yet readily available. The most promising approach is to use the hyperbolic phase modulation (linear swept frequency) system. The baseband signal

$$q(t) = A \sum_{i=1}^{M} D_i \cos(\omega_i t - \phi_i) \tag{4.25}$$

is sampled at a rate $2(f_2-f_1)$ where f_2 and f_1 are the upper and lower frequency limits respectively of the band pass filter. The sampling begins when $t \geq f_2/\dot{\omega}$, i.e. the signal travelling by the longest time path within the time window has arrived at the output of the receiving transducer. Thus the time duration for which the signal is sampled is $T_D \leq T_p - f_2/\dot{\omega}$, and the spacing between the spectral components is $\frac{1}{T_D}$. In general, ω_i is not a harmonic of $\frac{1}{T_D}$ and leakage (c.f. Bergland 1969) occurs from the ω_i spectral component into the adjacent spectral samples which occur at harmonics of $\frac{1}{T_D}$. This effect is shown in fig. 4.12 where the effect of various envelope functions (or data windows) is illustrated. The gain control signal g(t) must also be included to shape the envelope function:

$$\text{envelope} = A(t)B_i(t-\tau_i)\ H_{BPF}(\dot{\omega}\tau_i)g(t) \tag{4.26}$$

The leakage from a spectral component can be reduced by reducing the spectral sidelobe level as shown in fig. 4.12. However, such a reduction is made at the expense of broadening the width of the main spectral lobe. So, a compromise is necessary (c.f. Prabhu et al. 1977). The choice of the envelope function is equivalent to deconvolution filtering. Consider the spectral output $p(\dot{\omega}\tau)$, which is the impulse response of the system for a single path with a time delay τ. The deconvolution filter $h(\omega)$ required to change $p(\omega)$ back to an approximation of an impulse $e(\omega)$ can be calculated:

$$H_{BPF}(\dot{\omega}\tau)\big|\underline{\phi_{BPF}} \approx \text{constant} \tag{4.27}$$

$$B_i(t-\tau_i) \approx B_i(t) = C_i A(t) \propto A(t) \tag{4.28}$$

and set

$$g(t) = \text{constant}. \tag{4.29}$$

Then

$$\mathcal{F}^{-1}\{p(\dot{\omega}\tau)\} \propto A^2(t)\cos(\dot{\omega}\tau-\phi) = q(t) \tag{4.30}$$

the deconvolved output is:

$$e(\omega) = p(\dot{\omega}\tau) \circledast h(\omega) \tag{4.31}$$

$$= \mathcal{F}^{-1}\{\mathcal{F}\{p(\dot{\omega}\tau)\}\mathcal{F}\{h(\omega)\}\}$$

or

$$E(-t) = P(-t)\,H(-t) \tag{4.32}$$

where

$$e(\omega) = \mathcal{F}\{E(t)\}$$

Thus

$$E(t) = P(t)\,H(t) \tag{4.33}$$

The Wiener filter realisation of H(t) is:

$$H(t) = \frac{P^*(t)}{[P(t)]^2 + \bar{n}(t)^2} \tag{4.34}$$

If only the positive power spectrum is used to define $p(\dot{\omega}\tau)$, then H(t) will be complex and P(t) H(t) = E(t) will form an analytic signal (c.f.Di Franco and Rubin, 1968, Ch.2). If both positive and negative frequencies of the power spectrum are used, then H(t) is the required envelope function and

$$g(t) = H(t) \tag{4.35}$$

for the signals in the pass band of the filter.

The advantages of the hyperbolic phase modulation system are:

(i) Only medium speed clocks, and sample and hold circuits are needed.

(ii) A medium speed A.D.C. has sufficient throughput.

(iii) Only slow memory and a computer to perform one FFT (to obtain the spectrum) are required.

(iv) An envelope function gain control is required.

Note that all of the above are contained in most real-time FFT spectrum analysers. Thus an existing B-scan machine is easily modified to incorporate the above processing.

The hardware requirements for conventional improved time resolution are compared with those for the hyperbolic phase modulation processor in fig.4.13. The cost of adding filtering to produce improved time resolution is considerably less for the hyperbolic phase modulation system.

The linear frequency sweep circuit used is shown in fig. 4.14(a). With the exception of the positive feedback resistors R_1 and R_2, the circuit is that which was developed by Boys for the "ultrasonic cardiophone" (c.f. Kay et al. 1977). The original circuit suffered from several defects so detailed parameter measurements were obtained by the author of this thesis for a fixed water path signal delay. The base band signal was sampled at approximately 39 kHz to produce fig. 4.14(b). The comb structure in the figure was produced by a graphics routine which interpolated between the signal samples with straight lines. The power spectrum of the signal was obtained and plotted to yield fig. 4.14(c). The spectrum was spread over approximately 3 kHz. A "leaky" optical isolator in the ramp generation circuit was replaced, and the test repeated to yield the spectrum shown in fig. 4.14(d). The frequency-time graph shown in fig. 4.14(e) is obtained from detailed measurement of the times between the zero crossings of the base band signal voltage. On the basis of this graph, the first 4 msecs of signal samples are discarded since the non-linearity is due to the slow turnoff of the opto-isolator. The curve in fig. 4.14(e) shows an approximately linear decrease in frequency and hence control voltage with time. To correct this, a current

proportional to the output voltage (and hence time) is added to the positive feedback terminal via R_1 to increase the control voltage with time. After this modification, the non-linearity is measured as approximately 500 Hz in 1.2 MHz or .04%.

The circuit was placed in a warm room and the measurements were repeated for one hour. The position of the peak in the power spectrum was observed to shift from the 294^{th} harmonic to the 308^{th} harmonic. The classical heating exponential time variation is evident in fig. 4.14(f). The feedback capacitor in the ramp generator was replaced with a mylar film capacitor and the variation with temperature was reduced to ±1 harmonic.

The results of employing positive feedback, stabilizing timing components, reducing leakage and discarding the first four milliseconds of signal are summarized in figs 4.14(g)-(i). The spectral output is shown in fig. 4.14(g) and the spread spectral peak is shown in fig. 4.14(h). The extent of the spectral peak is less than 200 Hz, and about 100 Hz at the half amplitude points. A plot of the detected frequency versus time in fig. 4.14(i) shows excellent linearity.

The spectrum shown in fig. 4.14(h) exhibits quite low sidelobe levels. The variations in the signal envelope (shown in fig. 4.14(b)) reduce the spectral sidelobes to very low levels. Thus the gain is not varied with time during each frequency sweep.

The receiver circuitry given in fig. 4.15(a) was tested over a 100 dB range. The signal applied to the transmitting transducer was reduced in 10 dB steps from 0 dB (2 V_{RMS}) to -100 dB (20 μV_{RMS}). The results for 0 dB to -70 dB were essentially the same as those shown in fig. 4.15(b), but figs 4.15(c)-(e) for -80 dB to -100dB were quite different. The signal was band pass filtered between 10 kHz and 15 kHz by means of two 9-pole filters. The computer was used to set the gain g(t) constant so that the peak of the filtered signal was between 0.5V and 2.5V. The signal was then sampled at 39.0625 kHz to yield 1024 samples in

26.2 msecs (c.f. fig. 4.14(b)).

A comparison of figs 4.15(b) and 4.15(c) shows that the S/N of the filtered signal decreases noticeably when the signal attenuation exceeds 80 dB. For signal attenuations of 90 and 100 dB (c.f. figs. 4.15(d) and 4.15(e) respectively), the signal component of the power spectrum is not discernible from the noise. It is concluded that the receiver system operates satisfactorily over an 80 dB range.

Bandwidth sampling (deliberate signal aliasing) is employed in processing the filtered signals, and the effects are illustrated in fig. 4.16. An ultrasonic propagation path through 27.1 cm of water produces a spectral output at 11.41 kHz as shown in fig. 4.16(a). The system band pass filter limits are 10.0 kHz and 12.5 kHz. The sampling frequency is reduced from 39.06 kHz by factors of 2 to give sampling frequencies of 19.53, 9.76 and 4.883. The power spectra of the sampled signals are shown in figs 4.16(b), (c) and (d) respectively. Thus band pass sampling has aliased the 10-12.5 kHz signal down to a base band of 0-2.5 kHz. The lowest sampling rate still permits accurate measurement of the maximum energy propagation path time provided that the time is within ±12% of the propagation time through water only. The sample frequency of 4.883 kHz allows 150 samples to be measured in 30 msecs. The data set is supplemented with zeroes to form 512 samples which yield 256 spectral values 9.5 Hz apart. This method of resolution improvement allows the peak of the spectral component to be determined to within 0.08% (9.5 Hz in 11410 Hz). Supplementing the samples with zeroes does not alter the S/N of the detected signal.

The following novel nonlinear sampling technique was discovered during study of this signal compression technique. The transmitted signal is:

$$h(t) = A \cos (\omega_0 t + \tfrac{1}{2}\dot{\omega} t^2) \tag{4.36}$$

and the received signal is:

$$s(t) = B_i \cos [\omega_0 (t-\tau_i) + \tfrac{1}{2}\dot{\omega}(t-\tau_i)^2] \tag{4.37}$$

If $s(t)$ is sampled at times t_n when $h(t)$ is zero and $\dot{h}(t) > 0$, i.e. when

$$\omega_0 t_n + \tfrac{1}{2}\dot{\omega} t_n^2 = m\,2\pi \tag{4.38}$$

Then

$$\begin{aligned} s(t_n) &= B_i \cos[(\omega_0 t_n + \tfrac{1}{2}\dot{\omega} t_n^2) - \dot{\omega}\tau_i t_n + (\tfrac{1}{2}\dot{\omega}\tau_i^2 - \omega_0 \tau_i)] \\ &= B_i \cos[\omega_i t_n - \phi_i] \\ &\propto q(t_n) \end{aligned} \tag{4.39}$$

Thus the base band signal has been obtained without employing a multiplier and a low pass (or band pass) filter. Also if $\omega_0 > 2\pi\ 10^6$, then the normal sampling frequency of 39.6 KHz can be used to determine which particular value of m in (4.38) is used. Thus a sample is taken when $h(t) = 0$ and $\dot{h}(t) > 0$ immediately after the sample time determined by the 39.6 KHz signal. This gives a sample interval of 25.6 ± .5 μsec for an ultrasonic frequency of 1 MHz and 25.6 ± .2 μsec for 2.5 MHz. Thus the sample timing jitter is less than 2% for the worst case.

This sampling method does not employ a low pass filter so the system S/N is reduced. For this reason, the method was not used.

4.6 THE COMPUTER INTERFACE

To control and collect data from the ultrasonic scanner apparatus, some form of interface between the apparatus and the E.A.I. 640 digital computer is required. The scanner interface requires a minimum of two 12-bit words for position control, one 12-bit word for measurement data, two control signals and two interrupt signals. However, it was decided to build a binary data interface (BDI) for general use in the Electrical Engineering Department's hybrid computer laboratory. The author produced the initial specification and design for the BDI in 1973, but construction was delayed for several years because of financial constraints.

The output from the BDI is double buffered by two 128-bit memory latches. The first memory is loaded with up to 8 16-bit words. The entire contents of the first memory are transferred in parallel into the second memory when one of three things happen: the last 16-bit word is loaded into the first memory, the computer initiates the transfer, or an external signal (e.g. from the scanner) initiates the transfer. An alternative JAM mode transfers one 16-bit word into the appropriate space in both the first and second memories. Since the second output memory is usually loaded in parallel, the output is treated as a single 128-bit word. The latches which comprise the second memory are buffered to prevent the latch toggling with voltage transients on the output transmission lines. The latches comprising the second memory are also coupled together as a 128-bit shift register for serial data transfers under control of an external clock.

The data input to the BDI is limited to a maximum of 128 bits at a time. Serial data is input in multiples of 8 bits while parallel data is input in multiples of 16 bits. Any one of the 8 16-bit words is accessed by the computer via 16 8:1 multiplexers. Up to 8 words are sequentially read by the computer and when the last word is read, a BDI input load

signal is generated. Alternatively, the input load signal is generated by the computer or by an externally supplied load signal. A single 16-bit word may be loaded into an input memory and directly into the computer by using the BDI JAM input.

There are six separate interrupt requests available via the BDI. Four of these are available for general purpose use, and the other two are for use during the externally initiated data transfers used to load the input latches, or load the second output memory. The ultrasonic scanner generates a general purpose interrupt when faults occur in the digital servosystems. The general purpose interrupt is used to initiate fault clearing routines, which sound an alarm if the fault cannot be cleared. The interrupt on load line is only active when the scanner is stationary. The computer initiates a measurement sequence at a particular position, and the interrupt on load is used to control the flow of data from the scanner into the computer via the BDI.

4.7 THE NUMERICAL CONTROL SYSTEMS

The numerical control systems move the two ultrasonic transducers to the position (ξ,ϕ) at which a time delay measurement is made. The ξ and ϕ values are calculated by the digital computer, encoded as two 12-bit numbers and output to the control systems via the BDI. The transducers are attached to an aluminium alloy framework suspended above the water tank as shown in fig. 4.17(a).

Two identical stepper motors (Evershed Model FDD4, 4 phase, 200 steps/rev.) are used to drive the ξ, and ϕ positioning systems. The angular positioning system uses one motor to drive a triple start steel worm which engages a 300 tooth brass wheel. This combination yields an angular increment of 0.018^{o} for each motor step, or $2 * 10^{4}$ steps per scanner revolution. A 12-bit control word is used to cover the required positioning

range of 0-180°, so every fourth step of the motor is counted by the control system and the angular increment is .072°.

The angular positioning wheel (300 tooth) rotates on a degenerate kinematically located bearing (c.f. Braddick 1963, §3.3) formed by two circular vee tracks separated by hardened steel ball bearings. One track is machined into the stationary framework bearing surface and the other is underneath the wheel. Three teflon thrust rods applied to the top of the wheel produce sufficient bearing preload to maintain bearing contact at all positions. As the wheel rotates, it carries with it the second stepper motor and a suspended track for radial positioning.

The transducers are hung from the carriage which slides along the track suspended beneath the angular positioning wheel. Thus the transducers are positioned in a polar coordinate system. The carriage moves along the track on a semi-kinematic sliding rod bearing (c.f. Braddick 1963, §3.4). The carriage driving rack is above this bearing and the bearing preload is applied by two teflon thrust rods applied adjacent to the rack. The other side of the carriage is supported by a sliding rod - machined plate bearing which is preloaded by a central teflon thrust rod. The stepper motor drives the rack via a 3:1 brass bevel gear. The carriage moves 30 μm per step, but only every fourth step is counted by the control system and the position increment is 0.12 mm. The 12-bit control word permits positioning over 491.4 mm although this is restricted to ±165 mm.

Two identical controllers are used to drive the stepper motors. A block diagram of a controller is shown in fig. 4.17(b). The "position" of the open loop controller is set by photo-interrupter limit switches activated by the scanning mechanism. Once the zero position is set, the binary comparator compares the required position (set by the computer) with the position stored in the up/down position counter. If the positions are the same, no action is taken. When the positions are not the same, a

position increment or decrement signal is issued by the binary comparator and a positive or negative phase sequence is output to the stepper motors (via a power amplifier) by the four phase generator. One phase is gated to the up/down position counter so that only every fourth step is counted. This gives a controller position hysteresis of two steps which is considerably less than the backlash in the gearing systems driven by each motor. The computer is programmed to allow for the gearing backlash when the positions are decremented.

The absolute scan limits are set by photo-interrupters at -5.4^{o} and 286^{o}, and at -169 mm and 167 mm. These limits correspond to 3974 counts and 2809 counts respectively. To set the zero positions, the computer demands an absolute position of 8 counts, and then sets the two position counters to 4095 counts (2^{12}-1). Since each maximum position count is less than 4095-8 counts, the angular and radial positions are decremented until each zero position light beam is interrupted and each position counter set to zero. After a position counter is set to zero, the mechanism backs away from the light beam by 8 counts, so that the photo-interrupter is free to intercept a fault. The numerical control systems are then ready to begin operation. The limit switches, motor drive phase sequences, position counters and power supplies are continuously monitored and a computer interrupt signal requesting corrective action is generated when a fault occurs.

4.8 EXPERIMENTAL DIGITAL SERVOSYSTEMS

The purpose of this section is to describe some control system research and development on improving digital servomechanism performance. There are three subsections in all. The first is concerned with motor drive waveforms and increasing the motor output torque. In the second

subsection, an innovative incremental encoder pulse sorting circuit is examined, and in the final subsection, a maximum slew rate positioning system which is independent of load variations is described.

4.8.1 A Constant Current Switched Mode Power Amplifier

The four-phase Evershed stepper motor (Model FDD4/B50) used to drive the scanner has two centre tapped windings a and b as shown in fig. 4.18(a). The usual method of operation is to energize one half of a winding so that the flux produced by coil a is ϕ_{a+} or ϕ_{a-} depending on whether switch a_+ or switch a_- is closed. When switch a_+ is closed, switch a_- is open and vice versa. When the switches are closed in the following time sequence: a_+b_+, a_-b_+, a_-b_-, a_+b_- and a_+b_+, the total stator flux ϕ_T rotates through one revolution as sketched in fig. 4.18(a). The reverse switching sequence produces a flux which rotates in the opposite direction. There are effectively 50 poles per phase so the rotor rotates once for every 50 rotations of the stator flux. Thus 200 steps, or positions, for each revolution of the motor shaft are obtained.

The basic circuit is further developed to increase the speed at which the motor can move the scanner. The speed of rotation is dependent on the time taken for the flux in a coil to increase sufficiently for the motor torque to be greater than the load. The coil flux is proportional to the coil current:

$$i(t) = \frac{V}{R}\left(1 - e^{-\frac{R}{L}t}\right) \qquad (4.40)$$

where V is the supply voltage and R and L are the resistance and inductance of one half of a winding. The coil current is limited to 1.36A so that the motor does not overheat. The manufacturer (Evershed) recommends decreasing the coil time constant $(\frac{L}{R})$ by placing a series resistance $R_s = 4.5R$ between the winding centre tap and the supply. The voltage is

increased to maintain a maximum current of 1.35A. This technique, known as current forcing, decreases the current build up time constant to L/5.5R and hence the current limit is reached 5.5 times faster. The same result can also be obtained by applying a square voltage waveform to the coils. Tal (1977) shows that for a given motor dissipation, a square wave voltage drive is about 46% less efficient than the optimum sinusoidal current drive. At slow speeds the series resistor changes the square wave voltage drive to an approximately square wave current drive at the coils, and Tal calculates that this is only 10% less efficient than the optimum driver waveform.

For a permanent magnet rotor, the torque is proportional to the flux from the coils:

$$\phi_a = |\phi_{a+}| \propto \frac{V}{R} \tag{4.41}$$

If both halves of coil a are energized with the appropriate current, the total flux from coil a can be increased. To maintain the same total heat dissipation in the winding, the current must be reduced by a factor of $\sqrt{2}$. Hence the coil output is

$$\phi_a = \phi_{a+} - \phi_{a-} \propto 2\left(\frac{1}{\sqrt{2}}\frac{V}{R}\right) = \sqrt{2}\,\frac{V}{R} \tag{4.42}$$

Thus the flux, and hence the output torque is increased by 40%. The schematic of a circuit to produce this effect is shown in fig. 4.18(b) for a single winding. The time constant of the winding is still 2L/2R so to decrease the time taken for the current to reach 1.0A ($\approx 1.35/\sqrt{2}$), the ±5V winding is driven with a ±50V square wave. The current is monitored, and once the required value of 1.0A is reached, the switch to ground is opened and the winding current circulates through the free wheel diodes and the current sensor. When the current decreases to .9A the switch to ground is again closed and the current increases to the upper limit.

The hysteresis is incorporated to limit the switching frequency and hence the power dissipated by the transistor switch.

Static torque measurements for the motor-drive combination are shown in fig. 4.19(a). The maximum holding torque for both coils energised is stated to be 7.5 N-cm by the manufacturer, but a value of 12.6 ± 10% N-cm is obtained with the special driving circuit. The angular measurements are made by means of a curved glass galvanometer scale and a light source. A mirror is mounted on a wheel fastened to the motor shaft. The motor step size is 1.8°, and the measurement accuracy is $\pm.1^{\circ}$. Torque loading is applied with a spring balance attached to the wheel and the overall measurement accuracy is ±.1 Kg/cm.

Despite the crudity of these measurements, good correlation of results is obtained. Measurement of the dropout torque is more difficult as the measurement is made near an unstable position on the operating curve, hence the 10% accuracy. Significant increases in motor output (68%) are obtained with this special drive system.

An unregulated power supply (40-60V) is used in the units constructed and this limits the motor speed to 5000 steps per second at no load (c.f. 4000 steps per second with special Evershed drives). The power amplifiers are best described as constant current switched mode power supplies with a ±1A output. When in use, the power amplifiers produce 2 phases at ±1A. When the scanner is stationary, the power amplifiers are turned off so that the measurement noise is reduced. The switched mode system was initially unstable when power supply variations interacted with the current measurement circuit. This was overcome by using an optoisolator diode to monitor the voltage across a current sensing resistor. The diode acted as a threshold detector, and the photon coupling eliminated the common mode problems caused by the supply variations.

Nagasaka et al. (1974) use the sum of the two phase currents to control switching, but experimentation has shown that superior performance is obtained when each phase current is controlled separately. However, for three phase stepper motors, Boys and Dunlop (1978a) found that near optimal six step current waveforms are generated by using the largest phase current to control the switching of all phases.

The power amplifiers developed for the scanner have operated reliably for several years in the Electrical Engineering Department, and also in the Department of Radiology, Christchurch Hospital. The author has also been consulted by several other departments within the university (Civil, Mechanical and Chemical Engineering, and Physics) on problems associated with digital motor control systems.

4.8.2 A New Pulse Multiplication Circuit

There are two types of encoder used for position sensing in numerically controlled machinery: absolute and incremental. Absolute encoding systems use a preset datum and usually employ a grey code scale for position measurement. They are expensive, bulky and require protection in adverse environments. Incremental encoders are often used in non-critical processes where a position datum can be redefined from time to time. They require only a simple mark-space grating encoder which may even be mounted as a disc on the end of a motor shaft. They are relatively inexpensive and are usually quite small and hence easily protected.

Incremental changes in the physical position of machinery is sensed by observing the movement of a reference grating or sensor past a fixed grating. To reduce noise and alignment problems in optical encoder systems, it is common practice to use with gratings with a slightly different spacing (Vernier effect) or to incline the gratings at a slight angle so as to generate Moiré fringes. As the gratings move relative to each other, a series of moving fringes is produced. The fringe movement

is sensed optically to produce the encoder output which is usually converted to a binary signal so as to minimize parameter variations during transmission. Two sensors are used so that the direction of the movement can also be determined. The two sensor outputs (named A and B) form a bi-phase pair which has a quadrature phase relationship (as shown in fig. 4.20).

Each encoder output changes through one cycle when the reference grating is moved by one grating pitch (or line width). The usual method of incremental positioning counts the number of positive transitions in the signal A from one encoder to determine the number of grating pitches moved. The second signal B is examined at each count to see if it is high or low, and hence whether the position was incremented or decremented. However, as the grating is moved by one pitch, the signals A and B undergo four transitions. Thus a position increment of ¼ pitch can be detected. This process is described as pulse multiplication by four since where there was only one count before, there are now four counts.

The conventional method of obtaining the increased resolution is to differentiate the signals A, B, $\bar{A}$, $\bar{B}$ and take only the positive portions of the differentials to form A', B', $\bar{A}'$ and $\bar{B}'$. The pulses obtained from the transitions of signals A and B are gated through decision logic to count up or count down in the position counter.

$$UP = A.B' + \bar{A}'.B + \bar{A}.\bar{B}' + A'.\bar{B} \tag{4.43}$$

and

$$DOWN = A.\bar{B}' + A'.B + \bar{A}.B' + \bar{A}'.\bar{B} \tag{4.44}$$

These expressions cannot be simplified further and their implementation requires at least five standard logic packages and a dozen or so timing components. Various manufacturers have used considerable ingenuity to reduce the number of components (see for example, the encoder circuitry used in the Electronic Graphics calculator manufactured by

Numonics Corporation 1975). The Digital Equipment Corporation have even developed a special capacitor-diode-capacitor gate (DEC K184 module) to synthesize these functions.

The new technique developed by Boys and Dunlop (1978b) utilizes an integral signal processing technique rather than the conventional differential method. The noise performance of integral signal processing is considerably better than differential processing and counting rates up to 10^7 Hz are possible.

The Boolean representation of an integration is a delay, hence the integral of A is A_o. The UP and DOWN count expressions can thus be written:

$$UP = A.\bar{A}_o.\bar{B}.\bar{B}_o + A.A_o.B.\bar{B}_o + \bar{A}.A_o.B.B_o + \bar{A}.\bar{A}_o.B.\bar{B}_o \quad (4.45)$$

$$= (A.\bar{B}_o + \bar{A}.B_o) \cdot (\bar{A}_o.\bar{B} + A_o.B)$$

$$= (A \oplus B_o) \cdot (\bar{A}_o \oplus B) \quad (4.46)$$

since either $A = A_o$ or $B = B_o$ at any instant. Similarly

$$DOWN = (A_o \oplus B) \cdot (A \oplus \bar{B}_o) \quad (4.47)$$

Considerable care is taken to avoid spurious timing pulses when implementing these equations, and the circuit shown in fig. 4.21 is optimized for this. The circuit does not contain any extra timing components, and is implemented with three standard TTL packages. The outputs $\overline{UP}$ and $\overline{DOWN}$ have the correct format for direct connection to the standard 193 up-down binary counter. The integration or time delay is realized as a clocked data latch and so the circuitry produces output pulses with a time width of 6 gate delays. The complexity of the circuitry is much reduced and since external timing components are not used, the design is ideal for MSI implementation. Note also, that the output pulses are logic family compatible in speed and amplitude.

In some industrial applications, jitter on a counting edge (due to encoder vibration) causes problems if the pulse sorting circuitry is implemented with slow logic types. The problem is eliminated by synchronously gating the encoder outputs into two data latches so that A and B can only change at predetermined times. The data entry rate is set slightly slower than the speed at which the pulse sorting and up-down counting circuitry operates.

If the number of encoders is doubled to generate four quadraphase signals C D E and F, then putting

$$A = C \oplus E \tag{4.48}$$

and

$$B = D \oplus F \tag{4.49}$$

will generate 8 counts per pitch movement when the quadraphase signals are spaced 45^{o} apart. This can be extended to 2N encoders to obtain an incremental resolution of $\frac{1}{4N}$ of a grating pitch.

When synchronous data entry is employed, the circuitry is easily modified for position error counting such as occurs in tracking applications in paper, textile and steel rolling mills. The method has been found to work well experimentally and should give improved performance over existing encoders used in industrial environments. It is likely that the circuit will appear as a standard package for use with industry standard 193 up-down counters.

4.8.3 A Maximum Slew Rate Positioning System

A major problem with control systems is to achieve a fast response and good static accuracy. High response speed can be achieved with D.C. motors in conjunction with a bang-bang controller (giving maximum positive or negative acceleration). However, such systems do not exhibit good static accuracy and often have limit cycle problems. Conventional D.C.

machines produce considerable electrical noise during commutation and the brushless D.C. motor was developed to reduce this noise. The brushless D.C. machine often has a permanent magnet rotor and sequentially energizes the appropriate stator coils so as to produce orthogonal rotor and stator magnetic fields. The effect of mechanical commutation is achieved by electronic switches which are controlled by rotor position sensors. The machine does not have the maintenance problems associated with the ordinary brush commutator system and it can be used in explosive environments. However, these machines do not solve the static accuracy problem.

Stepper motors have excellent static accuracy performance, but this deteriorates when poling occurs (the rotor and stator magnetic fields lose synchronism). Poling only occurs if the speed or stepping rate demanded by the controller is too great for the motor to drive the load. A system has been constructed to derive the control clock from the rotor position so that the positioning speed and acceleration are maximized for any load at any speed. When load variations are likely to cause poling, static accuracy can only be maintained by employing position feedback. The pulse sorting circuitry described in the last subsection is used in conjunction with an encoder disc mounted on the rear motor shaft so as to implement an incremental position encoder. As the rotor moves through the -45° electrical position (c.f. fig. 4.19(a)), a position increment pulse is generated. This pulse is used as the control clock pulse to generate a step command which shifts the motor operating point from $\theta_e = -45^{\circ}$ to $\theta_e = -135^{\circ}$. Thus the motor operates over the maximum torque peak with an average angle of $\theta_e = -90^{\circ}$, and thus maintains the rotor and stator fields nearly orthogonal.

The usual synchronous stepped mode of operation produces an average torque $\bar{\tau}_s$ for a sinusoidal torque variation, and an average torque $\bar{\tau}_m$ for the maximum slew rate positioning. These are related as follows:

$$\bar{\tau}_s = \frac{2}{\pi}\int_{-90^o}^{0} -\tau_p \sin\theta_e \, d\theta_e = \frac{2}{\pi}\tau_p \tag{4.50}$$

$$\bar{\tau}_m = \frac{2}{\pi}\int_{-135^o}^{-45^o} -\tau_p \sin\theta_e \, d\theta_e = \sqrt{2}\,\frac{2}{\pi}\tau_p \tag{4.51}$$

$$= \sqrt{2}\,\bar{\tau}_s \tag{4.52}$$

For the triangular torque variation shown in fig. 4.19(a),

$$\bar{\tau}_s = \frac{2}{\pi}\left(\frac{\tau_p}{2}\,\frac{\pi}{2}\right) = \frac{\tau_p}{2} \tag{4.53}$$

$$\bar{\tau}_m = \frac{2}{\pi}\left(\frac{\tau_p}{2}\,\frac{\pi}{2} + \frac{\tau_p}{4}\,\frac{\pi}{2}\right) = 1.5\,\frac{\tau_p}{2} \tag{4.54}$$

$$= 1.5\,\bar{\tau}_s \tag{4.55}$$

Thus maximum slew rate positioning can achieve a 40% increase in torque for a sinusoidal static torque characteristic, and a 50% increase for the triangular torque variation measured.

Maximum slew rate positioning is usually implemented by increasing the frequency of the control clock or else changing the frequency in steps. Such open loop systems can fail and produce poling when the mechanical load varies too much. The approach used here, is to model the brushless D.C. motor and use a closed loop clock control. This permits the clock rate to change at the maximum rate permitted by the load, and thus to maximize the acceleration. Measurements made on the system using the Evershed stepper motor are shown in fig. 4.19(b). Excellent results are obtained and the high speed limit occurs only when the current amplifier output is voltage limited.

The method of constructing the encoding disc is worthy of mention. Braddick (1963, §3.10) calculates that for a point on the edge of a 5" diameter disc to be located to within 1 minute of arc, the centering error must be less than 0.0003 inches. One minute of arc would give an

accuracy of ±1% in determining the electrical angle, hence precision machining would normally be required to construct the encoder disc. The disc was constructed by fastening a blank disc on the motor shaft and bolting the motor to a Rotex punch so that the disc is only just clear of the die. The motor coils were then connected in series and energized with D.C. The disc was allowed to settle at an equilibrium position and a hole was then punched in the disc. The motor was then poled manually to the next equilibrium position and another hole punched. The process was repeated until 50 evenly spaced holes were punched near the perimeter of the disc. The radius at which the holes were made was $50d/\pi$ (where d is the diameter of the hole punched) so as to obtain an equal mark-space ratio from the optical encoders. The pulse multiplication circuitry was used to obtain the 200 step positions from the 50 holes. In addition, if the hole sensors for the encoder are placed in the same position as that occupied by the punch when forming the holes, then the step accuracy of ±3% does not affect the timing system. Thus this method of construction eliminates small errors in the motor pole positioning as long as the disc remains fixed in one position on the shaft.

During motor output measurements, the phase current was monitored and observed to vary with the motor speed. Frus and Kuo (1977) have used such current observations to detect the rotor movement, and hence to generate the required steps. Their method is to detect the $\theta_e = -45^\circ$ position approximately and then to generate a clock pulse after a time delay. For a given load, the motor speed is determined by the clock delay. The motor speed is also measured on a pulse to pulse basis so that load variations are allowed for. Without speed measurement checks, the motor speed can hunt if the time delay speed determination is not matched to the load. Undesirable mechanical resonances can also occur as the speed fluctuates. The great advantage of current sensing for closed loop control

is that the motor can be located some distance away from the control electronics. This is particularly advantageous in adverse environments.

Hammand and Mathur (1977) utilize phase plots of the rotor position (θ_e) and velocity (c.f. fig. 4.22) to determine the dynamic stability of a stepper motor. Trajectory curves on the phase plot are used to construct phase portraits for a single step, multistep stable and unstable operation, and for limit cycles employing constant frequency control clocks. Poling is clearly observed for unstable operation, and the angular increment for each position step is obtained by integrating the rotor velocity for one clock period. With the mechanical encoder method of clock generation developed for load independent maximum slew rate positioning, the phase trajectories are limited: $-\frac{3\pi}{4} < \theta_e \leq -\frac{\pi}{4}$, and are thus easily determined as shown in fig. 4.22. The phase portrait shown in fig. 4.22 is constructed for a constant load and the mathematical model is based on a sinusoidal static torque characteristic.

The mechanically determined step rate produces maximum slew rate positioning for all load variations right down to stall speed. The system achieves maximum acceleration and reaches a demand position in a minimum time. Depending on the total inertia and load braking, the system may over-shoot the position and need to step back slowly. Alternatively, the motor may use maximum reverse torque after some predetermined position so that the motor stops at the required position. This implies a predetermined load so in general, a simple mechanical brake is applied when the demand position is reached.

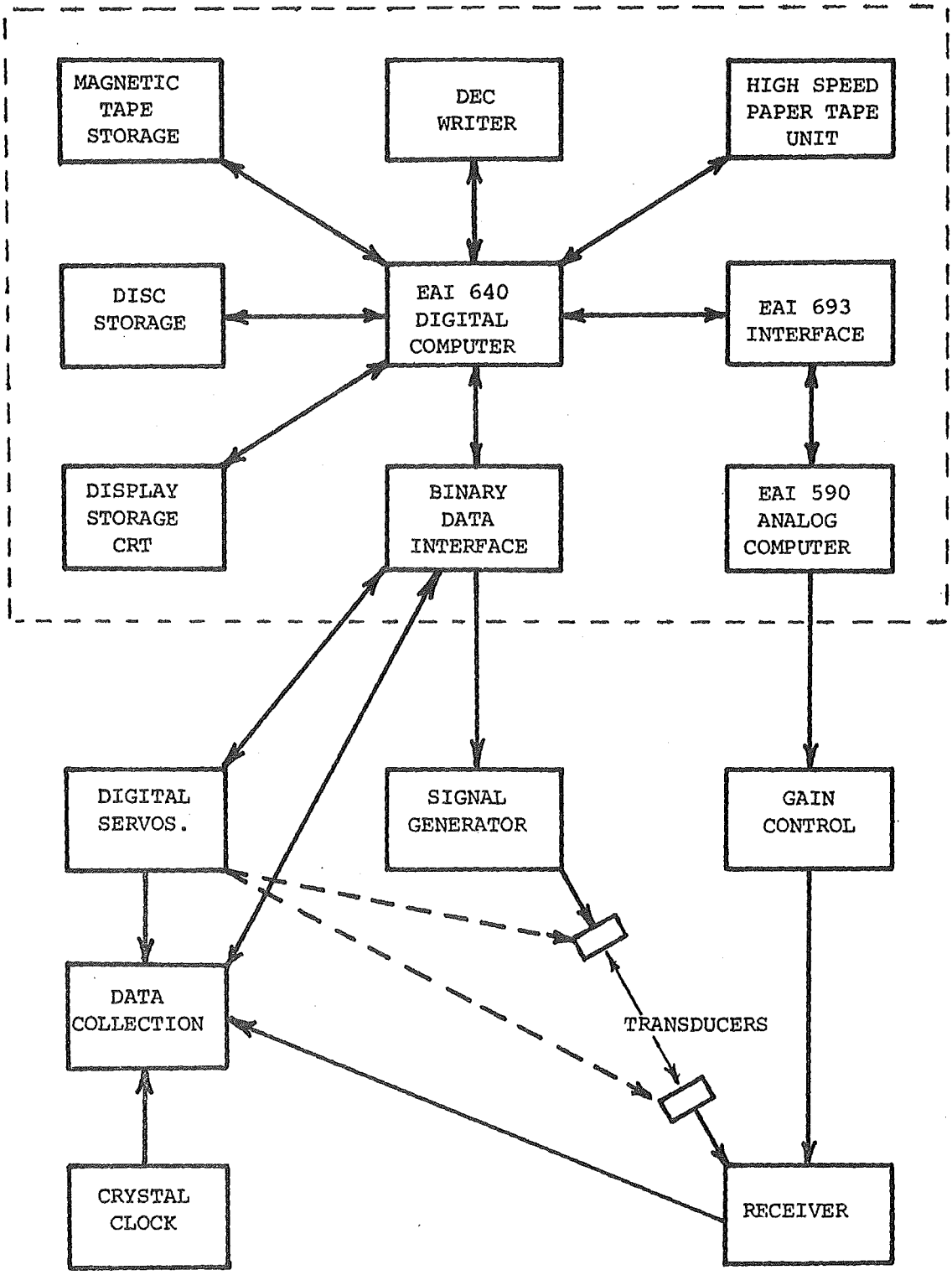

Fig. 4.1 The interconnections between the central processing unit and the attached subsystems. The upper 9 "blocks" are in the Hybrid Computer Laboratory

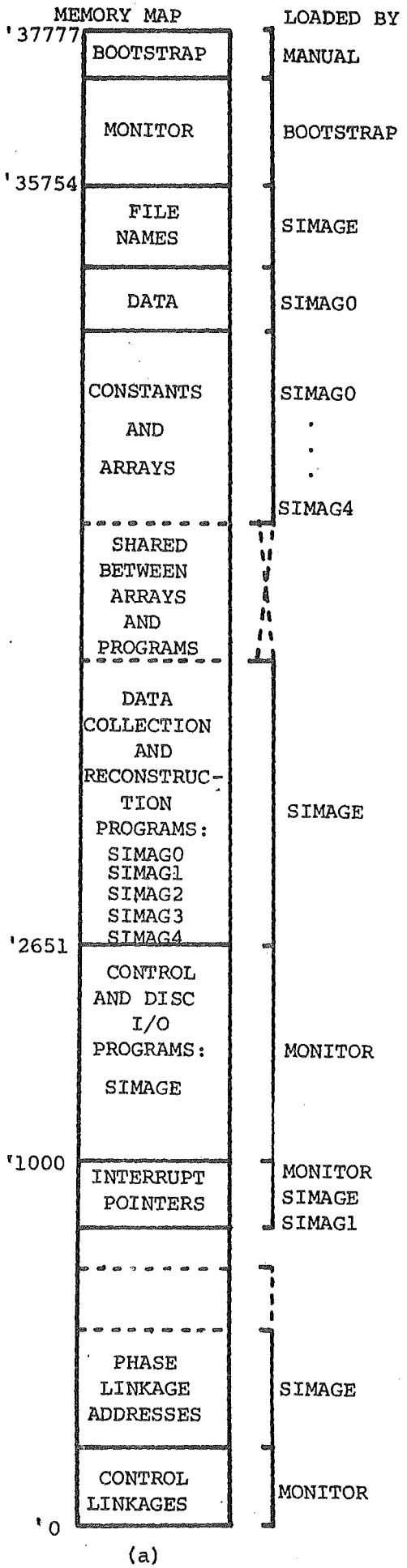

(a)

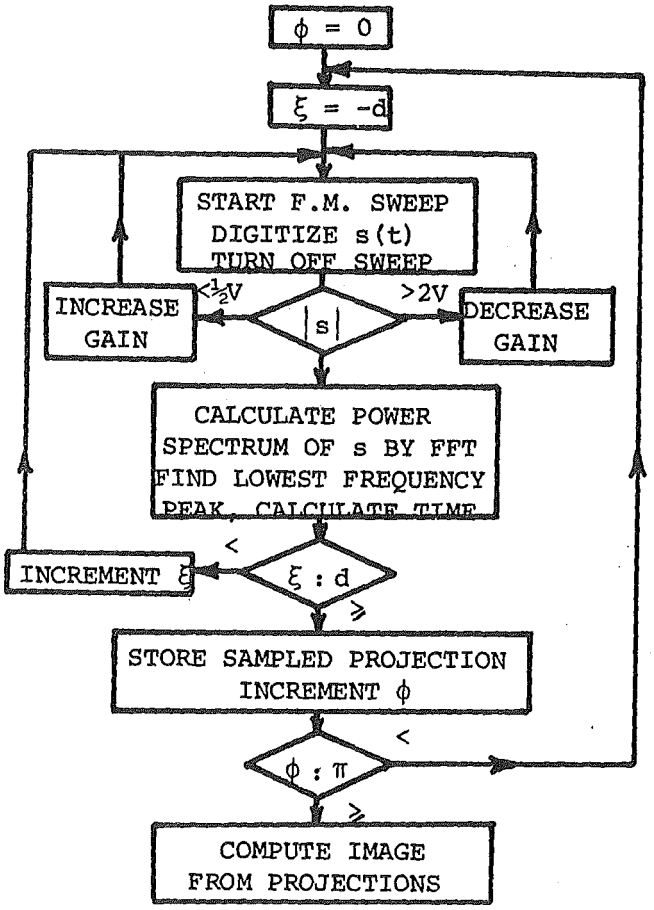

(b)

Fig. 4.2 Computer program organization:
(a) Utilization of the core memory for multi-phase overlay programs.
(b) The measurement flow chart for acoustic transmission imaging.

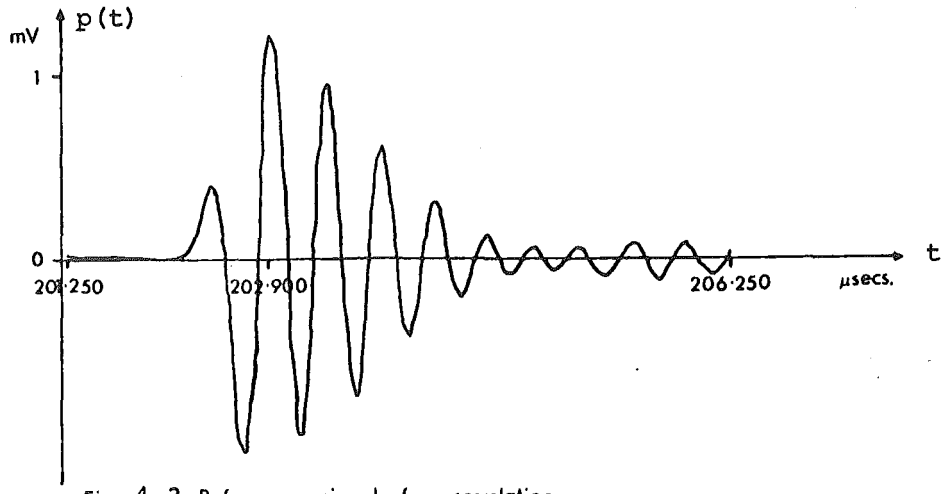

Fig. 4.3 Reference signal for correlation.

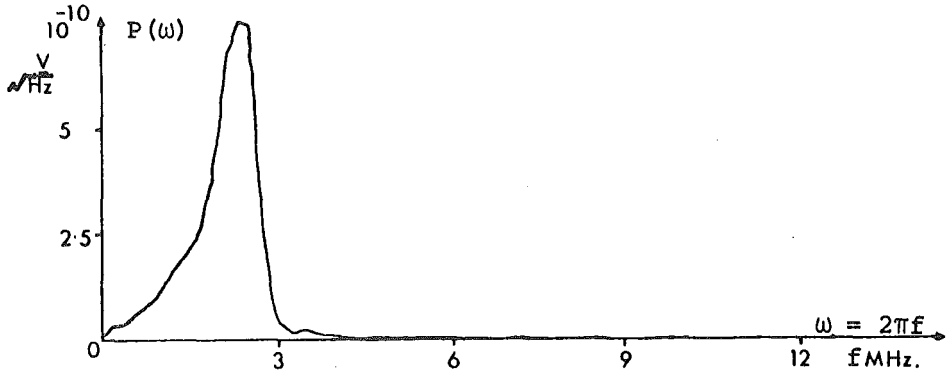

Fig. 4.4 Spectrum of the reference signal.

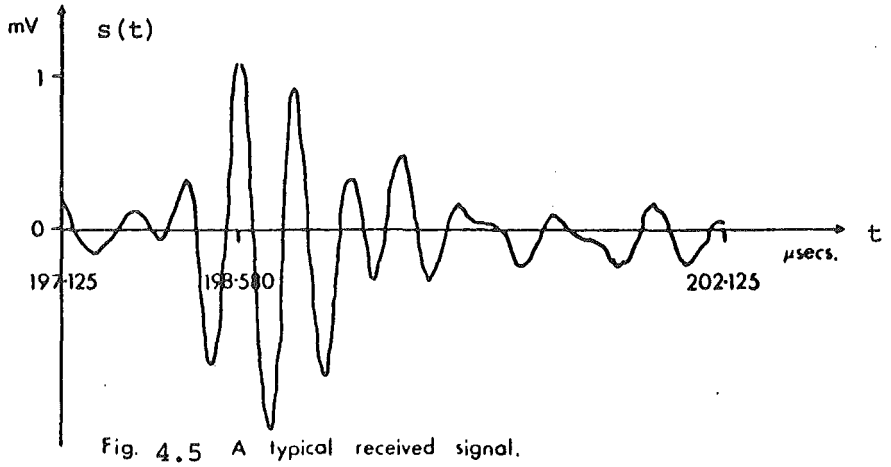

Fig. 4.5 A typical received signal.

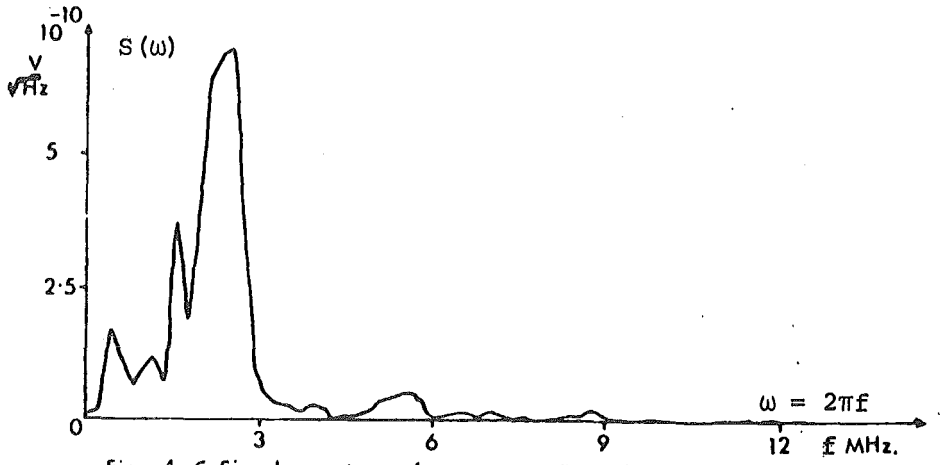

Fig. 4.6 Signal spectrum for s(t) in Fig. 4.5

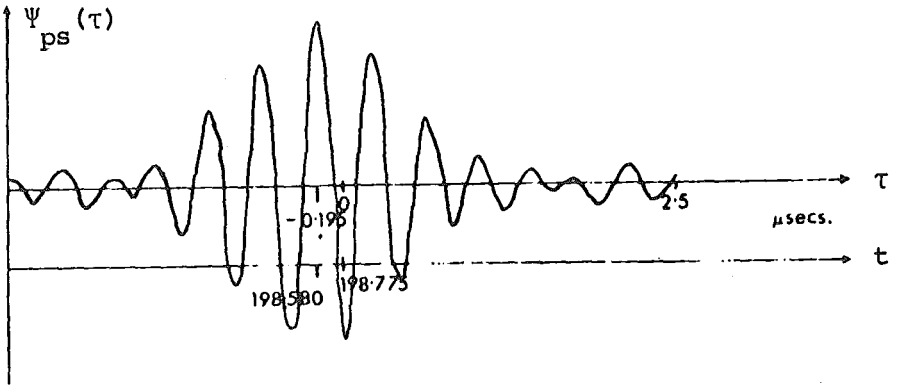

Fig. 4.7 Crosscorrelation of the signals in Figs. 4.3 & 4.5. This shows that the pulse arrived 0.195 μsecs before the refence when referred to the time windows.

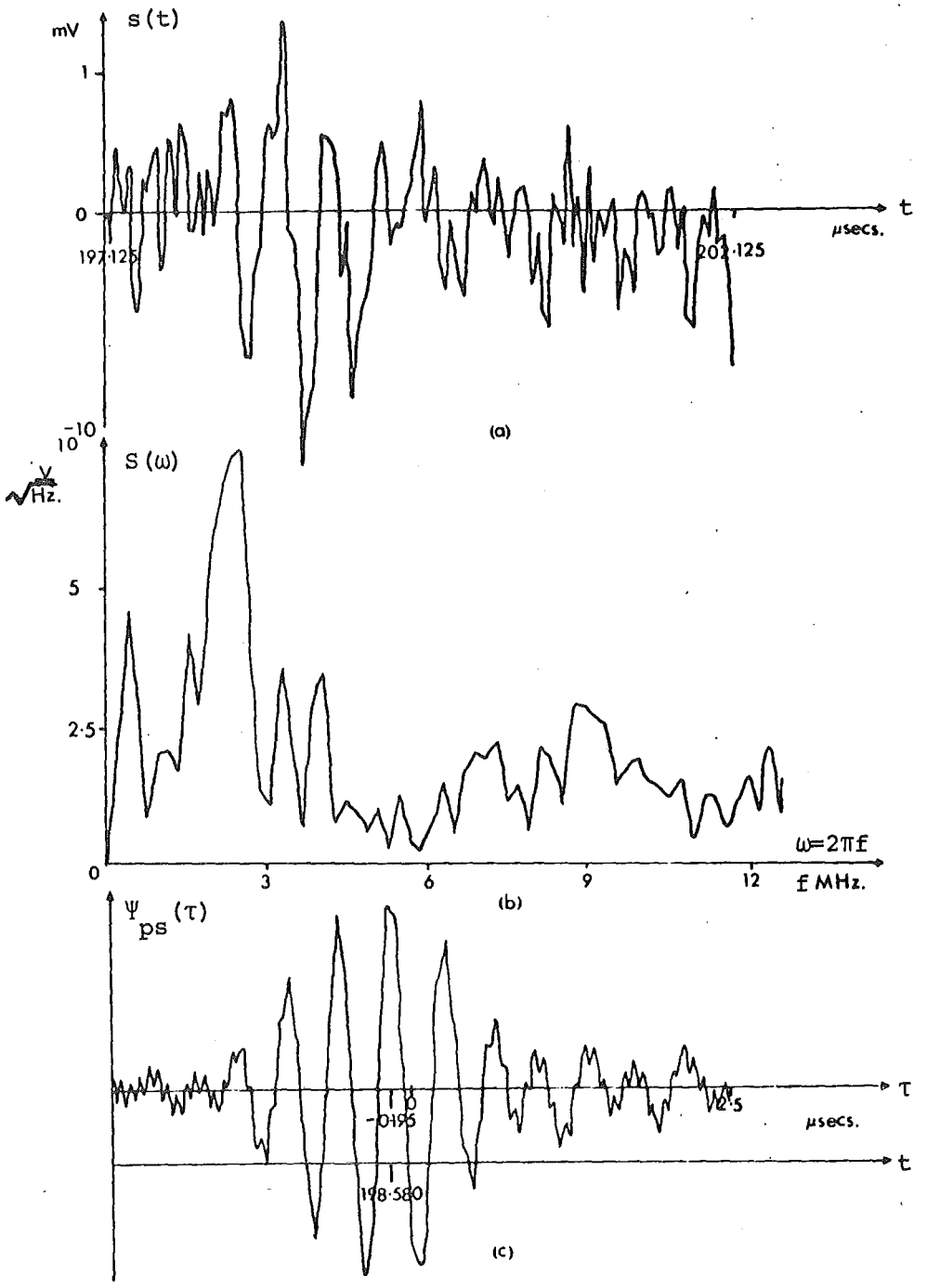

Fig. 4.8 Detection of pulse when signal masked by noise. The signal is shown in (a) and its spectrum in (b). The crosscorrelation of this signal with the refence p(t) is shown in (c).

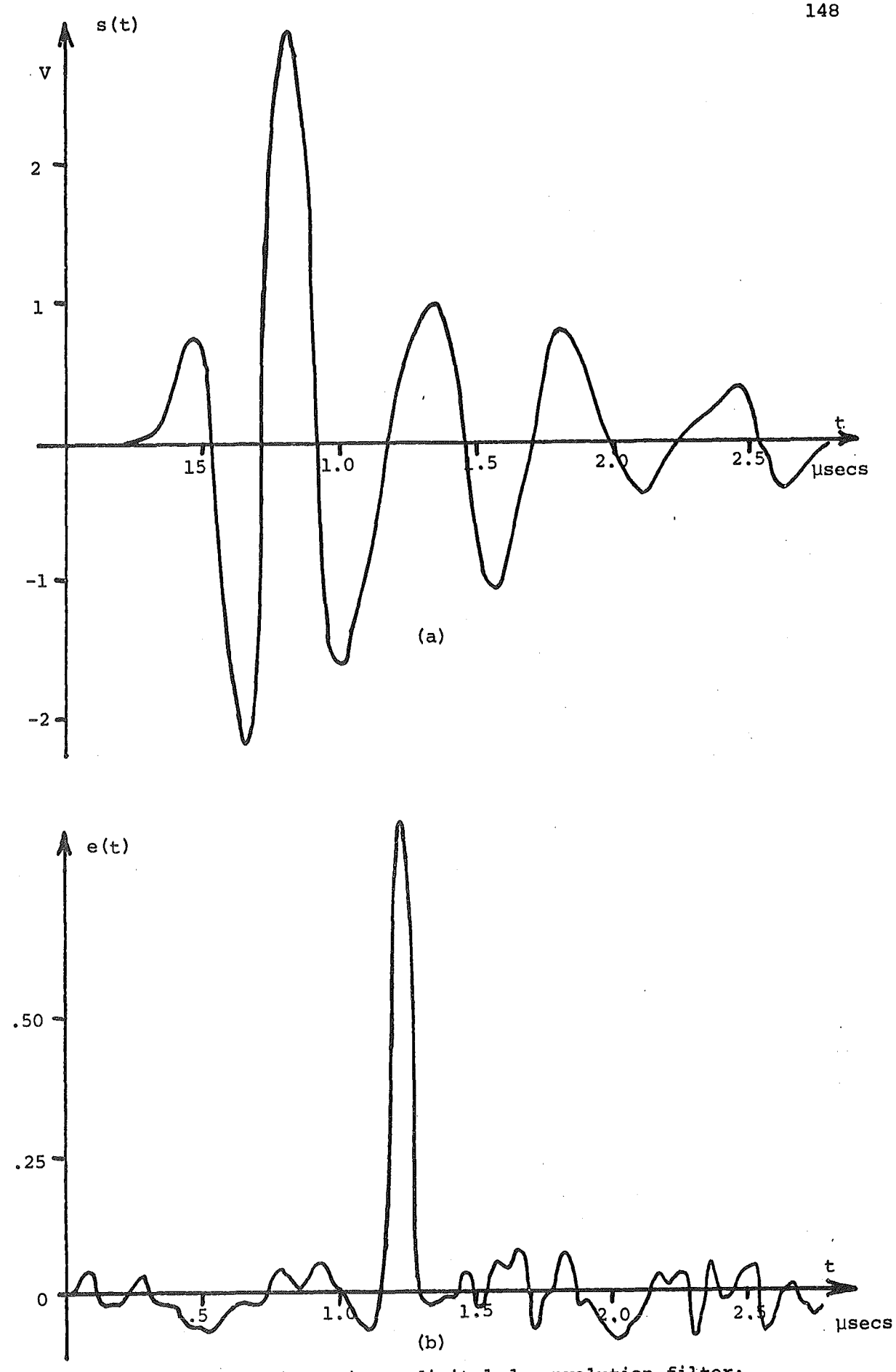

Fig. 4.9 Signal processing using a digital deconvolution filter: (a) filter input, (b) filter output.

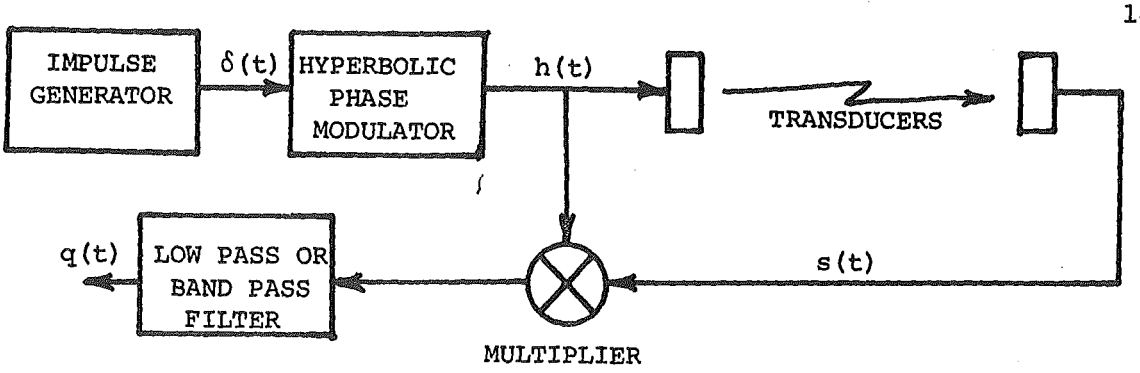

FIG. 4.10 The hyperbolic phase modulation system

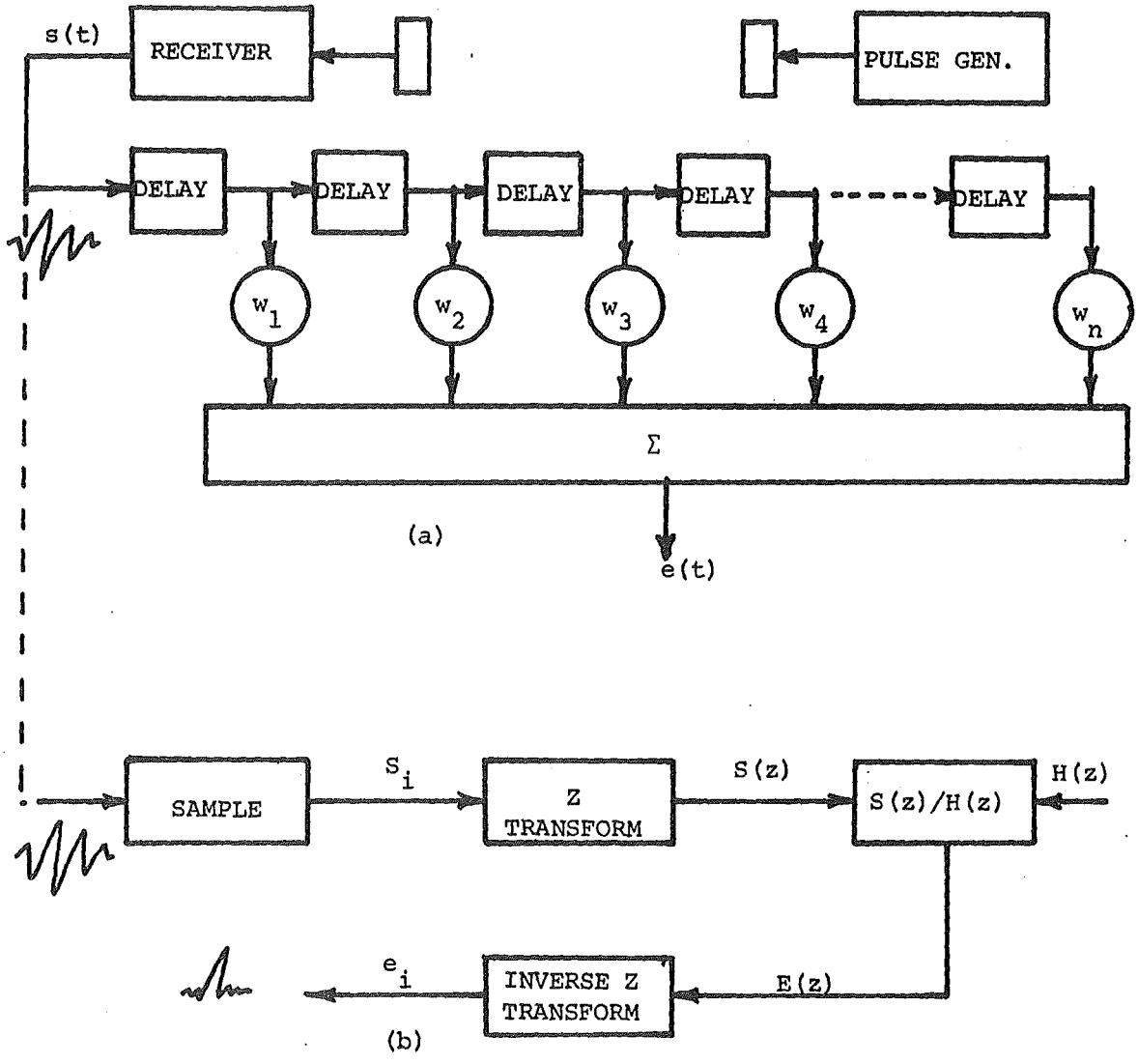

Fig. 4.11 Signal deconvolution filter implementation by:

(a) Non-recursive transversal filter (or cross correlator)

(b) Digital deconvolution - reduces to Wiener filtering when $z = j\omega$.

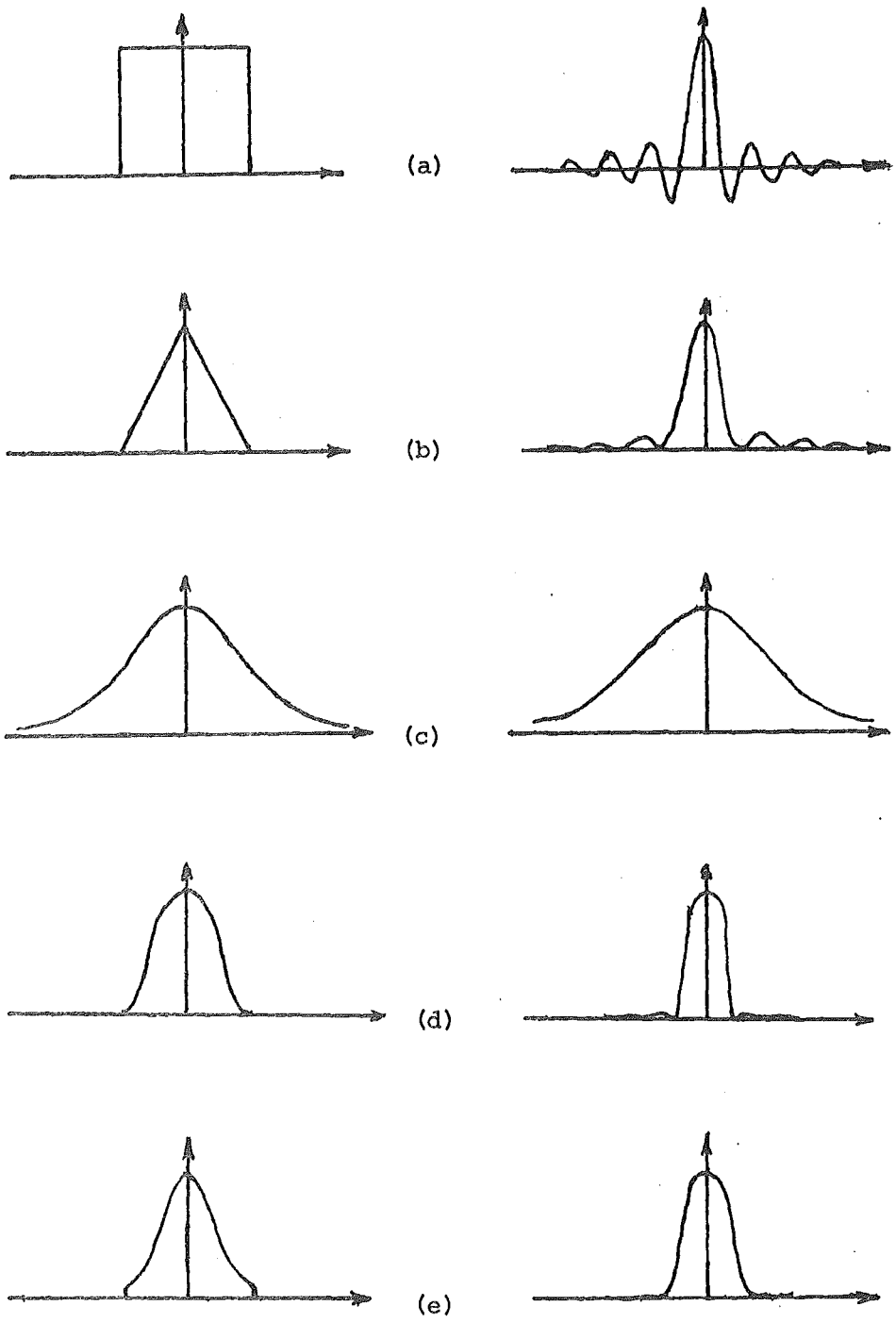

Fig. 4.12 The various window (or envelope) functions on the left are shown beside the corresponding point spread functions on the right. The peak to sidelobe ratio of the point spread functions decreases from -14 dB to -47 dB for figs (a) to (e). Note that the reduced sidelobe levels are obtained with a broader main lobe.

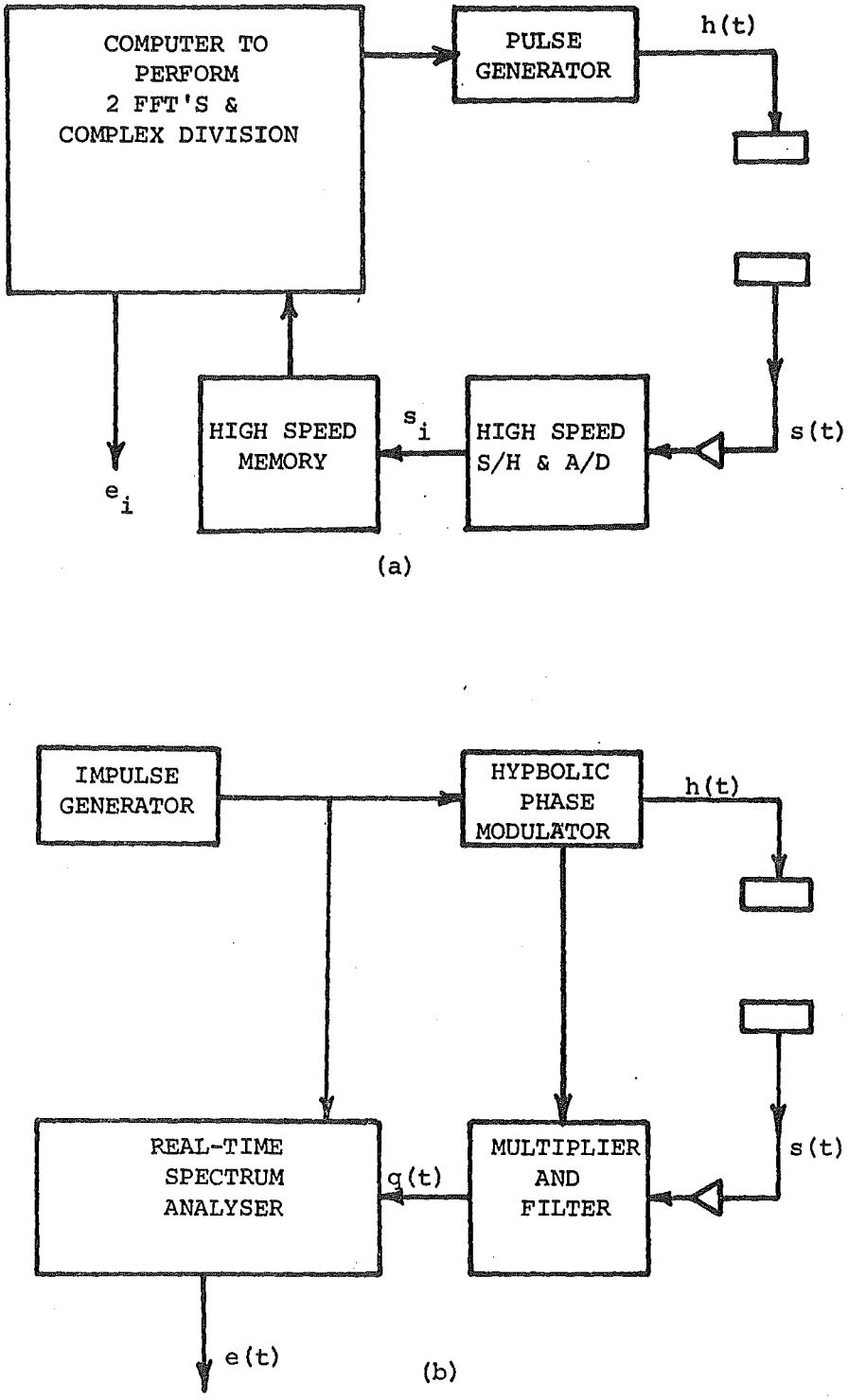

Fig. 4.13 System hardware for Wiener filtering to obtain improved time resolution:

(a) Conventional acoustic pulse transmissions.

(b) Hyperbolic phase modulation system.

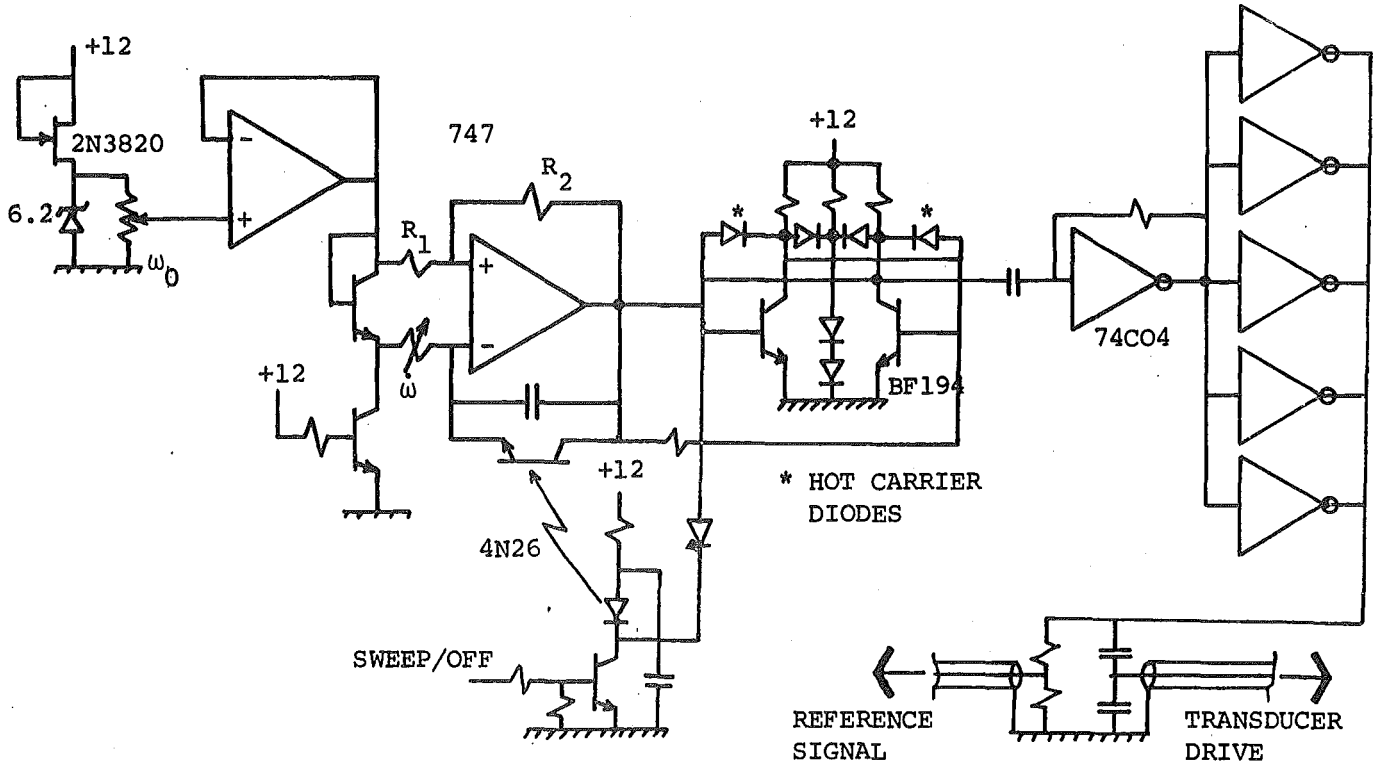

Fig. 4.14(a) The hyperbolic phase modulation circuit. Resistors R_1 and R_2 improve the system linearity (c.f. figs g and d).

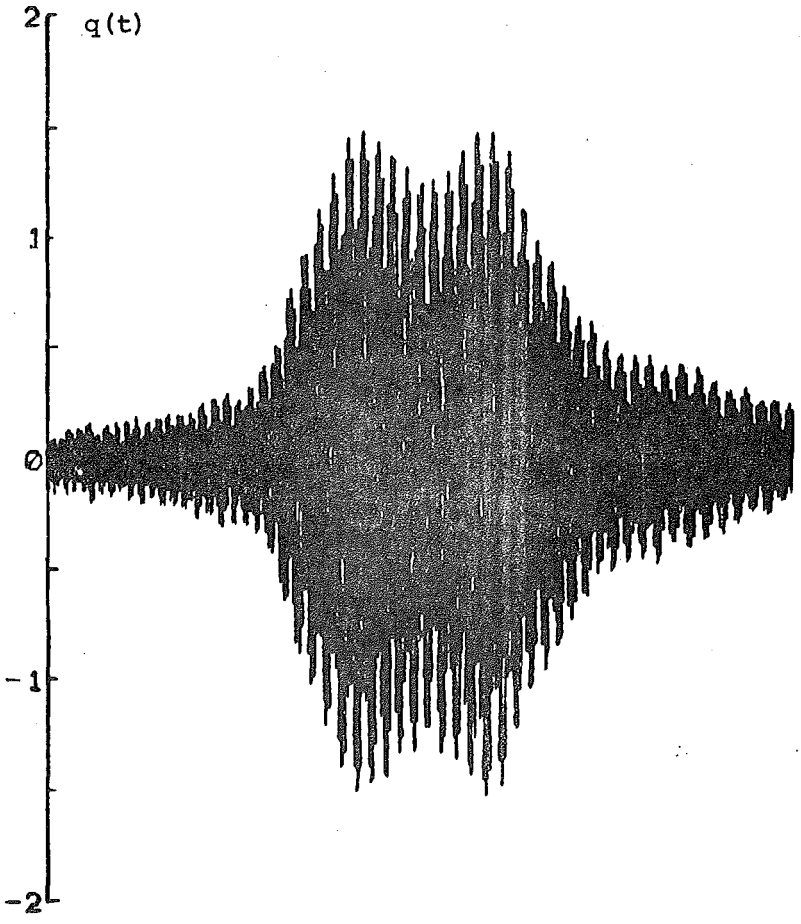

(b) The base band signal sampled at 39 kHz for 25 ms.

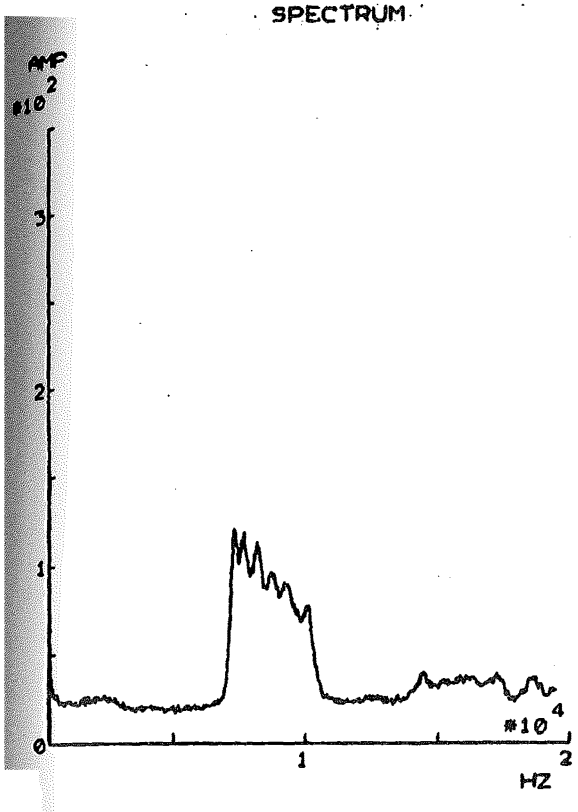

(c) Spectrum of q(t). Suspected faulty optoisolator (4N26).

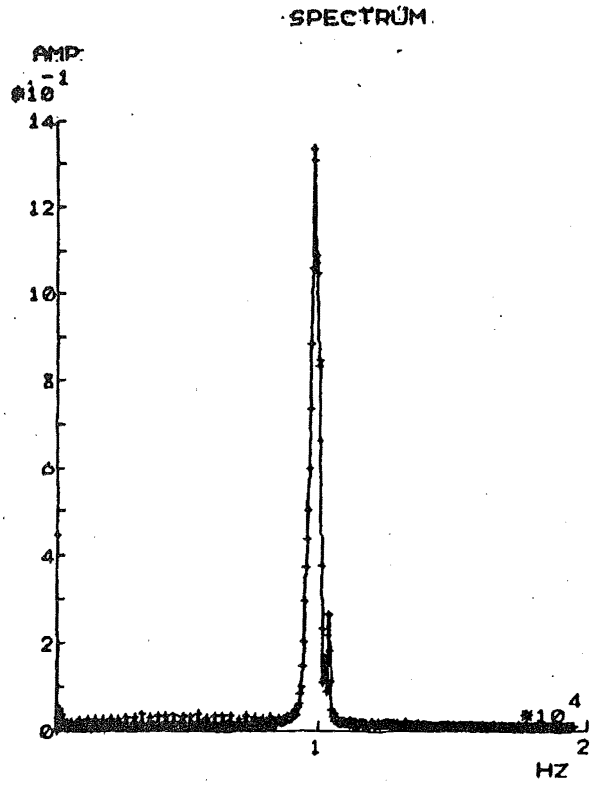

(d) Spectrum when optoisolator replaced.

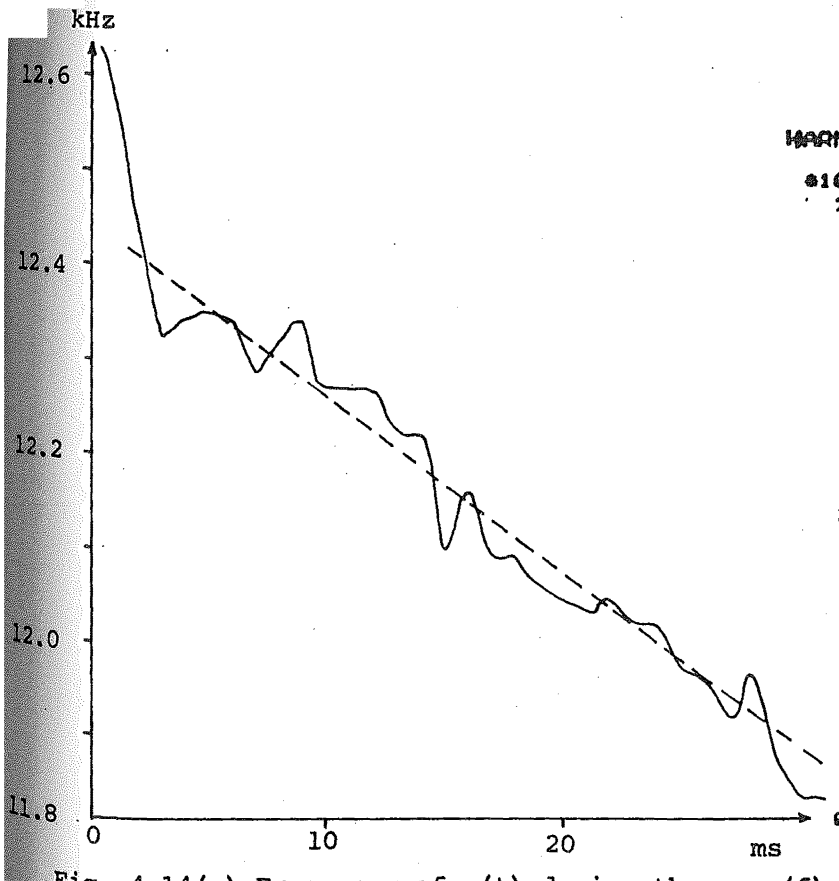

Fig. 4.14(e) Frequency of q(t) during the sweep. Note the approximately linear decrease in frequency with time.

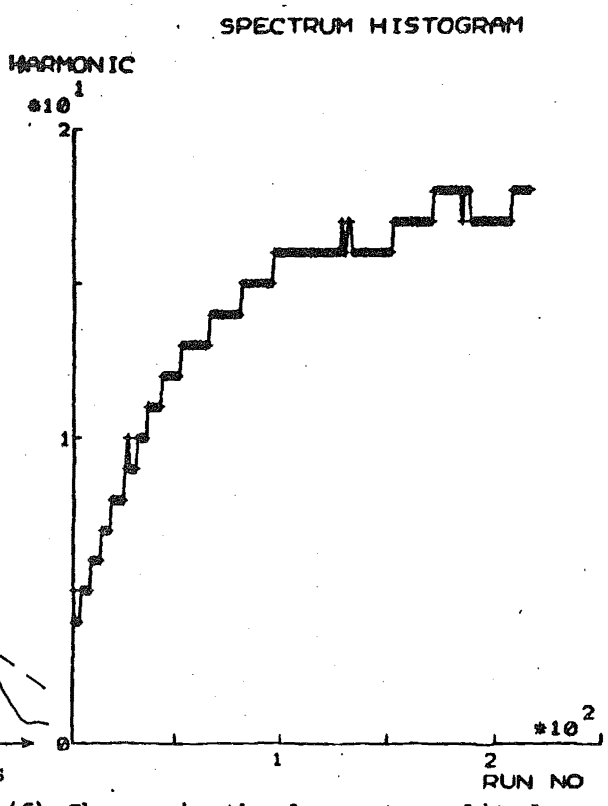

(f) Change in the largest amplitude harmonic of q(t) with elapsed time. Drift is caused by the integrating capacitor.

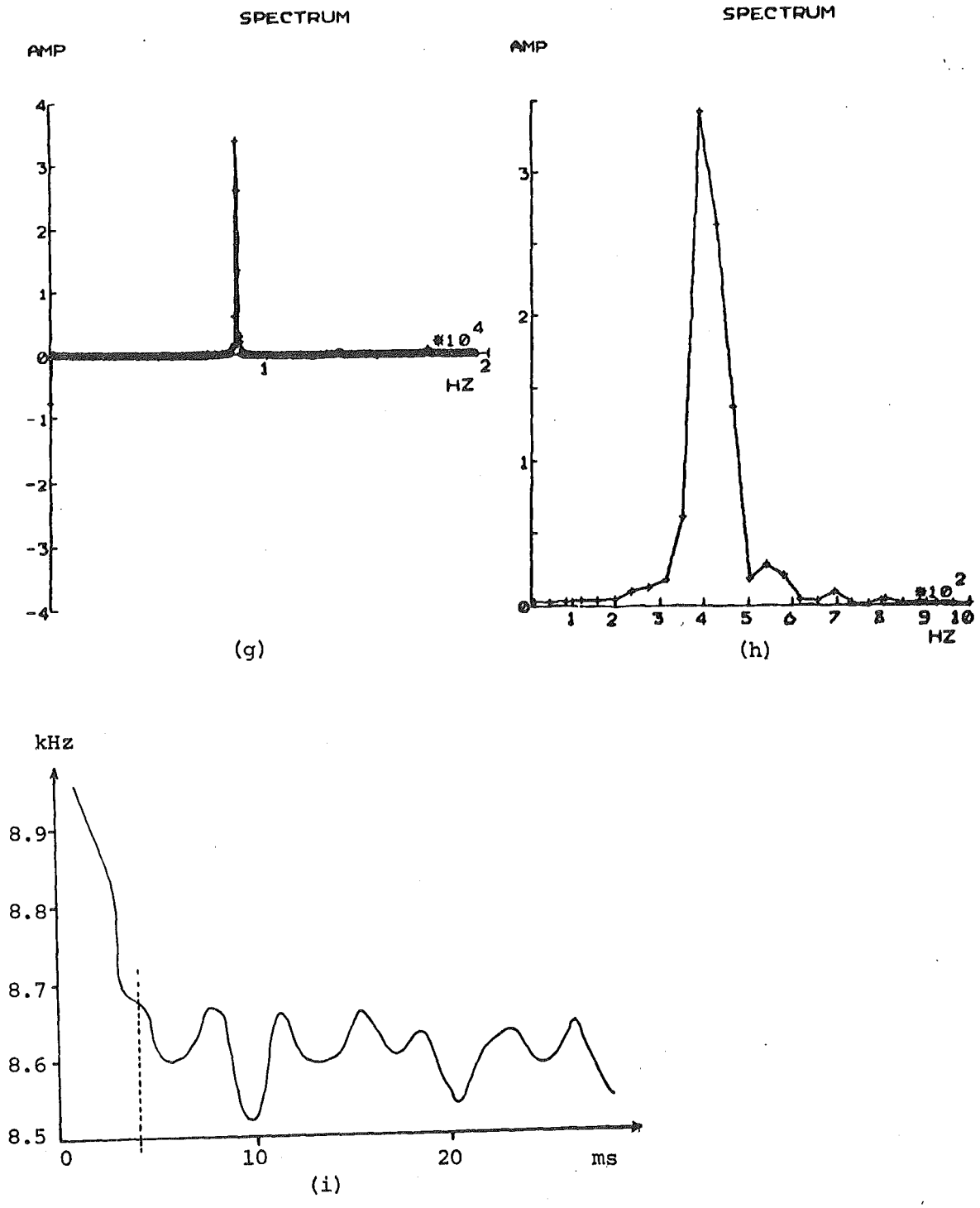

Fig. 4.14 The frequency content of q(t) after the circuit improvements. The spectrum is shown in (g) and an expanded section of it in (h). The frequency variation during the sweep is shown in (i). After 4 ms, the variation is less than ±50 Hz.

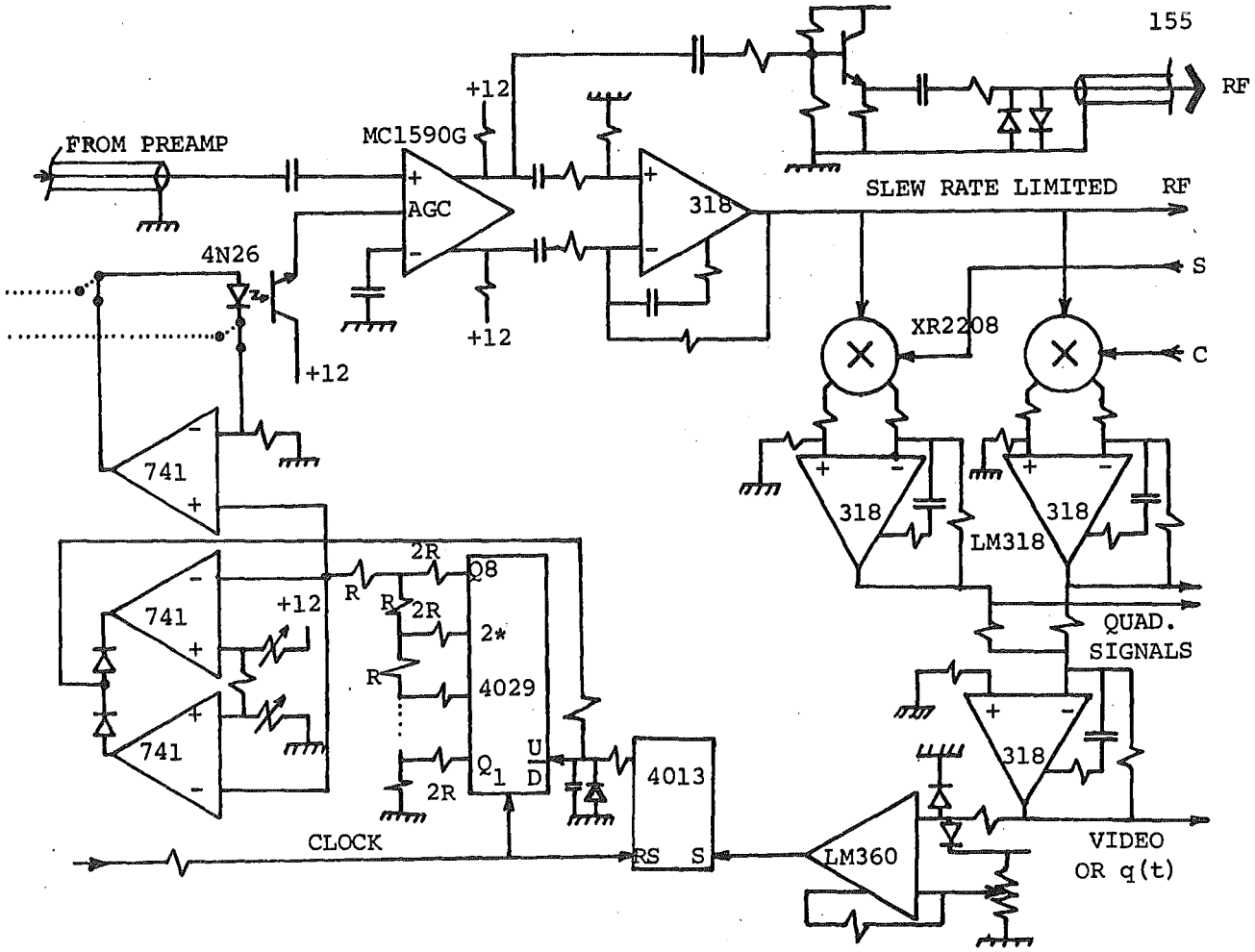

Fig. 4.15(a) Gain control circuit. Sine and cosine inputs generate quadrature outputs. For hyperbolic phase modulation, C is grounded and S is connected to the reference signal.

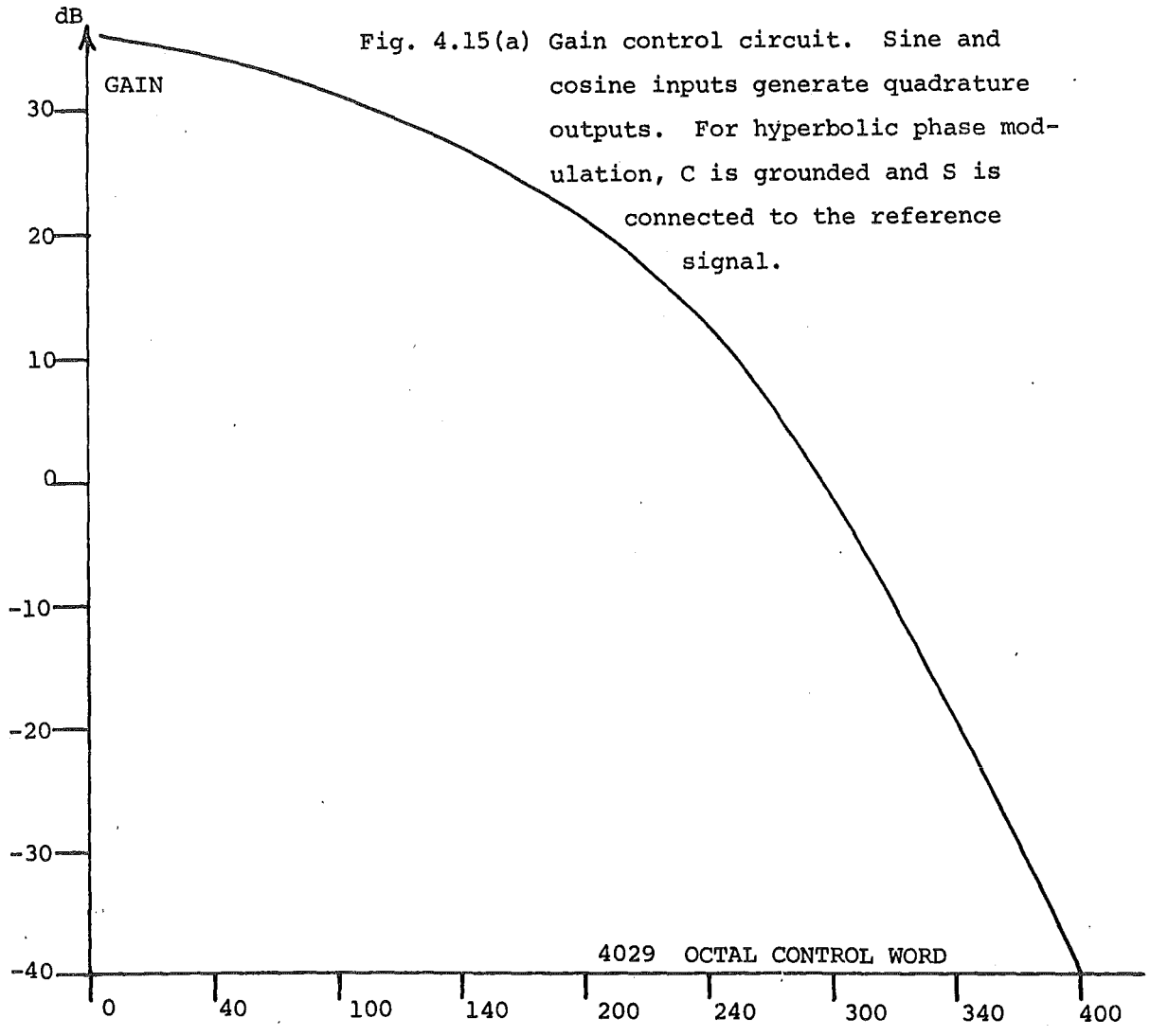

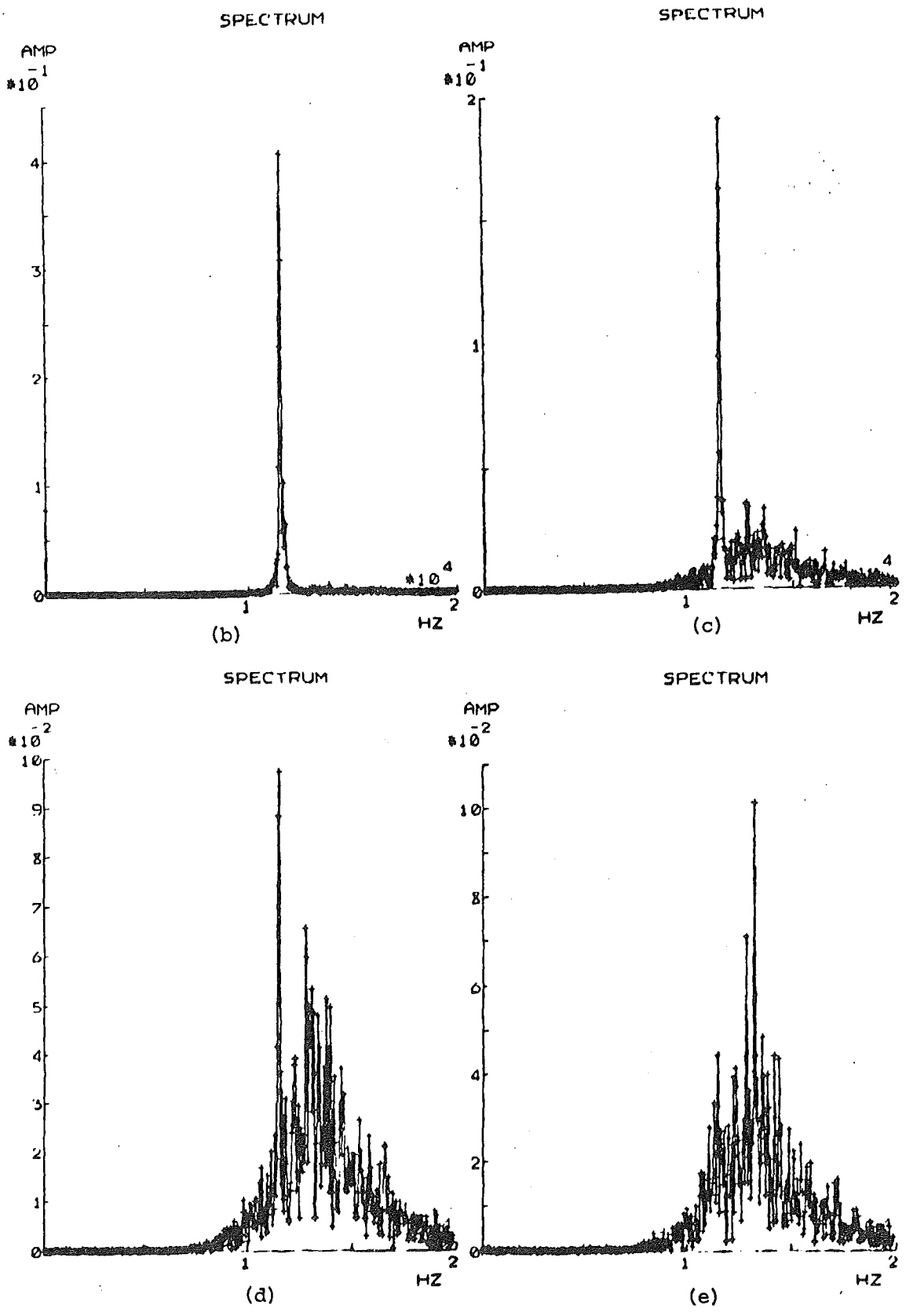

Fig. 4.15 Spectrum of q(t) when circuits in figs 4.14(a) and 4.15(a) are used. The spectrum in (b) is measured for signal path attenuations of 0 to -70 dB. Figs 4.15(c), (d) and (e) correspond to -80, -90 and -100 dB attenuations.

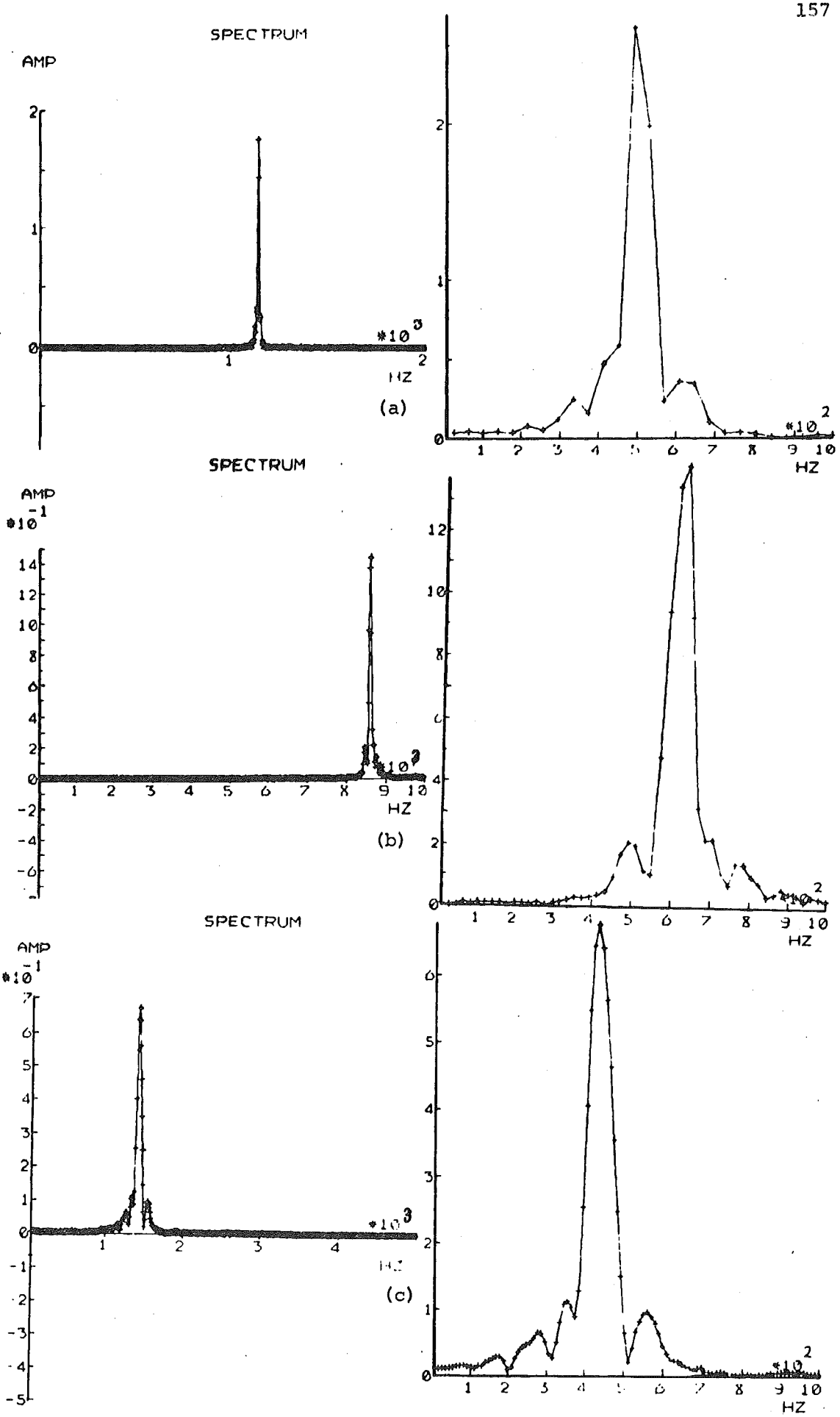

Fig. 4.16 PTO

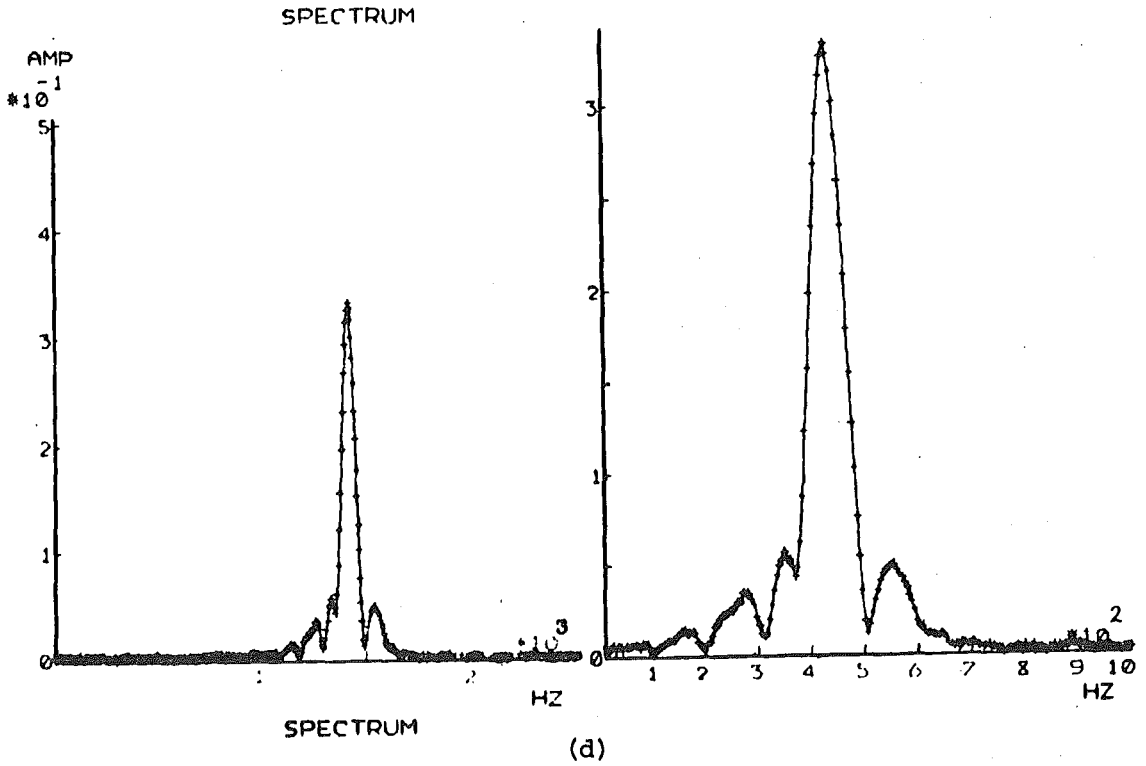

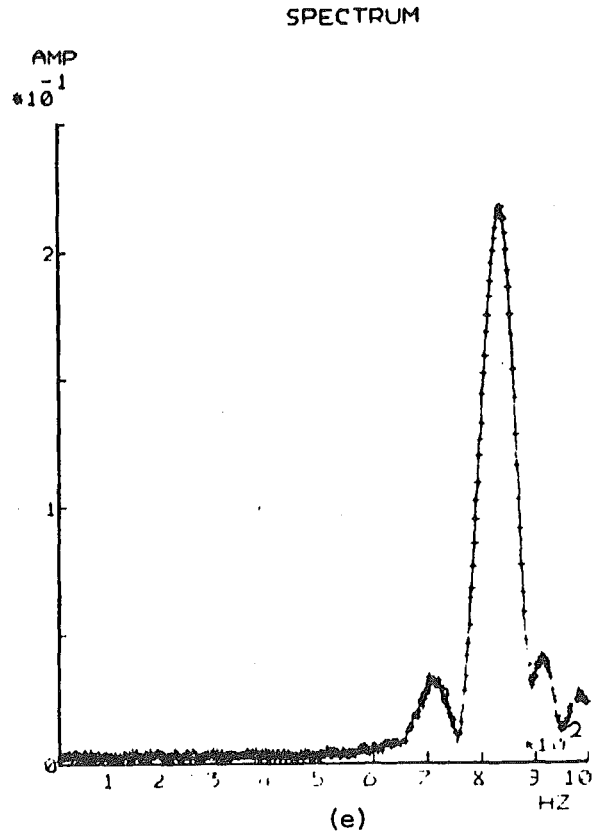

The spectra are computed from the same signal sampled at:

(a) 39.06 kHz

(b) 19.53 kHz

(c) 9.765 kHz

(d) 4.883 kHz

(e) 2.442 kHz

Fig. 4.16 The signal q(t) is band pass filtered (10 to 12.5 kHz) and sampled at the rates given. The sampled spectra in figs (b)-(e) are deliberately aliased. An enlarged portion of each spectrum is shown on the right.

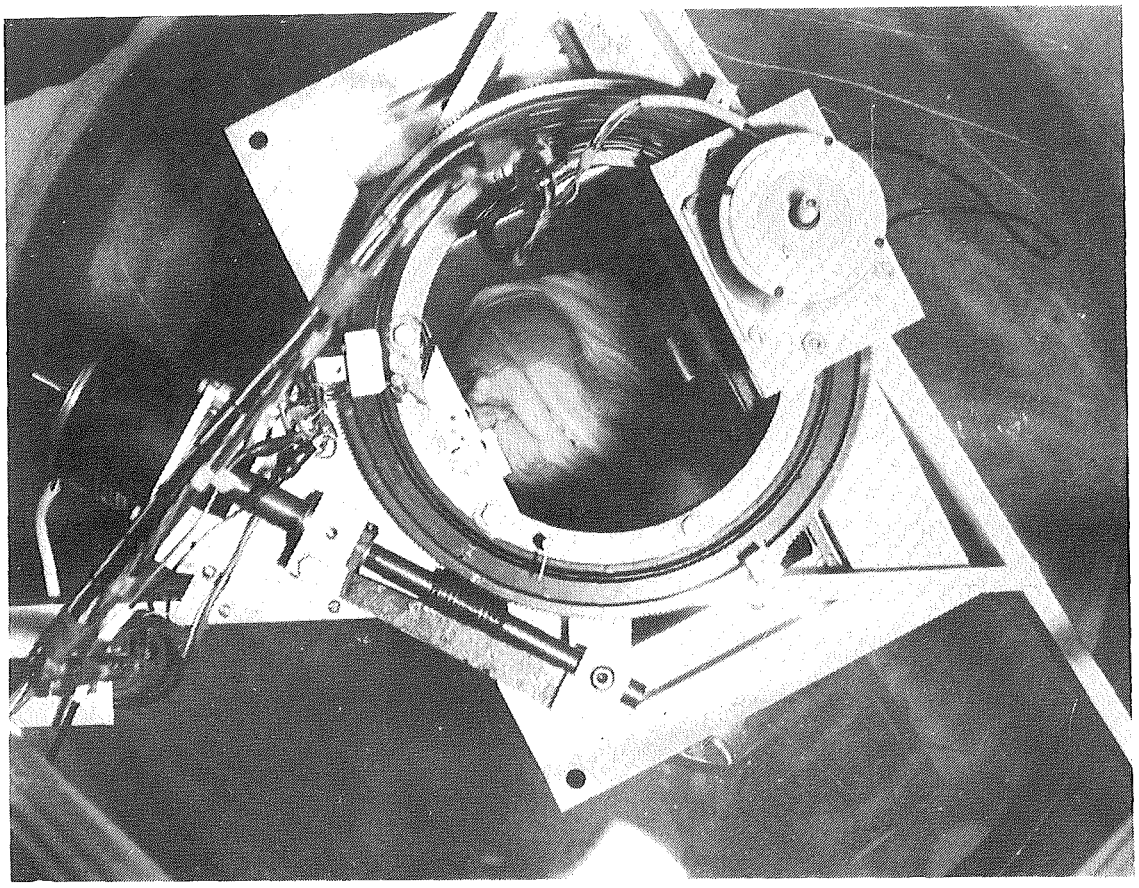

(a)

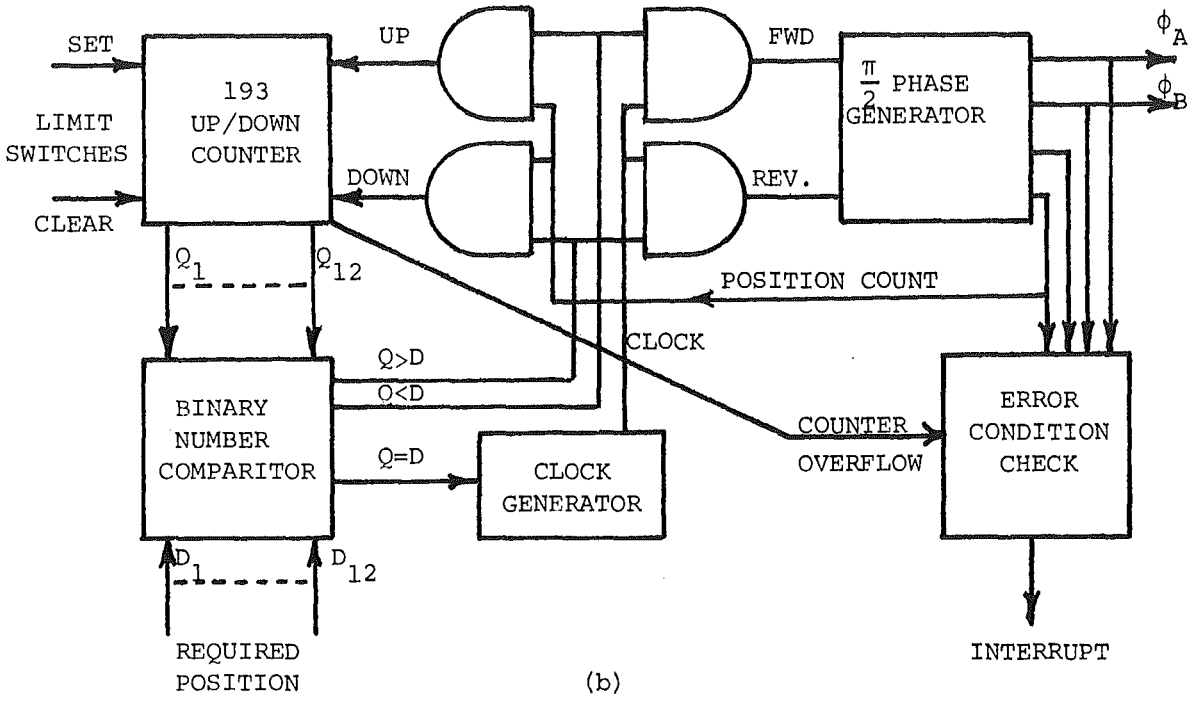

(b)

Fig. 4.17 Numerical control system.

(a) The scanner showing the angular position worm drive and associated stepper motor. The radial positioning stepper motor is visible end on.

(b) The digital servosystem controller. Phases ϕ_A and ϕ_B are a biphase pair (c.f. Fig. 4.20).

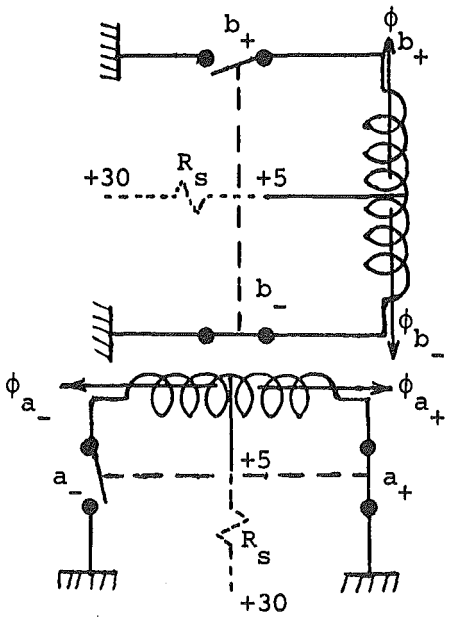

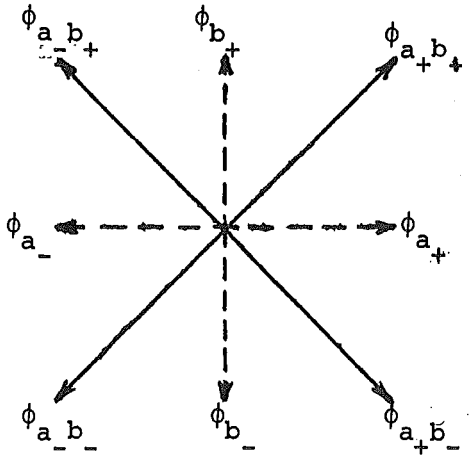

(a) Flux rotation-switching diagram

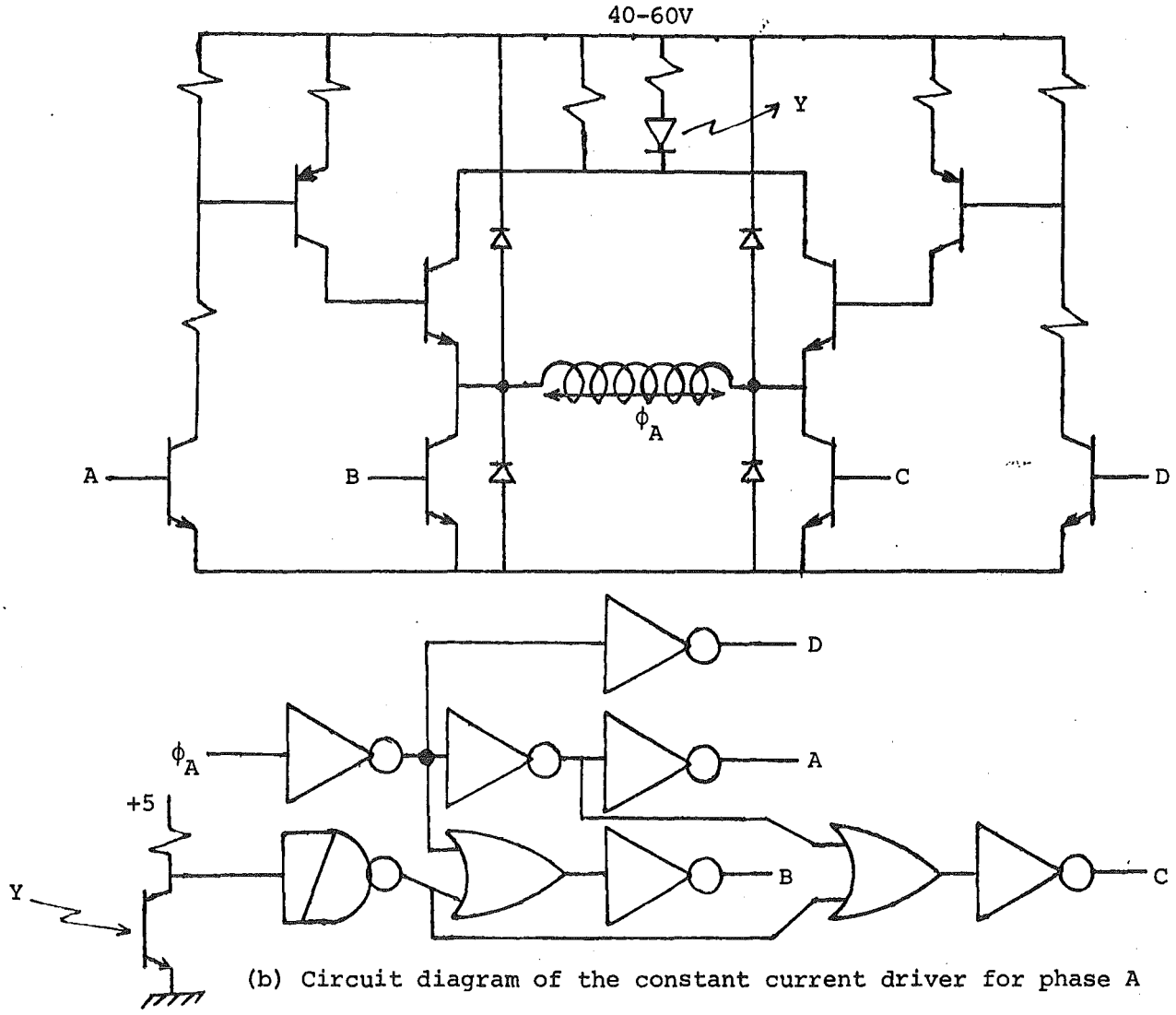

(b) Circuit diagram of the constant current driver for phase A

Fig. 4.18 Stepper motor drive systems.

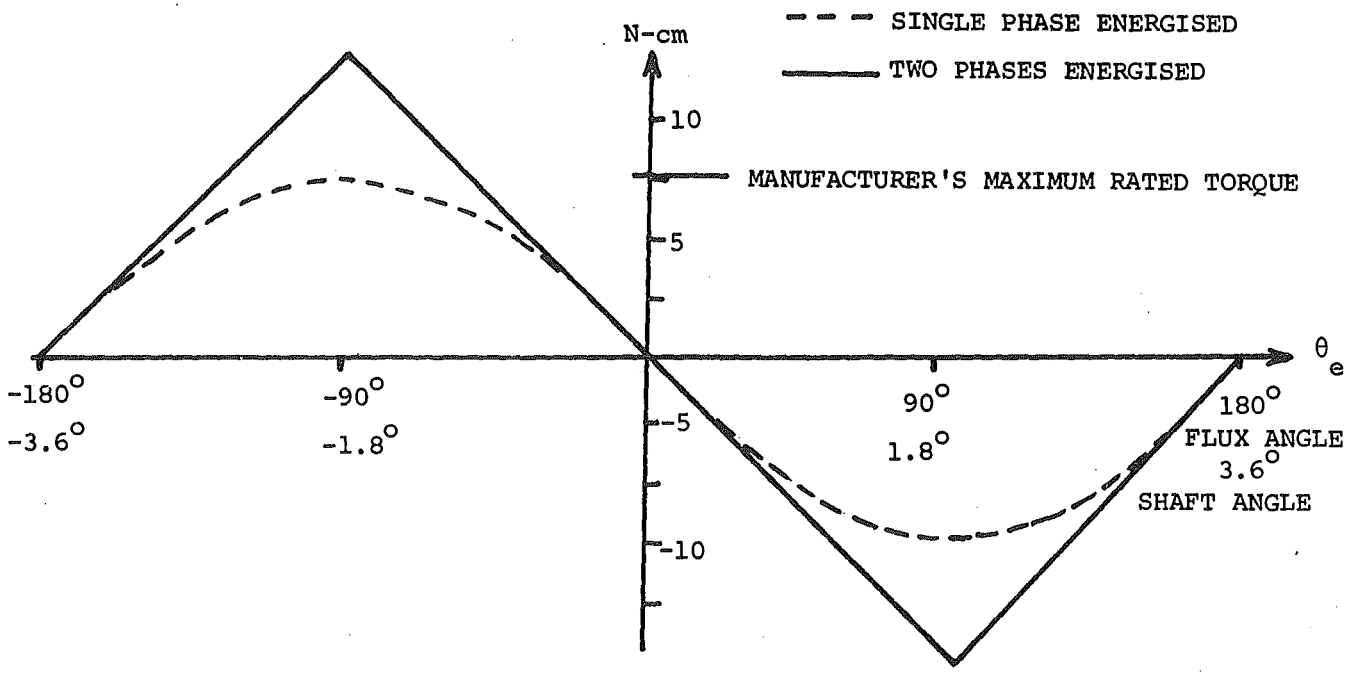

(a) Static torque curves for the Evershed FDD4/B50 stepper motors.

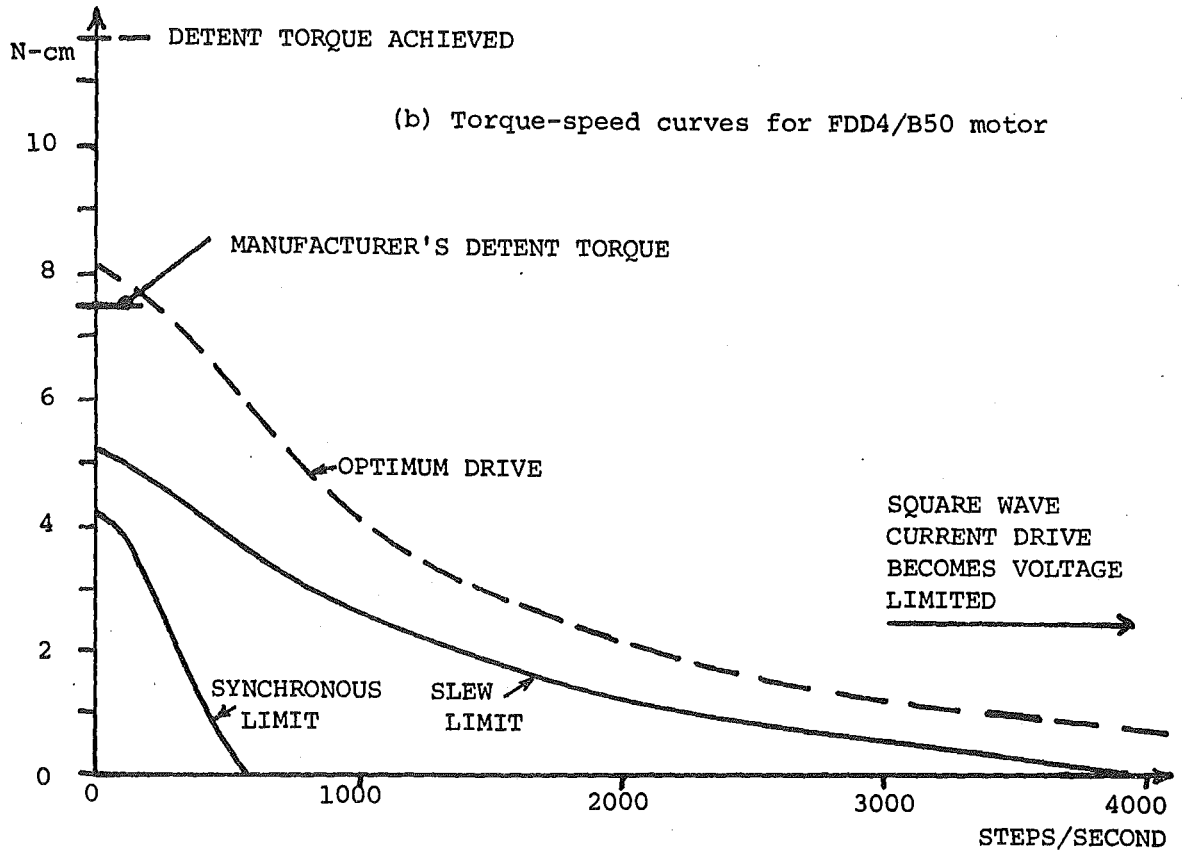

Fig. 4.19 Performance curves for the Evershed FDD4/B50 stepper motor and specially developed drive system.

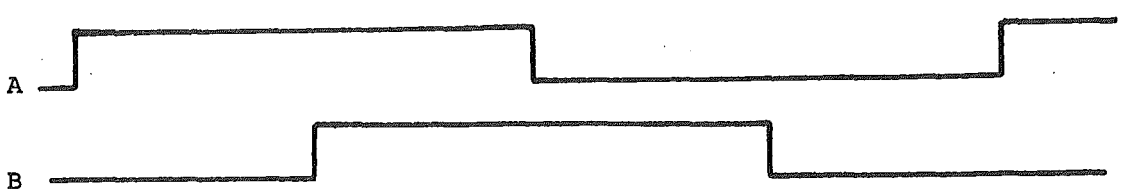

Fig. 4.20 A biphase pair

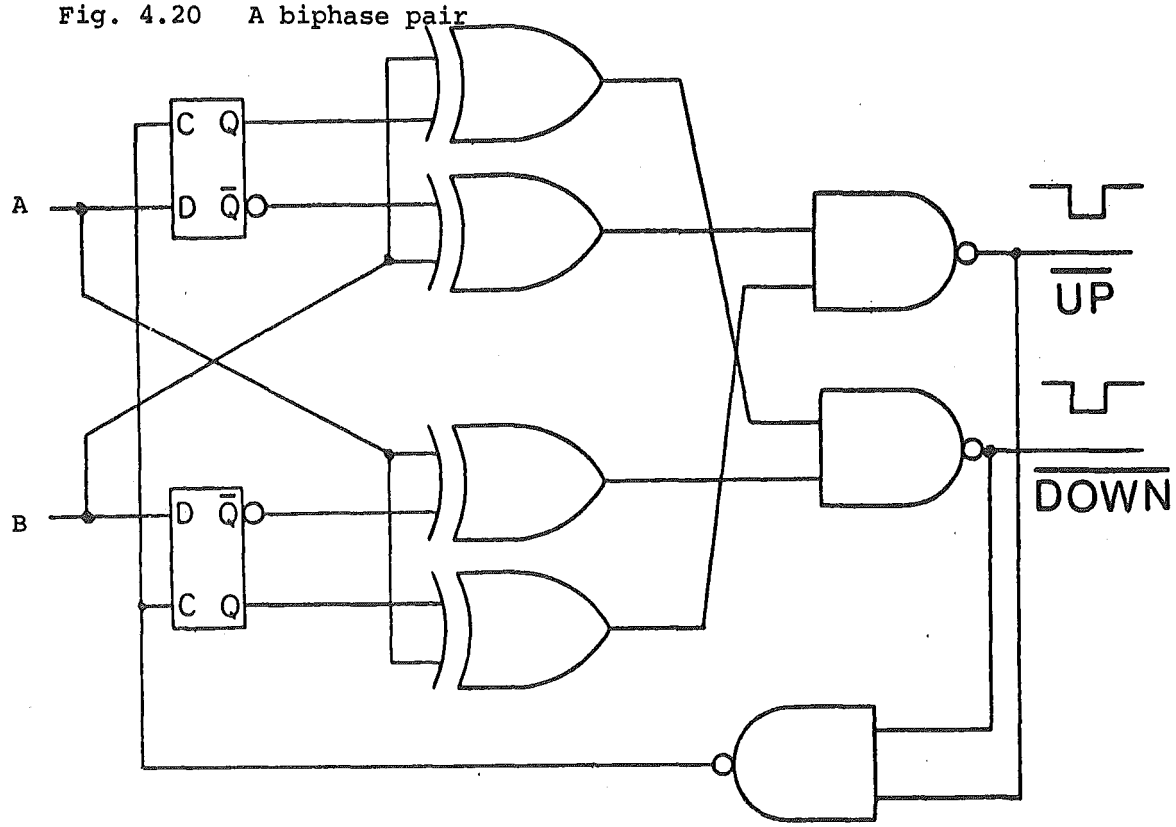

Fig. 4.21 Optimal biphase times 4 counting circuit employing a delay (1 bit digital integrator) in place of the usual analog differentiator. The output connects directly to 193 counters.

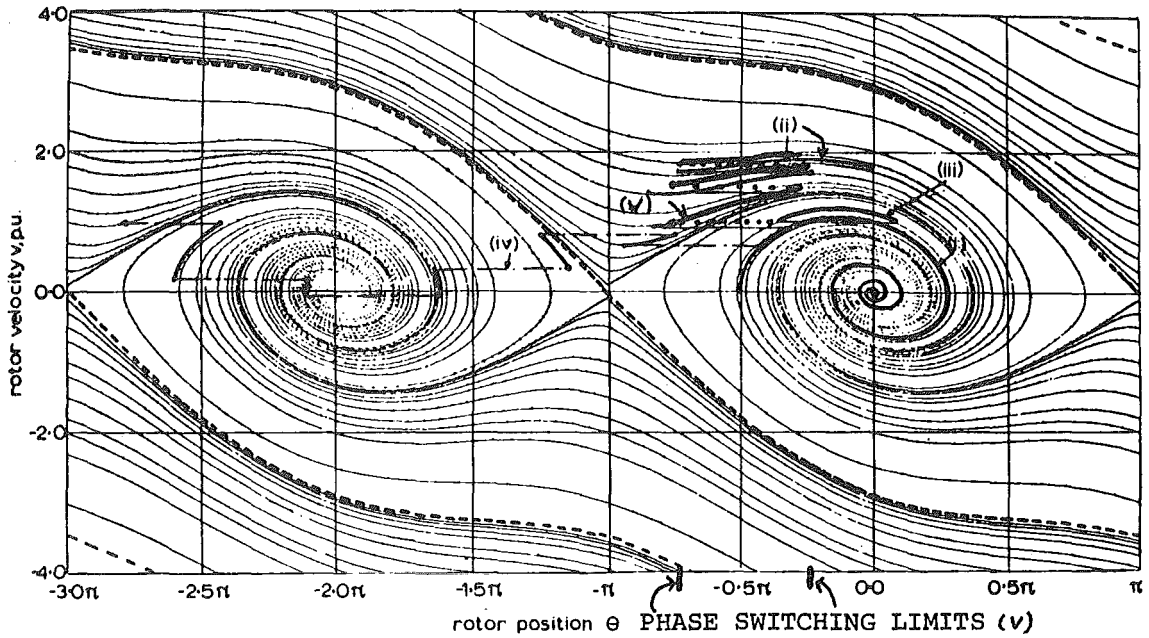

Fig. 4.22 Phase portrait of stepper motor trajectory for various control strategies: (i) single step, (ii) multistep stable, (iii) limit cycle, (iv) multistep unstable, (v) experimental controller.

CHAPTER FIVE

ULTRASONIC TRANSDUCER DESIGN AND TESTING

5.1 INTRODUCTION

A method of transducing an electrical signal from an ultrasonic pressure wave, and vice versa, is required for the ultrasonic scanner system described in chapter 4. Accurate measurement of the ultrasonic propagation time delays requires wide bandwidth transducers for transmission and reception. The transducers must radiate, or receive, ultrasonic pressure waves from water. Hence the ideal transducer would have a characteristic mechanical impedance of 1.48 M Rayls ($1.48 \times 10^{6} kgm^{-2}s^{-1}$, units named after Lord Rayleigh) so that the reflection coefficient would be zero for ultrasonic waves propagating between the transducer and the water load. The transducer should also have a low mechanical Q so that broad band signals could be transduced.

Unfortunately, the ideal transducer material does not exist and materials which approach the ideal (within a factor of 2 or 3) are very costly. The transducers which have been constructed by the author are similar to those used in conventional medical diagnostic apparatus since the scanner was designed primarily for studying biological tissues. Conventional pulse-echo diagnostic equipment for soft tissues operates with frequencies in the range of 1-5 MHz where the ultrasonic dispersion and attenuation are small (c.f. Eriksen et al. 1974). Experience within New Zealand in the design of wide band ultrasonic transducers to operate into a water load at these frequencies is limited. The author's early attempts at fabricating transducers are outlined here. They were not very successful, and only the final successful design is discussed in detail in the latter parts of this chapter. Transducers of a similar type of construction are reported by De Silets et al. (1978) and by Souquet and De Franould (1978). These authors publish results similar to those which are reported in this chapter. However, transducers used to obtain the published results were constructed with great care (e.g. dust free rooms

and centrifuged matching and backing sections) whereas the transducers reported in this chapter are easily constructed and the performance characteristics are repeatable. Foster and Hunt (1978) obtain agreement between theoretical predictions and experimental results, but some discrepancies are observed, especially for wide bandwidth pulses.

The first pair of transducers constructed were based on a sketch given by Wells (1969, Fig. 2.4). A 10 mm diameter PZT-4 (Vernitron trade name) piezoelectric ceramic, with a half-wave resonance of 1 MHz, was backed with an araldite (Ciba Co. Pty Ltd) block and used to radiate directly into water. The radiated signal had a narrow bandwidth, and there was considerable reflection from the rear surface of the backing block. A second design incorporated an air backed PZT4 ceramic which was coupled to the water load by two matching sections. The two quarter-wave matching sections were chosen on the basis of the binary weighting criteria developed by Collin (1955). These sections, constructed from crown glass and perspex, were ground flat to optical tolerances and bonded to the transducer using a contact cement. The removal of the backing block eliminated the rear reflection problem but the bandwidth was still very narrow (~ 120 kHz). A higher frequency was tried with an air backed 3 MHz quartz transducer bonded to a perspex matching section which was 1.25 wavelengths thick at resonance. A bandwidth of 400 kHz was obtained but 100V drive pulses were needed to obtain a 40 dB signal-to-noise ratio (such voltages were inconveniently high for use in the laboratory made available to the author).

The main bandwidth limitation is due to the high mechanical Q of the transducer material. This problem could be circumvented by using a high frequency (~ 40 MHz) crystal or ceramic disc in a sandwich structure resonant in the 1-5 MHz range (c.f. van Randeraat 1968 §8, and Smith 1972). Since such high frequency crystals are very thin and fragile, a

low Q lossy construction is preferred. A relatively low Q (~ 80) material, Philips PXE5 (similar to Vernitron PZT-5H) was finally chosen as the basis for the design of the author's transducers. This material was considerably cheaper than the equivalent material from other manufacturers (PZT5H-Venitron and Naval II-Channel). Twenty transducers were constructed and tested without exceeding grant allocations.

The construction of the transducers based on the PXE5 piezoelectric ceramic is described in section 5.2. In section 5.3, circuit models are developed to predict the transducer performance. In sections 5.4 and 5.5, an impulse testing method to obtain the transducer characteristics is described. Experimental results are discussed in the final section, 5.6.

5.2 CONSTRUCTION OF THE TRANSDUCERS

A very limited choice of piezoelectric materials was available to the author, who had to take careful account of the strength and handling characteristics of the chosen material as well as its long term stability. Hydroscopic materials (such as lithium sulphate which gives excellent receiver sensitivity) were not used because of waterproofing problems associated with immersion in the water tank. The stability of the piezoelectric material parameters is also important, and in this respect, PZT-5H, PXE5 and NAVAL II all exhibit good characteristics.

Piezoelectric ceramics are hard, chemically inert, and insensitive to humidity and atmospheric conditions. They also appear to be insensitive to underwater conditions, since repeated soakings of a leaky transducer in a water tank did not alter the transducer performance after it had been dried out and resealed. Quartz is the only other material commonly used for radio frequency transducers, but it is not particularly suitable for immersion in water since it is slightly hydroscopic and requires high driving voltages. Wells (1969) states: "The lead titanate

zirconates are superior to quartz as transducer materials in almost every practical respect at frequencies below about 15 MHz". The material PXE5 was selected for use since it fulfilled all the main requirements and it could be obtained within a few months of ordering it. The piezoelectric material was in the form of 1 mm thick discs of 10 mm diameter (nominal 2.0 MHz elements).

In order to select suitable backing and matching materials for the PXE5 discs, the acoustic parameters of a dozen different materials were measured. The results are recorded in table 5.1. A sample of each material was prepared as a 5 cm long 12.7 mm diameter cylinder. Accurate weighing and machining allowed the density of the samples to be determined within 0.6%. The velocity values were obtained by measuring the time for an ultrasonic pulse to travel the 5 cm length of the cylinder. The times were measured to within ±3% by using two 5 MHz 5 mm diameter transducers coupled to each end of the sample by a thin oil film. The sample and transducers were placed in a special measuring jig and held in contact by a rubber compression block at one end of the sample. The published velocity and density values for the common sample materials (bracketed in table 5.1) agree well with the values calculated from measurements. The values calculated for the less common sample materials are of similar accuracy. Also, the properties of filled epoxy materials are discussed in a recent article by Pelmore (1977).

The construction details of two types of transducer are shown in fig. 5.1. The brass cases were made from 12.7 mm tube so that the whole transducer could be inserted into a 12.7 mm collet for accurate machining. A 228.6 mm Hercus lathe was used for all construction work and was calibrated in .025 mm increments. In fig. 5.1 most of the metric dimensions were obtained by conversion from imperial measure. Various configurations of backing block were tested in conjunction with a three quarter-wave matching

transformer to the water load. The matching section was fabricated by mixing three parts (by weight) of aluminium powder with two parts of araldite (5 pts casting resin D to 1 part by weight of hardener HY951, Ciba). It was cast in place on the front of the piezoelectric disc.

The transducer was then tuned for maximum bandwidth by machining the matching section to reduce the thicknesses. The section thickness was reduced until the resonant peak due to the matching section had the same amplitude as that due to resonance of the piezoelectric disc. Bandwidth measurements were made each time the thickness was reduced. The matching section was made three quarters of a wavelength thick at the resonant frequency of the matching section in order to reduce the machining tolerances.

The reason for the two types of construction is now discussed. The first tentative construction efforts (transducers 1-3) utilized the ring clamped arrangement shown in fig. 5.1(a). The piezoelectric disc was firmly attached to the transducer case by a fillet of electrically conducting silver loaded araldite. This permitted the matching section to be machined with a reduced risk of bonding failure. Once the approximate matching layer thickness had been established, a batch of free edge (c.f. fig. 5.1(b)) transducers (4-9) was constructed in such a way that the matching sections required very little machining. Considerable care was required to minimize the machining forces so that the front face, PXE5 disc and backing section did not spearate or rotate in the brass housing. Transducers 4, 5 and 8 were constructed with the same backing and matching materials as were 6, 7 and 9. In addition, transducers 8 and 9 had a Naval II piezoelectric disc substituted for the PXE5. The difference in performance was not discernible despite the 10:1 price differential between the Naval II and PXE5.

The bandwidth of the second batch of transducers was limited to about 900 kHz, whereas the first batch of ring clamped transducers exhibited bandwidths up to 1 MHz. The difference was caused by the clamping effect of the brass transducer case on the outer edge of the front transducer face. The mechanical connection of the case to the transducer is not observed to reduce the transducer's dynamic range. The brass case is probably too thin to operate as a good acoustic conductor and radiator at the frequencies used. Nevertheless as a precaution, a pressure release barrier of granulated cork was inserted between the brass casing, and the PXE5 disc and backing block.

The third batch of transducers included four almost identical transducers (11-14) with a backing block which consisted of araldite loaded with tungsten and rubber powders. The four transducers were machined to obtain a three quarter-wave matching section at .725, .725, .737 and .737 mm. The measured bandwidths varied from 1.11 to 1.20 MHz. Thus the construction tolerances were very good and the transducer characteristics reproducible.

The wire connection to the rear silvered face of the PXE5 disc was made at the edge of the disc so that the wire could be pushed into a small joint gap in the cork insulator. The backing mixture was then cast in place and allowed to set overnight. The tungsten settled next to the rear surface of the PXE5 disc and thus produced a slightly graduated impedance taper from the PXE5 disc to the rubber plug which terminated the backing block.

Although the tungsten-araldite mixture was not centrifuged (c.f. Kossoff, 1966) quite satisfactory results were obtained with a bandwidth of 1.2 MHz for the 2.0 MHz PXE5 discs. Transducers number 6 and 16 were milled and lapped to obtain the cross sectional views shown in figs 5.2(a) and (b). Microscopic examination was used to check the dimensions, and neither voids nor bonding delaminations were found in either transducer.

Thus gravity casting of the mixtures was considered satisfactory. The mixture used for the backing block followed the suggestion of Washington (1961) in that a 2:1 mixture (by weight) of tungsten powder and araldite is used. Lutsch's (1962) technique of adding 10% (by volume) of rubber powder to the backing mixture is also incorporated so as to increase the attenuation of the pressure waves in the backing block.

The results obtained by Kossoff (1966) were useful for determining the most probable materials to give a wide bandwidth, but the increased bandwidth obtained through the damping of the ring clamped transducers was rather unexpected. Some theoretical models based on the construction dimensions and materials used are evaluated in the next section.

5.3 THEORETICAL MODELS AND MATHEMATICAL APPROACHES

The major problem encountered in the design of piezoelectric transducers is caused by the large acoustic mismatch between the transducer and the load. The lead titanate zirconate solid solutions (PZT ceramics) discovered by Jaffe et al. (1955) are strongly piezoelectric and have an acoustic impedance which is typically twenty times that of water (or tissue). Acoustic matching to the water load is achieved by intermediate quarter-wave and half-wave matching layers (c.f. McSkimin 1955, 1959, Brekhovsikh 1960, Redwood 1961, 1963 and Lynworth 1965).

Kossoff (1966) presents detailed computational results for a PZT-7A ceramic disc matched to a water load by quarter-wave matching sections of different materials. The effect of various types of backing material is also calculated to illustrate the trade off between sensitivity and bandwidth. The results obtained by Kossoff are not directly applicable here since the quarter-wave matching section is resonant at a fixed frequency

(the half-wave resonant frequency of the piezoelectric section). However, the results presented by Kossoff were a very useful check on the more general matching design programs developed by the author.

Mason (1948) presents accurate equivalent circuits for modeling the performance of ultrasonic transducers. The models are developed from the equations of motion of the piezoelectric material. They are particularly useful because they apply for arbitrary boundary conditions. However, it is often difficult to select the appropriate material constants used to define the circuit elements. In all, there are 144 material constants which relate the nine elastic stresses and three electric displacements to the nine elastic strains and three electric fields. In even the most anisotropic crystal structure, only 45 of the 144 material constants are different. For many systems, crystal symmetries further reduce the number of different constants. Meeker (1972) points out that for piezoelectric transducers general symmetries reduce the number of constants to 18 different piezoelectric constants and six different dielectric constants.

The thickness mode transducer is relatively simple since only the variables related to a single axis (in the thickness direction) are utilized. The equivalent circuit of a thickness mode piezoelectric transducer is shown in fig. 5.4. The circuit for a matching section, shown in fig. 5.3, is obtained by reducing the electrical/mechanical transformation ratio to zero. The equivalent circuit for the whole transducer is shown in fig. 5.5.

For the transmitting transducer, the transfer function $H_T(f)$ at frequency f is the ratio of the force $F_o(f)$ developed on the water load to the input voltage $V_i(f)$ at frequency f

$$H_T(f) = F_o(f)/V_i(f) \tag{5.1}$$

The receiving transfer function $H_R(f)$ relates the output voltage $V_o(f)$ to the force $F_i(f)$ applied by the water to the front face of the transducer:

$$H_R(f) = V_o(f)/F_i(f) \tag{5.2}$$

Attenuation of the pressure waves is neglected and the overall transduction transfer function is obtained:

$$H(f) = H_T(f)\ H_R(f)$$

$$= V_o(f)/V_i(f) \tag{5.3}$$

Straight forward mesh analysis or ladder circuit reduction techniques can be employed to evaluate the transfer functions defined by (5.1) and (5.2). When half-wave resonance of the matching section occurs, the models predict infinite impedances for the series elements. These infinite impedances are numerically and conceptually troublesome since they occur within the frequency range of interest - i.e. about the half-wave-resonant frequency of the piezoelectric section. Mason (1948, pp207-8) employs a circuit transformation suggested by Norton to obtain an equivalent circuit with finite series impedances within the frequency range of interest. Mason's circuit transformation only applies to an unbacked or symmetrically loaded piezoelectric section. Kossoff (1966) solves the problem for a general backing by introducing a negative impedance before applying Norton's transformation. Kossoff's equivalent circuit is shown in fig. 5.6. It is particularly useful for understanding series branch resonance and loading effects.

The transfer functions calculated from Kossoff's equivalent circuit and the initial circuit (fig. 5.5) are identical except at the half-wave resonant frequencies. The transfer function smoothly approaches

a single value as the frequency approaches the half-wave resonant frequency from a higher or lower frequency. The limiting value is the same as the value calculated from Kossoff's transformed equivalent circuit. Thus if very large series impedances occur, the transfer function at that frequency can be calculated by straightforward interpolation from the adjacent values, e.g. see fig. 5.7.

The transfer functions are evaluated by a ladder reduction technique applied to the T sections. Consider the transfer characteristics of the n^{th} matching section as shown in fig. 5.3. The n^{th} section is loaded by the input impedance $Z_{in_{n+1}}$ of the $n+1^{th}$ section. The n^{th} section presents a load of Z_{in_n} to the $n-1^{th}$ section. The input impedance and transfer function for that section shown in fig. 5.3 can then be calculated:

$$Z_{in_n} = W + \frac{Y(X+Z_{in_{n+1}})}{Y+X+Z_{in_{n+1}}} \tag{5.4}$$

$$H_n = \frac{YZ_{in_{n+1}}}{W(X+Y+Z_{in_{n+1}}) + Y(X+Z_{in_{n+1}})} \tag{5.5}$$

Highmore (1973) limits his analysis to symmetric T matching sections only:

$$W = X$$

$$= j Z_n \tan(k_n d_n/2) \tag{5.6}$$

$$Y = -j Z_n/\sin(k_n d_n) \tag{5.7}$$

Z_n, k_n and d_n are respectively the characteristic acoustic impedance, the wavenumber, and the thickness of the n^{th} matching section. Manipulation of (5.4)-(5.7) yields simplified characteristics for the

matching sections:

$$Z_{in_n} = jZ_n \tan\left(\frac{k_n d_n}{2}\right) + \frac{-jZ_n\{jZ_n \tan\left(\frac{k_n d_n}{2}\right) + Z_{in_{n+1}}\}}{\sin(k_n d_n)\{Z_{in_{n+1}} + jZ_n[\tan\left(\frac{k_n d_n}{2}\right) - \frac{1}{\sin(k_n d_n)}]\}} \tag{5.8}$$

The trigonometry relationship

$$\tan(\theta/2) = (1 - \cos\theta)/\sin\theta \tag{5.9}$$

is employed to reduce (5.8) to the form given by Highmore (1973):

$$Z_{in_n} = Z_n \frac{Z_{in_{n+1}} + jZ_n \tan(d_n d_n)}{Z_n + jZ_{in_{n+1}} \tan(k_n d_n)} \tag{5.10}$$

The transfer function is also readily obtained:

$$H_n = [\cos(k_n d_n) + j \frac{Z_n}{Z_{in}} \sin(k_n d_n)]^{-1} \tag{5.11}$$

(Note the typographical error in the equivalent equation derived by Highmore).

Highmore's method still suffers from the problem of infinite series impedances at the quarter-wave matching frequency:

$$d_n = \lambda/4 \tag{5.12}$$

$$k_n d_n = \pi/2 \tag{5.13}$$

$$|\tan(k_n d_n)| \to \infty \tag{5.14}$$

The quarter-wave resonant condition must be identified to avoid numerical problems with (5.10), i.e.

$$Z_{in_n} = Z_n^2/Z_{in_{n+1}} \tag{5.15}$$

The usual condition for a perfect quarter-wave match is obtained by equating Z_{in_n} and Z_{n-1}:

$$Z_n = (Z_{n-1}\, Z_{in_{n+1}})^{\frac{1}{2}} \qquad (5.16)$$

Highmore's ladder reduction technique is applicable to all the matching sections but not to the piezoelectric T section which is asymmetric. Also, the infinite series impedance problem can only be circumvented by testing for quarter-wave resonance and employing (5.15) in place of (5.10) when required. Note that Kossoff's (1966) matching section impedance equation also contains infinite terms at resonance.

The simple ladder reduction technique embodied in (5.4) and (5.5) is directly applicable to symmetric and asymmetric T sections. However, the series impedances become infinite at the half-wave resonances of the matching sections, but this is usually outside the frequency range of interest for the matching section. The limiting value approach gives the required results at the half-wave resonant frequencies. Exactly the same considerations apply to Highmore's symmetric T formulae at quarter-wave resonance. Thus the straight-forward ladder reduction technique is preferred to Highmore's method, since all transducer sections can be evaluated by a single routine employing (5.4) and (5.5). The effect of a very large series impedance is illustrated in fig. 5.7, in which the piezoelectric element has a half-wave resonant frequency of 2.8 MHz. The transmission transfer shows a 70 dB increase at 2.8 MHz due to numerical range problems.

Kossoff's (1966) results for matching piezoelectric ceramic transducers are readily obtained from (5.4) and (5.5). Figs 15 and 16 of Kossoff's paper seem to contain two labelling errors. The two values of k_q (the ratio of the load impedance to the impedance of the matching section) appear to have been interchanged for the PZT backed transducer transfer functions.

The effect of varying the matching section thickness was calculated for one of the PXE5 piezoelectric transducers described in section 5.2. The transducer was backed with the tungsten, araldite and rubber mixture with an aluminium powder in araldite front matching section. The results in fig. 5.8 are plotted on linear scales. They clearly show the resonances which occur as the thickness of the matching section is varied from .1 to 1.1 mm. The resonance at .3 mm thickness is due to quarter-wave matching at 2.6 MHz. Three quarter-wave resonance is evident at thicknesses of .8 to .9 mm, and 1.0 to 1.1 mm thickness. The quarter-wave resonant frequencies are .7 MHz and .87 MHz respectively with the three quarter-wave resonances at 2.1 MHz and 2.6 MHz respectively. A larger bandwidth is obtained from the transducer when the matching section resonates at a frequency higher than that at which the piezoelectric section resonates.

The thickness of the matching section was reduced until the amplitudes of the two largest resonant peaks in the transfer function were approximately equal. This occurred at thicknesses of .32 mm, .85 mm and 1.0 mm. The overall transfer function given in fig. 5.9 shows that a large third harmonic response is predicted by the simple circuit model. Kossoff (1966) points out that the high electro-mechanical coupling of the piezoelectric ceramics results in a nonintegral relationship between the fundamental and the overtone frequencies. Thus the measured third harmonic response would be different from that which is calculated from the simple model in fig. 5.5. The response is however observed in power spectrum measurements from 0 to 10 MHz shown in fig. 5.9.

The matching section .85 mm thick corresponds to the thickness employed for the transducer described in section 5.2. The results of detailed calculations of the transmission, reception and overall transfer functions are presented graphically in fig. 5.10. The peaks due to the various sections resonating at different frequencies are evident, particularly when the results are plotted on logarithmic scales.

Wells (1969, p.48) states: "Theoretical prediction of the bandwidth of a transducer is apt to be rather inaccurate, on account of the difficulties involved in estimating the various factors which control the frequency response. Therefore, it is generally better to measure the frequency response of a particular transducer by an experimental method". In the next section, a method is described for measuring the transient response of a transducer. The frequency response of a transducer is readily obtained from the measurements of the transient response.

5.4 ACOUSTIC MEASUREMENT TECHNIQUES

Having designed and constructed an ultrasonic transducer, it is necessary to measure its characteristics. The acoustic and electrical characteristics are both important. The measured electrical characteristics are examined in section 5.6.1, where they are related to methods of determining the efficiency of the transducer. The two acoustic characteristics of importance are beamwidth and bandwidth. For acoustic transmission time measurements, the beamwidth is not critical. The discussion presented in section 5.6.2 shows that the radiation is sufficiently concentrated to produce a well defined beam. The bandwidth is crucial for accurate time delay measurements. It can be measured by three different methods.

The first method of bandwidth measurement uses a standard hydrophone (or acoustic receiver) to measure the acoustic output of the transducer. The hydrophone must be accurately calibrated over the range of frequencies at which the transducer is tested. Great care is required to sense only the acoustic signal propagating by the shortest path between the transducer and the hydrophone. Multiple path propagation and standing waves cause difficulties when continuous wave, or monochromatic, measurements (these constitute the second method of bandwidth measurement) are made in water tanks of the order of size that is usually available

for testing. These difficulties can be overcome by employing bursts of acoustic radiation and turning off the receiver after the signal propagating by the shortest path is received.

Smith (1972) uses a gated oscillator in a large water tank so that the signal propagating by the shortest path between the transducer and the receiving hydrophone is separated from other signals. Gericke (1966) has devised an automatic measurement system in which a gated variable frequency, constant-amplitude oscillator is swept slowly in frequency from .3 to .12 MHz. The amplitude of the signal detected by the gated receiver is also plotted as a function of time (frequency). An interesting variation on these methods requires less equipment and displays the spectral response of a transducer on an oscilloscope CRT. This method uses the linear frequency sweep, signal multiplier and band pass filter system described in sections 4.4 and 4.5. The filter cutoff frequencies are set to reject all frequencies other than that which corresponds to propagation along the shortest path between the transducer and hydrophone. An additional advantage of this method is that the transducer radiates under approximately steady state conditions without incurring the disadvantages of conventional continuous wave excitation.

The transient performance of a transducer is often required. This can be inferred from frequency response measurements provided the phase at the various frequencies is accurately measured. Calibration of the hydrophone in terms of amplitude and phase is not simple, but it is required if the amplitude and phase of the transducer output is to be obtained. An accurately calibrated hydrophone is rarely available for the frequencies of interest in ultrasonic diagnosis. Also, the combined transfer function for a transmitting and a receiving transducer is usually required. Thus, the receiving transducer to be used in a system usually replaces the hydrophone. The acoustic transient cannot easily be

inferred from amplitude and phase measurements even when two identical transducers are used as a transmitter-receiver pair. The electrical loading on a particular transducer effectively produces two different transfer functions depending on whether the transducer receives or transmits ultrasound. It is consequently necessary to fabricate two essentially identical transducers in order to test the efficacy of a particular design. This is clearly inconvenient and is often impractical.

It is much more convenient to construct only a single transducer in order to test the efficacy of a particular design. The transducer is used for both transmission and reception. The transmitted signal is reflected back to the transducer to form a pulse-echo system. This is the basis of the third (and preferred) bandwidth measurement method. The system cannot employ continuous or slowly swept transmissions since the transducer would be transmitting and receiving at the same time and signal gating could not be employed to separate the signals. When a short duration electrical pulse is used to excite the transducer, the transmission-reception transient response of the transducer is represented by the waveform of the first echo received. The spectral response, and hence the bandwidth is inferred from the transient response.

The pulse-echo testing method was used to test each transducer design. A block diagram of the measurement system is shown in fig. 5.11(a). A Tektronix type 111 pre-trigger pulse generator and type 1S1 sampling unit are the essential components in the system. The sampling unit is operated in a delayed time base Tektronix oscilloscope.

The test transducer is clamped so that the front radiating face is just under the surface of the water in the tank. The vertically directed transducer beam is reflected from a 22.2 mm thick glass plate at the bottom of the tank. The echo received from the top of the glass plate decays before the echo is received from the bottom of the glass plate (c.f. fig. 5.14(a)). The preamplifier limits at ±1 V output which is the maximum allowable input to the sampling unit. The preamplifier takes some time

to recover from the excitation pulse. However, the echoes are received after the recovery is complete.

The pre-trigger pulse generator produces a -10 V pulse of 20 ns duration which has a power spectrum flat within .6 dB up to 10 MHz. The pulse is attenuated by 30 dB and input to the sampling unit. The measured pulse and its spectrum are shown in fig. 5.12. The first null in the spectrum is at 50 MHz and the spectral shape is close to the expected $|\mathrm{SINC}(f/50\ \mathrm{MHz})|$. The 1S1 sampling unit is subject to d.c. drift so an analog computer circuit is used as a high pass filter for the sampled signal. Thus the 0 Hz sample of the spectrum shown in fig. 5.12(b) is set to zero. The cut off frequency of the filter is 1.6 Hz. Thus the filter has negligible effect on the sampled waveform. The driving pulse measurements show that the transducers are excited by an almost flat spectrum over the band of frequencies of interest (1-10 MHz).

The system timing is illustrated in fig. 5.11(b). An external pulse triggers the Tektronix type 111 pre-trigger pulse generator. A pre-trigger pulse is output by the pulse generator to trigger the delayed time base. A -10 V pulse of 20 ns duration is output to the transducer 300 ns later. The transducer is shock excited by the 20 ns pulse and radiates an ultrasonic wave. About 200 μs later, the first ultrasonic echo returns to the transducer where it is converted to an electrical signal. Slightly (~1 μs) before this, the delayed time base outputs a pulse to trigger the internal voltage ramp of the 1S1 sampling unit. When the ramp voltage exceeds a reference voltage, a 300 ps sample of the signal voltage input to the sampling unit is obtained and stored. The stored voltage is output to a front panel plug and it is also displayed on the oscilloscope CRT at a "time position" proportional to the reference voltage. Each time the sampling unit is triggered, a new sample is obtained and the stored value is updated. The reference voltage is generated internally as a slow ramp by the sampling unit or is supplied

from an external source.

A transducer's transient response waveform is easily generated. Thus it is not inconvenient to obtain only one sample each time the transient is produced. To obtain all the samples of the transient waveform from a single transient would require an expensive high speed transient recorder. Since the transient waveform is produced in a repetitive manner, measurement S/N is improved by signal averaging.

5.5 AUTOMATED COMPUTER MEASUREMENTS

The Electrical Engineering Department's EAI 590 hybrid computer was used to control the sampling system described in the previous section. Plots of transducer impulse responses were first obtained using the analog computer. Later the full hybrid facility was used to acquire and digitize the impulse response waveforms. The power spectrum of the digitized waveform was computed so that the effective bandwidth of the waveform could be accurately estimated.

First the analog and then the digital sampling control systems are described in the following sub-sections.

5.5.1 Impulse Testing with the Analog Computer

The pulse-echo transient response measurement system described in section 5.4 requires two electrical inputs. The first input is a trigger pulse to the pulse generator. This is generated as a 1 kHz square wave derived from the crystal clock in the analog computer.

The second input to the sampling system is a reference voltage for the sampling unit. Recall from section 5.4 that the waveform can be sampled only after the delayed timebase, which is set manually, has triggered the sampling unit. It is here convenient to define the "time window" to be the time interval during which waveform samples are taken. The start of the time window occurs when the sampling unit is triggered,

and the end of the time window is set by the time base of the sampling unit. As the reference voltage is linearly increased from 0 V to 10 V, the waveform samples are obtained (at 1 kHz) at times which vary linearly from the beginning to the end of the time window.

The analog computer circuit shown in fig. 5.13 is used to generate the signal for the sampling unit. The integrator portion of the circuit generates the reference voltage which determines the time at which the waveform is sampled. The reference voltage varies linearly between the limits 0 and +10 V set by the two comparators. The reference voltage is also used for the X deflection of an X-Y plotter, while the comparators control the raising and lowering of the pen.

The Y deflection of the plotter is proportional to the waveform sample voltages output by the sampling unit. Thus as the reference voltage is changed from 0 to 10 V over 30 seconds, a plot of the transient response waveform is produced on the plotter. The second portion of the analog circuit removes the d.c. component of the sampled signal. The action of this filter is dependent on the frequency components of the sampled signal. With the 30 second sweep time used, the plotted waveforms did not change shape when the filter was disconnected.

The performance of the sampling system controlled by the analog computer was tested for the impulse response waveforms of an ultrasonic transducer. The results obtained are shown in fig. 5.14. Plot (a) is for a 20 μs time window and clearly shows the initial transient response followed by multiple echoes originating from the rear surface of the glass block. Notice that the echoes are distinct, and that a slight time drift is discernible between the two successive plots shown (in the 10-20 μs interval). In plot (b), the time scale has been expanded (0-5 μs) to show the time drifts soon after switching on the equipment. The six responses plotted in (b) are shifted relative to each other over a .2 μs range. Thus the time drift has occurred in the delayed timebase rather

than in the sampling unit. The drift in the delayed time base was not discernible after one hour of operation.

The plot in fig. 5.14(c) illustrates the effect of harmonics on the impulse response. The "raggy" waveform was obtained when the transducer was directed normal to the glass block. The transducer was then tilted away from the normal so that beam of the "third" harmonic (6-7 MHz) echo missed the transducer after the pulse was reflected. The main lobe at 2-3 MHz was about three times wider than the third harmonic lobe and thus the echo was received by the transducer. The smooth waveform at about 2 MHz in fig. 5.14(c) was obtained by inclining the transducer to remove the third harmonic from the response. This effect was verified by the spectral calculations described in subsection 5.5.2.

5.5.2 Impulse Testing with the Hybrid Computer

Hybrid computer operation is obtained by linking the digital computer to the analog computer. The 1 kHz clock in the analog computer controls the sample timing and the digital computer sampling loop, while the digital computer calculates the required sampling time within the time window. A number proportional to the required sample time is output to a DAM (Digital-Analog Multiplier) on the analog computer. The required sampling unit reference voltage is output by the DAM. The sampled signal input to the Y deflection of the X-Y plotter (fig. 5.13) is connected to an ADC input. Thus a sample is digitized and stored in the digital computer memory. The leading edge of the 1 kHz square wave used for system control triggers the pre-trigger pulse generator. The operation sequence outlined in fig. 5.11(b) then takes place. A sample voltage is output from the sampling unit to the ADC after about 200 μs. The trailing edge of the 1 kHz square wave is used to interrupt the digital computer from a pause instruction. The digital computer then inputs the sample

voltage via the ADC and stores it in an array. The next sample time number is calculated and output to the DAM. The process is repeated until the whole of the time window has been scanned. The interrupts are then blocked and the sample time set to the beginning of the time window. The start of the time window precedes the arrival of the echo. Thus the output of 1S1 sampling unit is the d.c. drift, and this is continuously cancelled by the integrating circuit shown in fig. 5.13.

The sample array obtained is then compared with the averaged samples of the transient response waveform stored in another array. For each sample time the deviance of the new sample is calculated. The average sample value for that particular sample time is then updated. The sum of the deviances over all the sample times is proportional to the noise power The sum of the squares of the averaged sample values is proportional to the signal power. Thus the S/N for a single sample set is calculated. This is multiplied by the square root of the number of averaging runs to obtain the S/N for the averaged samples. When the S/N < 50 dB, another sample set is obtained and the S/N calculation process repeated. When the S/N $\geq$ 50 dB, the sampling process is terminated and the averaged samples of the echo waveform displayed on the computer's storage CRT.

The FFT algorithm is used to calculate the spectrum of the sampled echo waveform. The spectrum is displayed on the computer's CRT. The bandwidth of the double transducing process is then calculated from the 3 dB points of the spectrum.

The timing and voltage jitter of the sampling system introduced no significant difficulty because a complete set of sample points is successively measured. If a single sample point is measured continuously until a certain S/N is obtained then d.c. drift in the 1S1 sampling unit output is troublesome. Burrel (1971) and Allen (1972) used a voltage ramp input near the end of the sampling window so that d.c. drifts and

timing drifts could be calculated by the computer and allowed for in the computations.

Such sophisticated measurement techniques were not required for analysis of the transducer transient response waveforms. The d.c. drift is removed by the high pass filter, and the timing jitter is <.5% in the time window.

5.6 RESULTS

The measurement system described in the previous section was used to measure the transient responses of transducers. The spectral response of each transducer was calculated from the transient response, and was related to the spectra predicted by the model. In addition, measured results of transducer beamwidth and efficiency are presented. The significance of the results is discussed in subsection 5.6.2.

5.6.1 Measured Results

The transient responses of transducers numbered 6, 9, 12 and 15 (refer to Section 5.2) to a -10 V pulse of 20 ns duration are shown in fig. 5.15. The spectrum calculated from each transient response is shown adjacent to it for the two frequency ranges [0,4 MHz] and [0,10 MHz). The effect of changing the thickness of the matching section of transducer number 11 is shown in fig. 5.16. The spectrum at particular matching thicknesses is shown adjacent to the transient response from which it was calculated. The thickness of the matching section was reduced until the two peaks in the spectral response were of equal amplitude. The band width of the transducer is then a maximum.

The effect on the transient responses of inclining the beam of the transducer slightly to the glass reflector was discussed in section 5.5.1. The effect of the inclination on the spectral response of

transducer number 7 is illustrated in fig. 5.17. When the beam of the transducer is perpendicular to the reflector, the transient response in fig. 5.17(a) is measured, and the spectral response in fig. 5.17(a) is calculated. If the transducer is inclined at approximately 2^{o} to the perpendicular, the higher harmonic responses are reduced to those shown in fig. 5.17(b). The final spectral response shown in figl 5.17(b) is calculated from the transient response shown in fig. 5.17(b).

A stroboscopic Schlieren imaging system (c.f. Hunter et al. 1964) was employed to image ultrasonic pulses as they propagated away from the transducer. The photographs shown in fig. 5.18 are for gated bursts of 1.98 MHz ultrasonic pulses from transducer number 15. The transducer is the dark shape protruding into the circular image field. The transducer was excited by 1, 2, 4 and 15 cycles of drive voltage per burst to give the results shown in fig. 5.18.

The admittance characteristics for transducer number 11 were measured on an electrical bridge and plotted in fig. 5.19(a). The two plots correspond to air and water loading of the transducer. The motional admittance loops or circle diagrams drawn from these plots are shown in fig. 5.19(b).

Fig. 5.19(c) shows the admittance characteristics for transducer number 15. These were measured with a network analyser. The plots were obtained for air loading and for castor oil loading (similar to water). The circle diagrams shown in fig. 5.19(d) are deduced from these plots. The efficiency of transducer number 15 is determined from the dimensions shown on the circle diagram (c.f. Tucker and Gazey 1966, ppl52-5):

$$\eta = \frac{d_2(d_1-d_2)}{d_1(a+d_2)} \qquad (5.17)$$

$$= .26$$

The efficiency of 26% is obtained at 1.97 MHz. At other frequencies, the efficiency can be calculated from fig. 5.15(d) provided allowance is

made for the double transducing process.

The continuous power delivered to the water load at 2 MHz was obtained by measuring the power supplied to the transducer drive circuitry. When the transducer was immersed in water, the drive circuitry required 100 μW more power than when the transducer was not immersed. From fig. 5.18, the diameter of the radiating area is estimated at 8 mm. Thus the acoustic intensity (with $\eta = .25$) is approximately 50 $\mu W/cm^2$. The average power during a 2 to 3 MHz frequency sweep will be less than this figure. The efficiency of transducer number 11 is 15% at 2.04 MHz and thus the acoustic power output will be less than the 50 $\mu W/cm^2$ peak of transducer number 15.

5.6.2 Discussion of Results

The transient response measurements and the subsequent spectral calculations yield spectra which are the same as those which could, in principle, be measured by continuous wave methods. Recalling the discussion presented in section 5.4, it will be remembered that the interpretation of continuous wave measurements is complicated by the many scattered and standing waves which are unavoidably present in any practical experimental apparatus. On the other hand, time-gated transmission and reception schemes allow straight forwardly interpretable measurements. The linearly swept frequency system discussed in section 5.4 is a measurement scheme that is particularly simple to interpret, but it requires two transducers.

The waveform shown in fig. 4.14(b) is the output of the band pass filter when the linearly swept frequency system is used with two almost identical transducers, numbers 11 and 12. The envelope of the waveform shown in fig. 4.14(b) is very similar to the spectral response shown in fig. 5.15(c). The latter is calculated from the transient response of transducer number 12. A major advantage of the transient measurement technique is that the spectral response is obtained from the one straight forward measurement on a single transducer.

Four transducers, 11, 12, 13 and 14, were constructed by edge clamping piezoelectric ceramic discs (c.f. section 5.2). The responses of these four transducers are very similar. Hence the construction method produces transducers with repeatable characteristics without employing high precision fabrication (commercial transducers built with identical materials using identical manufacturing methods can have a wide variety of operational discrepancies, c.f. Posakony 1975). The piezoelectric discs had a nominal frequency of 2 MHz and the transducers were mechanically tuned to yield a bandwidth of 1.2 MHz. However, the theoretical models employed in section 5.3 are based on lossless thickness mode vibrators. Transducers numbered 5 to 9 are of the free edge type of construction (c.f. section 5.2) for which the vibration losses are low. The spectral responses measured for these low loss transducers compare favourably with the results calculated from the models. A comparison of the measured results shown in figs 5.15(a) and (b) with the calculated spectra shown in fig. 5.9 (at .85mm) confirms the validity of the computations based on the models.

The radiation characteristics of the transducers are shown in fig. 5.18. These photographs are obtained when a short intense pulse of light (.3 μs) travels through castor oil into which the acoustic beam is emitted by the ultrasonic transducer. The acoustic pressure variations within the beam also produce a change in the optical refractive index of the water. The light travelling through the beam is affected by the refractive index changes. These changes are imaged by an optical system outside the fish tank which contains the castor oil and the transducer (c.f. Meyer 1978). Since the acoustic beam is approximately conical in shape, the light path through the beam is longest at the centre of the beam. In addition, the acoustic pressure is greatest near the centre of the beam and the light-sound interaction is most intense. The relatively

intense interaction combined with the longest interaction path length produces very clear images of the central portion of the beam, especially close to the transducer. For these reasons, the edges of the beam patterns are not defined as clearly as the central portions of the beams. Hence some error is associated with the inferred beamwidths.

The beamwidths inferred from the photographed patterns shown in fig. 5.18 are $12\pm3^{\circ}$ at 2 MHz. The beamwidth calculated for a 10 mm diameter disc transducer is 10.5° at 2 MHz. A closer inspection of the patterns shown in fig. 5.18 indicates that the wave patterns originate from an aperture having a diameter of approximately 8 mm. The acoustic wave patterns shown in fig. 5.18 are generated by edge clamped disc transducers. Recall from section 5.2 that the aperture in the brass case is 8 mm for the edge clamped disc transducers. The calculated beamwidth for an 8 mm diameter aperture is 13° at 2 MHz. Thus there is good agreement between the observed and calculated beamwidths.

The radiated acoustic power levels required for the hyperbolic phase encoded system are very low. Hill (1968) measured a peak output of 100 W/cm^2 for the most intense medical diagnostic equipment included in his survey. The peak output from the transducers driven by the phase encoding equipment is 50 $\mu W/cm^2$, some 60 dB less than the maximum level reported by Hill. The hyperbolic phase encoded system changes the signal frequency from 1.7 to 3.8 MHz and when transducer bandwidth limitations are considered, the average acoustic intensity is about 10 $\mu W/cm^2$. Thus the average intensity is 40 dB lower than .1 W/cm^2, the average level below which no adverse biological effects have been observed (c.f. Wells 1969, p226).

MATERIAL	VELOCITY km/s±5%	MASS gm±.1%	DENSITY $*10^3$ kg/m^3 ±.6%	IMPEDANCE M Rayls±6%
Araldite Epoxy Casting Resin (5 of D20 : 1 of HY951)	2.64(2.68)	7.43	1.17	3.09(3.00)
Perspex (Lucite)	2.71(2.65)	7.59	1.20(1.2)	3.25(3.2)
Aluminium	6.25(6.30)	17.2	2.71(2.70)	17.0(17.0)
Cast Iron	4.61(4.35)	45.2	7.17(7.7)	33.1(33.5)
Steel	5.73(6.10)	48.9	7.72(7.70)	44.3(47.0)
Brass	4.24(4.70)	53.3	8.42(8.50)	35.7(40.0)
Copper	4.55(5.00)	56.2	8.87(8.90)	40.3(44.5)
Dental Plaster (2.4 plaster : 1 water)	3.20	9.65	1.52	4.87
Aluminium powder/Araldite (1.5 : 1)	2.96	10.9	1.72	5.09
Araldite/Tungsten/Rubber (35 : 24 : 1)	2.15	12.4	1.96	4.21
Dental plaster/Araldite (1.3 : 1)	3.06	10.7	1.69	5.16
Iron/Araldite (2.7 : 1)	2.33	18.1	2.85	6.65

Table 5.1 Measured properties of materials and their mixtures (mixture ratios are by weight). The bracketed numbers are the published values.

TRANS-DUCER NUMBER	PIEZO-ELECTRIC MATERIAL	NOMINAL FREQUENCY (MHz)	THICKNESS (mm)	DIAMETER (mm)	TYPE OF CONSTRUCTION	BANDWIDTH (MHz)
1	PXE5	2.0	1.0	10.0	CE II	1.2
2	PXE5	2.0	1.0	10.0	CE I	.7
3	PXE5	2.0	1.0	10.0	CE II	1.1
4	PXE5	2.0	1.0	10.0	FE III	.87
5	PXE5	2.0	1.0	10.0	FE III	.87
6	PXE5	2.0	1.0	10.0	FE II	1.05
7	PXE5	2.0	1.0	10.0	FE II	1.00
8	NAVAL II	2.2	.9	9.25	FE III	.80
9	NAVAL II	2.2	.9	9.25	FE II	.95
11	PXE5	2.0	1.0	10.0	CE II	1.16
12	PXE5	2.0	1.0	10.0	CE II	1.11
13	PXE5	2.0	1.0	10.0	CE II	1.20
14	PXE5	2.0	1.0	10.0	CE II	1.20
15	PXE5	2.0	1.0	10.0	CE I	.79
16	PXE5	2.0	1.0	10.0	CE 0	.69
21	PXE5	2.0	1.0	10.0	CE III A 8	.72
22	PXE5	2.0	1.0	10.0	CE II A 8	1.04
23	PXE5	2.0	1.0	10.0	CE I A 5	.70
24	PXE5	2.0	1.0	10.0	CE I A 5	.78
25	PXE5	2.0	1.0	10.0	CE II A 5	.90
36	PXE5	4.0	.5	5.0	CE II F	1.13
37	PXE5	4.0	.5	5.0	CE II F	1.13

Table 5.2 Construction of the experimental transducers together with their measured bandwidths. The front matching sections of all transducers are made from the aluminium powder/araldite mixture.

CE clamped edge

FE free edge

0 air backing

I 25 mm araldite epoxy resin backing block.

II 25 mm araldite, tungsten and rubber powder backing.

III 25 mm araldite and powdered rubber.

F focussed aluminium/araldite lens for the matching section.

A annular ring (2) construction for beam shaping by apodization.

8 or 5 diameter (mm) of inside disc for annular construction.

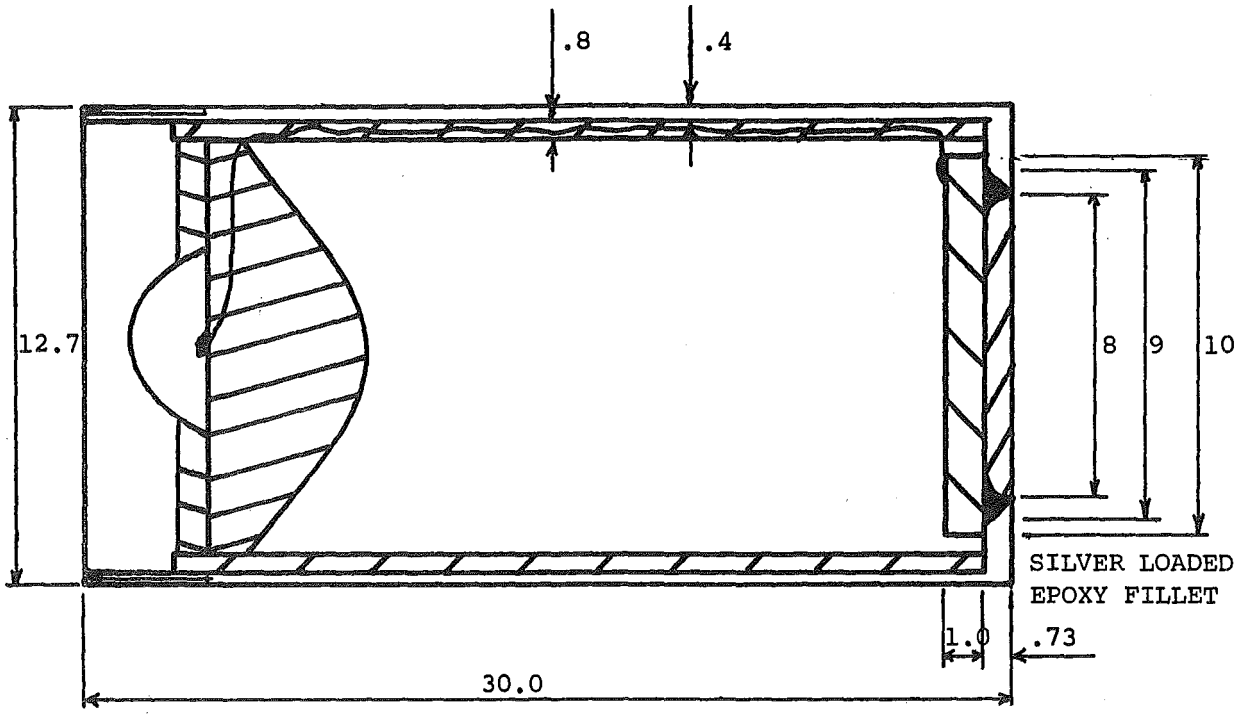

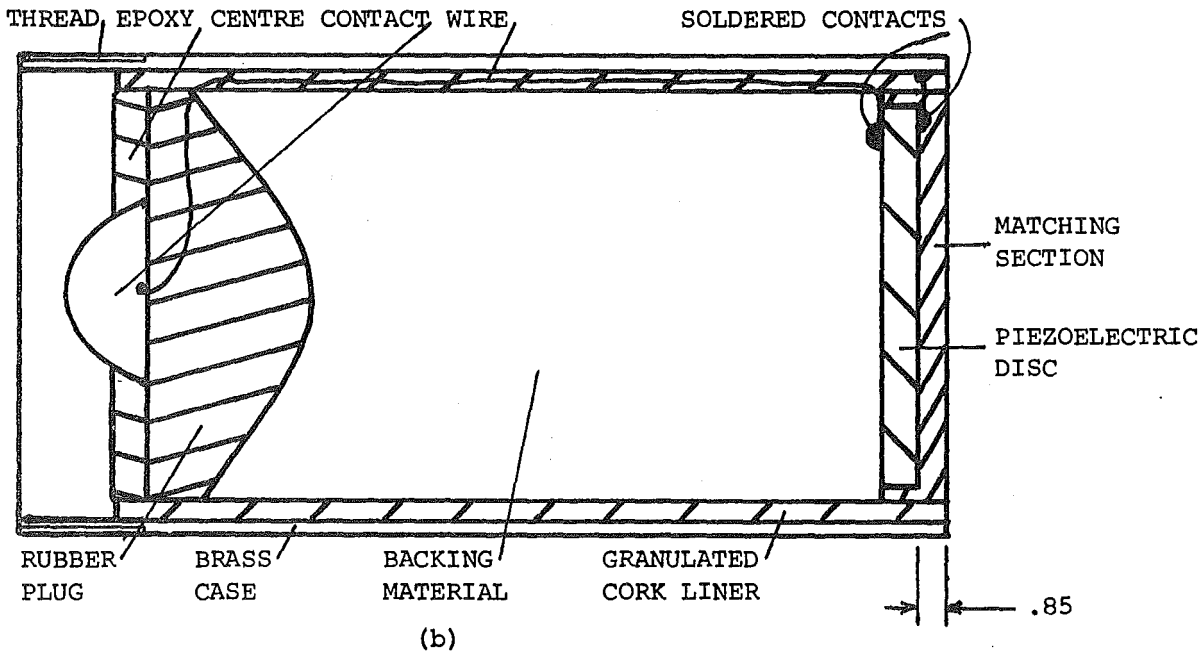

Fig. 5.1 Transducer construction details. Dimensions are in mm.

(a) Clamped edge construction. The outer edge of the front face of the piezoelectric disc is mechanically and electrically attached to the case by a fillet of silver loaded epoxy.

(b) Free edge transducer, i.e. not clamped to case.

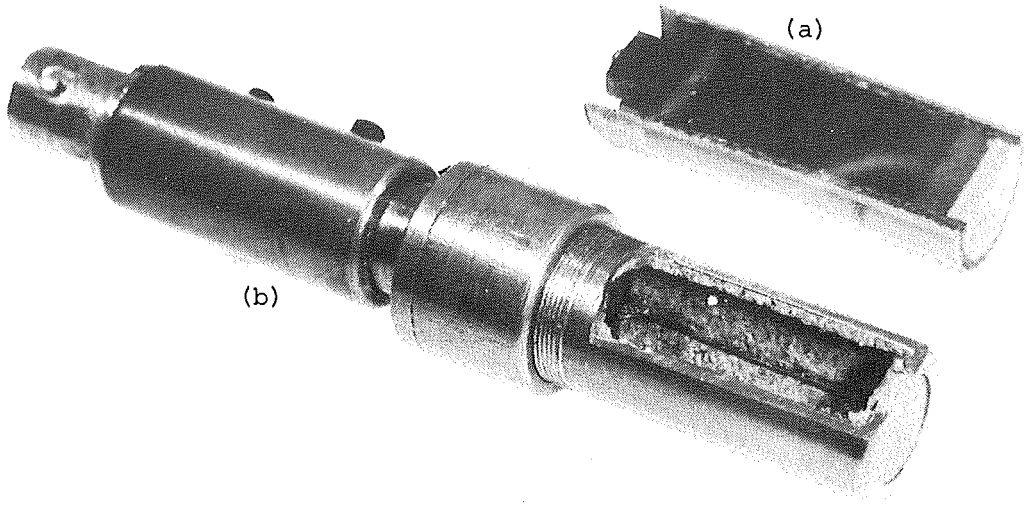

Fig. 5.2 Photographs showing the cross section details of the transducers. The upper free edge transducer (a) has a loaded epoxy backing. The lower clamped edge transducer (b) is air backed.

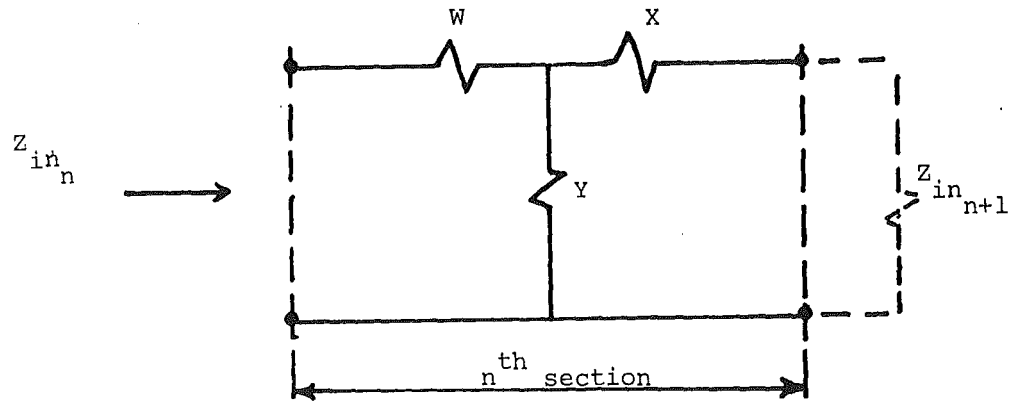

Fig. 5.3 T section model of the n^{th} transducer section. The section is terminated by $Z_{in_{n+1}}$ which is the load presented to it by the $n+1^{th}$ and following sections.

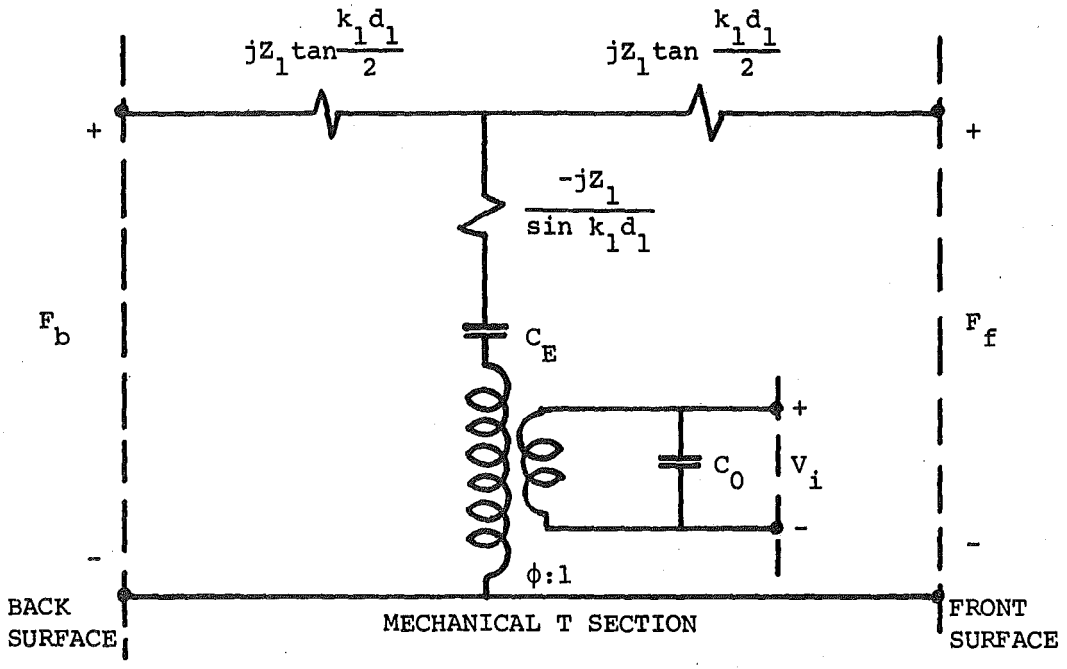

V_i	:	voltage across the piezoelectric element
F_b, F_f	:	forces at back and front surfaces
$C_0 = A\varepsilon_{33}^S/d_1$	:	clamped capacitance of the piezoelectric element
$\phi = C_0 h_{33}$	:	electrical/mechanical transformation ratio
$C_E = -C_0/\phi^2$	:	negative mechanical compliance
$Z_1 = A\rho_1 v_t^D$	:	characteristic mechanical impedance of the element
$k_1 = 2\pi/\lambda_1$	:	acoustic wavenumber in the element
ε_{33}^S	:	clamped dielectric constant of the element
A	:	area of the piezoelectric element
d_1	:	thickness of the piezoelectric element
v_t^D	:	velocity of compression wave along thickness axis
h_{33}	:	piezoelectric constant
ρ_1	:	density of section 1 (the piezoelectric element)
$\lambda_1 = v_t^D/f$	:	wavelength in section 1
f	:	frequency of the compressional wave

Fig. 5.4 The equivalent circuit of a thickness mode piezoelectric transducer.

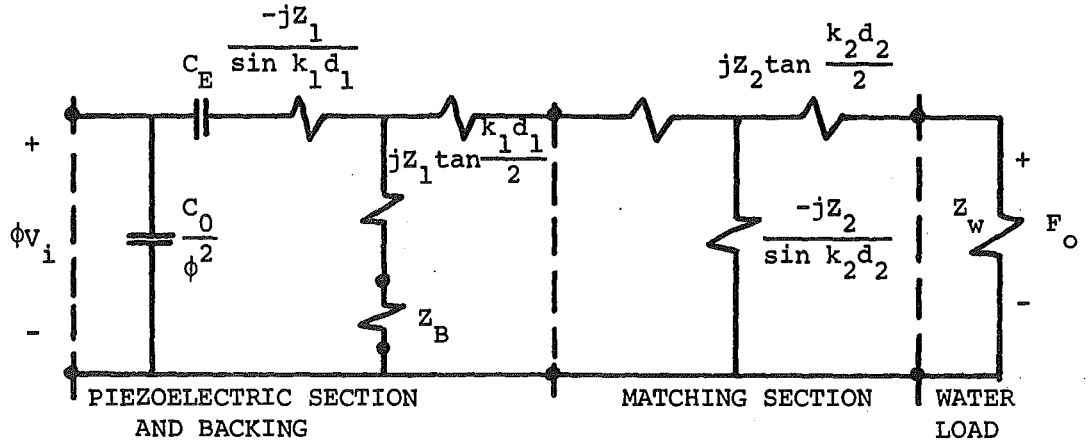

Fig. 5.5 Equivalent circuit for the backed and matched piezoelectric transducer. For the receiving circuit, the driving force is in series with Z_w and the output voltage ϕV_o developed across C_0/ϕ^2.

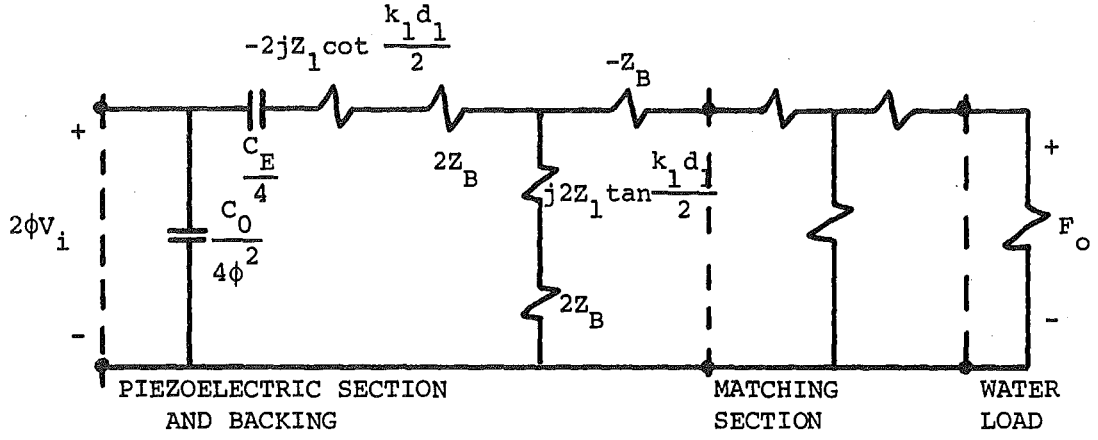

Fig. 5.6 Kossoff's equivalent circuit for the piezoelectric section and backing. Note that the series elements are infinite at integral-wave resonant frequencies, i.e. usually outside the frequency range of interest.

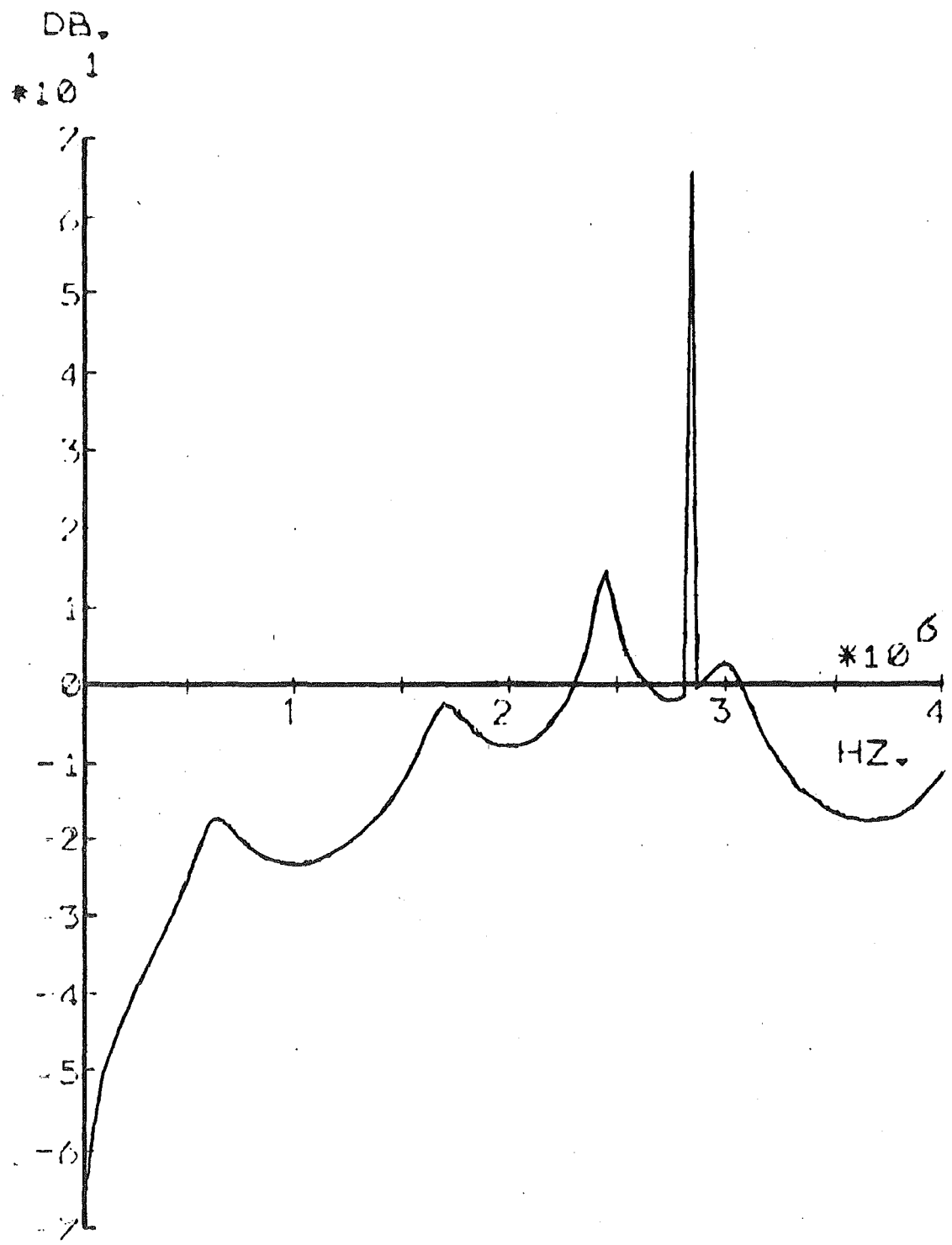

Fig. 5.7 The impedance of the piezoelectric element is infinite (or extremely large) at 2.8 MHz.

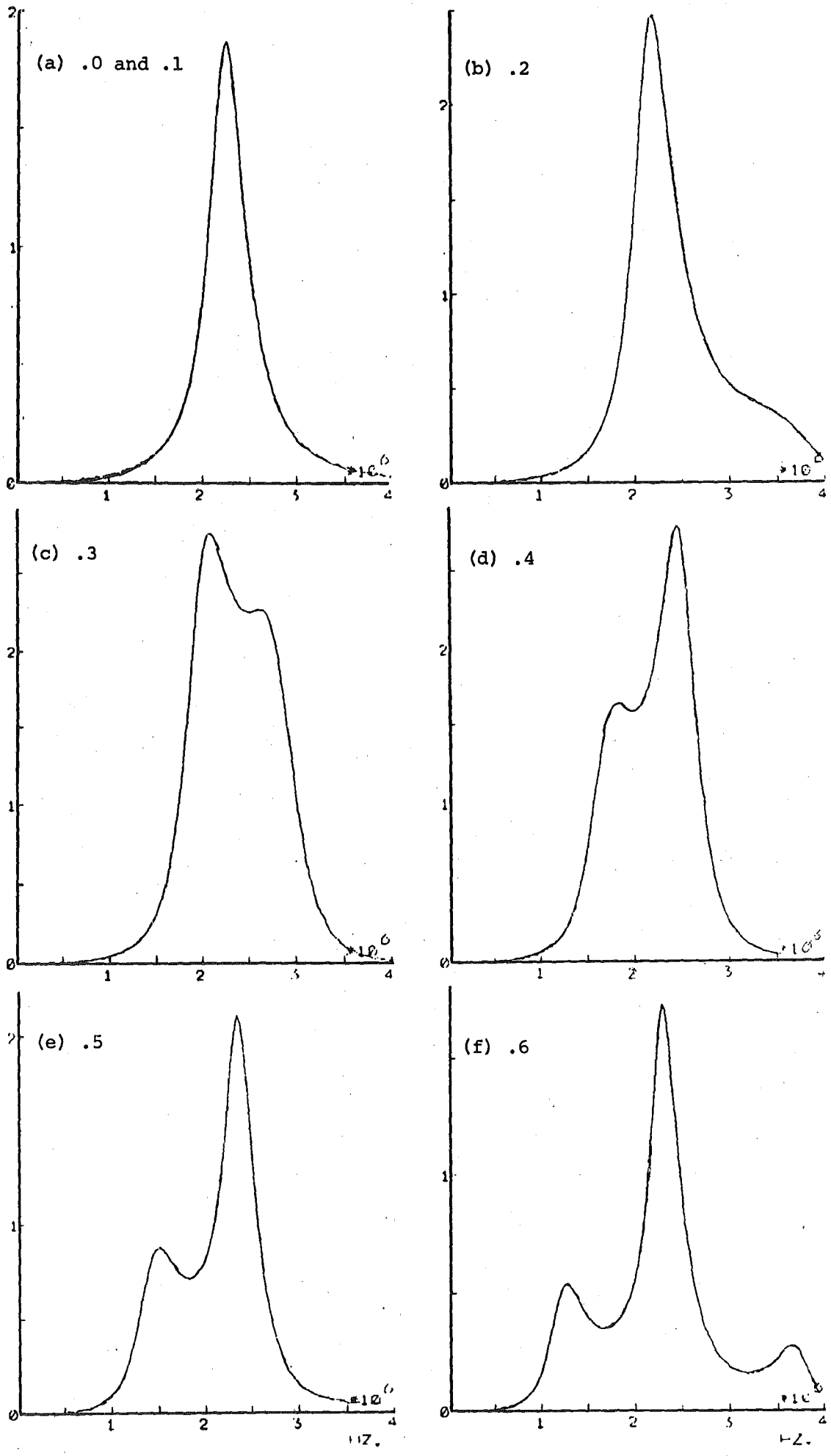

Fig. 5.8 continued over page

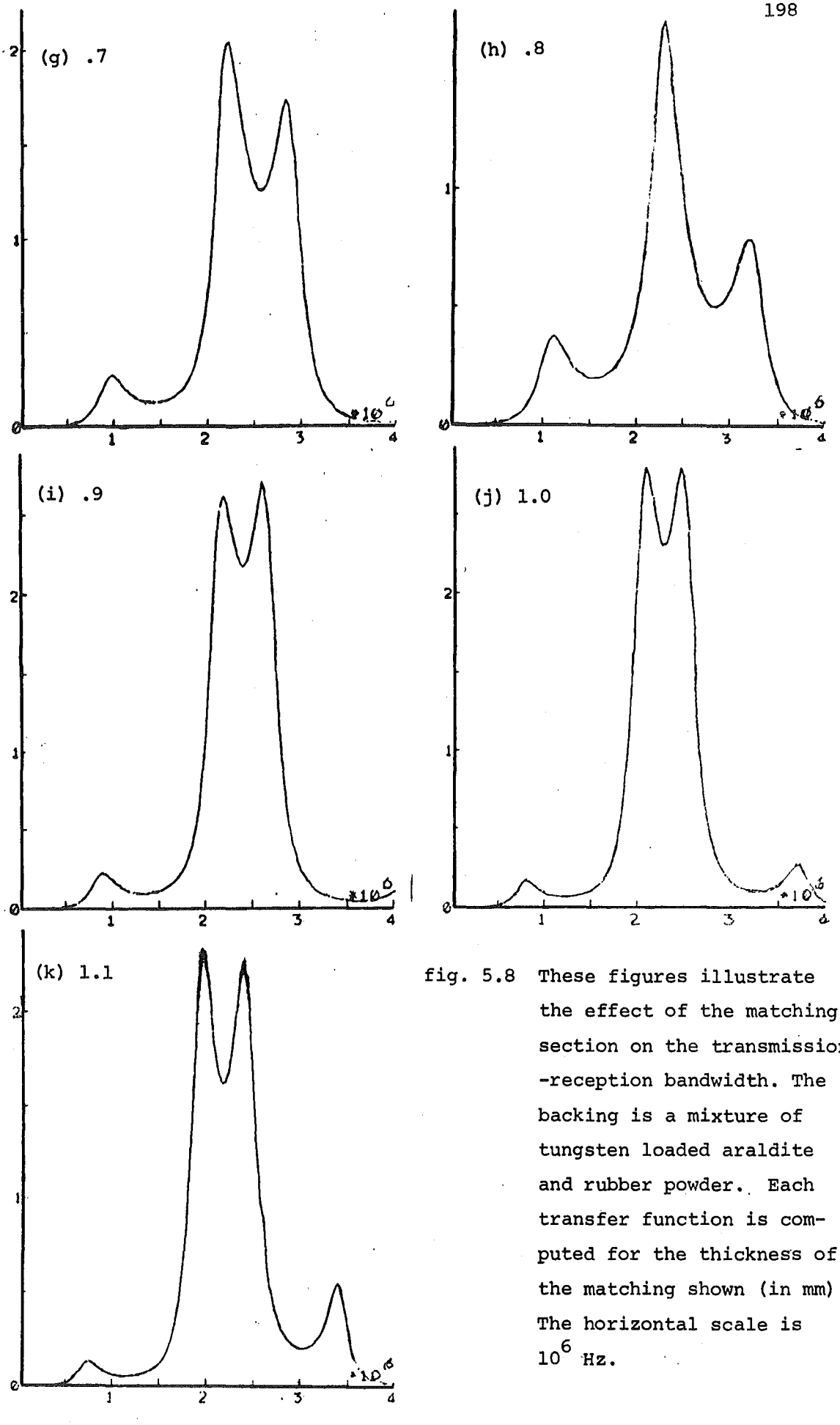

fig. 5.8 These figures illustrate the effect of the matching section on the transmission -reception bandwidth. The backing is a mixture of tungsten loaded araldite and rubber powder. Each transfer function is computed for the thickness of the matching shown (in mm). The horizontal scale is 10^6 Hz.

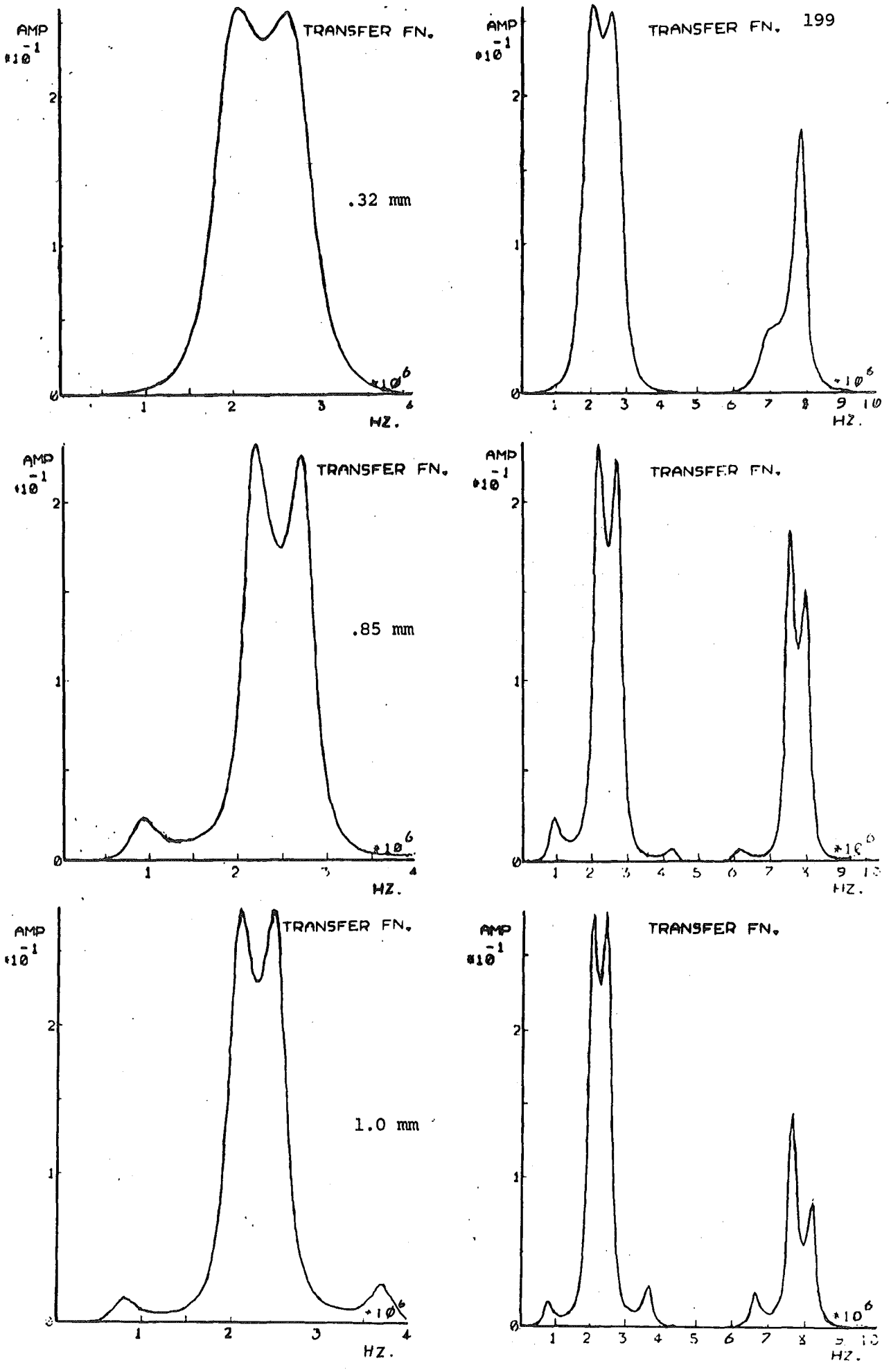

Fig. 5.9 Transducer responses calculated for the three matching section thicknesses shown. The fundamental and third harmonic responses are on the right (0-10 MHz).

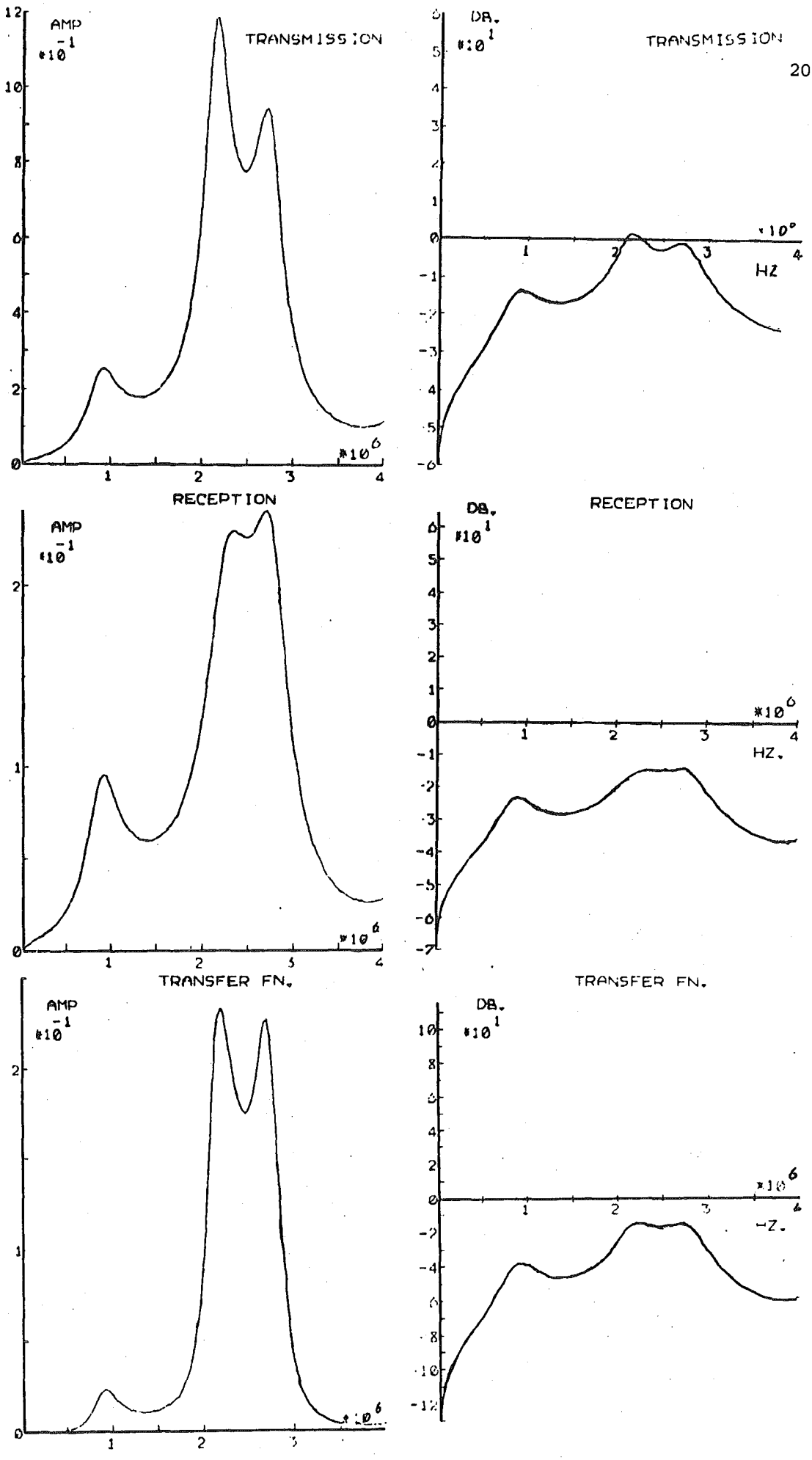

Fig. 5.10 Transmission, reception and overall transfer functions for a .85 mm matching section and a tungsten, araldite and rubber backing.

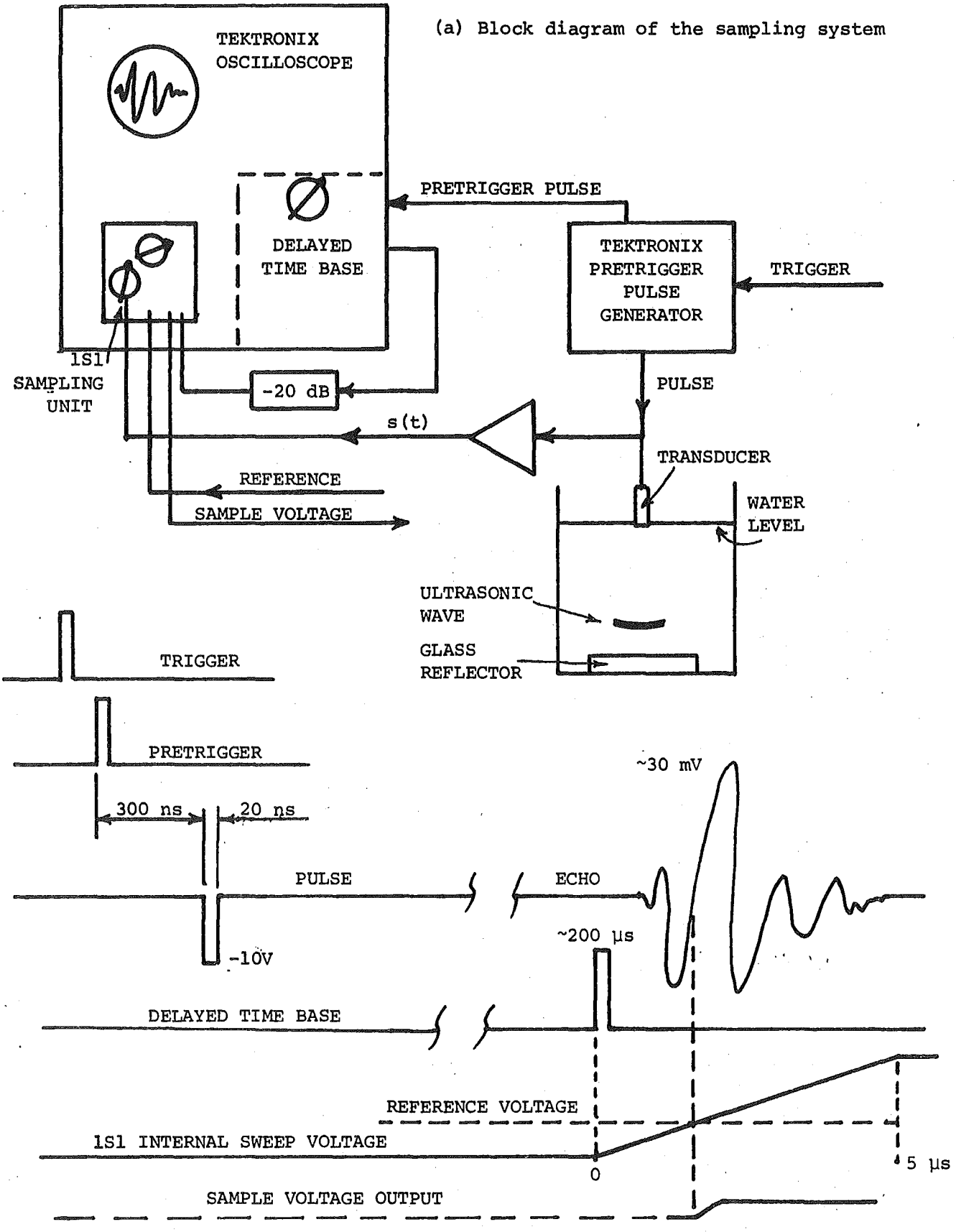

(b) Timing sequence for the sampling system.

Fig. 5.11 Apparatus and timing schematics for the high speed sampling system.

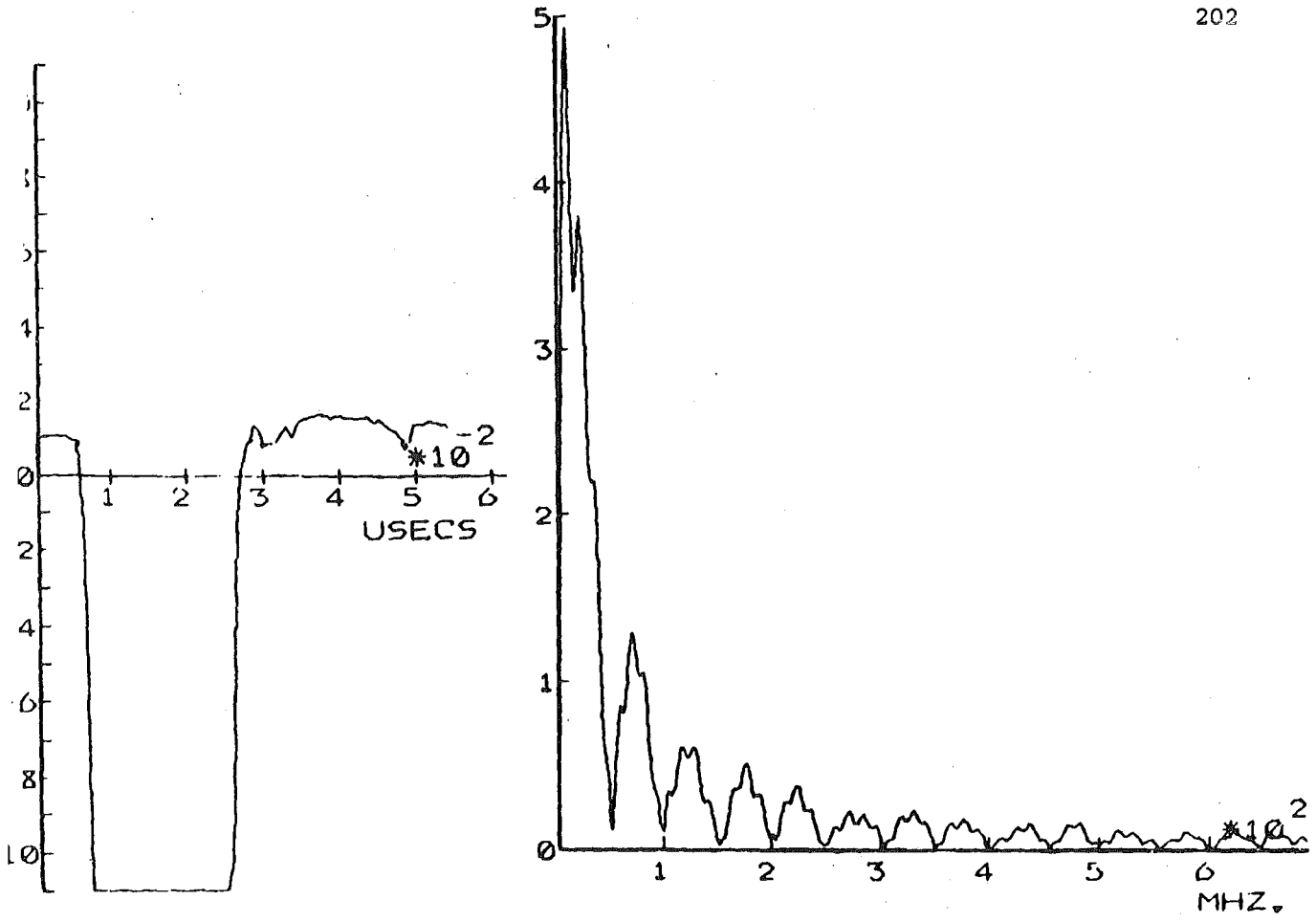

Fig. 5.12 The measured excitation pulse and its spectrum up to 700 MHz.

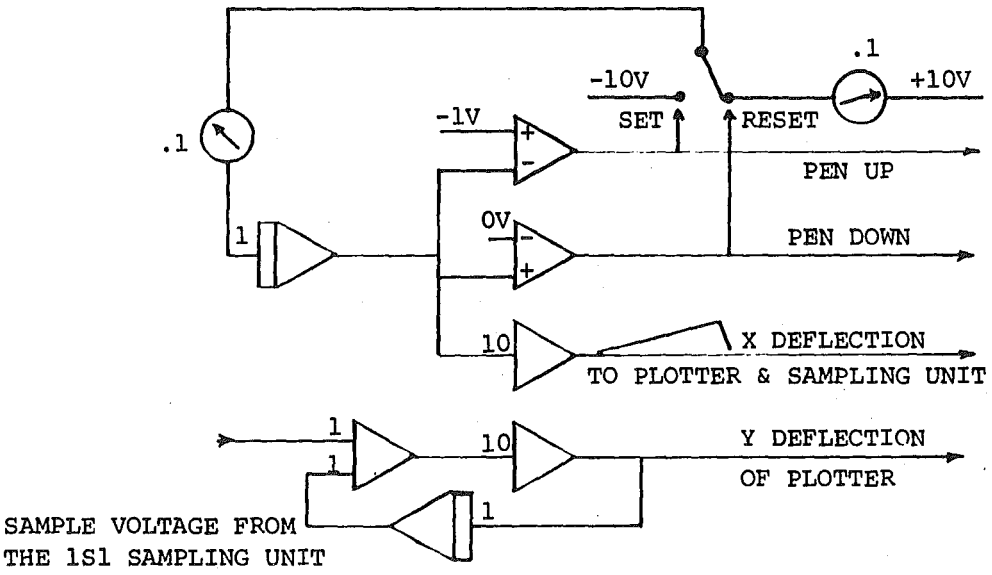

Fig. 5.13 Analog computer circuit to generate deflection voltages for the X-Y plotter and the sampling unit.

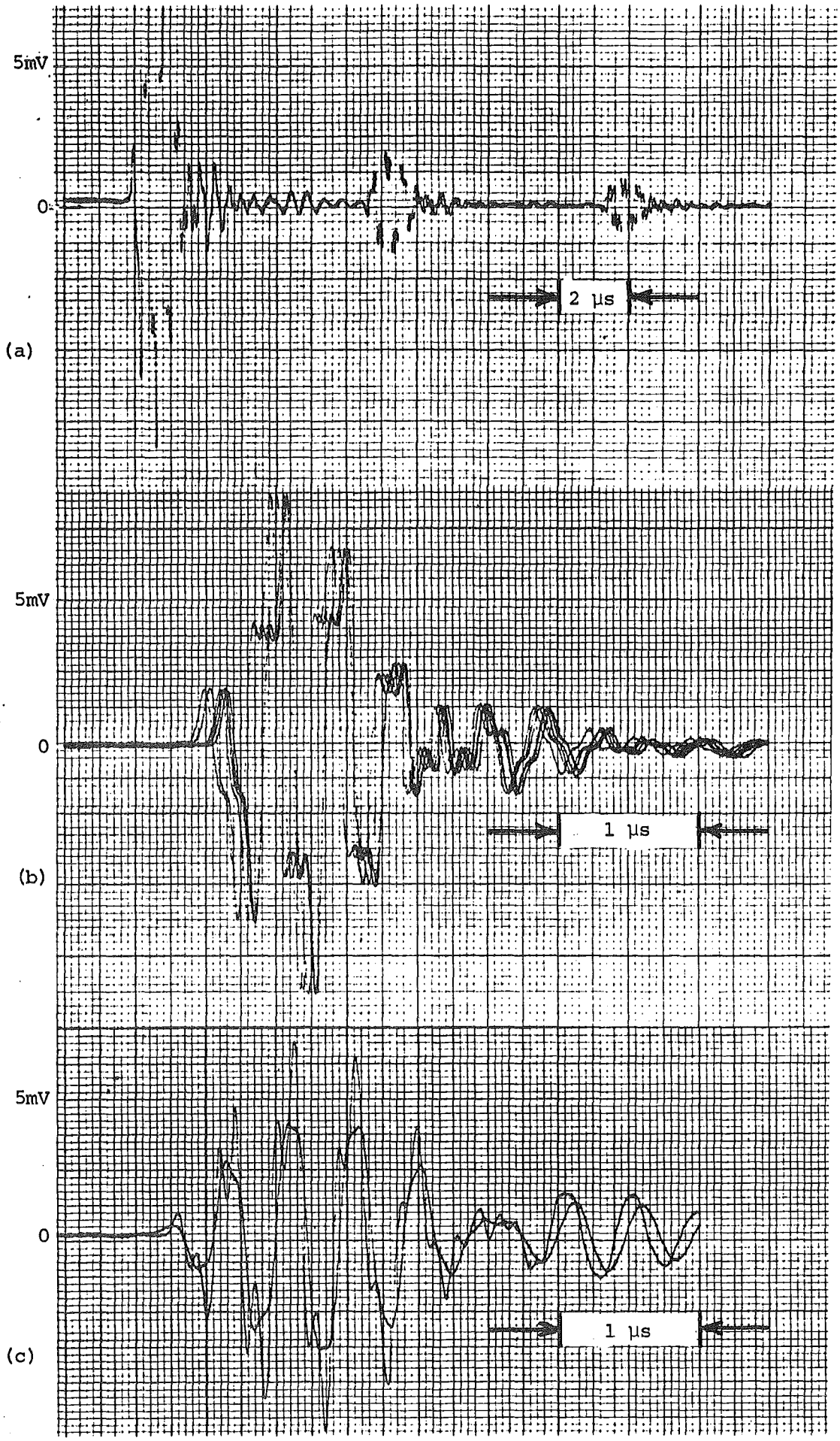

Fig. 5.14 Results of testing transducer number 7 with circuits in figs. 5.11 & 13
(a) Showing the timing drift in the 1S1 time base.
(b) Showing the timing drift in the delayed time base.
(c) Responses when the transducer is beamed vertically and 2^{o} off vertical.

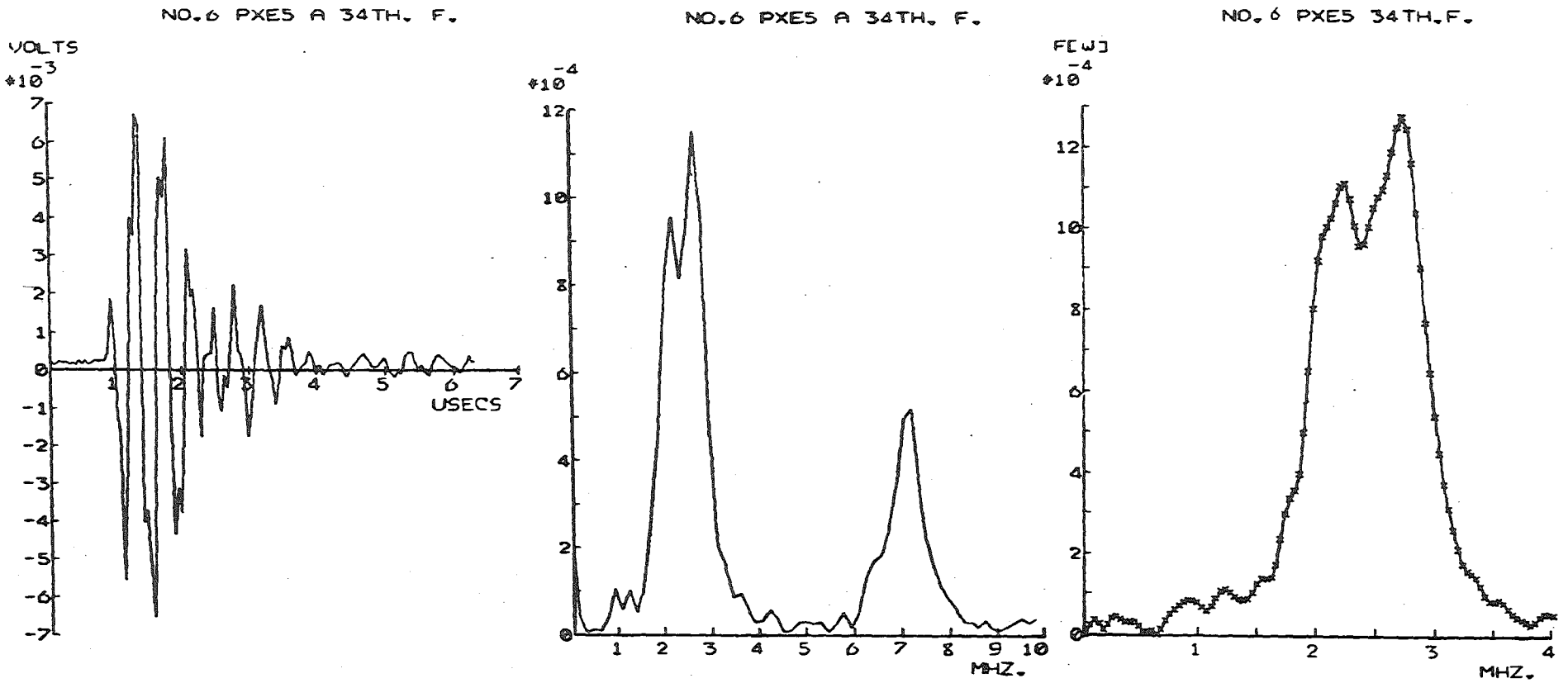

Fig. 5.15 The impulse response measured by the hybrid computer controlling the sampling system. The spectra are calculated (by the FFT) from the measured impulse response.
(a) Response of free edge type transducer, .86 mm matching section.

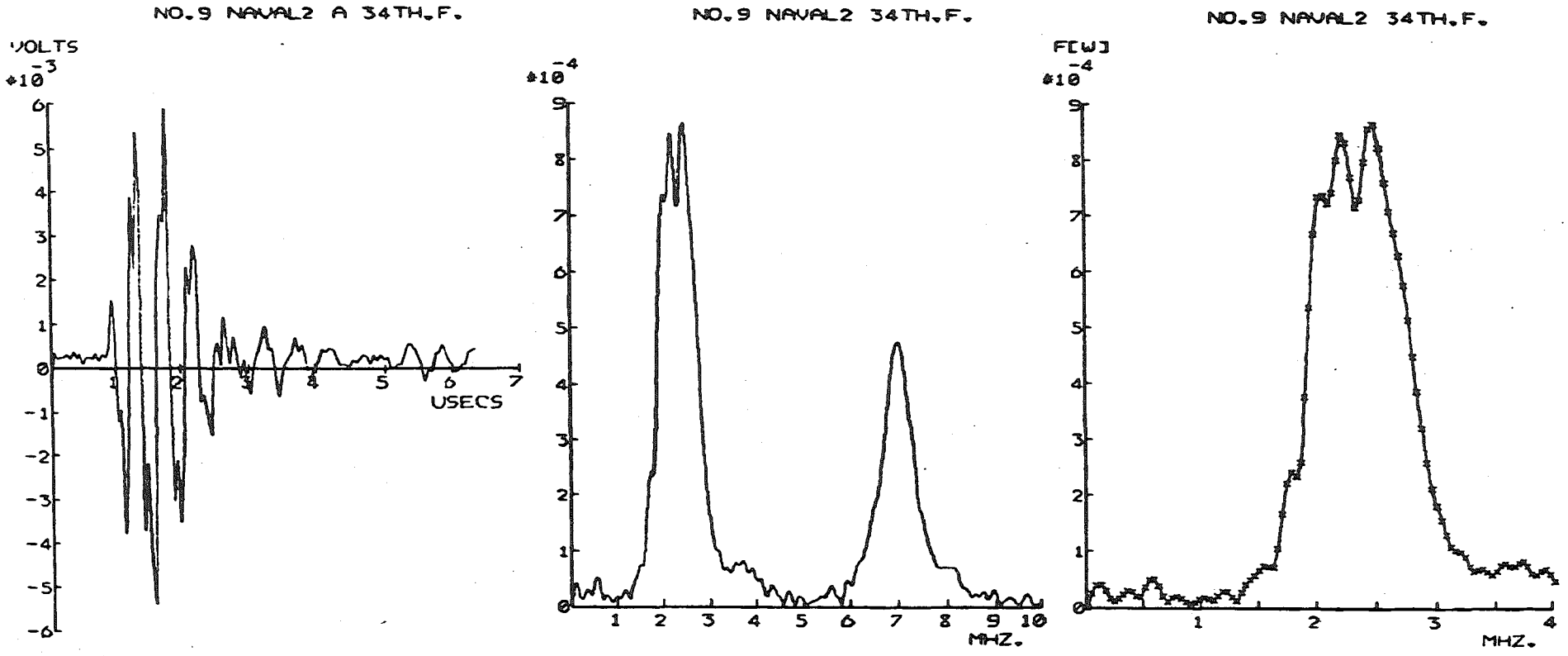

Fig. 5.15(b) This is the same as for (a) except a NAVAL2 piezoelectric disc has been used in place of the PXE5 disc.

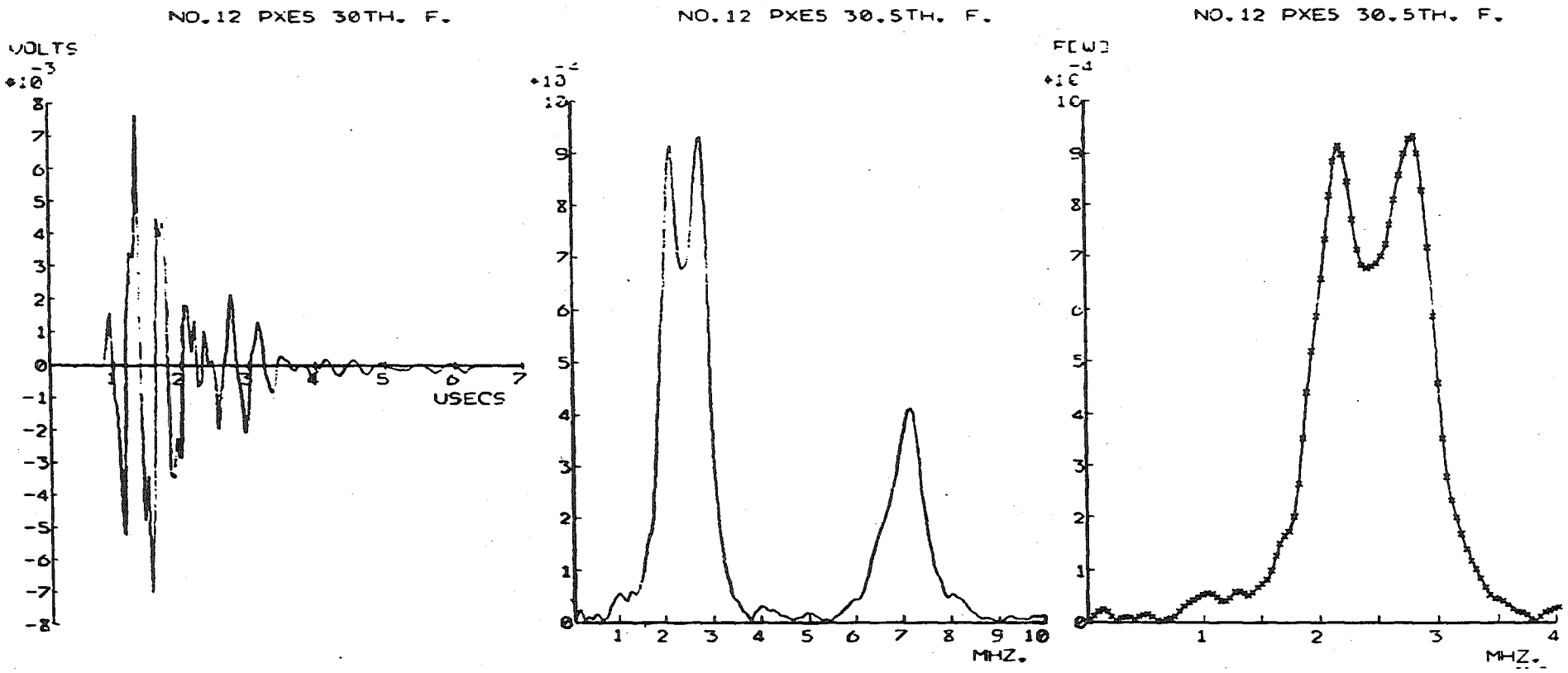

Fig. 5.15(c) Impulse and spectral responses of an edge clamped type of transducer. Transducer number 12 is backed with an araldite, tungsten and rubber powder mixture. The araldite and aluminium powder matching section is .77 mm thick.

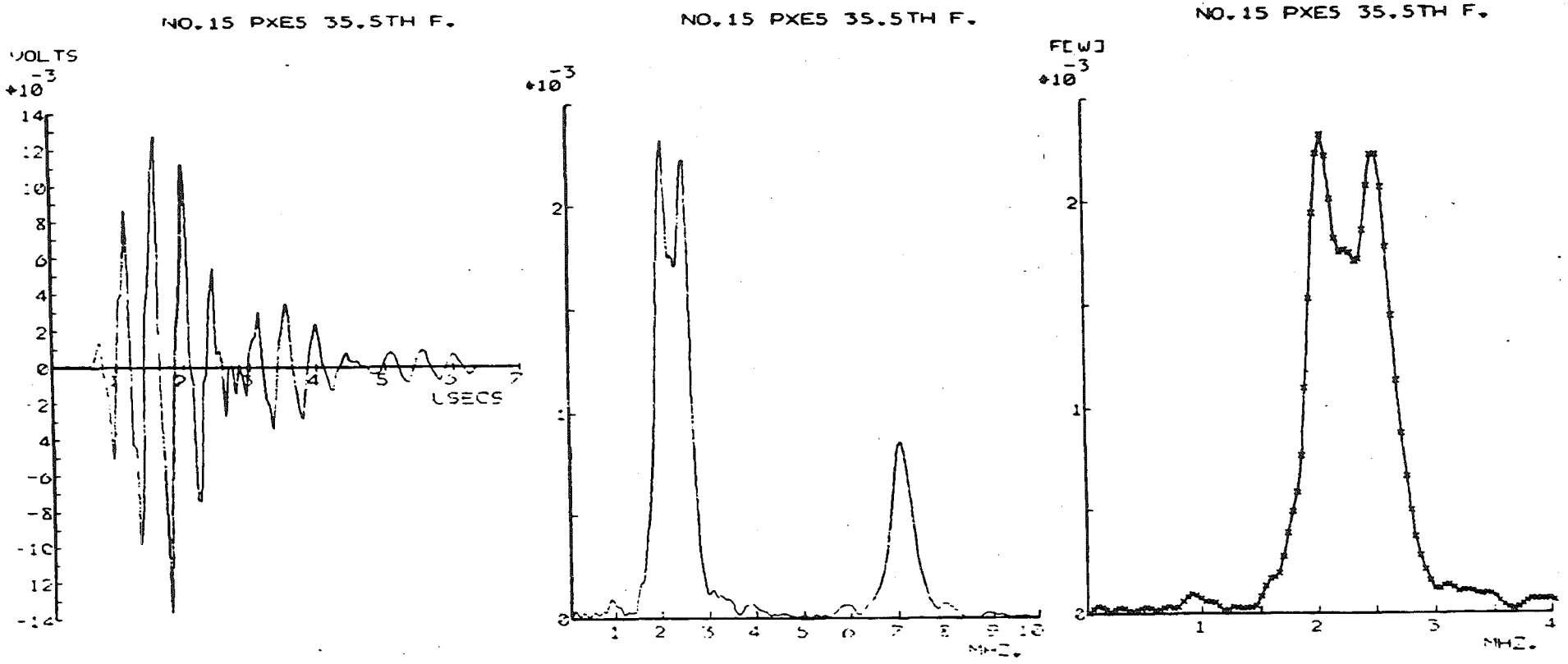

Fig. 5.15(d) Impulse and spectral responses of an araldite backed, edge clamped PXE5 transducer. The araldite and aluminium powder matching section is .90 mm (.0355") thick.

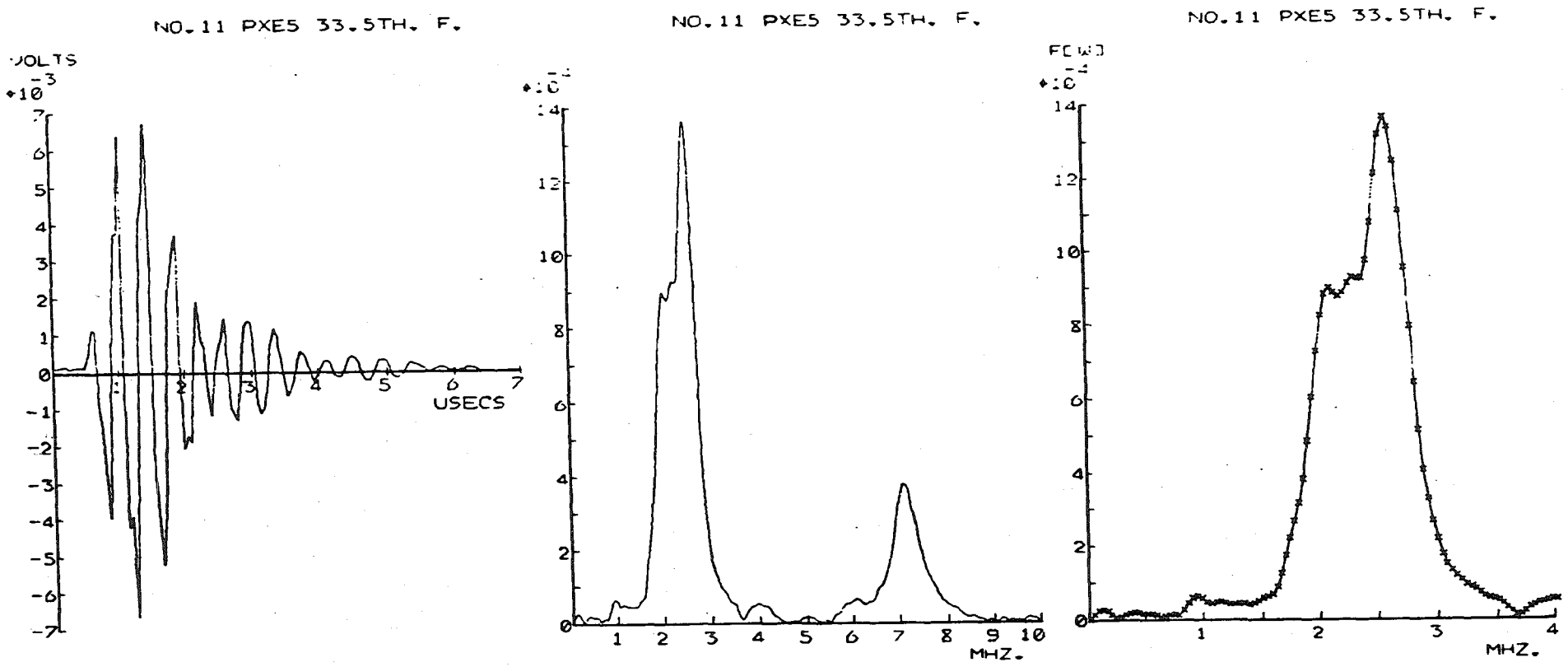

Fig. 5.16 Showing the effect of the matching section thickness on the measured impulse and frequency responses for transducer number 11. The thickness is: (a) .85 mm(.0335").

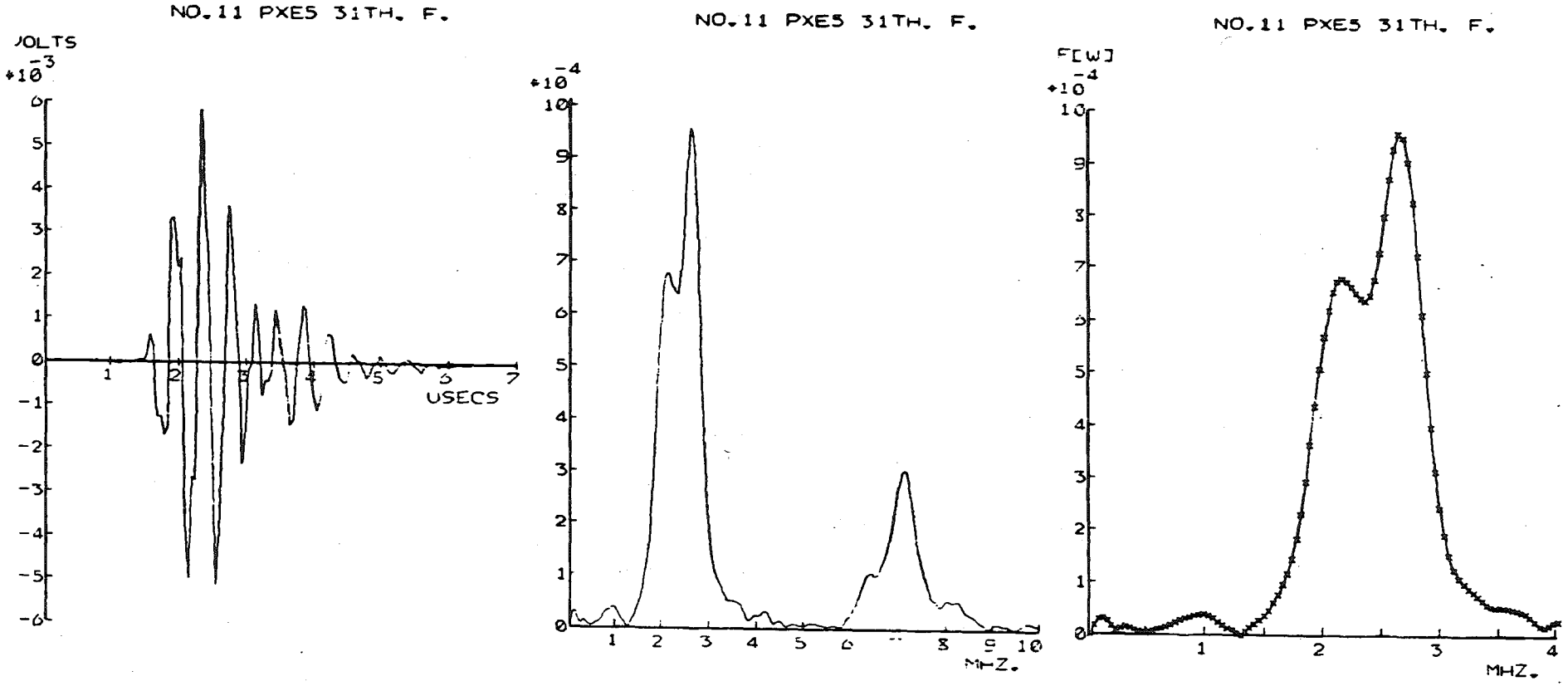

Fig. 5.16(b) .79 mm (.031")

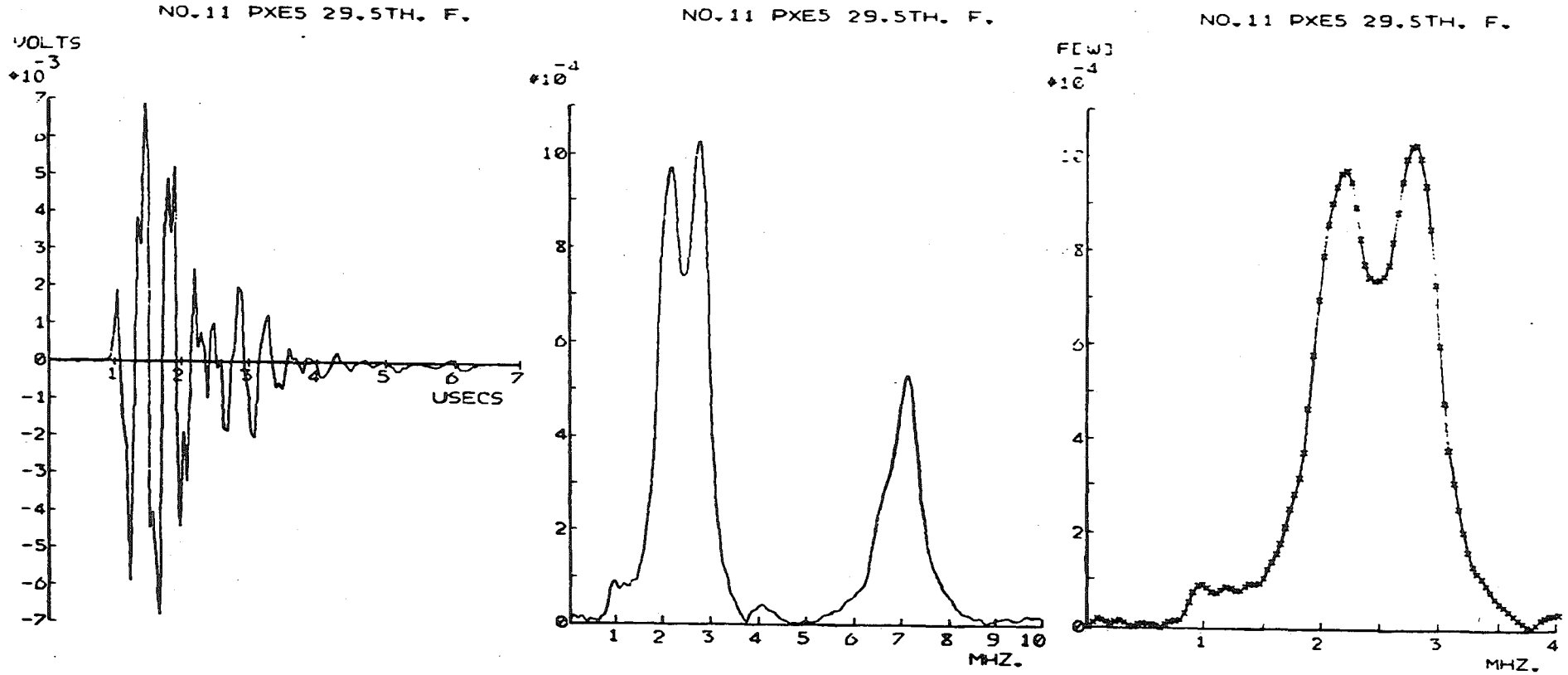

Fig. 5.16(c) .75 mm (.0295")

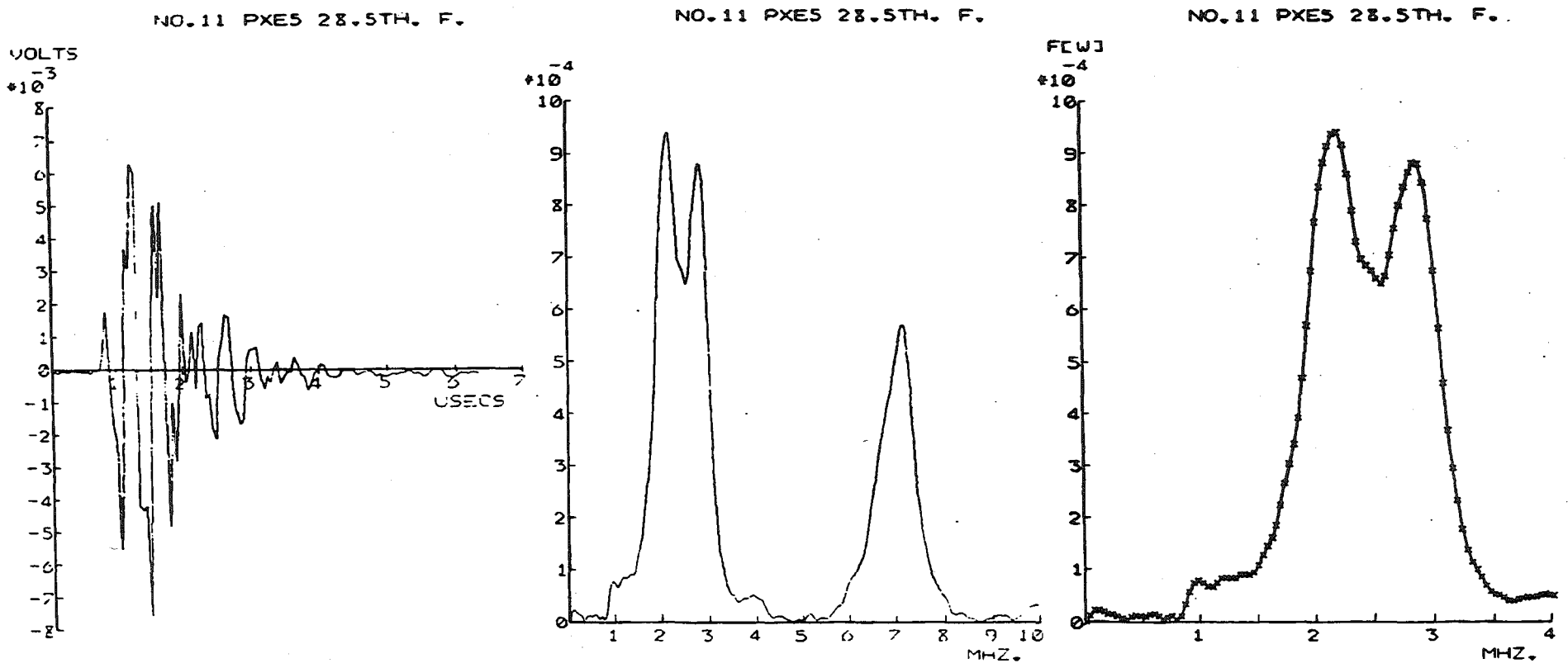

Fig. 5.16(d) .73 mm (.0285")

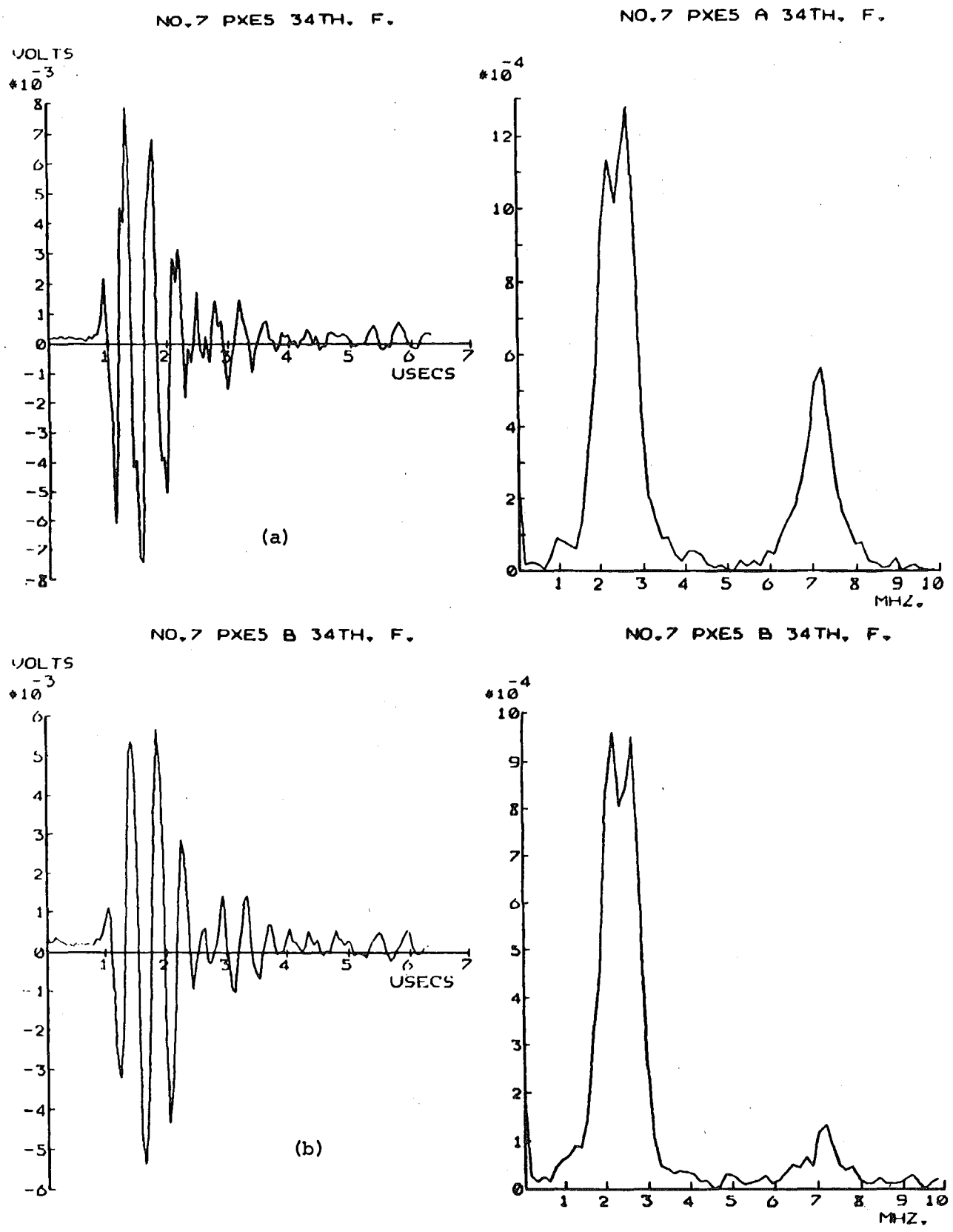

Fig. 5.17 Measurements to show that the third harmonic produces the raggy response wave form. The transducer is inclined to the glass target normal by: (a) 0° and (b) 2°. Note in fig. (b), that the third harmonic content of the signal is greatly reduced.

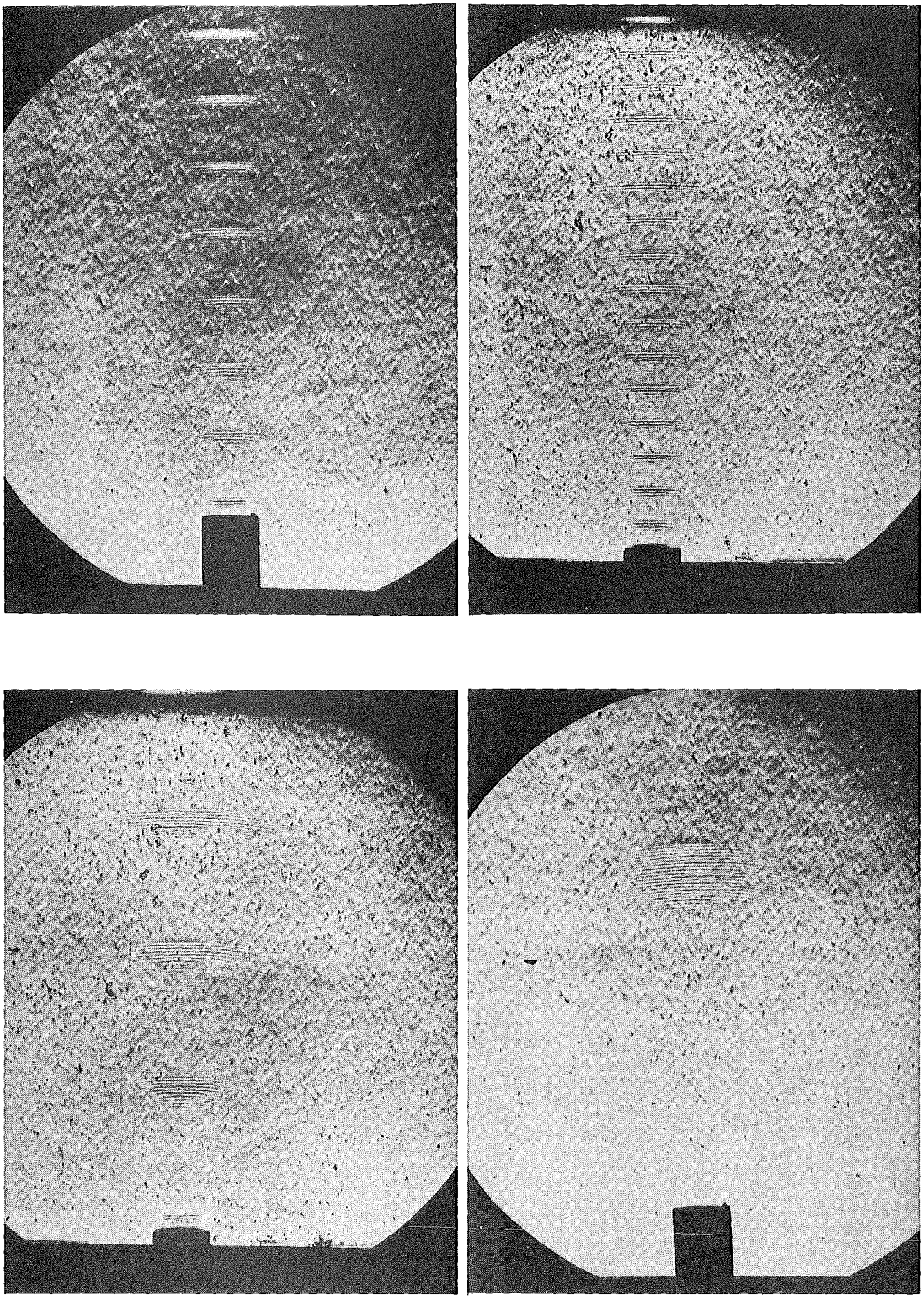

Fig. 5.18 Stroboscopic Schlieren photographs of short duration and long duration ultrasonic pulses radiated into castor oil by transducer number 15.

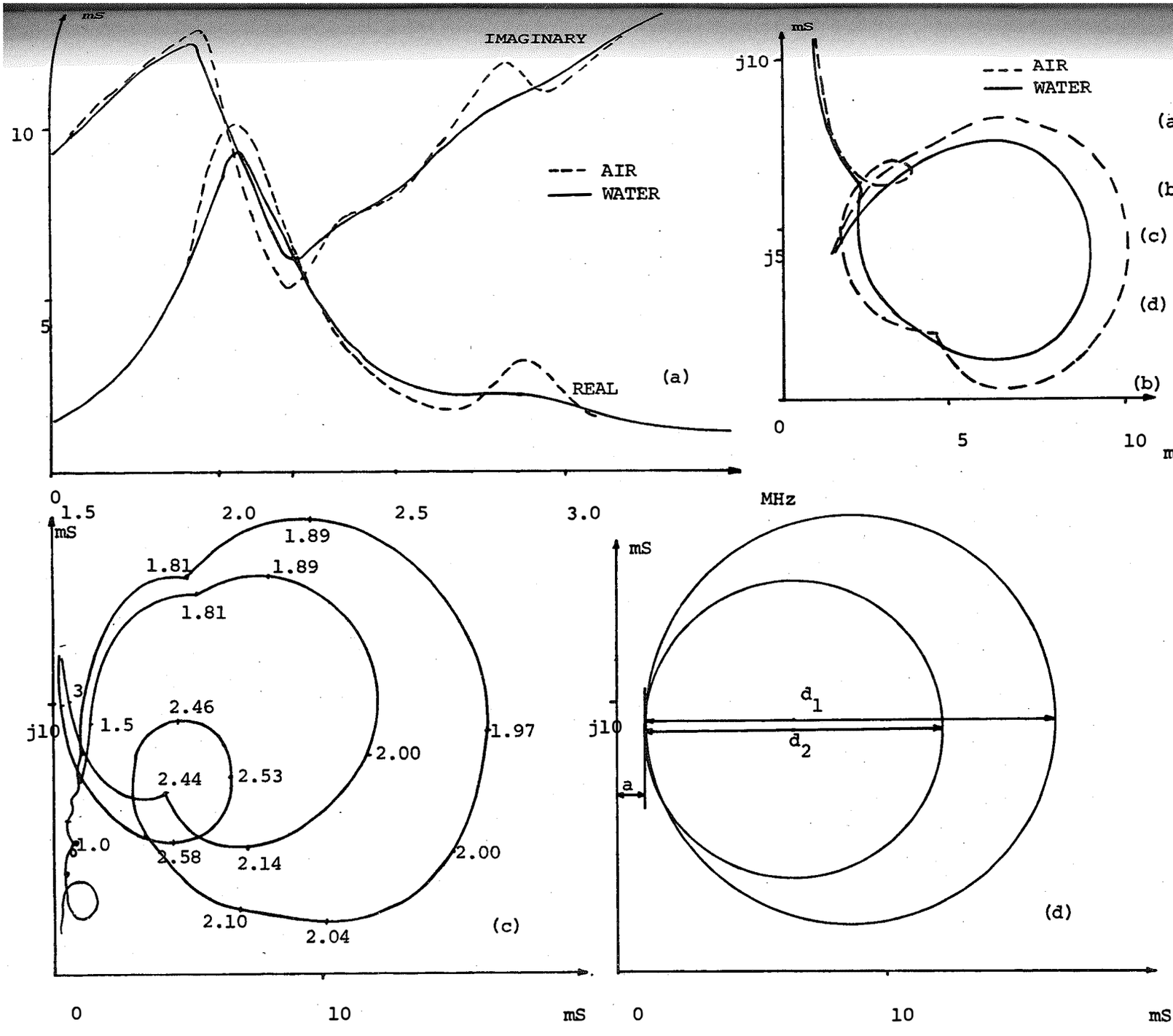

Fig. 5.19 Electrical admittance measurements.

(a) Susceptance and conductance plots for transducer number 11

(b) Circle diagram for transducer number 11

Circle diagram for transducer number 15

Schematic circle diagram for transducer number 15. The efficiency is

$$\eta = \frac{d_2(d_1 - d_2)}{d_1(a+d_2)}$$

$$= .26 \text{ at } 1.97 \text{ MHz}$$

CHAPTER SIX

EXPERIMENTAL AND COMPUTATIONAL RESULTS

6.1 REQUIREMENTS FOR SYSTEM SIMULATIONS

The central question with which the research reported in this thesis is concerned, is whether ultrasound can replace X-rays in computer assisted tomography. This chapter reports the results which the author has so far been able to obtain to support an affirmative answer to this question. A final answer can only be given after exhaustive clinical studies. Before that, many experimental studies are needed (such as those described in sections 6.4 and 6.5). However, some purely computational studies were first conducted to assess the feasibility of employing ultrasound for computed tomography.

Section 6.2 is concerned with reconstruction methods and establishing the number of measurements needed to produce an image having a prescribed resolution. The objects for which measurements have been simulated and reconstructions have been obtained are circular and square cylinders. These simple shapes may seem trivial, but the abrupt changes of velocity at their edges, and the sharp corners of the square represent critical tests for the reconstruction process.

The results of reconstructions from simulated acoustic propagation time delay measurements are reported in section 6.3. It is observed that two different images can be computed depending on whether the simulated time measurements are based on the shortest acoustic propagation time, or on the propagation time of the strongest acoustic pulse (c.f. section 3.3). Images computed from actual measurements of the shortest time for acoustic propagation through various phantoms are presented in section 6.4. In section 6.5, the computed images are based on measurements of the propagation time of the largest received pulse. The computational and experimental results are discussed in section 6.6.

6.2 STRAIGHT RAY PATH COMPUTATIONS

As was explained in sections 2.2 and 2.3, the great success of X-ray computed tomography is due in large part to the fact that X-rays travel in straight lines. This section is concerned with simulating the results which would be obtained if acoustic propagation occurred along straight ray paths. While such a simulation is non-physical, it is extremely useful in determining the ideal result obtainable from a set of measurements. The changes in the acoustic time delay are calculated to obtain an acoustic time delay projection (c.f. section 3.3).

$$\tilde{f}(\xi,\phi) = \int_{-\infty}^{\infty} \left(\frac{1}{V_w} - \frac{1}{V(x,y)}\right) d\eta' \qquad (6.1)$$

where (6.1) is obtained by combining (3.54) and (4.1). For straight ray paths, the integration path is a straight line parallel to the axis - implying that the calculation of the simulated measurement is straightforward.

An extremely useful feature of straight ray path calculations is that complicated objects may be built up by superimposing simple shapes. The projections for the complicated shapes are obtained by summing the corresponding projections of each simple shape, i.e.

$$\tilde{f}(\xi,\phi) = \sum_i \tilde{f}_i(\xi,\phi) \qquad (6.2)$$

where $\tilde{f}_i(\xi,\phi)$ represents the projection at angle ϕ of the i^{th} simple shape. Thus the linear processing involved in computing an image yields a final image which consists of the superimposed images of the simple shapes.

In this section, the results are divided into two groups depending on the symmetry of the shape of the object. The first group is comprised of circularly symmetric objects and the second group consists of non-

circularly symmetric objects. The accuracy of the reconstructed image of a circularly symmetric object depends on both the position of the object with respect to the centre of the scanning space and on which reconstruction method is used.

For the Fourier transform method of image reconstruction, the images are computed from (2.20) and (2.21):

$$\omega(x,y) = \mathcal{F}^{-1}_{\alpha,\beta}\{\Omega(\alpha,\beta)\} \tag{6.3}$$

where

$$\Omega(\alpha,\beta) \leftarrow \Lambda(\rho,\phi) = \mathcal{F}_{\xi}\{\tilde{f}(\xi,\phi)\} \tag{6.4}$$

Linear interpolation is used to form $\Omega(\alpha,\beta)$ from $\Lambda(\rho,\phi)$, which is calculated along radial lines at angles ϕ_i. Recall that M projections are measured at angles ϕ_i from 0 to ϕ_M, where $\phi_i = (i-1)\pi/M$. The Fourier transforms in (6.3) and (6.4) are evaluated by means of the FFT algorithm. The reconstruction process enhances the high spatial frequencies and also increases the effect of measurement and computation artefacts (c.f. section 2.3). A data window is applied to $\Omega(\alpha,\beta)$ to limit the high spatial frequencies. The particular data window which is used results in -50 dB sidelobe levels in the image domain (c.f. Prabhu et al. 1975).

Simulated straight ray path propagation delay times were calculated for a circular object centred on the centre of the scanning plane (c.f. section 3.1). Note that a circularly symmetric object is completely characterised by a single projection. The acoustic velocity is constant throughout the object. The images computed from the simulated projection are shown in fig. 6.1. Perspective views of these images are shown in fig. 6.2. The image computed by applying the FFT and the data window described in the last paragraph is shown in figs. 6.1(b) and 6.2(b). Figs. 6.1(a) and 6.2(a) show the image computed from the simulated projection

using the FFT but not the data window. The effect of the data window is most noticeable when the perspective image shown in fig. 6.2(b) is compared with that shown in fig. 6.2(a). Fig. 6.2(d) is a perspective grid presentation of fig. 6.2(b). When the same simulated projection is processed by the modified backprojection method, the computer images have the forms shown in fig. 6.1(c), for which M = 2, and in figs. 6.1(d) and 6.2(d) for which M = 30. The projections were modified by the Shepp-Logan (1974) spatial filter (c.f. section 2.3).

The differences between the Fourier and back projection reconstructed images are evident when the images shown in figs 6.1(b), 6.1(c) and 6.1(d) are compared. First compare figs 6.1(b) and 6.1(c) for which M = 2. The Fourier processing method produces a vastly superior result for the circular object in the centre of the scanning space. Because of symmetry, $\Lambda(\rho,\phi)$ is independent of ϕ and $\Omega(\alpha,\beta)$ is accurately determined by simple linear interpolation. Thus the image shown in fig. 6.1(b) is independent of M. This is not true for the modified back projection method.

When the circular object is not in the centre of the image, $|\Lambda(\rho,\phi)|$ is independent of ϕ but $\Lambda(\rho,\phi)$ is not. For a non-symmetric object, $|\Lambda(\rho,\phi)|$ is not independent of ϕ. Thus the image of an object, which is neither circularly symmetric nor centred in the scanning space, is not accurately computed unless many projections are measured. If insufficient projections are available, the linear interpolation scheme gives an inaccurate estimate of $\Omega(\alpha,\beta)$, and hence an inaccurate image.

The modified back projection method produces images which tend to be superior to the images produced by the Fourier method provided a sufficient number of projections are used. The relative accuracy of the reconstruction methods is illustrated by fig. 6.3 in which cross-sections through the centre of the images shown in figs 6.2(a), 6.2(b) and 6.2(c) are plotted. The solid line represents the actual velocity distribution in the object. Fig. 6.3 shows that the modified back projection method is also more accurate than the Fourier method. Consequently, the images

displayed in fig. 6.1 are misleading, in that they suggest that the Fourier method is superior to back projection which is only true for circularly symmetric objects centred in scanning space, i.e. for types of objects which never occur in situations of practical interest.

A non-symmetric diamond shaped object, centred at the centre of the scanning space (c.f. section 3.1) is ideal for testing the capabilities of the reconstruction algorithms for imaging sharp corners. The images shown in figs 6.4(a), 6.4(b) and 6.4(c) are computed from 30 projections of simulated acoustic time delay measurements, while the image shown in fig. 6.4(d) is computed from 90 projections. The images computed by the Fourier reconstruction method are shown in figs 6.4(a) and 6.4(b), and the perspective views of these images are shown in figs 6.5(a) and 6.5(b) respectively. The high spatial frequencies are not attenuated in the image shown in figs 6.4(a) and 6.5(a). The data window described earlier in this section was used to limit the high spatial frequencies in the image shown in figs 6.4(b) and 6.5(b). The effect of the data window is especially noticeable when fig. 6.5(a) is compared with fig. 6.5(b). The images computed by the back projection method using the Shepp-Logan spatial filter are shown in figs 6.4(c) and 6.4(d). Perspective views of these two images are shown in figs 6.5(c) and 6.5(d) respectively. Notice, from fig. 6.5(d), that the background noise, or ripple, is reduced in the computed image when the number of projections is increased. The perspective images shown in figs 6.5(e) and 6.5(f) are computed from 30 and 90 simulated projections respectively. Both images are computed by the modified back projection method using the spatial filter of Ramachandran et al. (1971). Comparisons of the perspective images shown in figs 6.5(c) and 6.5(e), for which M = 30, indicate that the Shepp-Logan spatial filter reduces the noise in the image and eliminates overshoot by slightly smoothing abrupt changes in the image.

The final set of results presented in this section is shown in fig. 6.6. The object, shown in fig. 6.6(a) is a "composite object" composed of five simple objects. The images shown in fig. 6.6 were reconstructed from 180 simulated projections, calculated at 1^{o} intervals in ϕ. The superiority of the modified back projection method (when the Shepp-Logan spatial filter is used) is evident when the image shown in fig. 6.6(c) is compared with the images shown in figs 6.6(a) and 6.6(b). The latter two images were computed by the Fourier transform method.

The results presented in this section suggest that the most accurate computational technique for reconstructing images is the modified back projection method. Of the two types of spatial filter that have been used to modify the projections, the Shepp-Logan filter is found to give better results.

6.3 CURVED RAY PATH SIMULATIONS

This section is concerned with simulations of acoustic transmission tomography with rays which obey Fermat's principle. Although diffraction effects are neglected, the ray paths often give an excellent approximation to the physical situation (c.f. Maward 1970). It is worth noting that rays are similarly useful for describing electromagnetism (c.f. James 1975, Chernov 1967).

At present, there is unfortunately no known theory for taking ray curvature into account during the image reconstruction. Recall from chapter two that the reconstruction algorithms are based on straight rays. Johnson et al. (1975) and Glover and Sharp (1977) calculate approximate ray paths for the velocity distribution in the computed image. The time differences between the propagation times along the computed ray paths, and the measured propagation times, are used to generate a new set of projections. The new set of projections is processed to produce a second

computed image. Another set of ray paths is calculated for this image and the process is repeated. Proof that this iterative method converges has yet to be published. Accordingly, in this section, although the simulated measurement values are computed using curved rays, the image computation is carried out using the straight ray reconstruction method. The purpose of this section is to illustrate the effects of this assumption.

The calculated ray paths terminate at the two transducers, i.e. at $\eta = \pm d$. Also, $V(x,y) = V_w$ for $|\eta| > d$ and so (6.1) is rewritten as

$$\tilde{f}(\xi,\phi) = \int_{-d}^{d}{}_{C} \left(\frac{1}{V_w} - \frac{1}{V(x,y)}\right) d\eta' \qquad (6.5)$$

The ray path C is chosen to minimize the value of $\tilde{f}$. The minimization is performed computationally. It is worth noting that care is needed to prevent the time required to calculate a ray path becoming excessive. Accurate time delay measurement simulations are rapidly calculated by adopting a Fibonacci search strategy (c.f. Himmelblau 1972, p42) together with the use of Snell's law to compute each trial ray path (c.f. section 3.3).

For the simulations presented in this section the simulated measurements are based on the shortest time delay for the acoustic pulse travelling between the two transducers. All calculations were carried out in single precision on an IBM 360/44. It is computationally efficient to use the FFT algorithm to compute images by the Fourier method. The high spatial frequencies in the images were attenuated by using Tukey's "interim" data window (c.f. Bergland 1969). This data window is in the form of an extended cosine-bell which smoothly attenuates the highest 10% of the spatial frequencies. The density variation in the computed image is obtained by successive character overprints on a standard line printer

(c.f. MacLeod 1970). In this section, the images are computed from simulations of 128 time delay measurements for each of the 32 projections used in the image reconstruction process.

A circular cylinder at the centre of the scanning space was the first object for which measurements were simulated. The cylinder is assumed to be surrounded with water and the time delay projections are calculated with various values of acoustic velocity assigned to the region inside the cylinder. The images computed from the calculated projections are shown in figs 6.7. Each image is normalized to have the same range of picture densities so that the range of velocities used, from 1.5 km/s to 6.0 km/s, is not evident in fig. 6.7. This allows the effects of refraction to be assessed without incurring additional processing to match the grey scales in the computed images. The images shown in fig. 6.7 show that when the velocity inside the cylinder is very different from the velocity of the surrounding water, the effects of acoustic ray curvature are most noticeable. The high velocity areas in the computed image spread into the adjacent lower velocity areas.

The diamond shaped object discussed in section 6.2 was also examined for a range of acoustic velocities from 1.5 km/s to 6.0 km/s. The images computed from the simulated measurements are shown in fig. 6.8. Notice that for the high velocity simulations, the effect of the highly curved rays is to cause the computed image to degenerate to an approximately circular shape. Perspective views of the computed images of the diamond shaped object are shown in fig. 6.9. The effects of refraction are very clear with this method of image display. The reconstructed image shown in fig. 6.9(a) is quite accurate because the acoustic velocity within the diamond shape is little different from that of water. Notice however, that there is some ripple within the image shown in fig. 6.9(a) despite the application of Tukey's "interim" data window. Also notice that as the effects on the images due to refraction increase, the ripples in the

computed images decrease. The ray curvature tends to reduce $|\partial\tilde{f}/\partial\xi|$ and so the high spatial frequencies in the image are also reduced.

The final set of results presented in this section relate to a crude model of a portion of the human anatomy. Three circular cylinders are used. A torso is represented by a water filled cylinder of 30 cm diameter. The spine is represented by a cylinder of 4 cm diameter and an acoustic velocity of 4080 m/s is allocated to this cylinder. An adjacent kidney is represented by another 4 cm diameter cylinder to which is assigned an acoustic velocity of 1566 m/s. The relative positions of the "kidney" and "spine" are shown in fig. 6.10(a), in which the outline of the torso is also shown. The transducers are always outside the torso during the simulation. The images computed from simulated straight and curved rays are shown in figs. 6.10(b) and (c) respectively. In the image shown in fig. 6.10(c), the "spine" is very blurred and has spread over the adjacent areas to the extent that the "kidney" is almost obscured. Fig. 6.10(d) is obtained by limiting to 10%, the dynamic range of the image shown in fig. 6.10(c). The "kidney" region is clearly defined in fig. 6.10(d), and the spread of the bony region is also obvious.

The results presented in this section suggest that acoustic time delay imaging is of use only when the acoustic velocity variation in a region does not exceed a few percent. Strong refraction limits the use of minimum propagation time delay measurements. However, it must be emphasised that measurements based on the propagation time of the strongest pulse (c.f. section 3.3) are useful in limiting the spread of the high velocity regions in the computed image as is made clear in sections 6.4 and 6.5.

6.4 RESULTS OBTAINED FROM IMPULSE PROPAGATION DELAY TIME MEASUREMENTS

The simulated results obtained in sections 6.2 and 6.3 are encouraging in that they suggest that useful images may be reconstructed in interesting practical situations. This section is concerned with showing how the images reconstructed from experimental data compare with the simulated images presented in section 6.3. It should be born in mind that, since this data is obtained from actual measurements, refraction and diffraction effects occur. Diffraction effects cannot be taken into account. Thus the reconstructed images tend to be inferior to those obtained for section 6.3.

The measurements reported in section 6.4.1 were obtained by direct observation of an oscilloscope trace. Thus it was possible to measure the time delay for the first acoustic pulse received, as well as the time delay of the strongest acoustic pulse received (c.f. section 3.3). Because these measurements were very tedious, it was decided to construct an automated measurement system to obtain the results presented in section 6.4.2.

6.4.1 Manual Measurements for Symmetric Objects

For the manual measurements, the transducers were positioned by hand and the time delays were estimated by observing an oscilloscope trace. In order to reduce the necessary number of measurements (very tedious because of being done manually), only circularly symmetric objects were investigated. Objects with high acoustic velocities are chosen so that the measured delay times are quite different from the time delays through water.

The symmetry and velocity requirements are fulfilled by a solid circular aluminium cylinder. The cylinder was positioned at the centre of the scanning space as shown in fig. 3.2(a). An 800 V thyratron drive was used to excite the transmitting transducer. The transducers were

relatively inefficient and had a narrow bandwidth centred on 1 MHz. When multipath acoustic propagation was observed, the delay times for each acoustic pulse were recorded. Thus, the minimum delay time pulse and the maximum amplitude pulse were separated. The projections shown in fig. 3.2(b) were measured.

The computed images shown in fig. 6.11 were obtained from the minimum delay time projection of the aluminium cylinder. The images computed from the maximum amplitude pulse delay time projection are shown in fig. 6.12. The images in both figures were computed by the modified back projection method. The Shepp-Logan spatial filter was used to modify the projections (c.f. section 2.3). The images shown in fig. 6.11 and 6.12 are on the same scale so that a direct comparison can be made between the images and between the perspective views. The minimum time measurements are greatly affected by refraction. The computed image shown in fig. 5.11(a) is in the form of a cylindrical shape approximately 30 cm across. The perspective views of this image, shown in figs 6.11 (b) and 6.11(c), indicate that the computed acoustic velocity varies appreciably throughout the cylinder. The images computed from the maximum amplitude pulse delay time projection are affected by refraction, but the physical extent of the images is more accurate. These images are shown in fig. 6.12 and are approximately 20 cm across. The diameter of the aluminium cylinder is 20.4 cm so the reconstruction is quite accurate. The effects of refraction are evident in the perspective view of fig. 6.12(a), which is shown in fig. 6.12(b). The computed velocity at the edge of the high velocity region is higher than in the actual object, but the values are quite accurate elsewhere in the image. This is shown in fig. 6.12(c) in which the highest velocity regions of the image shown in fig. 6.12(b) are truncated. The velocity over the central region of the image is almost constant.

6.4.2 Automated Time Delay Measurements

The results presented in this section are computed from measurements obtained by an automatic measurement system. The system is controlled by a computer which positions the transducers at the required measurement position (c.f. sections 4.6 and 4.7) and activates the measurement equipment. This equipment consists of a pulse generator, a 20 MHz crystal clock, a 16 bit fully synchronous counter, a 16 bit high speed latch and a receiving system with a digital gain control. The counter is clocked at 20 MHz. When it overflows, a 10 V pulse of 200 ns duration is applied to the transmitting transducer. The first pulse entering the receiver is detected and the resulting signal is used as a command to store the contents of the counter in the high speed latch. Thus the contents of the latch is a number which can be multiplied by 50 ns (1/20 MHz) to obtain the time delay for the first acoustic pulse received. The time at which a pulse is detected is slightly dependent on the amplitude of the receiver signal. Consequently, it was decided to maintain the signal amplitude constant to within .25 dB, by means of a digital gain control system (c.f. Dunlop and Boys 1978). The peak signal level is examined for 1.5 μs after a pulse is detected. If the peak level exceeds a preset threshold, the gain is decreased by .25 dB. Otherwise the gain is increased by .25 dB. The gain is changed each time the counter overflows. Thus, the A.G.C. system is independent of analog time constants and the pulse repetition rate.

The measured time delays are accurate to ±25 ns. The accuracy is improved by using the computer to read the number stored in the latch. Several hundred time delay measurements are obtained at each measurement position. Measurements which differ by more than 5% from the mean value are discarded and the mean is recalculated to improve the accuracy of the time delay measurement.

The multipath propagation problem was avoided by measuring time delay projections around an object in which the acoustic velocity was slightly lower than that of water. For this situation, the minimum time delay pulse is also the pulse which has the largest amplitude. Suitable cylindrical test objects were conveniently constructed from .1 mm thick mylar. These cylinders which had a variety of cross-sectional shapes, were then filled with a 50% methylated spirit-water mixture which had an acoustic velocity of approximately 1400 m/s.

The first test object had an approximately circular cross-section which is shown in fig. 6.13(a). The 32 measured projections were modified by the Shepp-Logan spatial filter. The image shown in fig. 6.13(b) is computed by the modified back projection method. The image levels were inverted to form a positive image. The computed image is very similar to the original object although small discrepancies are evident in the image. The perspective view of the computed image is shown in fig. 6.13(c). Notice that the object is set to one side of the circular image area, and that clutter (or noise) surrounds the image of the object. In fig. 6.13(d), the clutter is suppressed by raising the minimum level displayed in the image. This results in a clearly displayed computed image.

The second test object had an oblong cross section. The measurements were obtained and processed in the same manner as for the circular cylinder discussed above. The resulting computed images are shown in fig. 6.14. The computed image shown in fig. 6.14(a) had badly defined edges. The image clarity can be enhanced by displaying only those velocity values which are between the 50% and 60% extremities of the velocity values in the original image. This "enhanced" image is shown in fig. 6.14(b). The perspective views of the images shown in figs 6.14(a) and 6.14(b) are shown in figs 6.14(c) and 6.14(d) respectively. Although the oblong outline is reasonably well defined, the velocity within the

oblong portion is not constant. A comparison of figs 6.14(c) and 6.14(d) shows that the velocity varies by approximately 30%.

Measurements were made on a "composite" object consisting of both the circular and oblong mylar cylinders. Thirty time delay projections were measured and these were processed by the Fourier transform method. The computed image of the composite object is shown in fig. 6.15(a). The cross section of each cylinder is clearly defined. The perspective view of the computed image is shown in fig. 6.15(b). Notice that the computed velocities are approximately the same for each cross section. Figs. 6.15(c) and 6.15(d) show perspective views of the computed image, when the range of displayed velocities is thresholded.

The measurement system has performed well for the simple objects selected, and the acoustic velocities chosen. The results reported in this section demonstrate the practicality of a system for a few special cases. To cope with objects of more general shape and velocity distribution, a more sophisticated measurement procedure (such as that described in section 6.5) has to be devised.

6.5 HYPERBOLIC PHASE MODULATION MEASUREMENTS

A system based on the measurement methods described in section 6.4 is unsuitable for providing data for accurate reconstructions of a body section containing a range of acoustic velocities (refer to sections 3.3, 6.3 and 6.4.1). The central problem is to measure the acoustic propagation time delay along the ray path which most closely approximates to a straight line joining the two transducers. In most situations, this seems to be the ray path by which the largest amplitude acoustic pulse propagates. The time delay of this pulse cannot be obtained with the simple high speed level discriminator circuitry described in section 6.4. The use of more complex high speed timing circuitry is avoided by employing the hyperbolic phase (or linear frequency) modulation methods

(described in sections 4.4 and 4.5) to implement a matched filter. The output of this particular matched filter happens to be, in effect, a power spectrum. The frequency (excluding 0 Hz) at which the maximum value of the power spectrum occurs is proportional to the time taken for the maximum energy pulse to travel between the two transducers. The pulse transit time must be within the limits of the time window which is determined by the system's band pass filter (c.f. section 4.5).

The results reported in this section were presented at Ultrasonics International Conference in Brighton, England (Bates and Dunlop 1977).

A test object, or phantom, was constructed as a cylinder with thin mylar walls. The cross section of the cylinder is an upper case F, as shown in fig. 6.18(a). To test the measurement system, the F phantom was filled with methylated spirit and positioned in the centre of the scanning system. For the first system trials, the time window limits were set to 0 and 360 μs, which corresponded to spectral limits of approximately 0 and 20 kHz. The two measured time delay projections shown in fig. 6.18(b) were measured at 0° and 90° around the F phantom. The delay time through water has been subtracted from these measurements. Notice that the time delay measurements are quantized to about 20 levels. The quantization limits the measurement dynamic range and the quality of the computed image.

The simulations discussed in section 6.3 show that clearly recognizable images are obtained when the acoustic velocity variations are less than about 5% of the velocity of water. A useful wider range of image variations is accommodated if the time window is set to ±11% of the propagation time through water only. The base band signal was thus restricted to a 10 kHz to 12.5 kHz pass band which was sampled at 5 kHz (c.f. section 4.5). The measured data was also supplemented with zeroes (refer to Bergland (1969) for details of this technique which is of wide application and importance) to give 512 input values for the FFT power spectrum calculation. These changes produced an aliased power spectrum in

which the "picket-fence" effect (c.f. Bergland 1969) was much reduced. These changes were incorporated for the two projection measurements shown in fig. 6.18(c). The deleterious effects of quantization are seen to have been considerably reduced by these procedures. This method of measurement was used for the results presented in the remainder of this section.

6.5.1 Symmetric Objects

Several symmetric objects positioned at the centre of the scanning system have been examined. Many of the results obtained do not vary greatly from the symmetric object results reported in section 6.4.1. So only the most significant set of results is explicitly discussed.

A symmetric phantom was constructed from three concentric 0.1 mm thick mylar walled cylinders, as shown in fig. 6.16(a). Castor oil (acoustic velocity 1500 m/s) was used to fill the central and outer volumes, while the intermediate space was filled with distilled water. A simulated set of projections was calculated for straight ray paths and the computed image is shown in figs 6.16(b) and 6.16(c). A set of measured projections was then obtained. The image computed from the measured projections is shown in fig. 6.17(a). All of the images shown in figs 6.16 and 6.17 were computed by the modified back projection method, using the Shepp-Logan filter.

The image shown in fig. 6.17(b) is obtained from the computed image by limiting the acoustic velocities to those greater than the acoustic velocity of water. This image is almost identical to the ideal data image shown in fig. 6.16(b). While the two computed images in figs 6.16(b) and 6.17(b) are similar in extent, a comparison of the perspective images, shown in figs 6.16(c) and 6.17(c) respectively, shows that the computed velocity distributions are different. The increased acoustic velocity values calculated near the edges of the high velocity regions, as shown in fig. 6.17(c), are caused by acoustic refraction. The acoustic

refractive index of castor oil is 0.986 relative to water, so even a small amount of refraction has a quite noticeable effect on the computed image.

The sharp velocity discontinuities in the phantom are clearly defined at the correct positions in the image. Thus, the measurement method is seen to be capable of handling sudden discontinuities reasonably well. However, circular objects do not exhibit the strong refraction effects which occur at sharp corners in an object. These effects are examined in the following section.

6.5.2 Asymmetric Phantoms

Various shapes were investigated. The results confirmed the conclusions given previously in this chapter. The only results discussed explicitly here are those for the highly asymmetric phantom having the shape of an upper case F, as shown in fig. 6.18(a). The sets of measured projections shown in figs 6.18(b) and (c) have already been discussed in the introduction to this section. These measured projections closely approximate the exact values calculated for straight ray paths. This is probably due to the fact that the actual ray paths are either parallel or perpendicular to the mylar walls of the phantom. For $\phi = 0^{o}$ or $\phi = 90^{o}$, there is little refraction of the ultrasonic ray paths. Refraction is much more in evidence for intermediate values of ϕ. The results shown in fig. 6.19 were obtained when the F phantom was filled with methylated spirit, which has the comparatively large acoustic refractive index of 1.2 relative to distilled water. The image is reconstructed from 32 projections by means of the modified back projection method utilizing the Shepp-Logan filter. The image obtained is rather disappointing. The reason for this seems to be that the rays propagating through the F are strongly refracted for projections corresponding to values of ϕ other than 0^{o} or 90^{o}.

A second set of results was obtained with the F phantom filled with castor oil (v = 1500 m/s), which has an acoustic refractive index of 0.986 relative to distilled water. The results are shown in fig. 6.20. Images (a)-(d) are of the same reconstructed image with different settings of the image threshold window. Fig. 6.20(e) is a perspective view of the reconstructed image. The negative image computed from another set of measurements is shown in fig. 6.20(f). Measurement errors are clearly shown as dark bands across the image. An erroneous data point in a projection can thus be identified and set equal to the mean of the two adjacent data points. The obvious errors have been eliminated from fig. 6.20(f) to yield the positive image shown in fig. 6.20(g). Some errors are still evident near the sharp corners in the reconstruction, but they are significantly reduced in magnitude.

All but one of the images shown in fig. 6.20(a)-(g) have been reconstructed by the modified back projection method, using the Shepp-Logan filter. Fig. 6.20(e) was reconstructed by the Fourier method. For fig. 6.20(a)-(e) M = 90, and for figs 6.20(f) and (g) M = 32. Although the image quality in fig. 6.20(b) is better than in fig. 6.19(a), it is still not as good as that which would be obtained by X-ray computer assisted tomography. The lack of definition at the sharp corners of the phantom seems to be caused by the refraction (small as it is) of the rays.

6.5.3 Biological Specimens

Fig. 6.21 shows an image of a bovine kidney held in a plastic bag filled with tap water. The image has been reconstructed from 40 projections by the Fourier transform method. The central dark portion of the image corresponds to the fatty parts of the kidney, and the surrounding white portions correspond to the kidney tissue.

Another biological specimen examined was the head of a shark. Photographs of this are shown in fig. 6.22. The specimen had been soaked in a formalin solution for several months and was well preserved. Three acoustic velocity tomographs were taken through the shark's head at the levels shown in fig. 6.22(b). For each tomograph, 90 projections were each sampled at 63 points and the image was reconstructed by modified back projection, utilizing the Shepp-Logan spatial filter.

The tomograph nearest the nose is shown in fig. 6.23(a). The others are in order from the nose back. The scale of the image shown in fig. 6.23(a) is approximately 8% larger than that of the images shown in figs 6.23(b) and (c). This is because the distance between the sample points is slightly smaller for fig. 6.23(a). The head was sectioned to produce the photographs in fig. 6.24. The computed images can thus be compared directly with the actual cross sections. The outline of the head is visible as are the solid cartilage areas on each side of the head. The internal detail is not clear enough for analysis. Figs 6.23(a) and (c) show evidence of artefacts which extend beyond the limits of the head. However, fig. 6.23(b) appears relatively free from noise and the outline of the head is quite clear.

6.6 DISCUSSION OF RESULTS

The simulations and measurements reported in previous sections of this chapter have shown that, provided the acoustic velocity throughout a phantom varies by only a few percent from the surrounding fluid, useful images can be obtained by ultrasonic transmission tomography. The results also show that the most direct propagation paths (similar to X-ray propagation) produce the best results. The path travelled by the largest acoustic pulse received seems in most situations to be the straightest path. The hyperbolic phase modulation system is a convenient method for

measuring the acoustic propagation time for this path. The result is that the distortions due to strong acoustic refractions are confined to the areas in which the acoustic velocities are markedly different from the velocities of the surroundings. The simulations have also shown that minimum time measurements give approximately the same results when the acoustic velocity does not depart more than a few percent from that of water.

Reconstructions based on the modified back projection method produce results which are superior to those obtained by the Fourier transform method. The Shepp-Logan spatial deconvolution filter produces images which are less noisy than the other simple types of filter. Thus the Shepp-Logan filter is extensively used with the modified back projection technique.

The results obtained are affected by refraction because of two effects. The first effect is due to the use of a "straight ray" algorithm when the rays are actually curved. The second effect is caused by the finite beamwidth of the transducers. When a ray is refracted, the receiving transducer may be in a null of the transmitted beam for some, if not all, of the transmission period. This produces a low S/N and possibly a detection error which may show as a band across the image.

For situations where the acoustic velocity variations are less than 5%, smaller transducers operating at a higher frequency and with a wider beamwidth might well produce better quality images. The wider beamwidth would help to eliminate beam nulls in the transmission path, and the higher frequency would permit a wider bandwidth and hence increase the resolution of the time delay measurement.

In vivo measurements have not been attempted because of the time taken to obtain a time delay measurement. Each time delay is inferred from a power spectrum which requires approximately 6 s to compute on the E.A.I. 640 (the FFT subroutines supplied by E.A.I. required 15 s). An

image of a biological specimen typically requires about 90 projections. Thus the time taken to sample each projection at 63 points is about 9.5 hours. Immobility for such a period is best obtained with dead specimens.

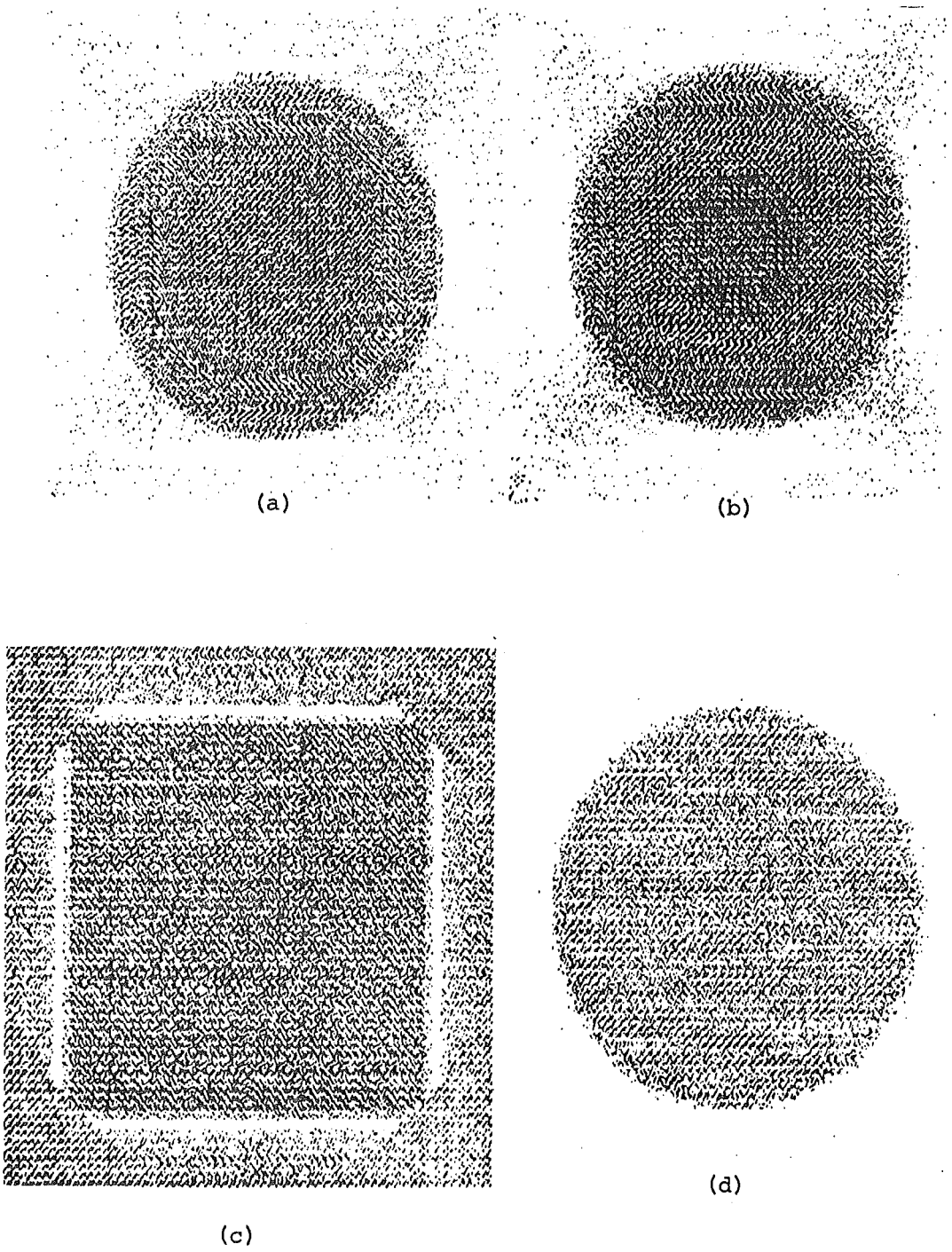

Fig. 6.1 Images of a circularly symmetric phantom computed from simulated straight ray propagation delay times. The images were computed as follows:

(a) FFT method from two projections.

(b) As for (a) but the spatial frequencies are windowed.

(c) Modified back projection method for two projections.

(d) As for (c) but using 30 projections.

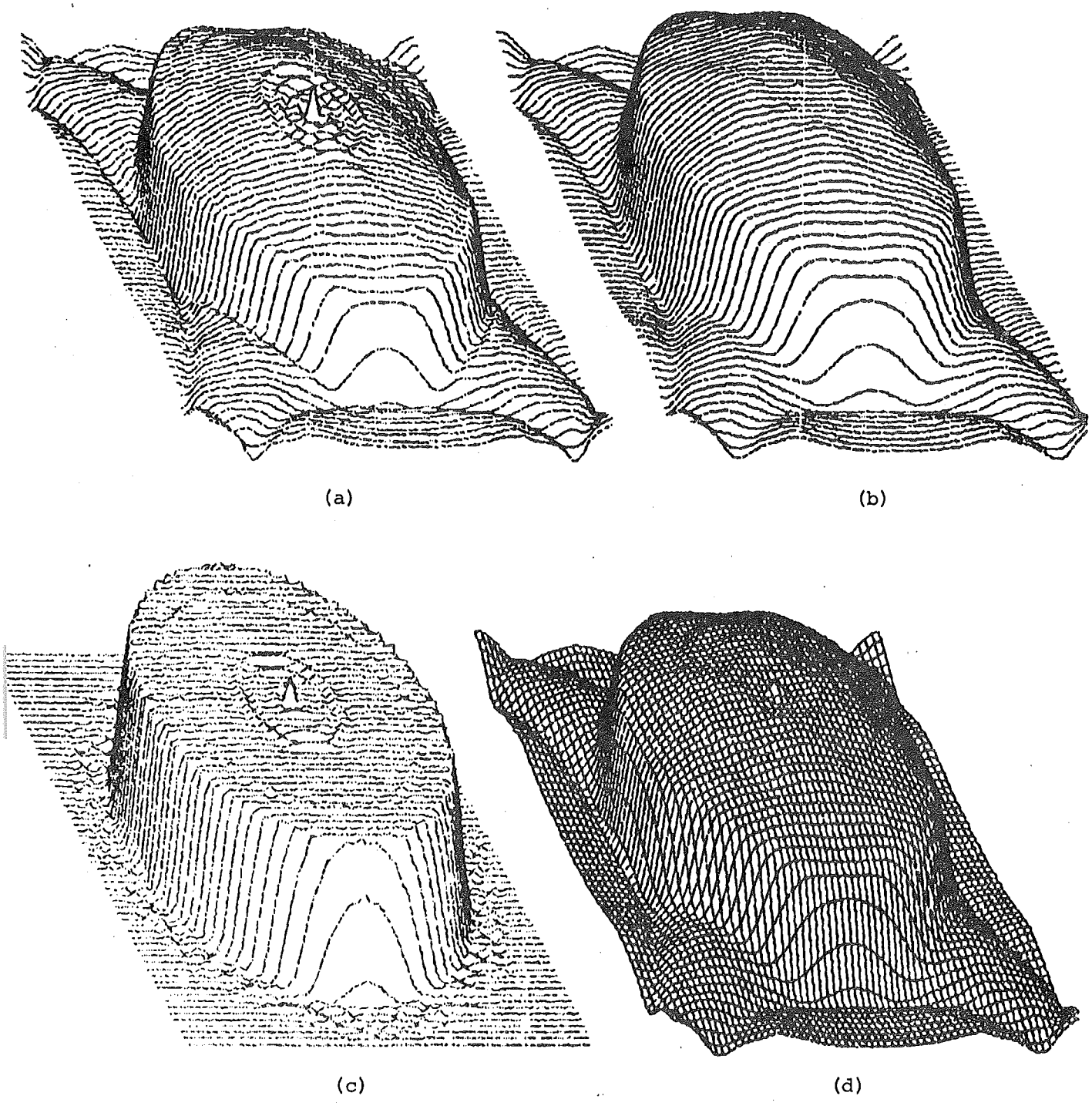

Fig. 6.2 Perspective view of the velocity distributions in the images shown in fig. 6.1.

(a) Perspective view of fig. 6.1(a)

(b) Perpsective view of fig. 6.1(b)

(c) Perspective view of fig. 6.1(d)

(d) Perspective grid presentation of fig. 6.2(b).

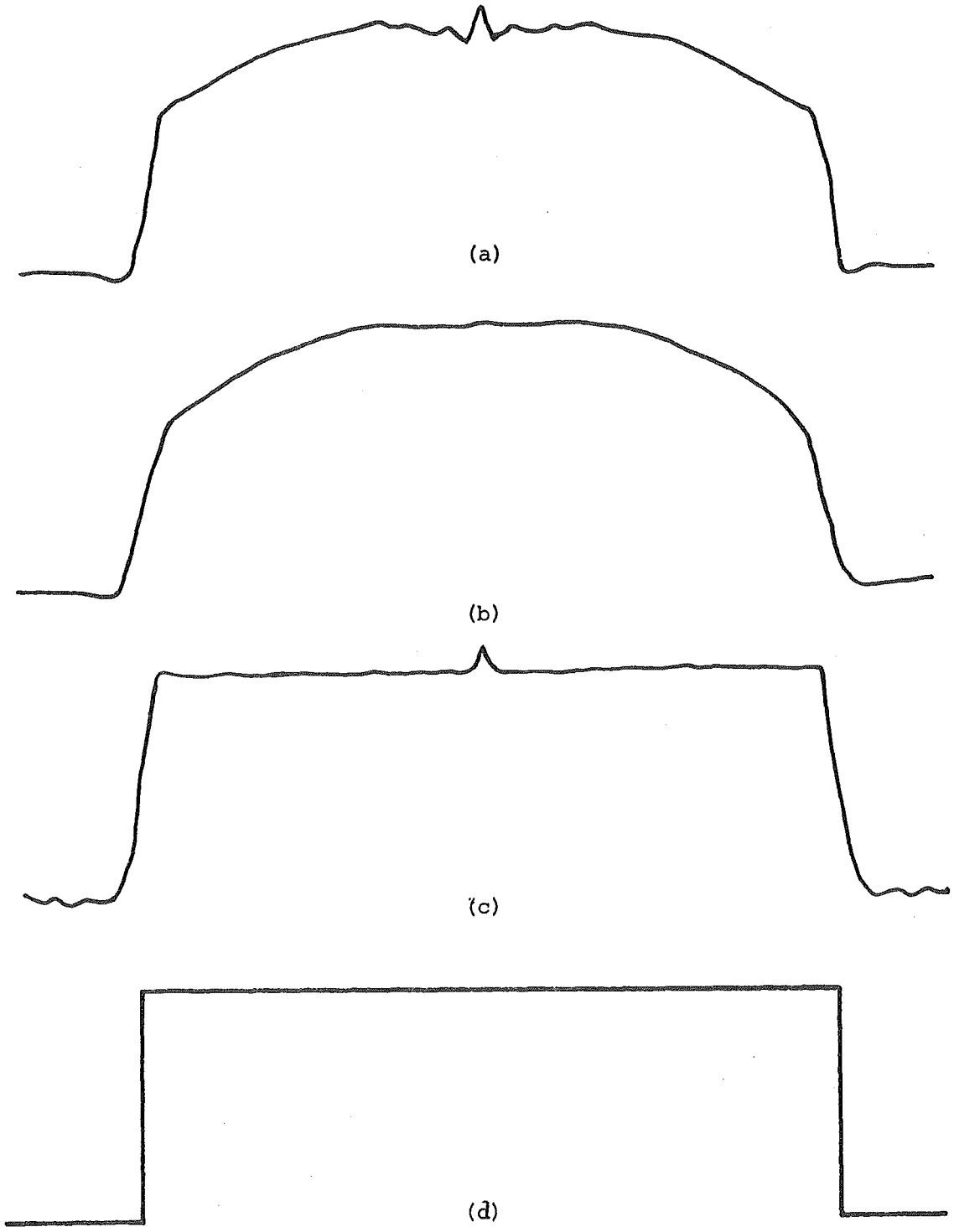

Fig. 6.3 Velocity distribution through the centre of the images shown in figs. 6.2.

(a) Velocity distribution through image shown in 6.2(a)

(b) Velocity distribution through image shown in 6.2(b)

(c) Velocity distribution through image shown in 6.2(c)

(d) Velocity distribution through the original cylinder.

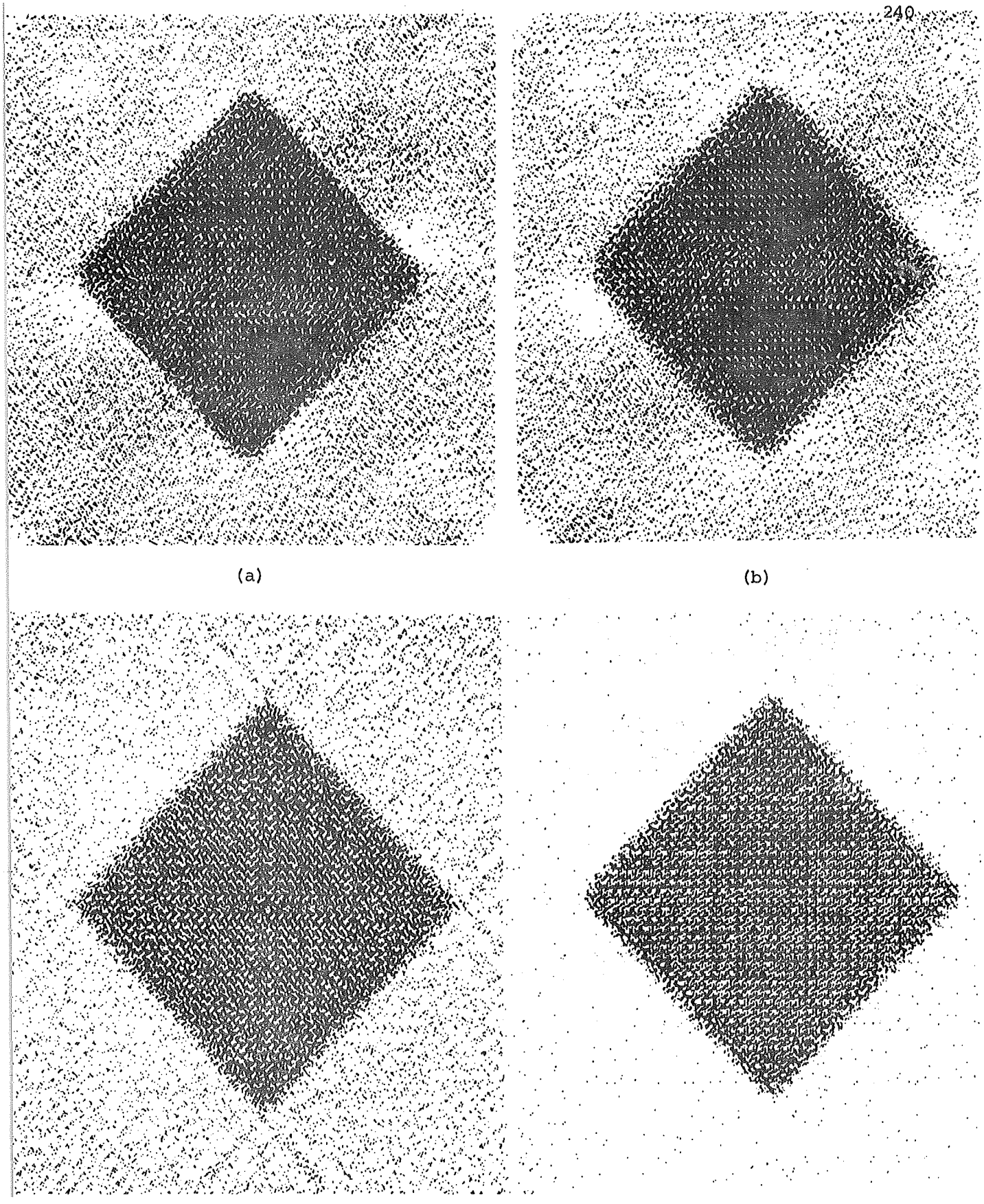

(a) (b)

(c) (d)

Fig. 6.4 Images computed from 30 projections of simulated straight ray path time delay measurements for a diamond shaped phantom.
Computed by the FFT method: (a) not windowed, (b) windowed.
Computed by the modified back projection method using the Shepp-Logan spatial filter: (c) 30 projections, (d) 90 projections.

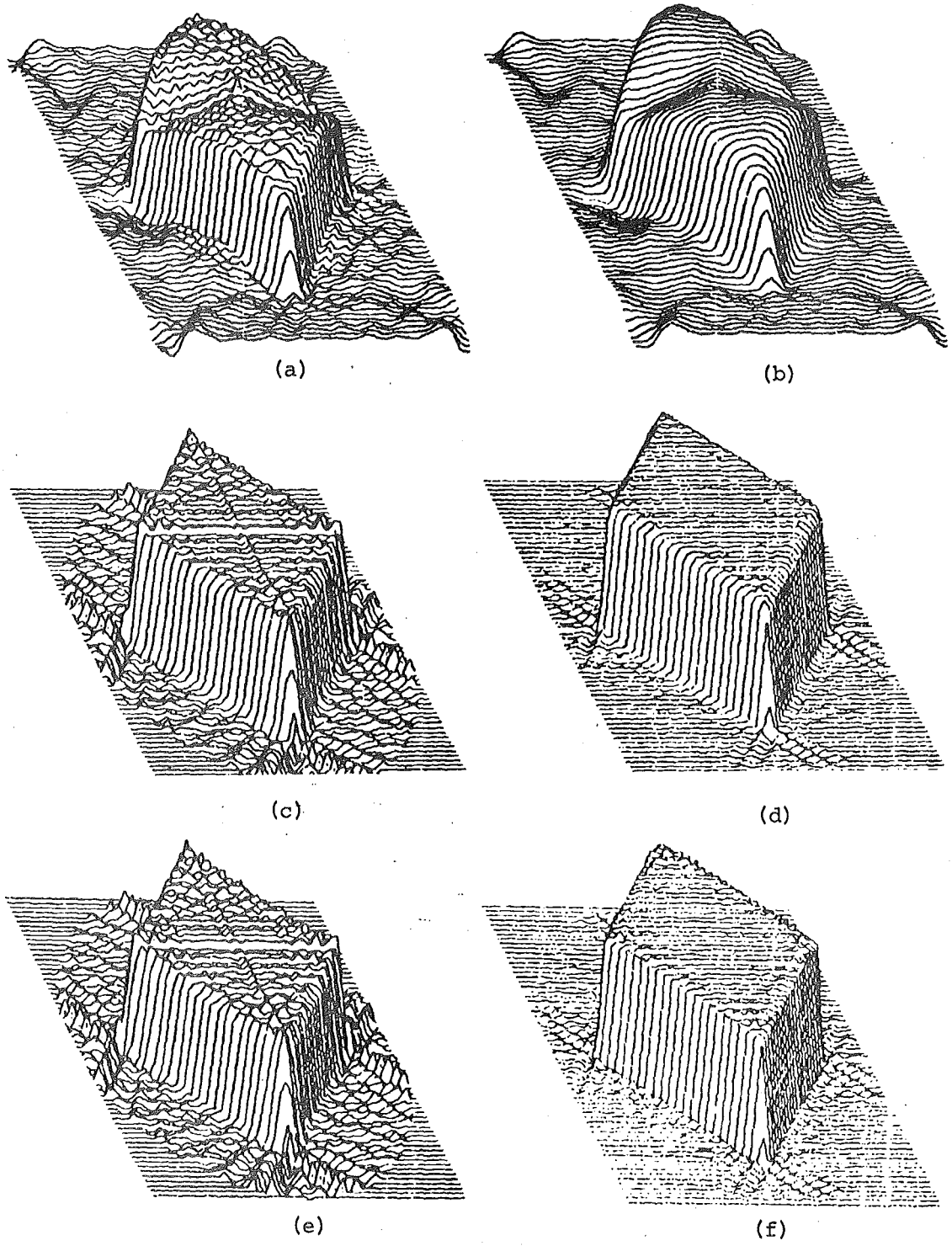

Fig. 6.5 (a)-(d) Perspective views of the images shown in fig. 6.4(a)-(d), (e) and (f) correspond to (c) and (d) except the Ramachandran spatial filter is used.

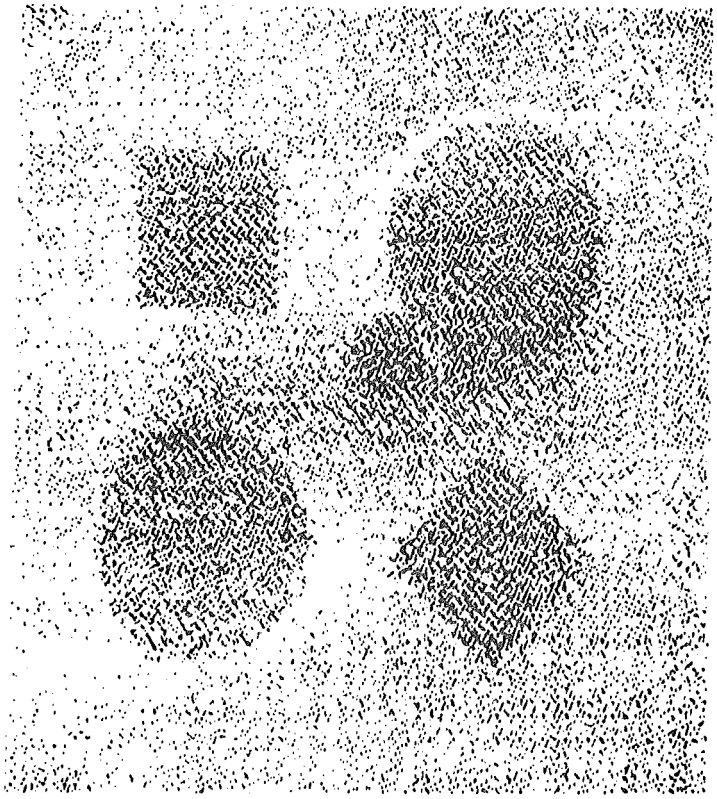

(a)

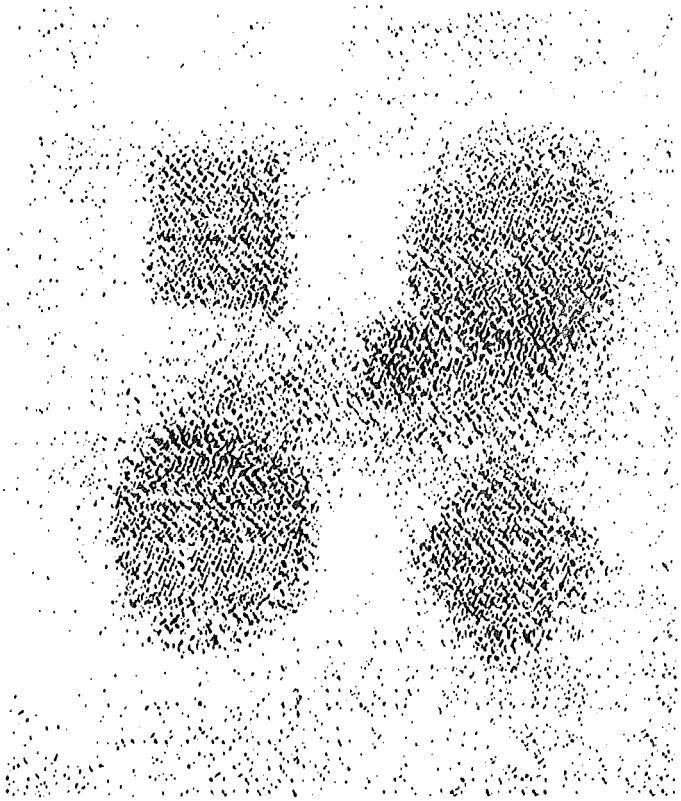

(b)

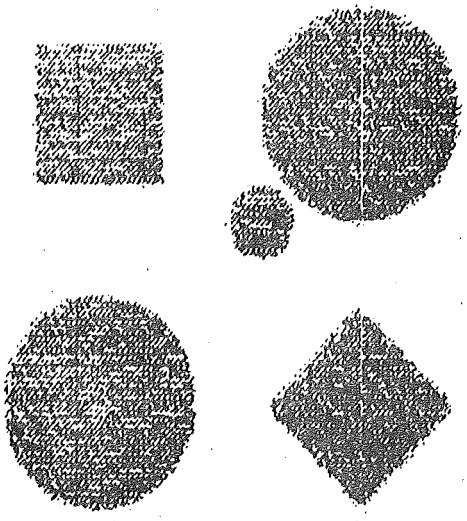

(c)

(a) Computed by FFT method - no windowing.

(b) As for (a) but a spatial frequency window is used.

(c) Computed by the modified back projection method using the Shepp-Logan spatial filter.

Fig. 6.6 Images computed from 90 projections of simulated straight ray path time delay measurements of a composite object.

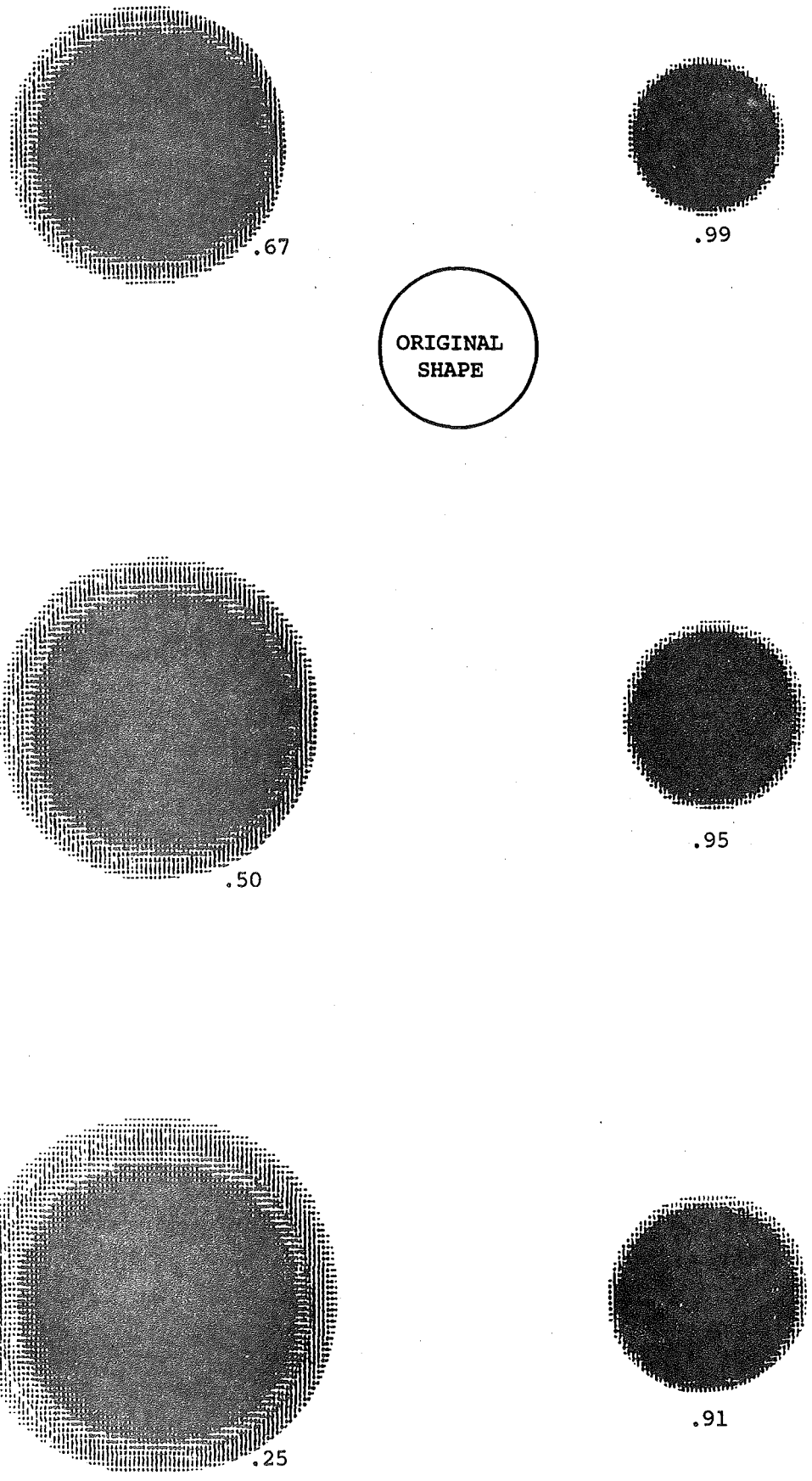

Fig. 6.7 Images computed from simulated measurements based on the shortest time for acoustic propagation through the circular shape. The acoustic refractive index used inside the original shape is noted for each image.

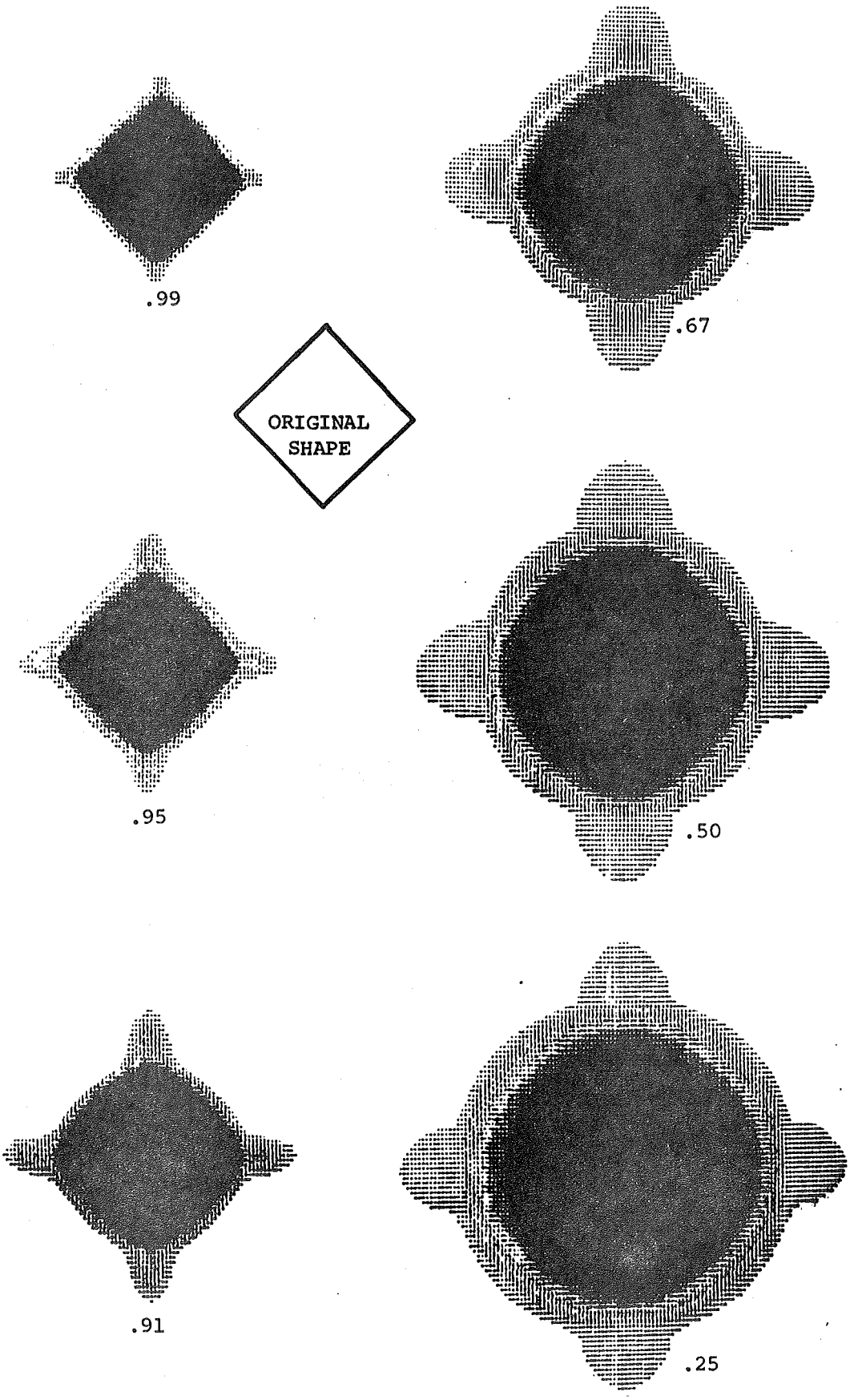

Fig. 6.8 Images computed from simulated measurements based on the shortest time for acoustic propagation through the diamond shape. The acoustic refractive index used inside the original shape is noted for each image.

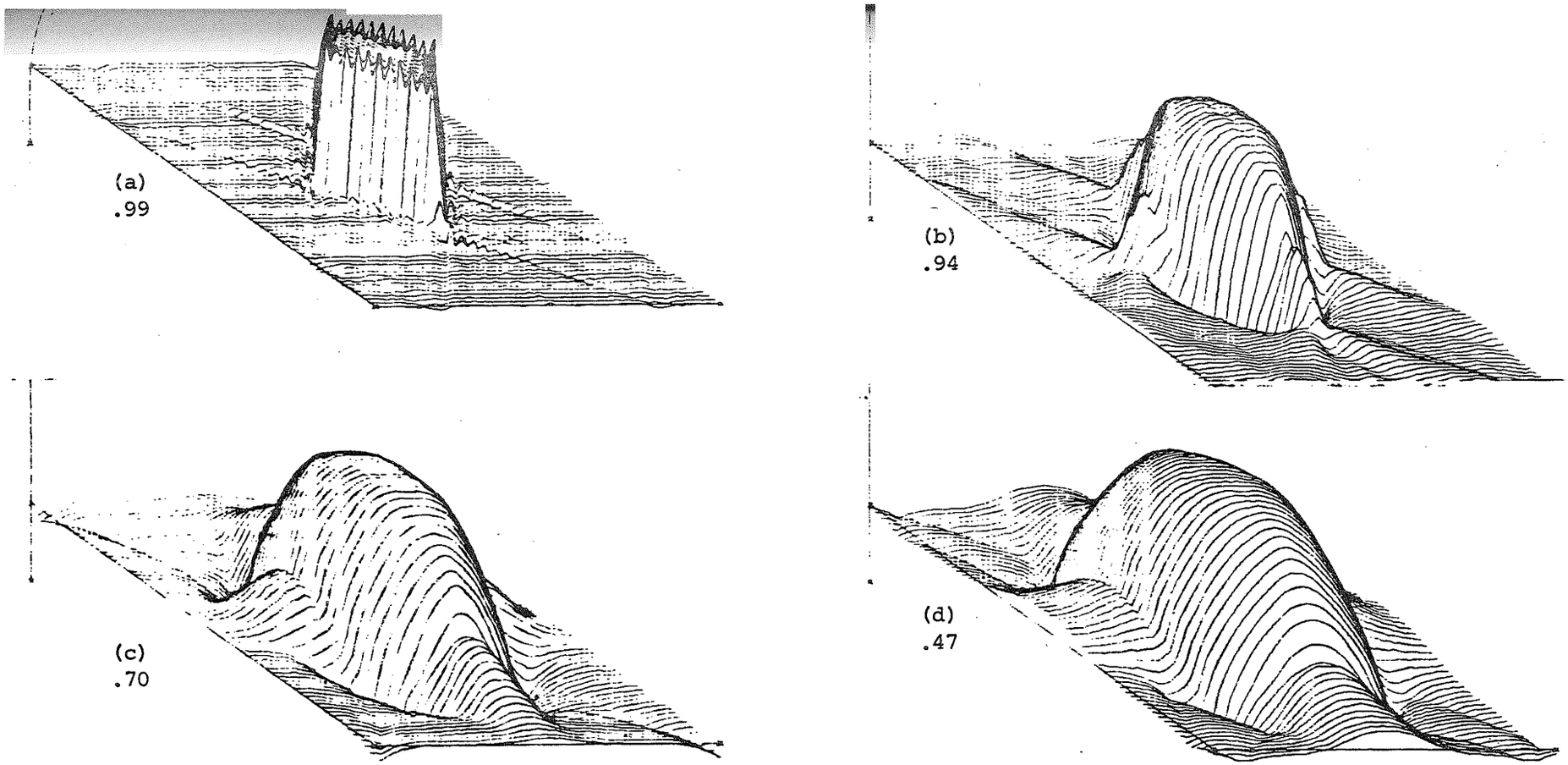

Fig. 6.9 Perspective views of images computed by the FFT method using Tukey's interim data window to limit the spatial frequencies. The simulated minimum time delay measurements are for the diamond shape using the acoustic refractive indices shown.

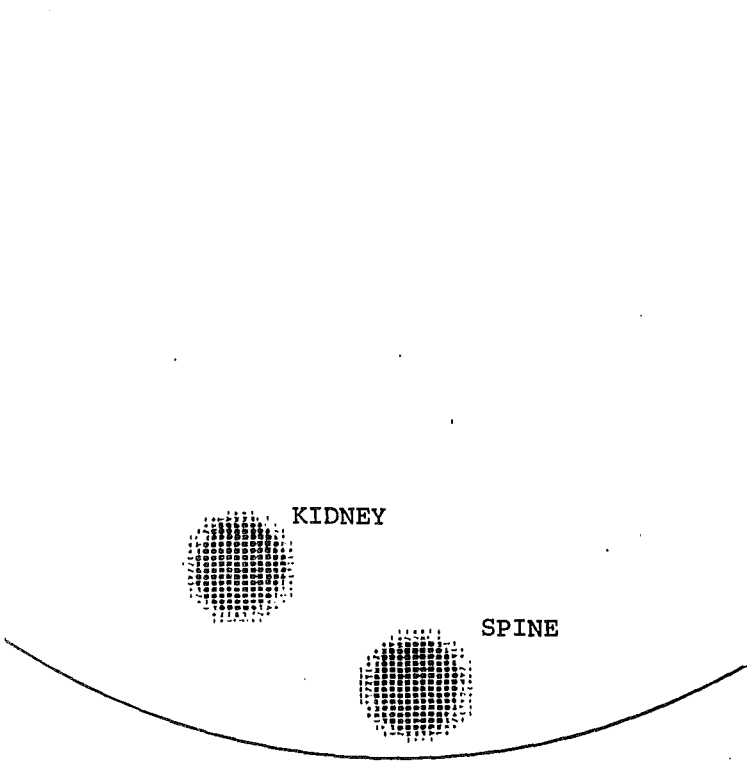

(a)

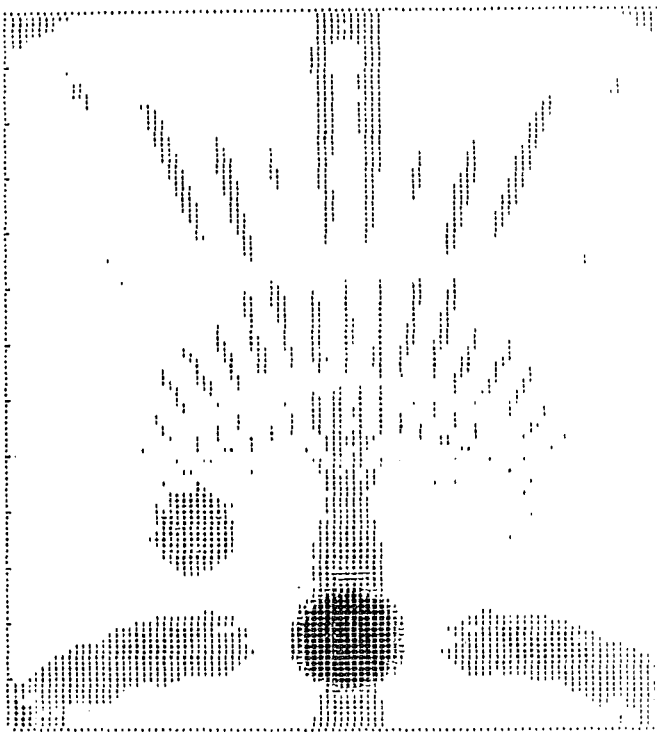

(b)

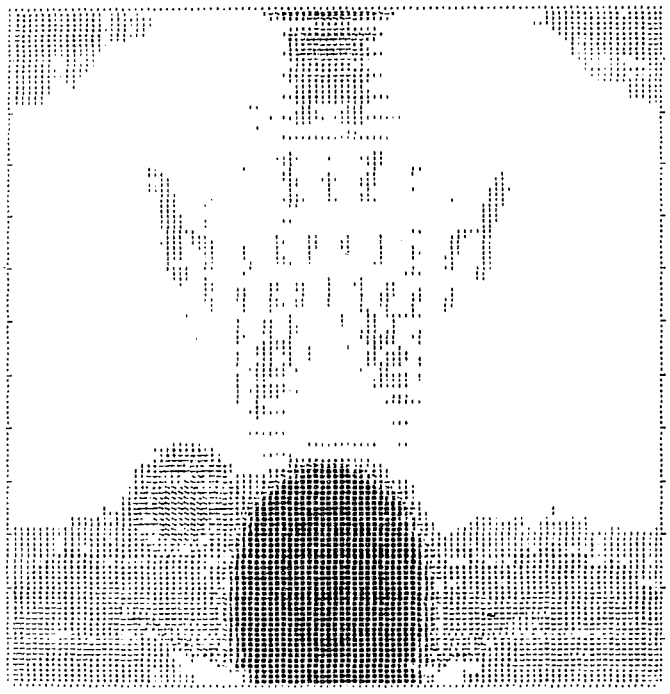

(c)

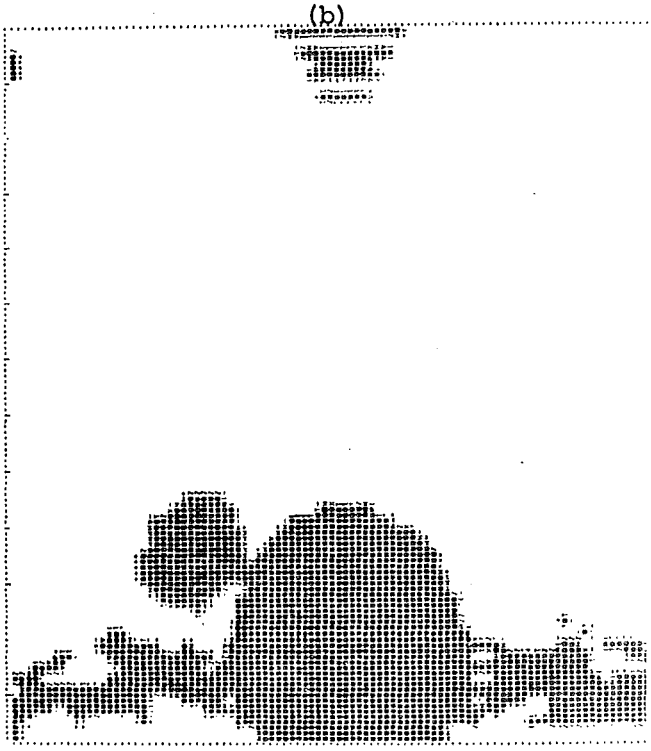

(d)

Fig. 6.10 Images computed from simulated measurements for a model of the torso (shown in a). Straight ray paths are employed for the simulated measurements used to compute (b). Simulated acoustic ray paths are used for (c). A limited range of the image in (c) is shown in (d).

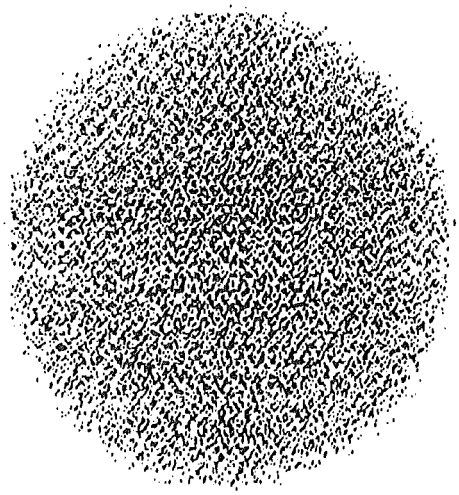

(a)

(b)

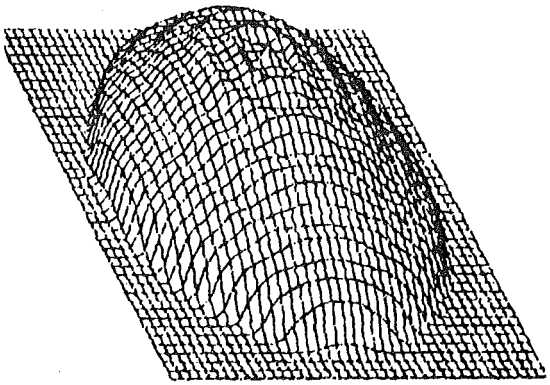

(c)

(a) The computed image of the aluminium cylinder is almost 30 cm in diameter.

(b) Perspective view of (a) showing that the velocity distribution is not constant throughout the computed image.

(c) Perspective grid presentation of (b).

Fig. 6.11 Images computed from the measured shortest time delay for acoustic propagation through an aluminium cylinder (20.4 cm diameter). The time delay projection is shown in fig. 3.2(b).

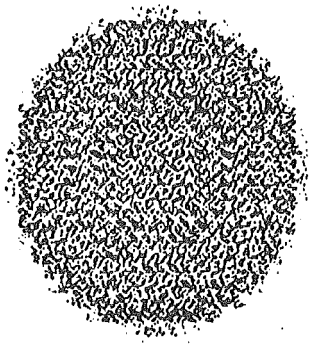

(a)

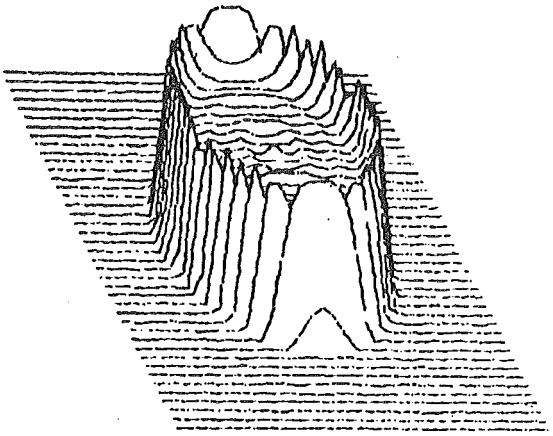

(b)

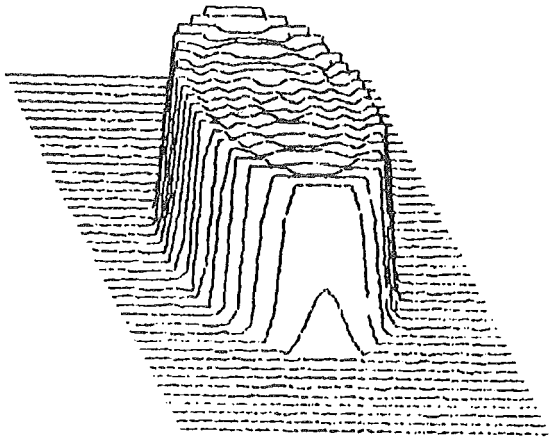

(c)

(a) The computed image of the aluminium cylinder is approximately 20 cm in diameter.

(b) A perspective view of (a). The velocity values are too high at the edges of the cylindrical image. Image range 0-1 is displayed.

(c) As for (b) with the image display window set 0-.65.

Fig. 6.12 Images computed from the measured time delay of the largest amplitude acoustic pulse to propagate through an aluminium cylinder (20.4 cm diameter). The time delay projection is shown is fig. 3.2(b).

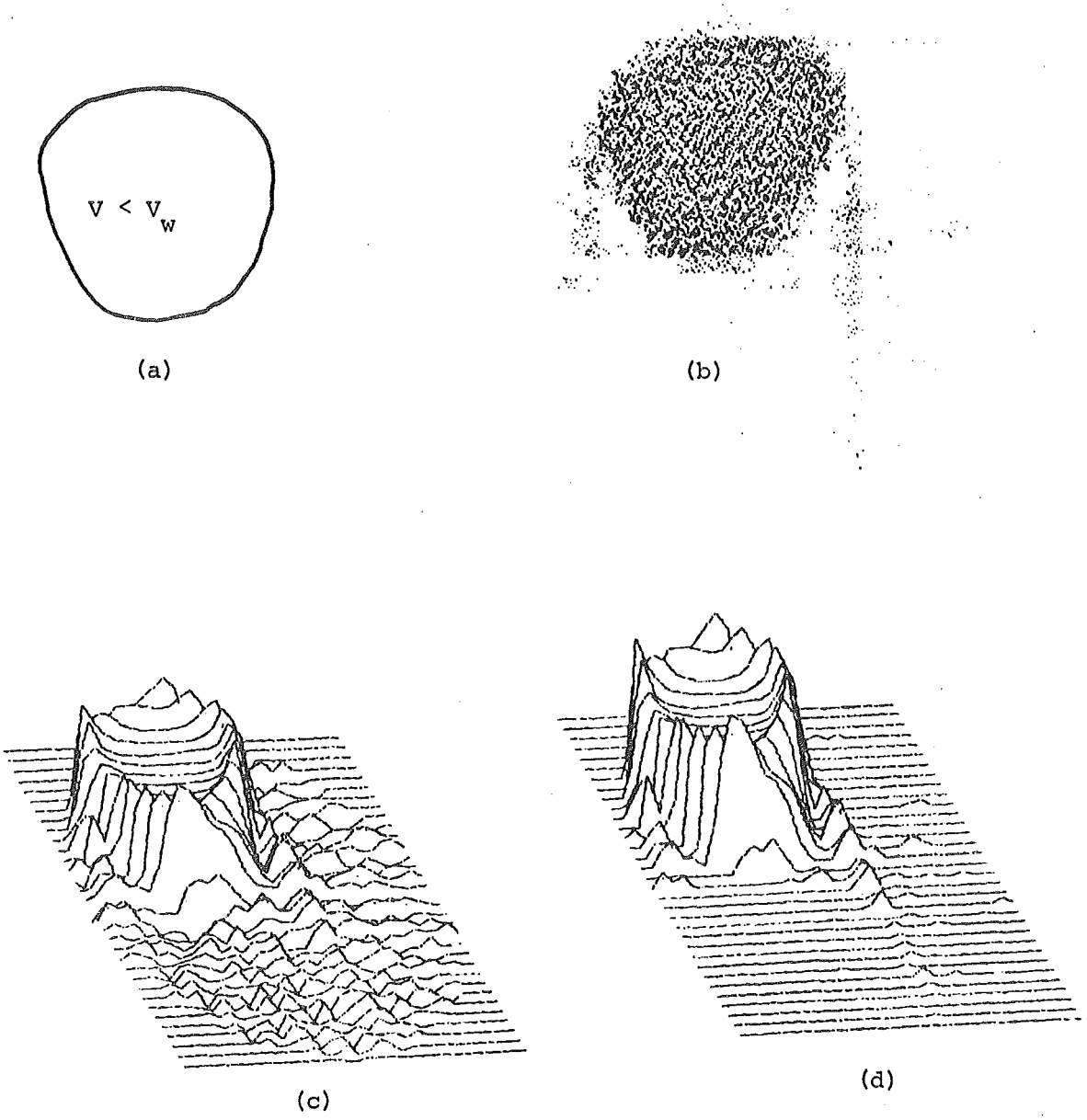

Fig. 6.13 Results of the automated minimum time measurements on a roughly circular mylar walled phantom filled with methylated spirit. Images computed by the modified back projection method using the Shepp-Logan filter.

(a) Outline of the phantom.

(b) Computed image, displayed range is .3-1.

(c) Perspective view of velocity distribution. Displayed range 0-1.

(d) Perspective view of velocity distribution. Displayed range .3-1.

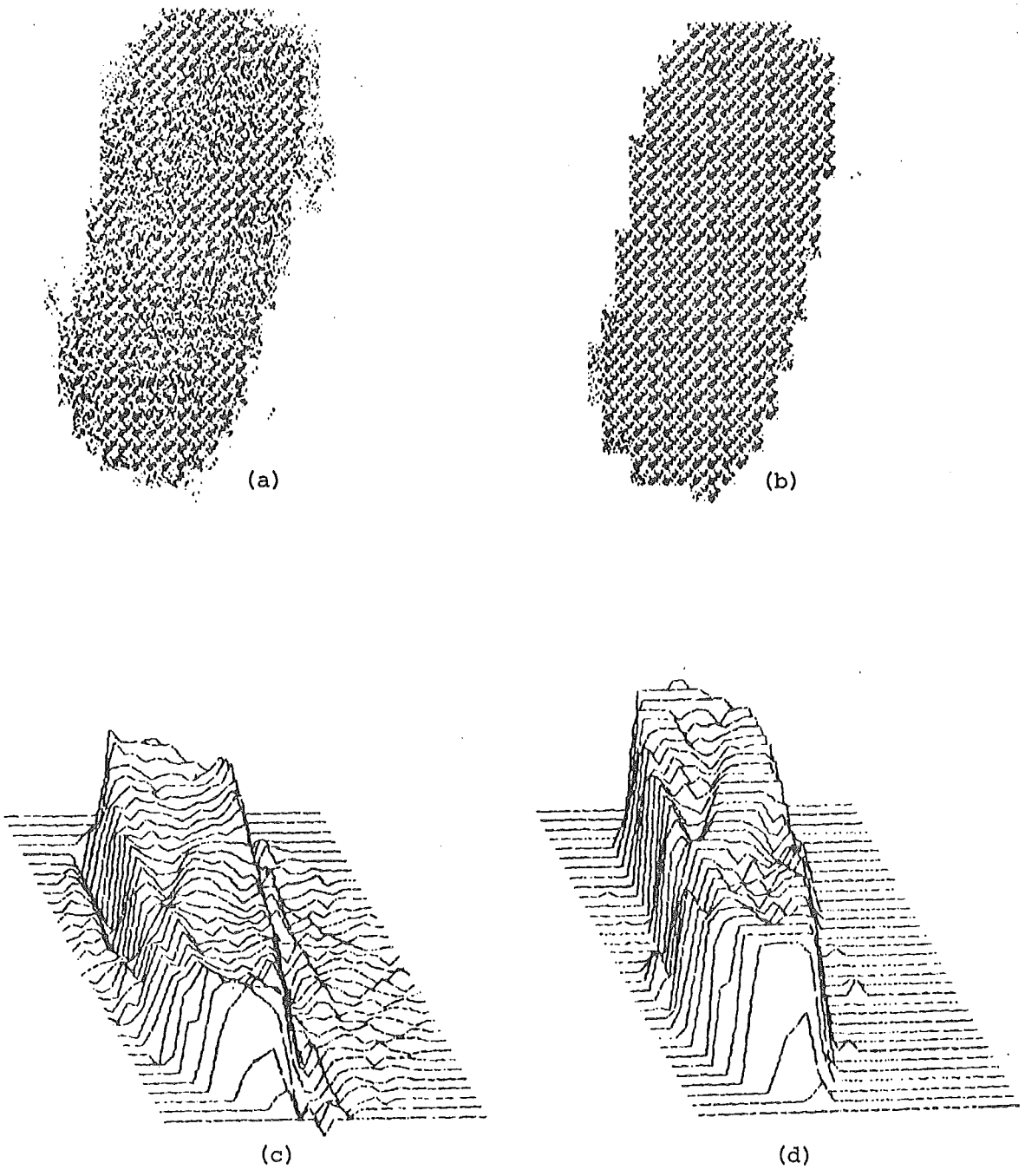

Fig. 6.14 Images computed from automated minimum time measurements on an oblong mylar walled phantom filled with methylated spirit.
Images computed by the modified back projection method using the Shepp-Logan filter.
Image range displayed is: (a) .3-.8 (b) .5-.6 (c) 0-1 (d) .3-.8.

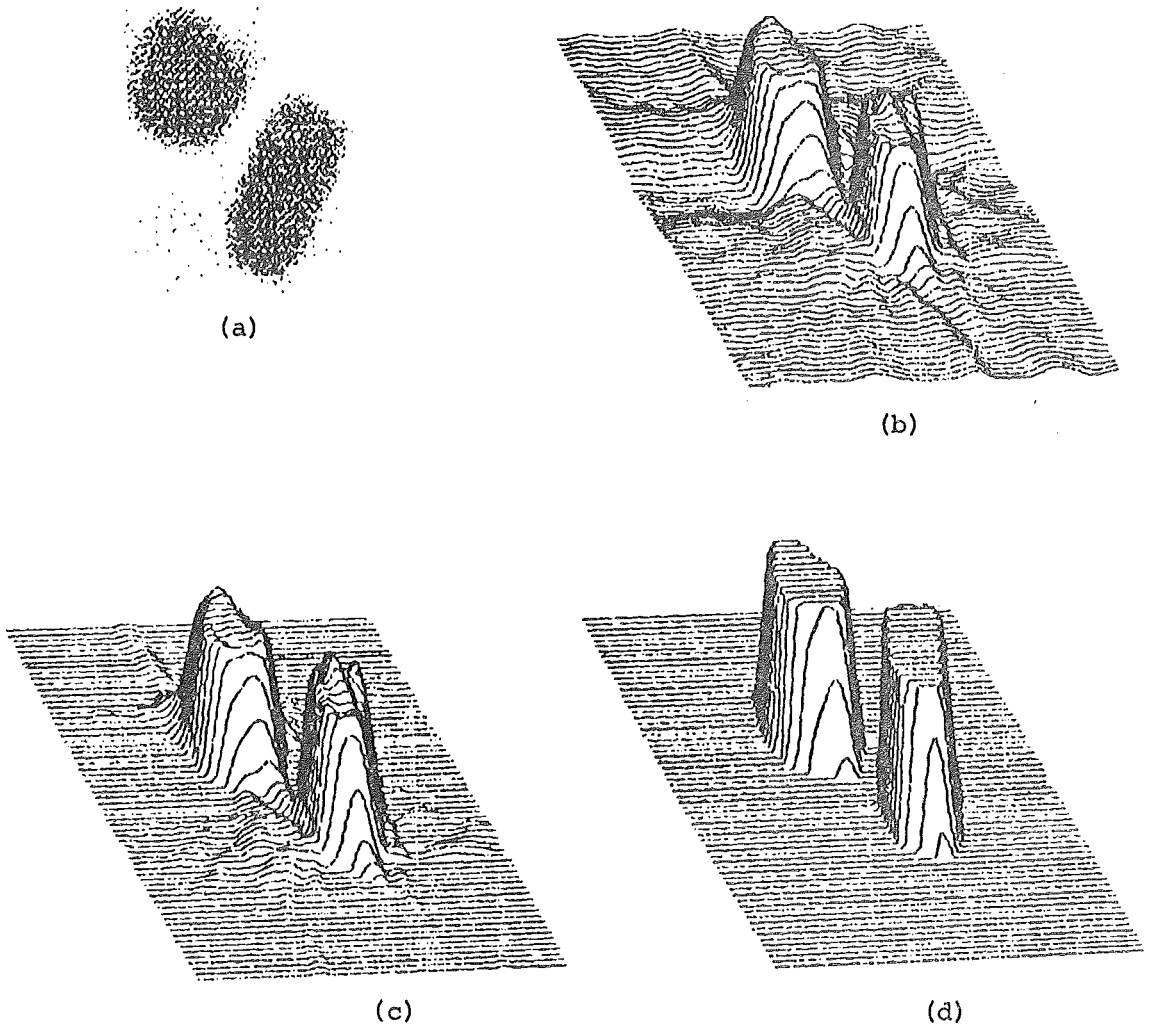

Fig. 6.15 Results of automated minimum time measurements on a composite object consisting of the two phantoms shown in figs. 6.13 and 6.14. The phantoms are filled with methylated spirit and the images are computed by the FFT method. The image range displayed is: (a) .2-1 (b) 0-1 (c) .2-1 (d) .3-.7.

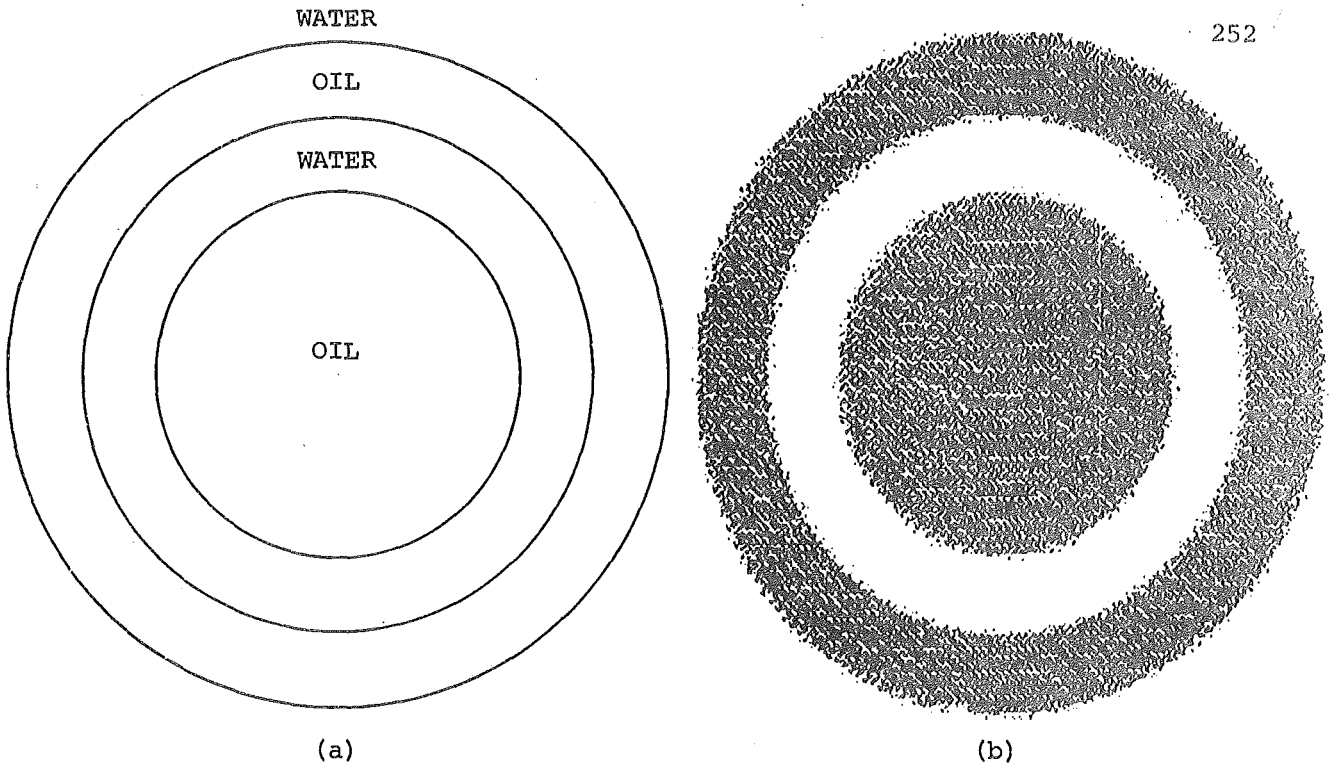

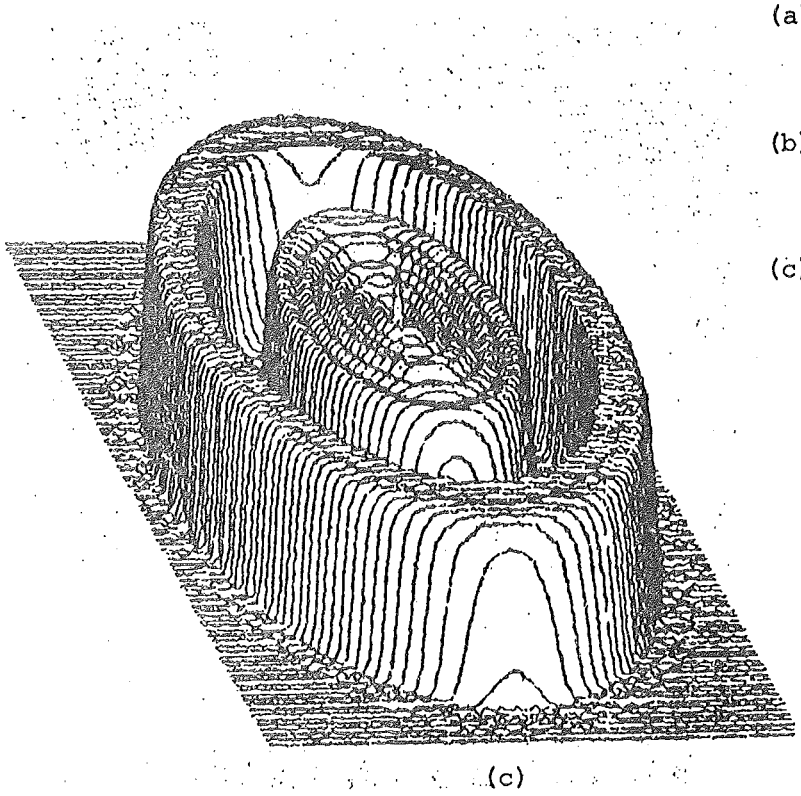

(a) Geometry of the composite phantom.

(b) Image computed by the modified back projection method.

(c) Perspective view of the image. Displayed range 0-1.

Fig. 6.16 Images computed from projections of simulated straight ray path acoustic time delay measurements for a circularly symmetric composite object consisting of three concentric mylar walled cylinders.

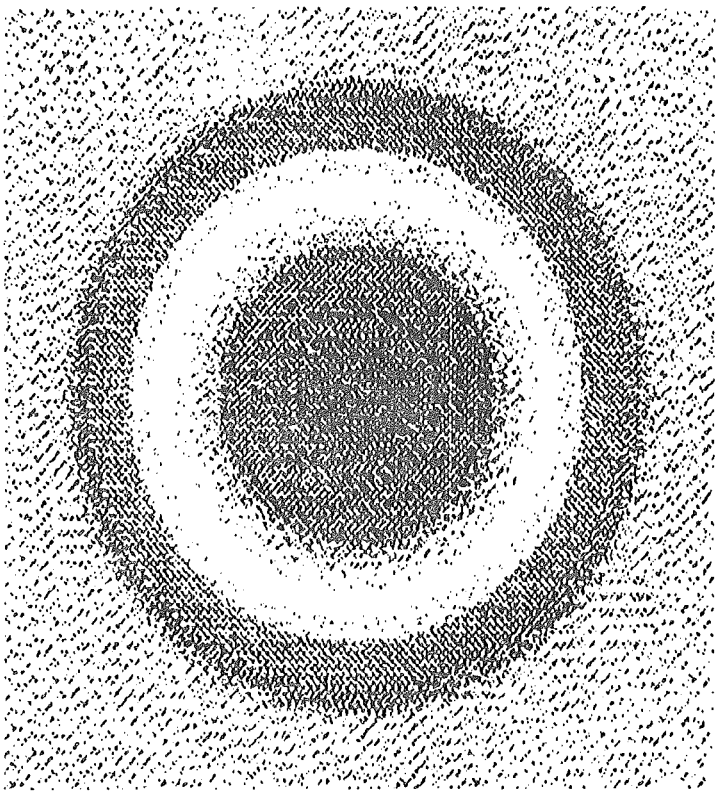

(a)

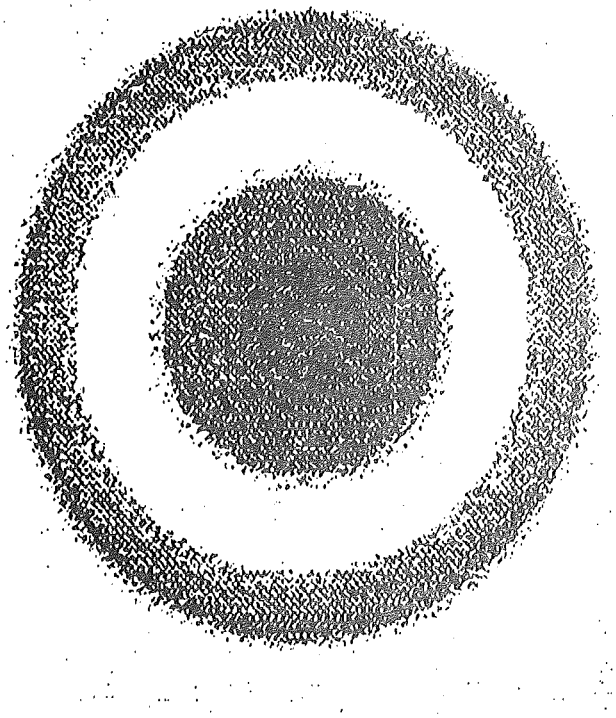

(b)

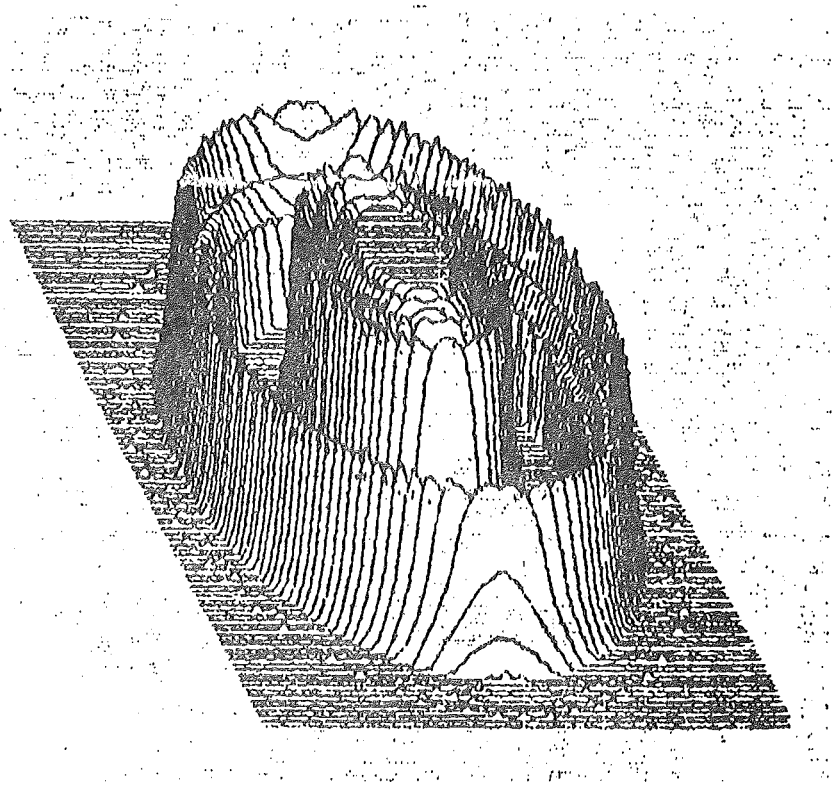

(c)

(a) Image computed by the modified back projection method. Displayed range 0-1.

(b) Displayed range is .24-1.

(c) Perspective view of (b).

Fig. 6.17 Images computed from measurements on the castor oil (n = .986) and water filled phantom shown in fig. 6.16(a). The largest amplitude acoustic pulse propagation path time delay is measured automatically by the computer controlled hyperbolic phase modulation system.

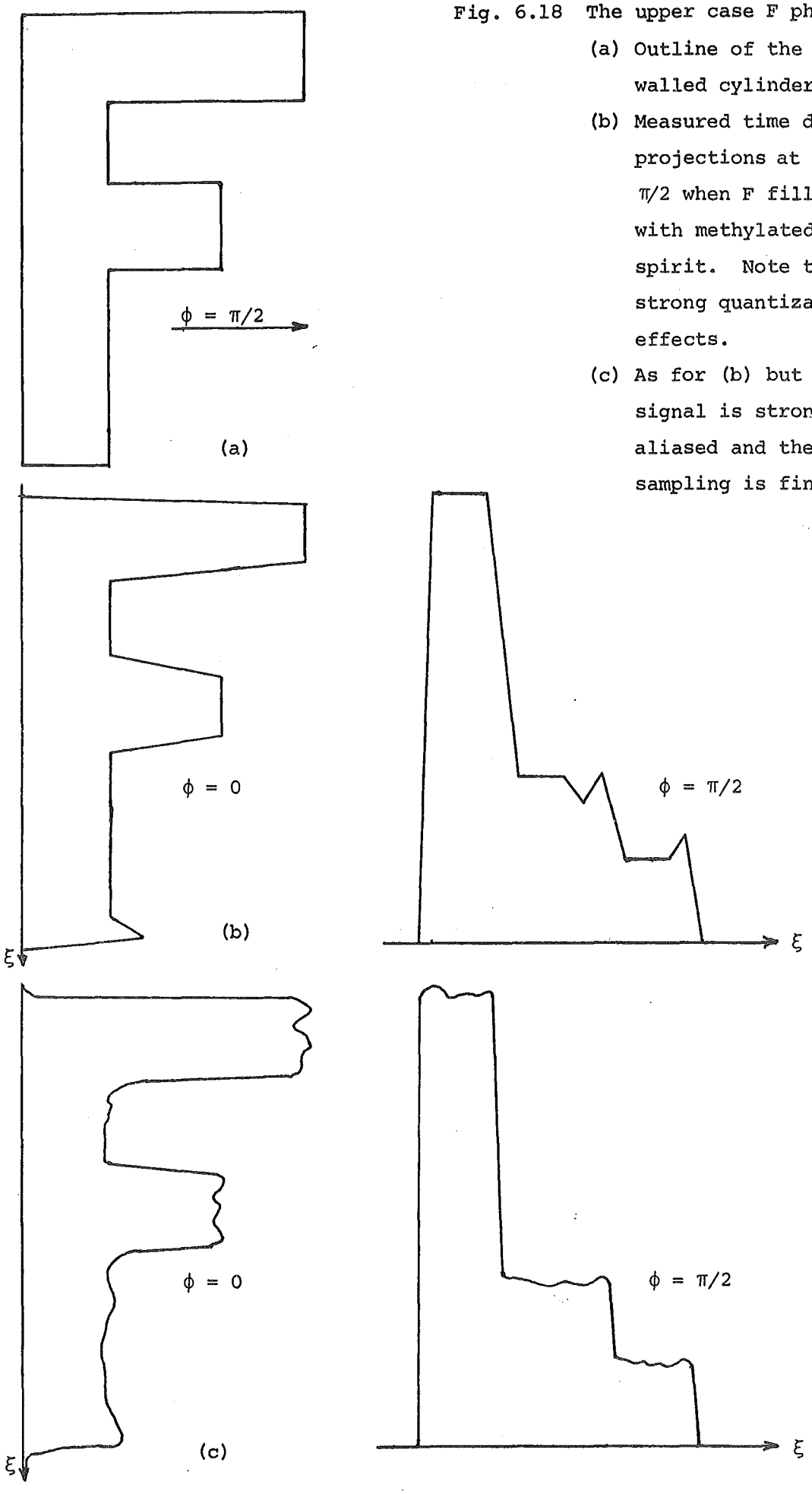

Fig. 6.18 The upper case F phantom:

(a) Outline of the mylar walled cylinder.

(b) Measured time delay projections at 0 and $\pi/2$ when F filled with methylated spirit. Note the strong quantization effects.

(c) As for (b) but the signal is strongly aliased and the spatial sampling is finer.

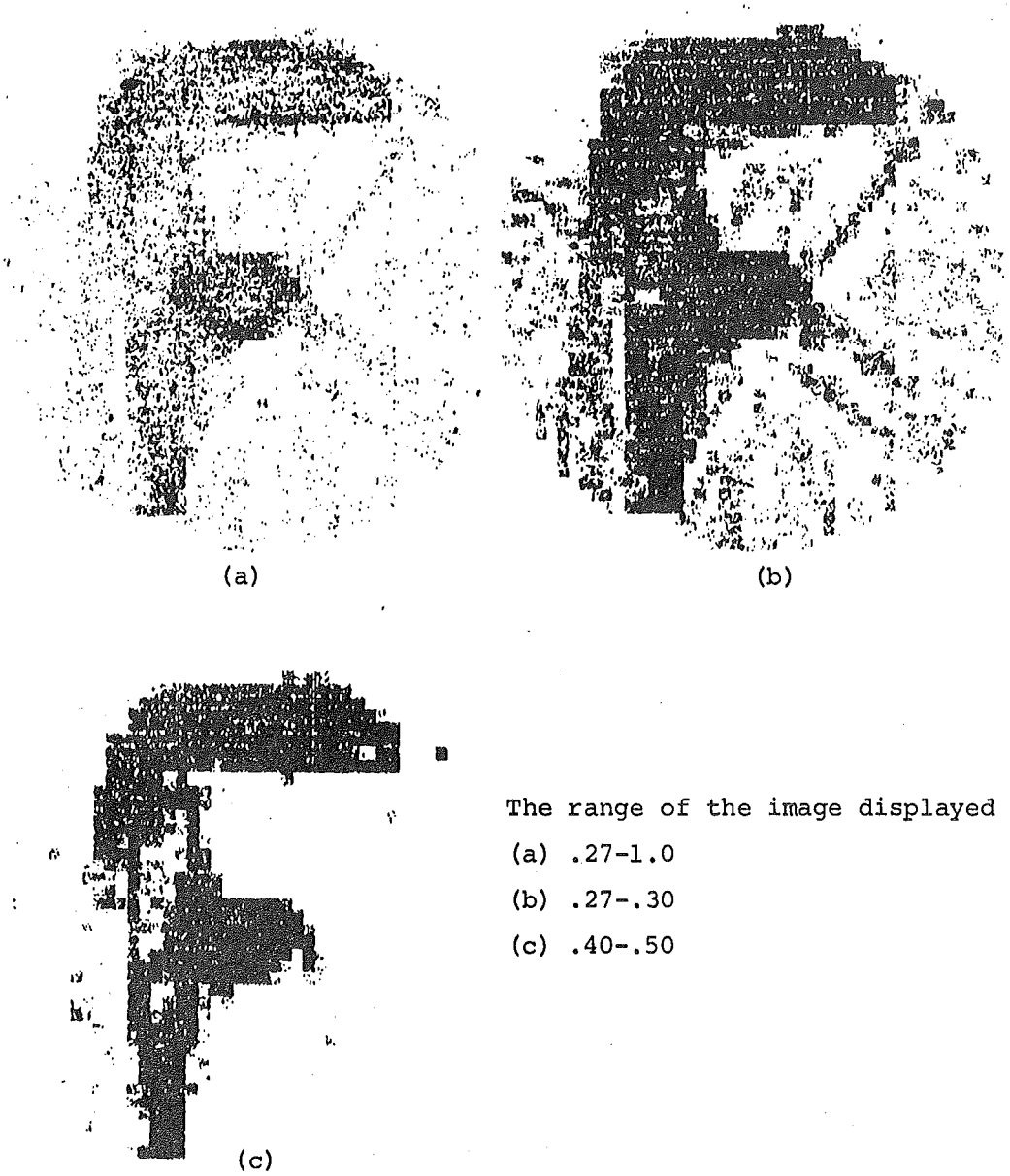

The range of the image displayed is:

(a) .27-1.0

(b) .27-.30

(c) .40-.50

Fig. 6.19 Images computed from measured largest amplitude acoustic propagation path time delays through the upper case F phantom when it is filled with methylated spirit (n = 1.19).

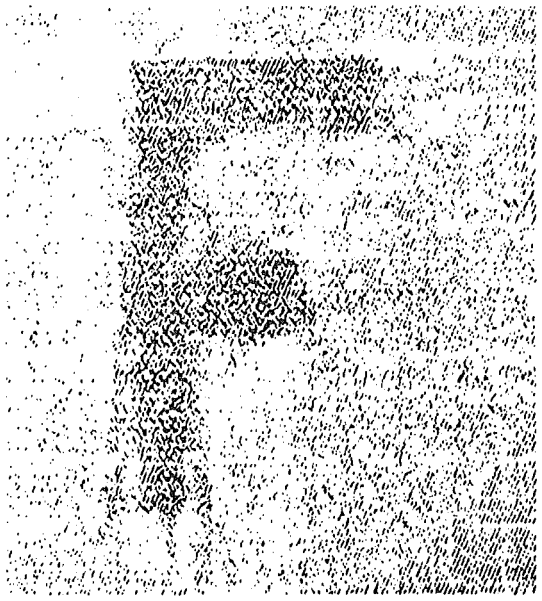

(a)

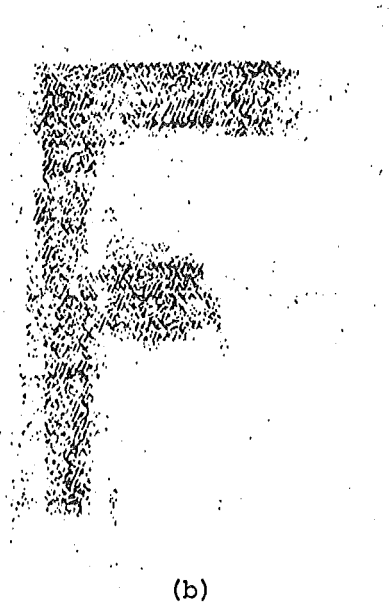

(b)

(c)

(d)

Fig. 6.20 PTO

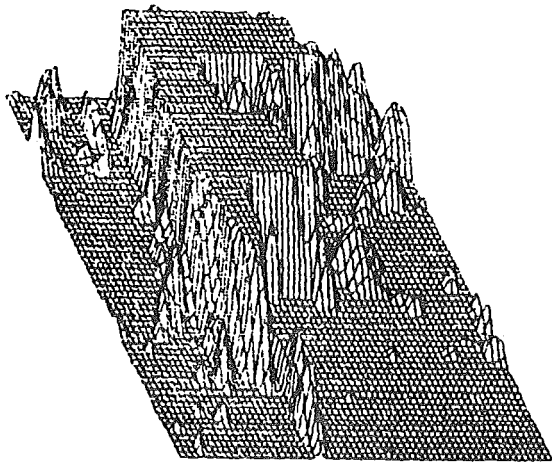

(e)

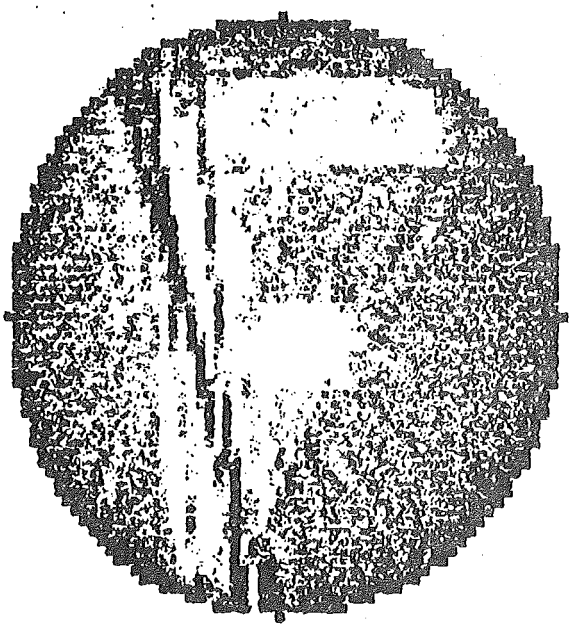

(f)

(g)

The displayed image range is:

(a) 0-1	(b) .27-1.0
(c) .2-.7	(d) .0-.34
(e) .4-.6	(f) .25-.50
(g) .7-.85	

Fig. 6.20 Images computed from 90 projections of the upper case F phantom when it is filled with castor oil (n = 0.985). The time delay of the transmission propagating by the maximum energy path is measured at 63 points on each projection. A negative image computed from 32 projections is shown in (f). Note the bars across the image due to measurement errors. The erroneous measurements are equated with the adjacent measured values to yield the positive image shown in (g).

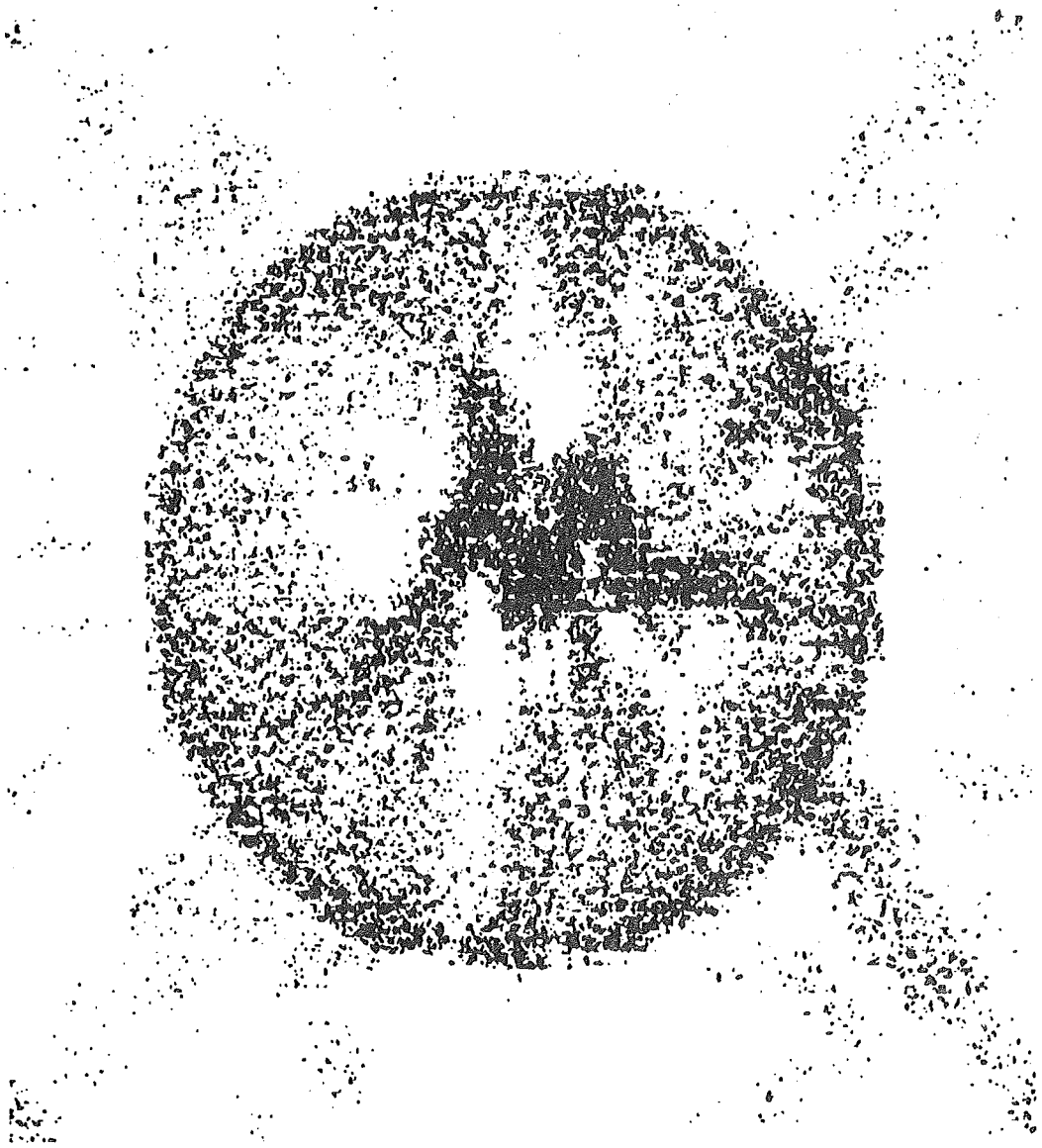

Fig. 6.21 Computed image of a bovine kidney. Each time delay projection is sampled at 45 points spaced 4.5 mm apart, and 40 projections are measured. The modified back projection method together with the Shepp-Logan spatial filter is used to compute the image. Note the fatty connective tissue in the dark central region.

(a)

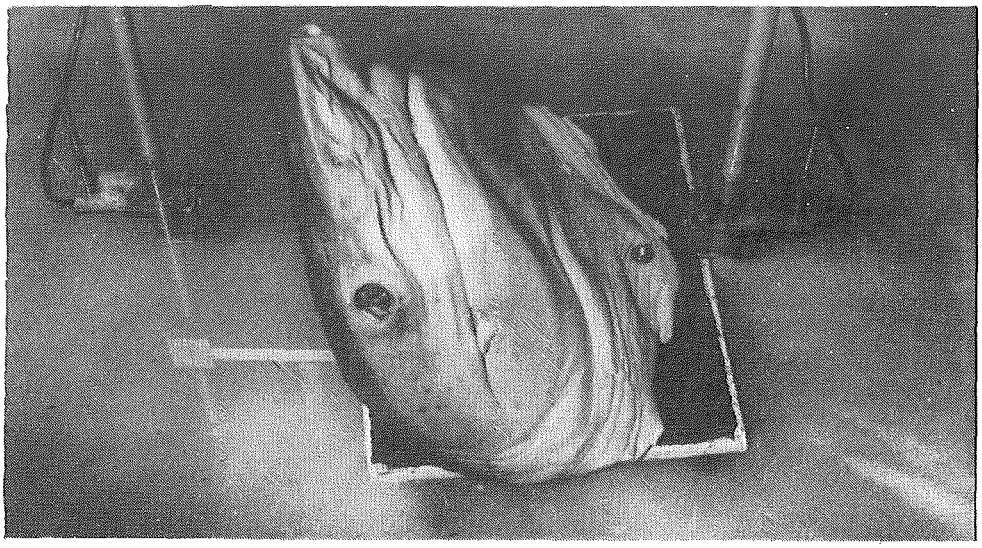

(b)

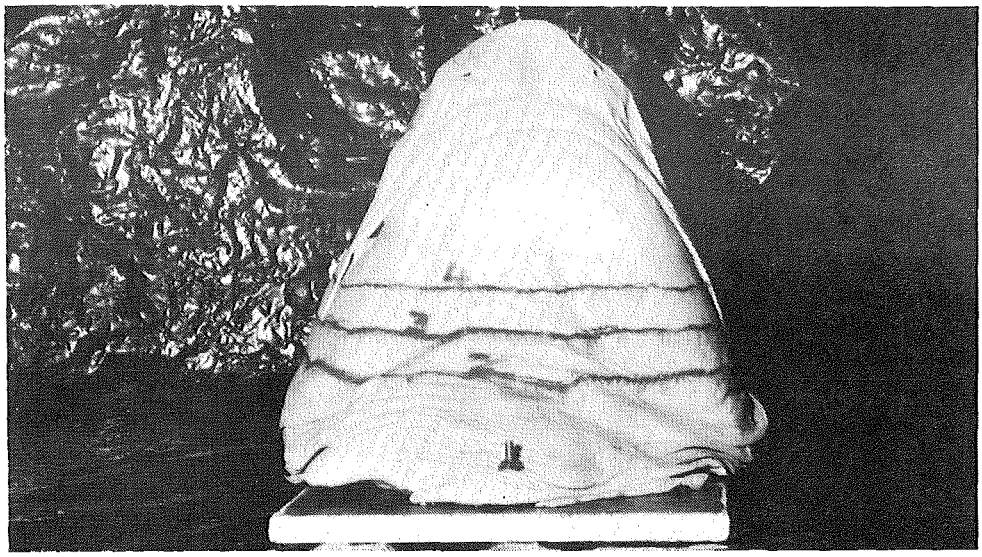

(c)

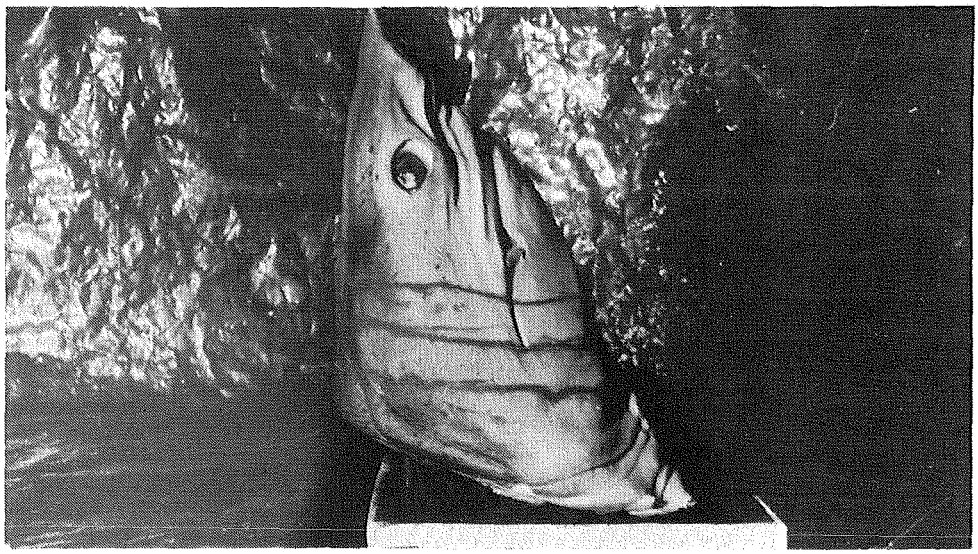

Fig. 6.22 Photographs of the shark's head showing:
(a) The transmitting and receiving transducers
(b) and (c) The axial tomograph planes.

(a) .4-1.0
Nose section

(b) .35-.90
Middle section

(c) .4-.6
Rear section

Fig. 6.23 Images computed from measured projections of the shark head cross sections shown in figs 6.22(b) and (c).

(a)

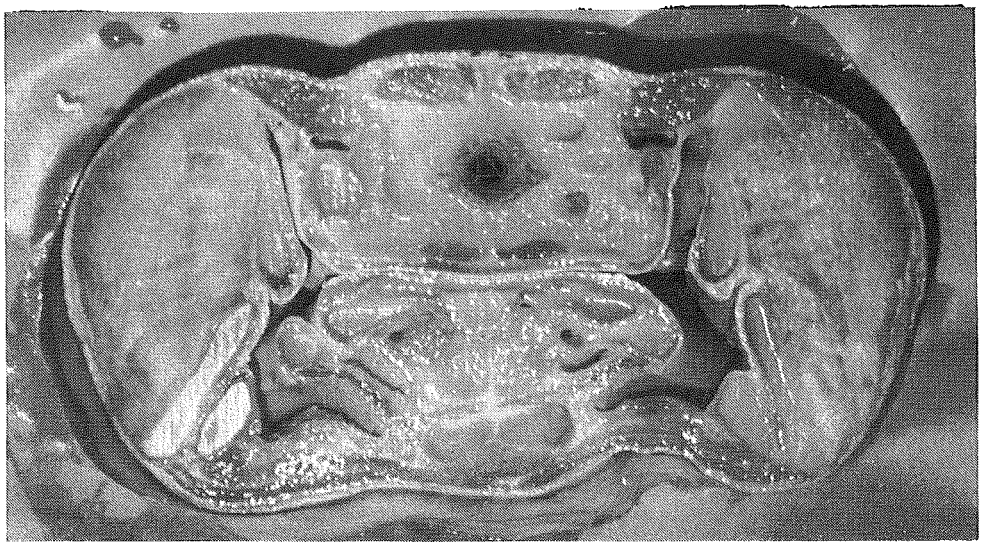

(b)

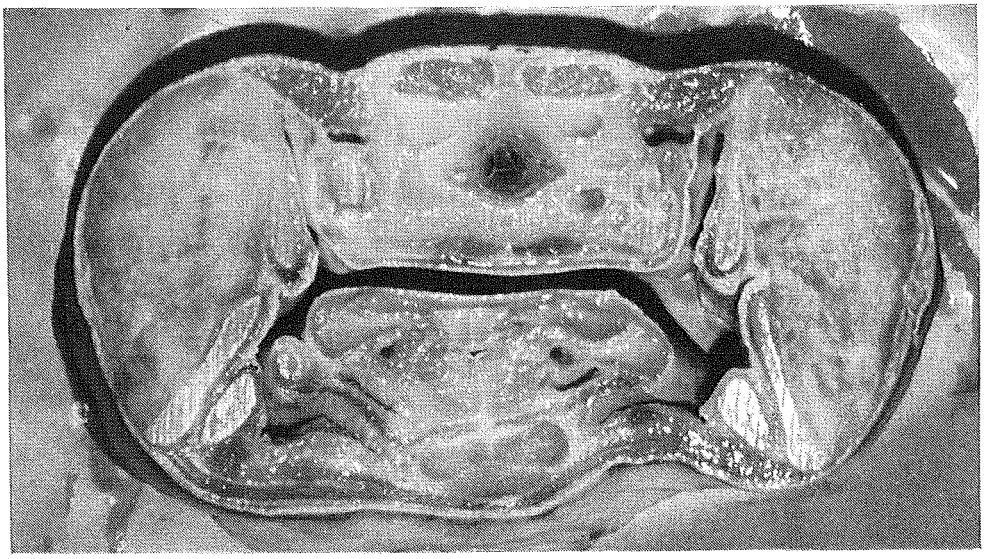

(c)

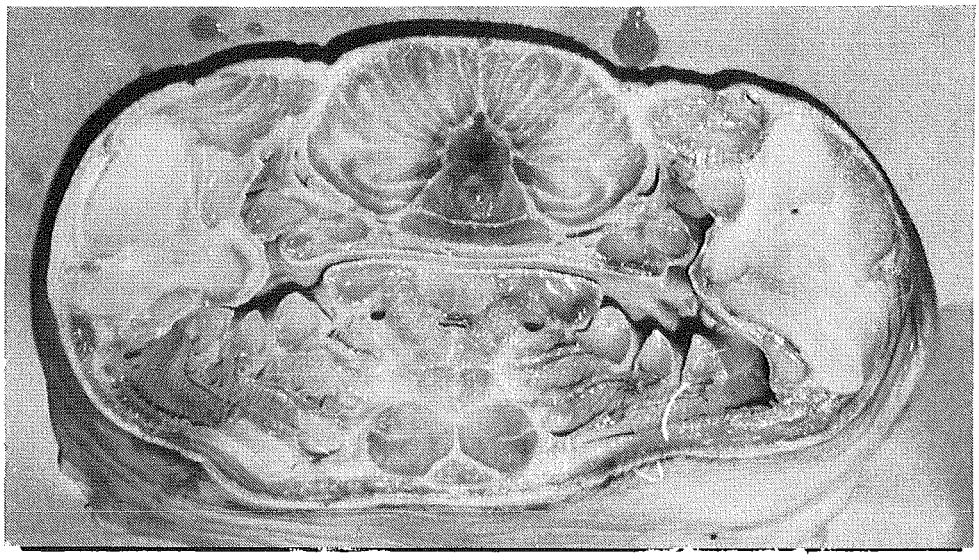

Fig. 6.24 Photographs of the actual cross sections through the shark's head at the positions shown in figs 6.22(b) and (c). Compare (a)-(c) above with figs 6.23(a)-(c).

CHAPTER SEVEN

CONCLUSIONS AND SUGGESTIONS FOR FURTHER RESEARCH

7.1 SUMMARY OF TECHNIQUES AND RESULTS

An ultrasonic transmission tomographic system has been constructed and images have been obtained with it. The actual quantity which is imaged is the acoustic velocity distribution throughout a cross-section of the body.

The image reconstruction procedure involves two main steps. First, it is necessary to measure a set of time delay projections corresponding to the most direct propagation paths between the transmitting and receiving transducers. Second, the image must be reconstructed without introducing computational artefacts. Because the funding for the work described in this thesis was very limited, it was only possible to build systems that make measurements tediously and reconstruct images slowly (by comparison with the state of the art). However, a design for a practicable, efficient measurement and image reconstruction system is described (see section 7.4).

Images can be rapidly reconstructed from measurements when the Fourier reconstruction method and the fast Fourier transform are utilized. Unfortunately, an accurate reconstruction requires the use of a transform with effectively infinite limits rather than the finite sized transform (i.e. a Fourier series) which is implemented on a computer. The finite sized transforms introduce additional artefacts, caused by the sampling process (c.f. Bergland, 1969). The modified back projection method, while being appreciably slower than the Fourier method, introduces negligible extra artefacts other than those due to the unavoidable incompleteness of any practical set of measured projections (c.f. Lewitt and Bates, 1978a,b,c, Lewitt, Bates and Peters 1978). Measurement noise is found to be a major contributor to those artefacts (in the computed image) which possess a high spatial frequency content. The effect of the measurement noise is reduced when the Shepp-Logan spatial filter is used to modify the projections. In addition, this filter produces only a small amount of

ripple or overshoot at sharp discontinuities in the modified projections.

Measurement of the time delays for the most direct propagation path (the path closest to a straight line) between the transmitting and receiving transducers is not straightforward. The results obtained from simulations and measurements based on the shortest acoustic propagation time show that acoustic refraction tends to reduce the high spatial frequency variations in the projections and, hence, in the computed images. In particular, high velocity regions are imaged as occupying an increased area. Thus details of regions adjacent to a high velocity region are obscured, to some extent, in the computed image.

The results of simulations and measurements based on the propagation time of the maximum energy acoustic pulse suggest that the edges of strongly refracting regions can be accurately defined in the computed image. These results also show that the computed acoustic velocities tend to be incorrect near the edges of a strongly refracting region.

The theoretical basis of acoustic propagation has been examined (see chapter 3). Equations are developed to describe acoustic wave propagation in an inhomogeneous medium. Only linear signal interactions with the medium are considered. So, the equations are valid only for signals of "small" amplitude. An improvement to the Rytov approximation is evaluated for scattering from a penetrable cylinder. The computations are restricted to a single cylinder in which the velocity does not vary. Analytical solutions for the scattered field are compared with the results obtained using the various approximations. The additional accuracy obtained with the improved Rytov approximation is greatest in the far field of the scatterer.

The computed images presented in chapter 6 are not only of phantoms but also of biological specimens. The physiology of biological specimens is quite variable and measurements are not easily duplicated. Thus, phantoms were extensively used to evaluate the performance of the acoustic

transmission imaging system. The phantoms examined are tabulated in table 7.1 together with the measurement parameters and reconstruction details. The conclusion drawn from these phantom studies is that the potential of ultrasonic transmission tomography is greatest for bodies throughout which the acoustic velocity shows little variation (less than 5%, say).

7.2 POSSIBLE APPLICATIONS

One possible application of ultrasonic transmission tomography is the measurement of fluid flow distributions (e.g. blood circulation, exhaust systems, pipe and channel flows).

Another application is to image timber defects before milling. MacDonald (1976) has used mechanically scanned ultrasonic transducers to measure the time delay through a plank immersed in water. A time delay shadowgraph (c.f. section 1.6) of a plank is formed. Wood is anisotropic with respect to the sound velocity (up to three times greater along the grain than across it), so knots, rot and splits can be readily detected by ultrasonic through transmission. Timber savings of 15-35% are claimed for the simple two-dimensional plank measurement system. Cross sections of whole trees could be computed by the methods and techniques used to obtain the results presented in chapter 6. Another promising area of application is the medical diagnosis of growths and cancers in the breasts or testicles. These soft tissue areas contain materials which have a small range of acoustic velocities.

The work reported in this thesis has only been concerned with imaging stationary bodies. Johnson et al. (1975) suggest that useful images can be obtained from measurements of fluids in motion. However, useful results have yet to be reported. The author attempted to image flow patterns in moving fluids, but the experimental difficulties prevented useful results being obtained. A circular cylinder full of water was

stirred at rotational speeds of up to 2600 r.p.m. The transmitting and receiving transducers were scanned across opposite sides of the rotated volume. To obtain a measure of the fluid velocity, two sets of ultrasonic delay projections were measured with the transmitting and receiving transducers being exchanged for the second set. At slow stirring speeds, the differences between the two sets of projections were less than the measurement noise. At speeds high enough to permit useful data to be sensed, it was impossible to prevent air bubbles being stirred into the fluid. These bubbles scattered so much of the ultrasound that the projections again become effectively uninterpretable.

The area of perhaps the greatest potential for ultrasonic transmission tomography is as a clinical aid in the examination of the female breast. The breast exhibits fairly small velocity (less than 5% relative to water) and density variations. Thus conventional pulse-echo imaging systems must make use of very low intensity echoes, whereas transmission systems can operate with whatever ultrasonic signal levels are convenient and safe. In addition, the ultrasonic ray paths are nearly straight (c.f. fig. 12, Glover and Sharp, 1977) and image distortion due to refraction is minimal.

With conventional breast X-ray examinations, the presence of growths (or lumps) is inferred from evidence of calcification in the milk ducts. The linear dimensions of the calcifications are often less than 1 mm, whereas the growths may be several centimetres across. Also, the examination exposes the breast to quite a high X-ray dose (typically 1 rad.). The problem of risk versus benefit in breast X-ray examinations has been reduced to simplistic terms for public comprehension and has caused widespread concern. Lester (1977) discusses the clinical and radiological aspects of mamography and concludes that the benefits to the patient outweigh the risks. In a statistical study of breast X-ray examinations, Gregg (1977) concludes that women between the ages of 34 and

50 benefit greatly from mamography. However, for women between the ages of 20 and 34, randomly subjected to breast X-ray examinations, the benefits are marginal. One will die (within five years) as a result of the examination because of a radiation induced cancer for every two that survive five years because an existing cancer is detected and removed (i.e. the odds are not as good as for Russian roulette).

Ultrasonic irradiation at the levels used for clinical diagnosis appears quite safe. However, if a resolution of the order of 1 mm is to be achieved then quite small transducers, operating at high frequencies (say 20 MHz), are probably necessary. It is possible that the higher intensities, which would consequently have to be used, might be dangerous. However, the ultrasonic intensities required for transmission imaging are much less than those required for pulse-echo imaging (c.f. fig. 1.1).

A patient with a palpable lump in a breast will request a breast examination because it is obviously needed. However, other patients will request a breast examination because a breast does not "feel right". Even though breast cancer is often not found in such patients, it sometimes develops some years after an X-ray examination. The high X-ray dose absorbed during the examination may actually stimulate the growth, but it should be remembered that another possibility is that changes in the mechanical properties of the breast are a precursor to cancer.

Routine screening of many patients by means of ultrasonic transmission tomography would permit changes in the acoustic propagation characteristics of female breasts to be correlated with age, child bearing, lactation and cancer. Glover and Sharp (1977) have already produced ultrasonic transmission tomographs of large breast cancers. It is preferrable to monitor, detect and remove cancer growths before breast removal is required. Breast tissue is quite variable and may be fibrous or fatty.

Thus images of both of a patient's breasts are needed so that significant, rather than apparent, discrepancies can be detected and closely examined. The routine use of ultrasound for female breast examinations could well permit many breast cancers to be detected without the risk of an X-ray examination stimulating a cancer growth, especially for women in the 20-34 year age group.

7.3 SIGNAL DISPERSION AND DETECTION

Each ultrasonic transmission measurement is used to estimate the propagation time between the two transducers. The transmission must have a wide bandwidth if the estimate is to be made to a useful accuracy. Attenuation of an acoustic transmission is usually frequency dependent and the higher frequency components of an acoustic signal are attenuated most. Dispersive absorption (i.e. different attenuation for various frequency components) is similar to X-ray beam hardening (c.f. section 2.4). This by itself is not serious provided the attenuation effects can be eliminated a posteriori. In general, this is not possible. However, with the hyperbolic phase encoding system (described in sections 4.4 and 4.5), the frequency of the transmission is proportional to time. Hence time dependent signal gain can be introduced electronically to counteract the frequency dependence of the acoustic portion of the signal path. An estimate of the required gain-time profile is obtained from a preliminary transmission, and then the gain is varied during a second transmission over the same path.

Velocity dispersion (the frequency dependence of the propagation velocity) affects the relative phase of spectral components of a received pulse. If the velocity dispersion is large enough, the pulse is not recognizable and the matched filter cannot give optimal detection. Fortunately, velocity dispersion in biological materials is virtually negligible in the

frequency range [1 MHz, 10 MHz] used for diagnostic ultrasonics (c.f. Erickson 1974, and Wells 1969, p5).

For ultrasonic transmission tomography, improved resolution can only be obtained by using larger bandwidths and higher ultrasonic frequencies. Such frequencies would have to be higher than 10 MHz and velocity dispersion could well become a problem. However, the relative attenuation of the spectral components is less for a given bandwidth at higher frequencies.

The amount of velocity dispersion present for a selected propagation path can be estimated from hyperbolic phase modulation time delay measurements. The power spectrum of the base band signal measured by the detection system contains a series of peaks. Each peak corresponds to a particular ultrasonic propagation path and it would approximate a delta function for an ideal system of infinite bandwidth, provided the signals propagate in a dispersionless medium. If the propagation paths were dispersive, the response of the receiver to a signal propagating along a single path would be spread over many adjacent spectral components. In practice, the spectral components belonging to different propagation paths can usually be separated by standard windowing techniques (c.f. Bergland 1969). The base band signal can then be computed, using the FFT, for a single path. The power spectrum can also be supplemented with zeroes so as to interpolate between the time domain samples of the base band signal (refer to the discussion in section 4.5). Analysis of the times between the zero crossings of the base band signal gives a measure of the ultrasonic velocity dispersion, because each portion of the base band signal corresponds to a particular narrow band of frequencies in the transmitted signal.

The frequency dependence of the ultrasonic attenuation can be measured in the same manner, but allowance must be made for the transducers. Transducer bandwidth effects can be allowed for in the computations, but the beamwidth also changes as the frequency is swept. The signal

amplitude variations due to beamwidth changes can only be eliminated by orienting the transducers so that the propagation path is along the bore sight of each transducer.

7.4 PRACTICAL SYSTEM CONFIGURATIONS

Movement of the body during the transmission measurements produces streaky lines in the reconstructed image. These image artefacts are visible in the acoustic velocity tomographs of the breast published by Glover and Sharp (1977, examine their figs 8 and 9). Such artefacts can be eliminated by completing the measurements in a short enough time (say less than 20 seconds, in clinical practice). Images for use in clinical examinations should be rapidly reconstructed so that the patient can be re-scanned if movement artefacts are observed.

The fourth generation of X-ray scanners (c.f. Chapter 2) surround the patient with a ring of X-ray detectors and use either multiple X-ray sources, or else a source which rotates rapidly around the patient. Multiple X-ray sources and detectors have been used by researchers at the Mayo Institute to freeze the motion of the beating heart (c.f. Johnson et al. 1974, Robb et al. 1974). The mechanical dynamics of the cardiac cycle are derived from computed images of 20 adjacent planes which are obtained at a rate of 60 sets per second (c.f. Sturm et al. 1975).

For an ultrasonic system, the transducer can act as a transmitter or as a receiver of ultrasound. This feature is utilized in the proposed real-time ultrasonic scanner sketched in fig. 7.1. For ease of explanation, only eight transducers are shown in the sketch. The number, denoted by N_T, of transducers needed for a workable system is greater than 100. A cylindrical transducer is able to receive ultrasonic radiation from all directions in the plane of the tomograph. Alekseev (1976) has developed techniques for increasing the bandwidth of such cylindrical transducers.

Each transducer is connected to a saturable, fast-recovery preamplifier. The time T_{ij} for a pulse to propagate from the i^{th} transmitting transducer to the j^{th} receiving transducer is measured by timing hardware attached to the j^{th} preamplifier. The output from each timer is accessed by the computer via a multiplexer. The computer also controls the multiplexer which connects the transmitter to one of the N_T transducers, i.e. the transmitting transducer. Each transmission is received by N_T-1 transducers. Thus N_T (N_T-1) separate measurements are possible (56 for N_T = 8, c.f. fig. 7.1). Since T_{ij} and T_{ji} are usually the same, only $N_T(N_T-1)/2$ measurements are required.

The expense of parallel timing hardware is halved if only half of the transducers are used for the time delay measurements. The receiving transducers are selected as follows. Two semicircles are defined with transducers around the circumference and the transmitting transducer on the common diameter. The transducers on one semicircle are connected to the preamplifiers and timing hardware. After each transmission, the next transmitting transducer is selected along with the next set of receiving transducers. When each transducer has been used for transmission, all possible time delays have been measured for propagation, in one direction, between all of the transducers.

Possible trade-offs between hardware and measurement time are now discussed. If 101 transducers are arranged around the perimeter of a circle, then 50 preamplifiers and timing units are required. Assuming the transmissions are repeated at 1.01 kHz, the minimum measurement time is 0.1 sec. If only a single preamplifier and timing unit is available, then the transmission is repeated 50 times by each transmitting transducer. The preamplifier is connected to each of the 50 receiving transducers for the duration of one transmission. The total measurement time is then 5 secs. The use of say five preamplifiers and timers would make the total

measurement time 1 sec.

Dick et al. (1977) point out that an A.G.C. system is required for reliable time measurements if a straight forward threshold detection timing system is used. The gain is calculated from measurements of the peak value of the received signal. The 50 preamplifiers would be followed by 50 variable gain amplifiers and 50 peak detectors. Thus rapid time delay measurements with a single large amplitude acoustic pulse requires a considerable amount of hardware.

Signal processing can be employed to reduce the amount of hardware without increasing the time required for the measurements. For any transmission, the propagation time delays measured at any two adjacent receiving transducers is usually ordered. The propagation time delay to the transducer farthest from the transmitting transducer is greater than the time delay to the nearest transducer because the propagation distance is greater. Provided the pulses are received in this order, the signals from all of the receiving transducers are added to yield one composite signal. The largest amplitude pulse occurring within a specified time interval in the composite signal is attributed to the signal from a particular receiving transducer. The time at which that pulse occurs is the propagation time delay to the particular transducer. Matched filtering, as discussed in sections 4.3 and 4.4, is required to minimize the overlap of pulses. If the pulses from adjacent receiving transducers overlap, then the signal from every second (or third or fourth) receiving transducers is summed to yield two (or three or four) composite signals. A sufficient number of composite signals is chosen so as to minimize the ambiguity associated with attributing a particular pulse in the composite signal to a particular transducer.

The signal summation method of hardware reduction should be satisfactory for diaphanous objects but is likely to introduce significant errors if strong acoustic refractions or reflections occur. When the signal summation method is not used, hardware reductions are obtained by

increasing the total measurement time. It is worth noting, that if the signal at every transducer is recorded, then both B-scan and velocity distribution images can be computed. The two sets of information can be combined to compute more accurate images.

PHANTOM	FIGURE	MEASUREMENT METHOD	NUMBER OF PROJECTIONS	NUMBER OF SAMPLES PER PROJECTION	RECONSTRUCTION METHOD	FILTER EMPLOYED
Circular aluminium cylinder	6.11	ST	90	41	MBP	SL
Circular aluminium cylinder	6.12	ME	90	41	MBP	SL
Round mylar phantom	6.13	ST	32	33	MBP	SL
Oblong mylar phantom	6.14	ST	32	33	MBP	SL
Composite mylar phantom	6.15	ST	30	40	FFT	P
Three circularly symmetric mylar cylinders	6.17	ME	90	101	MBP	SL
Mylar F cylinder containing:						
1. methylated spirit	6.19	ME	32	45	MBP	SL
2. Castor oil	6.20	ME	90	63	MBP	SL

Table 7.1 Summary of phantom measurement parameters:

ST	Shortest time	ME	Maximum energy
MBP	Modified back projection	FFT	Fast Fourier transform
SL	Shepp-Logan	P	Prabhu et al.

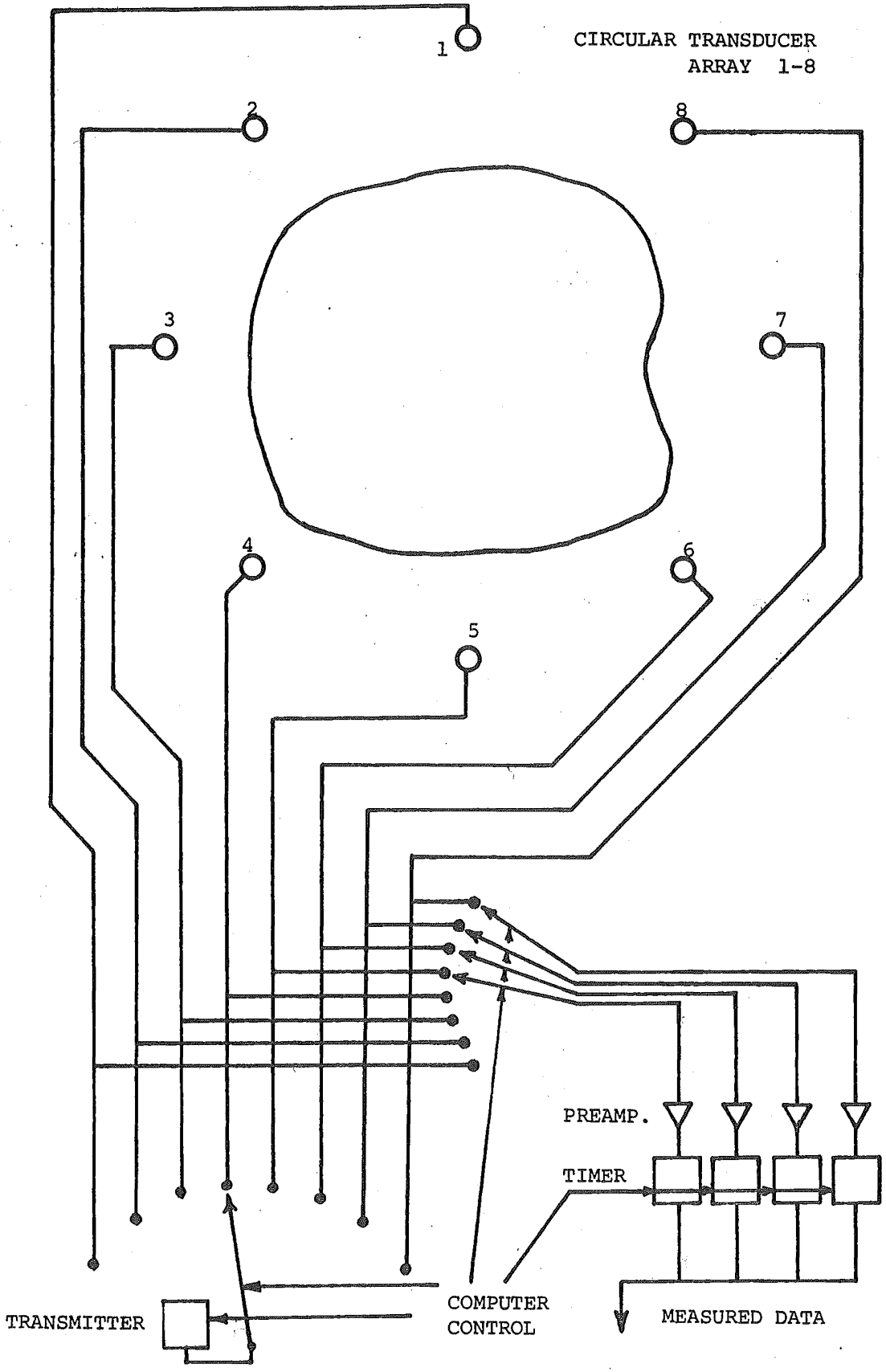

Fig. 7.1 Schematic of the real-time ultrasonic transmission imaging scanner. Multiplexer positions are for transducer 4 transmitting and 5, 6, 7 and 8 receiving.

REFERENCES

Abramowitz M and Stegun IA (Eds) 1965 Handbook of Mathematical Functions, Dover Publications, N.Y.

Alekseev BN 1976 Increasing bandwidth of a cylindrical piezoceramic transducer by means of two transition layers. Sov. Ph. A. R. 22 (2) 101-104.

Allen JR 1972 Pulse analysis of antennas, M.E. thesis, University of Canterbury, Christchurch, N.Z.

Altmann F and Waltner J 1959 The treatment of Meniere's disease with ultrasonic waves: a preliminary report Arch. Otolaryng. 69: 1 S7.

Altshuler S 1958 Variational principles for the wave function in scattering theory Phys. Rev. 109 (5) 1830-1836.

Alvarez RE and Macovski A 1975 Utilization of simple energy-spectrum measurements in X-ray computerized tomography, in Proc. of Conf. On Processing for 2-D and 3-D Reconstructions from Projections, Stanford, Aug. 4-7 (Opt. Soc. Am) MD1-4.

Amisano P 1955 Three-dimensional stratigraphic examination - Axial transverse stratigraphy. Part II Am. J. Roent. Rad. Ther. Nucl. Med. 74 777-789.

An S, Tao-Hsin W, Shih-Yuan A, Shih-Lian C, Hsiang-Hue W, Chih-Chang H and Kuo-Juei Y 1962 The use of pulsed ultrasound in clinical diagnosis Chin. med. J. 81 315-325.

Andrew DS 1964 Ultrasonography in pregnancy - an inquiry into its safety. Br. J. Radiol. 37 185-186.

Andrews JR and Starva RJ 1937 Planigraphy II. Mathematical analysis of the methods, description of the apparatus and experimental proof Am. J. Roent. Rad. Ther. 38 145-151.

Arslan M 1960 Ultrasonic surgery to the labyrinth in patients with Meniere's disease, in Proc. 12th Internat. Surg. Congress, Rome 3 S2398.

Baker D 1969 Pulsed ultrasonic doppler flowmeter - Biological and engineering applications IEEE Ultrasonics Symposium (Sept.) 24-26.

Ballantine HT, Bolt RH, Hueter TF and Ludwig GD 1950 On the detection of intracranial pathology by ultrasound Science N.Y. 112 525-528.

Ballantine HT, Hueter TF and Bolt RH 1954 On the use of ultrasound for tumour detection JASA26 (4) 581.

Barbe DF, Baker WD and Davis KL 1978 Signal processing with charge-coupled devices IEEE Trans. Elec. Dev. ED-25 (2) 108-124.

Basauri L and Lele PP 1962 A simple method for production of trackless lesions with focussed ultrasound: statistical evaluation of the effects of radiation on the central nervous system of the cat J Physiol., Lond. 160 513-534.

Bates RHT and Peters TM 1971 Towards improvements in tomography N.Z. J. Sci. 14 883-896.

Bates RHT and Ng FL 1972 Polarisation-source formulation of electro-magnetism and dielectric-loaded waveguides Proc. IEE 119 (11) 1568-1574.

Bates RHT, Lewitt RM, Peters TM and Smith PR 1975 in Image Processing for 2-D and 3-D Reconstructions from Projections, Stanford, Aug. 4-7, (Opt. Soc. Am.), WA2-1 to 4.

Bates RHT, Boerner WM and Dunlop GR 1976 An extended Rytov approximation and its significance for remote sensing and inverse scattering Optics Comm. 18 421-423.

Bates RHT and Dunlop GR 1977 Inverse scattering and tomography, in Ultrasonics International 1977 (Conference Proceedings) IPC Science and Technology Press, Guildford, England.

Baum G and Greenwood I 1958 The application of ultrasonic locating techniques to ophthalmology A.M.A. Arch. Ophthal. 60 263-297.

Baum G and Greenwood I 1961 Orbital lesion location by three-dimensional ultrasonography N.Y. State J. Med. 61 4149-4157.

Baum G 1973 Ultrasound mamography, in Second World Congress on Ultrasonics in Medicine, Rotterdam June 4-8.

Beattie JW 1975 Tomographic reconstruction from fan beam geometry using Radon's integration method IEEE Trans. Nucl. Sci. NS-22 (1) 359-363.

Bergland GD 1969 A guided tour of the fast Fourier transform IEEE Spectrum 41-52.

Berry MV and Gibbs DF 1970 The interpretation of optical projections Proc. Roy. Soc. Lond. A314 143-152.

Bocage AEM 1922 French Patent #536464.

Böck J and Ossoinig K (Eds.) 1971 Ultrasonographia Medica, I World Congress, Ultrasonic Diagnostics in Medicine and SIDUO III, Wiener Medizinische Akademie, Vienna.

Booth N (Ed.) 1975 Acoustical Holography Vol. 6, Plenum Press, New York - London.

Born M and Wolf E 1970 Principles of Optics, Pergamon Press, London.

Boys JT and Dunlop GR 1978a Economical stepper motors for speed control applications, submitted to IEE Journal on Electric Power Applications.

Boys JT and Dunlop GR 1978b Pulse multiplication by four, submitted to IEE Journal on Electronic Circuits and Systems.

Bracewell RN 1956 Strip integration in radio astronomy Aust. J. Phys. 9 198-217.

Bracewell RN and Riddle AC 1967 Inversion of fan-beam scans in radio astronomy Astrophys. J. 150 427-434.

Bracewell RN and Wernecke SJ 1975 Image reconstruction over a finite field of view J. Opt. Soc. Am. 65 (11) 427-434.

Braddick HJJ 1963 The Physics of Experimental Method (2nd Ed.) Chapman and Hall, London.

Brekhovskikh LM 1960 Waves in Layered Media, Academic Press, New York.

Brock RD et al. 1973 Ultrasound and chromosome aberrations Med. J. Aust. 2 533-536.

Brooks RA and Di Chiro G 1976 Principles of computer assisted tomography (CAT) in radiographic and radioisotopic imaging Phys. Med. Biol. 21 689-732.

Brooks RA and Weiss GH 1976 Interpolation problems in image reconstruction S.P.I.E. Opt. Inst. in Med. 90 (5) 313-319.

Buckton KE and Baker CK 1972 An investigation into possible chromosome damaging effects of ultrasound on human blood cells Br. J. Radiol. 45 340-342.

Burckhardt CB 1978 Speckle in ultrasound B-mode scans IEEE Trans. Son. and Ultrason. SU-25 (1) 1-6.

Burnett CR, Hirschberg JG and Mack JE 1958 Handbook of Physics (Condon EU and Odishaw H Eds) McGraw-Hill, New York, 6-92.

Burrel GA 1971 Transients on antennas, Ph.D. thesis, University of Canterbury, Christchurch, New Zealand.

Carter AWL and Wild JP 1964 Some correction processes for annular aerial systems Proc. Roy. Soc. A282 252.

Chernak ES, Rodriquez-Antunez A, Jelden GL, Dhaliwal RS and Lavik PS 1975 Use of computed tomography for radiation-therapy treatment planning Radiology 117 (3) 613-614.

Chernov L 1967 Wave Propagation in a Random Medium, Dover, New York.

Clendinning J and Oliver JG 1969 Principles and Use of Surveying Instruments (third edition) Van Nostrand Reinhold, London.

Coakley WT et al. 1972 Examination of lymphocytes for chromosome aberrations after ultrasonic irradiation Br. J. Radiol. 45 328-332.

Collin RE 1955 Theory and design of wide-band multisection quarter-wave transformers Proc. I.R.E. 179-185.

Coleman DJ and Carlin B 1967 Transducer alignment and electronic measurement of visual axis dimensions in the human eye using time-amplitude ultrasound, in Ultrasonics in Ophthalmology Symp., Münster Karger, Basel 207-214.

Computers in Biology and Medicine 6 (4) October, 1976. Special issue: Advances in picture reconstruction - theory and applications.

Cooley JW and Tukey JW 1965 An algorithm for the machine generation of complex Fourier series Math. Comp. 19 297-301.

Cormack AM 1963 Representation of a function by its line integrals, with some radiological applications, I J. Appl. Phys. 34 2722-2728.

Cormack AM 1964 Representation of a function by its line integrals, with some radiological applications, II J. Appl. Phys. 35 2908-2912.

Cormack AM 1973 Reconstruction of densities from their projections with applications in radiological physics Phys. Med. Biol. 18 (2) 195-207.

Crowther RA, de Rosier DJ and Klug A 1970 The reconstruction of a three-dimensional structure from projections and its application to electron microscopy Proc. Roy. Soc. Lond. A317 319-340.

Curtis JC 1965 Action of intense ultrasound on the intact mouse liver, in Ultrasonic Energy (Kelly E - Ed.) University of Illinois Press, Urbana, U.S.A., 85-109.

Dainty JC and Shaw R 1974 Image Science; principles, analysis and evaluation of photographic-type imaging processes, Academic Press, London.

Das Y and Boerner WM 1976 Modulation transfer functions of tomographic systems Med. Biol. Eng. 14 65-68.

Das Y and Boerner WM 1978 On radar target shape estimation using algorithms for reconstruction from projections IEEE Trans. Ant. Prop. AP-26 (2) 274-279.

Das Y 1977 Application of concepts of image reconstruction from projections and Radon transform theory to radar target identification, Ph.D. Thesis, University of Manitoba, Canada.

de Rosier DJ and Klug A 1968 Reconstruction of three-dimensional structures from electron micrographs Nature 217 130-134.

de Silets CS, Fraser JD and Kino GS 1978 The design of efficient broadband piezoelectric transducers IEEE Trans. Son. Ultrason. SU-25 (3) 115-125.

de Vlieger M, White DN and McCready VR (Eds) 1974 Ultrasonics in Medicine, Proceedings of the Second World Congress, Excerpta Medica Amersterdam.

Dick DE, Bay HP and Carson PL 1977 Hardware design of an ultrasound CT scanner Biomed. Sci. Instrum. 13 31-35.

Di Franco JV and Rubin WL 1968 Radar Detection, Prentice-Hall, N.J.

Donald I, MacVicar J and Brown TG 1958 Investigation of abdominal masses by pulsed ultrasound Lancet 1 (7032) 1188-1194.

Doornbos P and Somer JC 1972 An electronically variable analogue delay line achieved by fast consecutively commutated capacitors, Progress Report No. PR3, Institute of Medical Physics TNO, Utrecht, The Netherlands, p.109.

Du Bois JL 1970 Larger aperture acoustic image converters, in Acoustical Holography Vol. 2, (Metherell and Lamore Eds.) Plenum Press, New York-London, 59-68.

Duck FA 1975 In Summary of Ultrasonics Conference 1975 Ultrasonics 159.

Dunlop GR, Boerner WM and Bates RHT 1976 On an extended Rytov approximation and its comparison with the Born approximation, in Digest of

Papers, AP-S International Symposium, IEEE catalog no. 76 CH1121-3AP.

Dunlop GR and Boys JT 1978 A versatile A.G.C. for pulse transmission systems, submitted to Ultrasonics.

Dunn F and Fry FJ 1971 Ultrasonic threshold dosages for the mammalian central nervous system IEEE Trans. Biomed. Eng. BME-18 253-256.

Dussik KT 1942 Possibility of using mechanical high frequency vibrations as a diagnostic aid Z. Neurol. Psychiat. 174 153-168.

Dussik KT, Dussik F and Wyt L 1947 Auf dem wege zur hyperphonographie des gehirnes Wien. med. Wschr. 97 425-429.

Dussik KT 1954 Am. J. Phys. Med. 33.

Edholm P 1960 The tomogram. Its information and content Acta Radiol. Suppl. 193

Eggleton RC and Johnston KW 1974 Real time mechanical scanning system compared with array techniques, in 1974 Ultrasonics Symposium, IEEE catalogue No. 74, CHO896-1SU, 16-18.

El-Sum HMA 1952 Ph.D. Thesis, Stanford University.

Eriksen KR, Fry FJ and Jones JP 1974 Ultrasound in medicine - a review IEEE Trans. Son. Ultrason. SU-21 (3) 144-170.

Eriksen KR, O'Loughlin BJ, Flynn JJ, Pisa EJ, Wreede JE, Greer KE, Stauffer B and Metherell AF 1975 Through-transmission acoustical holography for medical imaging - a status report, in Acoustical Holography Vol. 6 (N. Booth Ed.) Plenum Press, New York-London, 15-55.

Etter LE (Ed.) 1965 The Science of Ionizing Radiation, C.C. Thomas, Springfield, Illinois.

Feigenbaum H, Zaky A and Waldhausen JA 1967 Use of reflected ultrasound in detecting pericardial effusion Am. J. Cardiol. 19 84-90.

Felsen LB and Marcuvitz N 1973 Radiation and Scattering of Waves, Prentice-Hall, Englewood Cliffs, N.J.

Ferrer PL, Bottlieb S, Kallos N, Wexler H and Miale A 1975 Applications of diagnostic ultrasound and radionuclides to cardiovascular diagnosis. Part III. Seminars in Nuclear Medicine 15 (4).

Firestone FA 1942 U.S. Patent #2,280,226.

Firestone FA 1946 The supersonic reflectoscope, an instrument for inspecting the interior of solid parts by means of sound waves. JASA 17 287-299.

Fitch CE 1964 An optical Schlieren system for ultrasound imaging Materials Evaluation 22 (3) 124-127.

Foster FS and Hunt JW 1978 The design and characterization of short pulse ultrasound transducers Ultrasonics 16 (3) 116-122.

Franklin D, Baker D, Ellis R and Rushmer R 1959 A pulsed ultrasonic flowmeter I.R.E. Trans. on Med. Electronics ME-6 (4) 204-206.

Franklin D, Schlegel W and Rushmer R 1961 Blood flow measured by Doppler frequency shift of back scattered ultrasound Sci. 132 564-565.

Fraser J, Havlice J, Kino GS, Leung W, Shaw HG, Joda K, Waugh J, Winslow DK and Zitelli LT 1974 A two-dimensional electronically focussed imaging system, in 1974 Ultrasonics Symposium Proceedings, IEEE Catalogue No. 74 CHO 896-1SU, 19-23.

French LA, Wilk JJ and Neal D 1951 Attempts to determine harmful effects of pulsed ultrasonic vibrations Cancer N.Y. 4 342-344.

Fritz-Niggli H and Böni A 1950 Biological experiments on drosophila melanogaster with supersonic vibrations. Science N.Y. 112 120-122.

Frus JR and Kuo BC 1977 Waveform sensing closes the loop in step motor control Prod. Eng. 24 (2) 47-49.

Fry WJ, Wulff VJ, Tucker D and Fry FJ 1950 Physical factors involved in ultrasonically induced changes in living systems. I. Identification of non-temperature effects JASA 22 867-876.

Fry WJ, Leichner GH, Okuyama D, Fry FJ and Fry EK 1968 Ultrasonic visualisation system employing new scanning and presentation methods JASA 44 (5) 1324-1338.

Fry FJ, Kossoff G, Eggleton RC and Dunn F 1970 Threshold ultrasonic dosages for structural changes in the mammalian brain JASA 48 (6) 1413-1417.

Gabor D 1948 A new microscopic principle Nature 161 777.

Gabor D 1949 Microscopy by reconstructed wavefronts I Proc. Roy. Soc. (London) A197 454.

Gado M and Phelps M 1975 Peripheral zone of increased density in cranial computed tomography Radiology 117 (1) 71-74.

Garg AG and Taylor AR 1967 An investigation into the effect of pulsed ultrasound on the brain. Ultrasonics 5 208-212.

Gericke OR 1966 Experimental determination of ultrasonic transducer frequency response Materials Evaluation 24 409-411.

Gilbert PFC 1972 Iterative methods for the reconstruction of three-dimensional objects from projections J. Theor. Biol. 36 105-117.

Gilbert BK et al. 1976a A real-time hardware system for digital processing of wide-band video images IEEE Trans. Comp. C-25 (11) 1089-1100.

Gilbert BK et al. 1976b A programmable dynamic memory allocation system for input/output of digital data into standard computer memories at 40 Megasamples/s IEEE Trans. Comp. C-25 (11) 1101-1109.

Glover GH and Sharp JC 1977 Reconstruction of ultrasound propagation speed distributions in soft tissue: time-of-flight tomography IEEE Trans. Son. Ultrason. SU-24 (4) 229-234.

Goetz GG 1970 Real-time holographic reconstruction by electro-optic modulation Appl. Phys. Lett. 17 (July) 63.

Goldman RG 1962 Electronic acoustic image converter JASA 34 514-515.

Goldstein H 1953 Classical Mechanics, Addison Wesley, Mass.

Goodman JW 1968 Introduction to Fourier optics, McGraw-Hill, N.Y.

Goodman JW 1975 Statistical properties of laser speckle patterns. Laser speckle and related phenomena (J.C. Dainty Ed.) Springer-Verlag 9-75.

Gordon D 1959 Echoencephalography: ultrasonic rays in diagnostic radiology Br. Med. J. i 1500-1504.

Gordon R, Bender R and Herman GT 1970 Algebraic reconstruction techniques (ART) for three-dimensional electron microscopy and X-ray photography J. Theor. Biol. 29 471-481.

Gori E and Guattari G 1971 Effects of coherence on the degree of freedom of an image J. Opt. Soc. Am. 61 36.

Gottlieb S, Sheps D, Myerbury RJ and Miale A 1975 Applications of diagnostic ultrasound and radionucleidesto cardiovascular diagnosis. Part I Acquired cardiovascular disease in the adult. Seminars in Nuclear Medicine 15 (4) 353-386.

Grant DG 1972 Tomosynthesis: a three-dimensional radiographic imaging technique IEEE Trans. Biomed. Eng. BME-19 20-28.

Green PS, Macovski A and Ramsey SD 1970 Coherent optical detection of ultrasonic images using electronic scanning App. Phys. Lett. 16 265.

Green PS 1971 A new liquid surface-relief method of acoustic image conversion, in Acoustical Holography Vol. 3, Plenum Press, New York-London (AF Metherell Ed.).

Green PS (Editor) 1974 Acoustical Holography Volume 5, Plenum Press, New York-London.

Greenleaf JF, Johnson SA, Lee SL, Herman GT and Wood EH 1974 Algebraic reconstruction of spatial distributions of acoustic absorption within tissue from their two-dimensional acoustic projections, in Acoustical Holography Vol. 5 (P.S. Green Ed.) Plenum Press, New York-London 591-603.

Greenleaf JF, Johnson SA, Samayoa WF and Duck FA 1975 Reconstruction of spatial distributions of refraction indices in tissue from time of flight profiles, in Topical meeting on Image Processing for 2-D and 3-D Reconstruction from Projections: Theory and Practice in Medicine and the Physical Sciences, Aug. 4-7, Stanford Univ.

Gregg EC 1977 Radiation risks with diagnostic X-rays Radiology 123 (2) 447-453.

Groh G and Kock M 1970 3-D display of X-ray images by means of holography Applied Optics 9 775-777.

GrossmannG 1935 Practical considerations of tomography Fortschr. i.d. Geb. d. Röntgenstrahlen 52 44.

Güttner W, Fielder G and Pätzold J 1952 Über ultraschallabbildungen am menschlichen schädel (On ultrasonic pictures of the human skull) Acustica 2 (4) 148-56.

Hammand AE and Mathur RM 1977 Dynamic performance of permanent-magnet stepping motors Proc. IEE 124 (7) 651-5.

Haugen M, Farrall W, Herrick J and Baldes E 1955 An ultrasonic flow meter Proc. Nat. Electronics Conf. II 465-475.

Hawley SA, MacLeod RM and Dunn F 1963 Degradation of DNA by intense noncavitating ultrasound JASA 35 1285-1287.

Hazzard deW G and Litz ML (Eds) 1977 Symposium on Biological Effects and Characterizations of Ultrasound Sources, held Rockville, Maryland June 2-3, published by U.S. Dept Health, Education and Welfare, HEW publication (FDA) 78-8048.

Herman GT, Lakshminarayanan AV and Naparstek A 1976a Convolution reconstruction techniques for divergent beams. Special issue of Computers in Biology and Medicine 6 (4) 259-272.

Herman GJ and Lent A 1976 Iterative reconstruction algorithms. Special issue of Computers in Biology and Medicine 6 (4) 273-294.

Herrick JF 1953 Temperatures produced in tissues by ultrasound: experimental study using various techniques JASA 25 12-16.

Herrick JF and Krusen FH 1954 Ultrasound and medicine. A survey of experimental studies JASA 26 236-240.

Hersey JB 1977 A chronicle of man's use of ocean acoustics Oceanus 20 (2) 8-21.

Hertz CH and Edler J 1954 Use of ultrasonic reflectoscope for continuous recording of movements of heart walls K. fysiogr. Sällsk. Lund Förh 24 40-48.

Heyser RC 1967 Acoustical measurements by time delay spectrometry J. Audio Eng. Soc. 15 370.

Heyser RC and Le Croissette DH 1974 A new ultrasonic imaging system using time delay spectrometry Ultrasound in Med. & Biol. 1 119-131.

Highmore PJ 1973 Impedance matching at ultrasonic frequencies using thin transition layers, in Ultrasonic International 1973 Conference Proceedings, IPC Science and Technology Press 112-118.

Hildebrand BP and Haines KA 1969 Holography by scanning J. Opt. Soc. Am. 59 1.

Hildebrand BP and Brendon BB 1972 An Introduction to Acoustical Holography, Plenum Press, New York-London.

Hill CR 1968 The possibility of hazard in medical and industrial applications of ultrasound Brit. J. Radiol. 41 (488) 561-9.

Hill CR 1971 Acoustic intensity measurement on ultrasonic diagnostic devices. Ultrasonographic Medica 2 (J. Bock and K. Ossoining Eds.) Vienna Academy of Medicine 21-27.

Himmelblau DM 1972 Applied nonlinear programming, McGraw-Hill.

Holmes JH and Howry DH 1963 Ultrasonic diagnosis of abdominal disease Am. J. dig. Dis. 8 12-32.

Horn BKP 1978 Density reconstruction using arbitary ray-simpling schemes Proc. IEEE 66 (5) 551-562.

Hounsfield GN 1972 British patent #1283915.

Hounsfield GN 1973 Computerised transverse axial scanning (tomography). Part I Description of System Brit. J. Radiol. 46 1016-1022.

Hounsfield GN 1976 in Reconstructive tomography in diagnostic radiology and nuclear medicine (Ed. M.M. Ter-Pogossian) Baltimore: University Park.

Howery DH and Bliss W 1952 Ultrasonic Visualisation of soft tissue structures of the body J. Lab. and Clin. Med. 40 579-592.

Hubelbank M and Tretiak OJ 1970 Focussed ultrasonic transducer design, in Quarterly Progress Report #98, Research Laboratory of Electronics, M.I.T. 169-177.

Huetter TF and Bolt RH 1951 An ultrasonic method for outlining the cerebral ventricles JASA 23 160-167.

Huffman DA 1962 The generation of impulse-equivalent pulse trains IRE Trans. Info. Th. IT-8 S10-S16.

Huffman DL 1974 A modification of Huffman's impulse-equivalent pulse trains to increase signal energy utilization IEEE Trans. Info. Th. 7 559-561.

Hughes DE, Chou JTY, Warwick R and Pond J 1963 The effect of focussed ultrasound on the permeability of frog muscle Biochim. Biophys. Acta 75 137-139.

Hunter HH, Ensminger D, Stutz DE and Ullrich OA 1964 Stroboscopic Schlieren system for the visual observation of pulsed ultrasonic waves Proc. IEEE 52 744-745.

Hurwitz H 1975 Entropy reduction in Bayesian analysis of measurements Phys. Rev. A12 698-704.

Iwata K and Nagata R 1975 Calculation of refractive index distribution from interferograms using the Born and Rytov's approximation Jap. J. Appl. Phys. 14 suppl. 14-1, 379-83.

Jacobs JE, Berger H and Collis WJ 1963 An investigation of the limitations to the maximum attainable sensitivity in acoustical image converters IEEE Trans. Ultrasonic Eng. UE-10 (2) 83-88.

Jacobs JE 1967 Performance of the ultrasound microscope Matrls. Eval. 25 (3) 41-45.

Jacobs JE 1968a Present status of ultrasound image converter systems Trans. N.Y. Acad. Sci. Ser. II 30 444-456.

Jacobs JE 1968b Ultrasonic image converter systems utilizing electron-scanning techniques IEEE Trans. Sonics and Ultrason. SU-15 146-152.

Jacobs JE, Reimann K and Buss L 1968c Use of colour display techniques to enhance sensitivity of the ultrasound camera Materials Evaluation 26 (8) 155-158.

Jacobs JE and Peterson 1974 Advances in the Sokoloff tube, in Acoustical Holography Vol. 5 (Green Ed.) Plenum Press, New York-London, 633-645.

Jaffe B, Roth RS and Marzullo S 1955 Properties of piezoelectric ceramics in solid-solution series lead titanate-lead zirconate-lead oxide: tin oxide and lead titanate-lead hafnate J. Res. natn. Bur. Stand. 55 239-254.

James GL 1976 Geometrical Theory of Diffraction for Electromagnetic Waves, Peter Peregrinus (IEE electromagnetic wave series).

James JA, Dalton GA, Freundlich HF, Bullen MA, Wells PNT, Hughes DE and Chan JTY 1963 Histological, thermal and biochemical effects of ultrasound on the labyrinth and temporal bone Acta oto-lar. 57 306-311.

Jeppsson S 1961 Echoehcephalography IV. The mid-line-echo; an evaluation of its usefulness for diagnosing intracranial expansivities and an investigation into its sources Acta. chir. Scand. Suppl. 272.

Johnson SA, Robb RA, Greenleaf JF, Ritman EL, Gilbert BK, Storma MT, Sjostrand JD, Donald DE, Herman GT, Sturm RE and Wood EH 1974 Dynamic three-dimensional reconstruction of the beating heart and lungs from multiplanar roentgen-television images Mayo Clinic Proc. 49 958-963.

Johnson SA, Greenleaf JF, Chu A, Sjostrand JD, Gilbert BK and Wood EH 1975 Reconstruction of material characteristics from highly refraction distorted projections by ray tracing. In Topical Meeting on Image Processing for 2-D and 3-D Reconstruction from Projections: Theory and Practice in Medicine and the Physical Sciences, Aug. 4-7, Stanford Univ.

Jordan EC and Balmain KG 1968 Electromagnetic Waves and Radiating Systems Prentice-Hall, Inglewood Cliffs, N.J.

Junginger HG and Van Haeringen W 1972 Calculation of three-dimensional refractive-index field using phase integrals Optics Comm. 5 (1) 1-4.

Kalmus H, Hedrick A and Pardue D 1954 The acoustic flowmeter using electronic switching I.R.E. Trans. on Ultrasonics Engineering UE-1 49-62.

Kay L, Boys JT, Clark GRS and Mason JL 1977 The echocardiophone: a new means for observing spatial movement of the heart Ultrasonics 15 (3) 136-141.

Keller JB 1969 Accuracy and validity of the Born and Rytov approximations J. Opt. Soc. Am. 59 (8) 1003-4.

Kisslo J, Von Ramm OT and Thurston FL 1976 Cardiac imaging using a phased array ultrasound system II. Clinical technique and application Circulation 53 (2) 262-267.

Klug A and Crowther RA 1972 Three-dimensional image reconstruction from the viewpoint of information theory Nature 238 435-440.

Kock WE 1970 Holography can help radar find new performance horizons Electronics (Oct. 12th).

Korpel A 1966 Visualization of the cross-section of a sound beam by Bragg diffraction of light Appl. Phys. Lett. 9 425.

Korpel A 1968 Acoustic imaging by diffracted light, I. Two-dimensional interaction IEEE Trans. Sonics Ultrason. SU-15 153-157.

Korpel A and Desmares P 1969 Rapid sampling of acoustic holograms by laser-scanning techniques JASA 45 881.

Korpel A, Whitman RL and Ahmed M 1974 Elimination of spurious detail in acoustic images, in Acoustical Holography Vol. 5 (P.S. Green Ed.) Plenum Press, 373-390.

Kossoff G 1963a Design of narrow-beamwidth transducers JASA 35 905-912.

Kossoff G 1963b Visualisation of abdominal masses using ultrasound Proc. I.R.E. Australia.

Kossoff G, Robinson DE, Liu LN and Garrett WJ 1964 Design criteria for ultrasonic visualisation systems Ultrasonics 2 29-38.

Kossoff G 1964 Design of the CAL ultrasonic generator for the treatment of Meniere's disease IEEE Trans. Son. Ultrason. SU-2 95.

Kossoff G 1966 The effects of backing and matching on the performance of piezoelectric ceramic transducers IEEE Trans. Son. Ultrason. SU-13 (1) 20-30.

Kossoff G, Robinson DE and Garrett WJ 1968 Ultrasonic two-dimensional visualisation for medical diagnosis JASA 44 (5) 1310-1318.

Kossoff G, Fry FJ and Eggleton TC 1971 Application of digital computers to control ultrasonic visualisation equipment (Böck and Ossoinig Eds) Ultrasonographia Medica I.

Kossoff G 1972 Improved techniques in ultrasonic cross sectional echography Ultrasonics 10 221-227.

Kossoff G 1973 Ultrasonic research in medicine in Australia - a review, in Ultrasonics International 1973 Conference Proceedings.

Kossoff G 1974 Display techniques in ultrasound pulse echo investigations: a review J. Clin. Ultras. 2 (1) 61-72.

Kossoff G, Garrett WJ and Radovanovich 1974 Grey scale echography in obstetrics and gynaecology Aust. Radiol. XVIII (1) 63-111.

Kreuzer JL and Vogel PE 1969 Acoustic holographic techniques for non-destructive testing, in Acoustical Holography Vol. 1 (Metherell et al. Eds) Plenum Press, N.Y.

Lakshminarayanan AV 1975 Reconstruction from divergent ray data, Dept. Computer Sci., N.Y. State Univ., Buffalo, Tech. Report 92.

Langevin P 1918 French Patent #505,703.

Langevin P 1921 British Patent #145,691.

Lathi BP 1968 Communication Systems, Wiley, New York.

Leary GA 1967 Basic techniques for applying ultrasonics to ophthalmic measurement and diagnosis Ultrasonics 6 84-87.

Ledley RS 1976 Introduction to computerized tomography Computers in Biology and Medicine 6 (4) 234-246.

Leith EN, Upatnieks J and Haines KA 1965 Microscopy by wavefront reconstruction J Opt. Soc. Am. 55 (8) 981-986.

Lele PP 1963 Effects of focussed ultrasonic radiation on peripheral nerve, with observations on local heating Expl. Neurol. 8 47-83.

Lele PP 1967 Production of deep focal lesions of focussed ultrasound - current status Ultrasonics 5 105-112.

Lemons RA and Quate CF 1974 Scanning acoustic microscope, in IEEE Ultrason. Symp. Proc. IEEE catalog no. 73 CHO 807-8 SU, 18-21.

Lester RG 1977 Risk versus benefit in mammography Radiology 124 (1) 1-5.

Lewitt RM 1977 Contributions to image reconstruction, Ph.D. thesis, University of Canterbury, Christchurch, New Zealand.

Lewitt RM and Bates RHT 1978a Image reconstruction from projections. Part I General theoretical considerations Optik 50 (1) 19-33.

Lewitt RM, Bates RHT and Peters TM 1978 Image reconstruction from projections. Part II Modified back-projection methods Optik 50 (2) 85-109.

Lewitt RM and Bates RHT 1978b Image reconstruction from projections. Part III. Projection completion methods (theory) Optik 50 (3) 189-204.

Lewitt RM and Bates RHT 1978c Image reconstructions from projections. Part IV Projection completion methods (computational examples) Optik 50 (4) 269-278.

Liebesny JP and Lele PP 1973 (Oct.) Enhancement of ultrasonic B-scan by chromatic encoding, presented at 18th annual meeting of A.I.U.M.

Lighthill MJ 1958 Introduction to Fourier Analysis and Generalized Functions, Cambridge University Press.

Linden DA 1959 A discussion of sampling theorems Proc. I.R.E. 1219-1226.

Lindstrom P 1954 Prefrontal ultrasonic irradiation - a substitute for lobotomy A.M.A. Arch. Neurol. and Psych. 72 399-425.

Lobdell DD 1968 A nonlinearly processed array for enhanced azimuthal resolution IEEE Trans. Sonics Ultrason. SU-15 (4) 202.

Lowenthal S and Belvaux Y 1967a Observation of phase objects by optically processed Hilbert transform App. Phys. Let. 11 (2) 49-51.

Lowenthal S and Belvaux Y 1967b Pattern recognition by spatial frequency filtering Optica Acta (Internat.) 14 (3) 245-258.

Lutsch A 1962 Solid mixtures with specified impedances and high attenuation for ultrasonic waves JASA 34 131-132.

Lynworth LC 1965 Ultrasonic impedance matching from solids to gases IEEE Trans. Sonics Ultrason. SU-12 (2) 37-48.

McCullough EC, Baker HL, Houser OW and Freese DF 1974 An evaluation of the quantitative and radiation features of a scanning X-ray transverse axial tomograph: The EMI scanner Radiology 111 709.

MacDonald KA 1976 Computer recognition of lumber quality, in Automated inspection and product control, Second International Conference Proc. (IIT Research Institute) Chicago, USA (Oct.).

McDonnell 1975 Nonrecursive image restoration using a finite filter array Optik 43 159-174.

MacIntosh IJC and Davey DA 1970 Chromosome aberrations induced by an ultrasonic foetal pulse detector Br. Med. J. 4 92-93.

MacIntosh IJC and Davey DA 1972 Relationship between intensity of ultrasound and induction of chromosome aberrations Br. J. Radiol. 45 320-327.

MacLeod IDG 1970 Pictorial output from a line-printer IEEE Trans. Comp. C-19 160-162.

Macovski A and Norton SJ 1975 High-resolution B-scan systems using a circular array, in Acoustical Holography Vol. 6, (N. Booth Ed.) Plenum Press, N.Y., 121-144.

Macovski A, Alvarez RE, Chan J.L-H, Stonestrom JP and Zatz LM 1976 Energy dependent reconstruction in X-ray computerized tomography Computers in Biology and Medicine 6 (4) 325-336 (Special Issue).

McSherry DH, Alfrey CD and Wright KE 1972 Signal processing of digital ultrasound data, presented to the 17th Annual Meeting of the American Institute of Ultrasound in Medicine, Philadelphia, Pa.

McSherry DH 1973 Digital processing systems for diagnostic ultrasound data. Proc. of Second World Conference on Ultrasonics in Medicine (de Vlieyer White and McCready Eds.) 325-331.

McSherry DH 1974 Computer processing of diagnostic ultrasonic data IEEE Trans. Sonics Ultrason. SU-21 91-97.

McSkimin HJ 1955 Transducer design for ultrasonic delay lines JASA 27 302-309.

McSkimin HJ 1959 Performance of high-frequency barium titanate transducers for generating ultrasonic waves in liquids JASA 31 (11) 1519-22.

Maginness MG 1970 Ultrasonic determination of the internal structure of solids, Ph.D. Thesis, University of Canterbury, N.Z.

Maginness MG 1972 The reconstruction of elastic wave fields from measurements over a transducer array J. Sound Vib. 20 (2) 219-240.

Marom E, Mueller RK, Koppelmann RF and Zilinskas G 1971 Design and preliminary test of an underwater viewing system using sound holography, in Acoustical Holography 3 (Metherell Ed.) Plenum Press, N.Y., 191.

Mason WP 1948 Electromechanical Transducers and Wave Filters, second edition, Van Nostrand, N.J.

Mawardi OK 1970 On the theory of acoustical imaging, in Acoustical Holography Vol. 2 (Metherell AF and Lamore L Eds.) Plenum Press N.Y. 23-37.

Meeker TR 1972 Thickness mode piezoelectric transducers Ultrasonics 10 (1) 26-36.

Melton HE 1971 Electronic focal scanning for improved resolution in ultrasound imaging, Ph.D. thesis, Duke University, Durham, N.C., U.S.A.

Mersereau RM 1976 Direct Fourier transform techniques in 3-D image reconstruction Computers in Biology and Medicine 6 (4) 247-258 (special issue).

Metherell AF, El-Sum HMA and Lamore L (Editors) 1969 Acoustical Holography Volume 1, Plenum Press, New York-London.

Metherell AF and Lamore L (Editors) 1970 Acoustical Holography Volume 2, Plenum Press, New York-London.

Metherell AF (Editor) 1971 Acoustical Holography Volume 3, Plenum Press, New York-London.

Meyer RF 1978 - private communication.

Mezrich R and Vilkomerson DHR 1975 Ultrasonic phase contrast imaging Appl. Phys. Letts 27 (4) 177-179.

Miller LD, Joyner CR, Dudrick SJ and Eskin DJ 1967 Clinical use of ultrasound in the early diagnosis of pulmonary embolism Ann. Surg. 166 381-392.

Miller EB, Smith SW and Thurston FL 1974 A study of near field ultrasonic beam patterns from a pulsed linear array, in Acoustical Holography Vol. 5 (Ed. PS Green) Plenum Press, N.Y., p261.

Mueller RK and Sheridon NK 1966 Sound holograms and optical reconstructions Appl. Phys. Letters 9 328.

Mueller RK 1971 Acoustic holography Proc. IEEE 59 (9) 1319-1334.

Nagasaka N and Shinohara K 1974 Study of large-capacity electric pulse motors Electr. Eng. Jap. 94 (3) 101-109.

Numonics Corporation 1975 Service Manual for the Electronic Graphics Calculator.

Oksala A and Lehtinen A 1957 Über die diagnostische verwendung von ultraschall in der augenheilkunde, Ophthalmologica z.f. Augenheilkunde 134 (6) 387-395.

Oppenheim BE 1975 in Image Processing for 2-D and 3-D Reconstructions from projections, Stanford, Aug. 4-7, (Opt. Soc. Am.), Wal 1-4.

Oschepkov PK, Rosenberg LD and Semennikov YuB 1955 Electronacoustic converter for the visualisation of acoustic images Soviet Phys. - Acoustics 1 362-391.

Pang SC and Genna S 1975 A Fourier convolution fan geometry reconstruction algorithm: simulation studies, noise propagation, and polychromatic degradation, in Workshop on Reconstruction Tomography in Diagnostic Radiology and Nuclear Medicine, San Juan, April 17-19, 1975.

Patrick MK 1966 Ultrasound in physiotherapy Ultrasonics 4 10-14.

Pelmore JM 1977 The ultrasonic properties of some filled epoxy materials, in Ultrasonics International 1977 (Conference Proceedings) IPS Science and Technology Press, U.K., 316-322.

Peronneau PA and Leger F 1969 Doppler ultrasonic pulsed blood flow meter, in 8th Internat. Conf. on Med. and Biol. Eng.

Peters TM 1973 Image reconstruction from projections, Ph.D. Thesis, University of Canterbury, N.Z.

Peters TM 1974a Spatial filtering to improve transverse tomography IEEE Trans. Bio-Med. Eng. BME-21 (3) 214-219.

Peters TM 1974b Image reconstruction from projections measured with diverging rays, in International Workshop on Image Reconstruction Techniques, Brookhaven National Lab., N.Y., Conference Proc., July 16-19.

Peters TM 1975 Enhanced display of three-dimensional data from computerized X-ray tomograms Comput. Biol. & Med. 5 49-52.

Peters TM and Lewitt RM 1977 Computed tomography with fan beam geometry. Journal of Computer Assisted Tomography 1 (4).

Pistema DA 1975 in Image Processing for 2-D and 3-D Reconstruction from Projections, Stanford, Aug. 4-7, (Opt. Soc. Am.) MA12-1 to 4.

Pohlman R, Richter R and Parow E 1939 Über die ausbreitung und absorption des ultraschalls im menschlichen gewebe und seine therapeutische wirkung an ischias und plerusneuralgia. Dtsh. Med. Wschf. 65 251.

Pond J and Dyson M 1967 A device for the study of the effects of ultrasound in tissue growth in rabbit's ears. J. Scient. Instrum. 44 165-166.

Posakony GJ 1975 Engineering aspects of ultrasonic piezoelectric transducer design, 1975 Ultrasonics Symposium Proceedings (IEEE Cat. No. 75 CHO 994-45U) 1-9.

Prabhu KMM and Reddy VU 1975 Synthesis of windows from raised cosine pulse Electron. Lett. 11 (8) 161-163.

Prabhu KMM, Reddy VU and Agrawal JP 1977 Performance comparison of data windows Electronics Letters. 13 (20) 600-1.

Preis D 1977 Least-squares time domain deconvolution for transversal-filter equalisers Electronics Letters 13 (12) 356-357.

Pringot J et al. 1977 Diagnostic value of CT scanning by comparison with ultrasonography and retrograde pancreatography. Presented to Symposium on total body computerized tomography, Heidelberg, Germany.

Quate CF, Wilkinson CDW and Winslow DW 1965 Interaction of light and microwave sound Proc. IEEE 53 (10) 1604-1628.

Quate CF, Havlice J and Goodman J 1968 Acoustic microscope Stanford University Microwave Lab. Report #1701.

Radon J 1917 Über die bestimmung von funktionen durch ihre integralwerte längs gewisser Mannigfaltigkeiten Ber. Verh. Sächs. Akad. 69 262-278.

Ramachandran GN and Lakshminarayanan AV 1971 Three-dimensional reconstruction from radiographs and electron micrographs: Application of convolutions instead of Fourier transforms Proc. Nat. Acad. Sc. USA 68 2236-2240.

Redman JD, Wolton WD and Shuttleworth E 1968 Uses of holography to make truly three-dimensional X-ray images Nature 220 58.

Redwood M 1961 Transient performance of a piezoelectric transducer JASA 33 527-536.

Redwood M 1963 A study of waveforms in the generation and detection of short ultrasonic pulses Appl. Mater. Res. 2 76-84.

Reed IS, Truong TK, Chang CM and Kwoh 1978 3-D reconstruction for diverging X-ray beams IEEE Trans. Nuc. Sci. NS-25 (3) 1006-1009.

Reid J and Wild J 1952 Application of echo ranging techniques in determination of structure of biological tissues Sci. 115 226-230.

Reintjes F (Editor) 1952 Principles of Radar (3rd Edition) McGraw-Hill, N.Y.

Report of the advisory committee on the biological effects of ionizing radiations 1972. The effects on populations of exposure to low levels of ionizing radiations, Natl. Acad. of Sciences, Washington, D.C.

Rich C, Klinik E, Smith R and Graham B 1966 Measurement of bone mass from ultrasonic transmission time Proc. Soc. Exp. Biol. 123 282-285.

Ritman EL, Sturm RE and Wood EH 1976 in Reconstructive Tomography in Diagnostic Radiology and Nuclear Medicine (Ed. MM Ter-Pogossian) Baltimore: University Park.

Robb RA, Greenleaf JF, Ritman EL, Johnson SA, Sjostrand J, Herman GT and Wood EH 1974 Three-dimensional visualization of the intact thorax and contents: A technique for cross-section reconstruction from multiplanar X-ray views Computers Biomed. Res. 7 395-419.

Robinson DE and Kossoff G 1966 An ultrasonic echo-encephaloscope for the examination of the human brain Proc. I.R.E. 27 39-44.

Robinson DE 1972a Ultrasonic systems for medical diagnostic visualisation, M.I.T. Quarterly Progress Report #104, 289-305.

Robinson DE 1972b Display of three-dimensional ultrasonic data for medical diagnosis JASA 52 673-687.

Robinson DE 1974 Private communication during a visit to the Advanced Techniques Section, Ultrasonics Institute, Sydney.

Robinson EA 1966 Multichannel Z-transforms and minimum delay Geophysics 31 482.

Robinson EA 1967 Multichannel time series analysis with digital computer programs, Holden-Day, San Francisco.

Rogers TGH 1975 Computerised treatment planning in Christchurch N.Z. Med. Phys. & Biol. Eng. 2 (4).

Röntgen WK 1895 First paper on X-rays read to the Society of Physics and Medical Science, Wurzburg University (28th Dec.).

Rowley PD 1969 Quantitative interpretation of three-dimensional weakly refractive phase objects using holographic interferometry J. Opt. Soc. Am. 59 1496-1498 (Erratum, ibid 60, 705).

Satomura S 1957 Ultrasonic doppler method for inspection of cardiac function Jour. Acoust. Soc. Japan 29 (11) 1181-1185.

Segal BL, Likoff W, Asperger Z and Kingsley B 1966 Ultrasonic diagnosis of abdominal aortic aneurism Am. J. Cardiol. 17 101-103.

Shepp LA and Logan BF 1974 The Fourier reconstruction of a head section IEEE Trans. Nucl. Sci. 21 21.

Skudrzyk EJ 1971 The Foundations of Acoustics, Springer-Verlag, N.Y.

Smith PR, Peters TM and Bates RHT 1973 Image reconstruction from finite numbers of projections J. Phys. A6 361-382.

Smith RB and Brendon BB 1969 Refinements and variations in liquid surface and scanned ultrasound holography IEEE Trans. Sonics Ultrason. SU-16 29.

Smith RP 1972 Transduction and audible displays for broadband sonar systems, Ph.D. thesis, University of Canterbury, Ch.Ch., N.Z.

Smyth MG 1966 Animal toxicity studies with ultrasound at diagnostic power levels, in Diagnostic Ultrasound (G Grossman et al. - Eds) Plenum Press, N.Y., 296-299.

Sokoloff SY 1929 Zur frage der fortpflanzung ultrakusticher schwingungen in verschiedenen körpern Elektr. Nachr. Technik 6 454-461.

Sokoloff SY 1937 Ultrasonic image converter U.S. patent #2,164,185

Somaini U and Ackroyd MH 1974 Uniform complex codes with low auto-correlation sidelobes IEEE Trans. Info. Th. IT-20 (5) 689-91.

Somer JC 1968 Electronic sector scanning for ultrasonic diagnosis Ultrasonics 6 (3) 153.

Somer JC 1971 Electronic sector scanning with ultrasonic beams, (Böck and Ossoinig Eds.) Ultrasonographia Medica I.

Somer JC 1973 Electronic sector scanning in cerebral diagnostics. I. Principle and technical development (de Vlieger, White and McCready Eds) Proc. Second World Conf. Ultrasonics in Medicine.

Souquet J and De Franould PH 1978 Results on low-loss wideband ultrasonic transducers for non-invasive medical examination Elec. Letts 14 (8) 235-236.

Stauffer H, Henny G and Blackstone A 1962 Stereoscopic televised fluoroscopy Radiology 79 30.

Stieve FE 1972 Über den bildaufbau in der tomgraphie bei ein-und Mehrdimensionaler Verwischung Fortschr. Röntgenst. 116 253-273.

Sturm RE, Ritman EL and Wood EH 1975 Quantitative three-dimensional dynamic imaging of structure and function of the cardiopulmonary and circulatory systems in all regions of the body, in Proceedings of the Cardiovascular Imaging and Image Processing: Ultrasound, Angiography and Isotopes Meeting, Stanford University (July 10-12).

Takagi SF, Higashino S, Shikurya T and Osawa N 1960 The actions of ultrasound on the myelinated nerve, the spinal cord and the brain Jap. J. Physiol. 10 183-193.

Takahashi S 1965 Conformation radiotherapy. Rotation techniques as applied to radiography and radiotherapy of cancer Acta Radiol. Suppl. 242.

Tal J 1977 Control modes of step motors IEEE Trans. Aerosp. Electron. Syst. AES-13 (1) 56-61.

Talbot F 1836 - Phil. Mag. 9 401.

Taylor KJW, Carpenter DA and McCready VR 1973 Gray scale echography in the diagnosis of intrahepatic disease J. Clinical Ultrasound 1 (4) 284-287.

Thurston FL and Von Ramm OT 1973 Electronic beam scanning for ultrasonic imaging. (de Vlieger, White and McCready Eds) Proc. Second World Conf. Ultrasonics in Medicine.

Topical meeting on Image Processing for 2-D and 3-D reconstructions from projections; theory and practice in medicine and the physical sciences, held at Stanford University, Aug. 4-7, 1975 (Opt. Soc. Am.)

Toraldo di Francia G 1969 Degrees of freedom of an image J. Opt. Soc. Am. 59 799.

Tremewan RN 1975 A non-invasive in vivo velocity measuring technique using pulsed ultrasound, M.E. report, University of Canterbury, N.Z.

Tretiak OJ, Eden M and Simon W 1969 Internal structure from X-ray images, Proc. 8th Int. Conf. on Med. Biol. Eng., Chicago Ill., July 20-25.

Tucker DG and Gazey BK 1966 Applied Underwater Acoustics, Pergamon Press.

Ueda M and Murata K 1976 Analysis of the directional pattern of dynamic focussing transducers J. Acoust. Soc. Jap. 32 (6) 355-361.

Uginčius P 1969 Acoustic-ray equations for a moving, inhomogeneous medium JASA 37 (3) 476.

Utsunomiya 1977 Medical diagnostics: visual/aural techniques IEEE Spectrum (Sept.) 69-70.

Vallebona A 1930 A modified technique of roentgenographic dissociation of shadows applied to the study of the skull Radiol. Med. 17, 1090-1097.

Vallebona A 1947 Nouvelle méthode roentgenstratigraphique Radiol. Clin. 47.

Vallebona A 1955 Three-dimensional stratigraphic scintigraphic examination. Axial transverse stratigraphy. Part I Am. J. Roent. Rad. Ther. Nucl. Med. 74 769-776.

van Randeraat J (Ed.) 1968 Piezoelectric ceramics, Technical Publications Department, Electronic Components and Materials Division, N.V. Philips, Eindhoven.

Vilkomerson D 1974 Acoustic imaging with thin annular apertures, in Acoustical Holography Vol. 5 (PS Green Ed.) Plenum Press, N.Y., 283-316.

Vilkomerson D and Hurley B 1975 Progress in annular-array imaging, in Acoustical Holography Vol. 6 (N. Booth Ed.) Plenum Press, N.Y., 145-164.

Von Ramm OT and Thurston FL 1976 Cardiac imaging using a phased array ultrasound system I. System design. Circulation 53 (2) 258-262.

Wade W (Ed.) 1972 Acoustical Holography Volume 4, Plenum Press, New York-London.

Washington ABG 1961 The design of piezoelectric ultrasonic probes Br. J. non-destr. Test. 3 56-63.

Watson GN 1966 A Treatise on the Theory of Bessel Functions, Cambridge C.U.P.

Weinstein FS 1978 Accurate fan-beam reconstruction Proc. IEEE 66 (5) 608-9.

Wells PNT 1968 The effect of ultrasonic irradiation on the survival of Daphnia magna J. Exp. Biol. 49 61-70.

Wells PNT 1969 Physical principles of ultrasonic diagnosis, Academic Press, London.

Wells WH 1970 Acoustical imaging with linear transducer arrays, in Acoustical Holography Vol. 2 (Metherell and Lamore Eds.) Plenum Press, N.Y., 87.

Wells PNT 1974 Medical ultrasonic diagnosis IEE Electronics and Power 16th May 367-370.

Wild JP 1965 A new method for image formation with annular apertures and an application in radio astronomy Proc. Roy. Soc. A286 449.

Wild J 1950 The use of ultrasound pulses for measurement of biologic tissues and the detection of tissue density changes Surg. 127 (2) 183-188.

Wolf E 1969 Three-dimensional structure determination of semi-transparent objects from holographic data Opt. Commun. 1 (4) 153-6.

Wood RW and Loomis AL 1927 The physical and biological effects of high frequency sound waves of great intensity Phil. Mag. (7th series) 4 417-436.

Yokoi H and Ito K 1972a Ultrasonic diagnostic equipment with colour display unit for simultaneous tomogram method Toshiba Review (76) 1-8.

Yokoi H and Ito K 1972b Ultrasonic diagnostic equipment with colour display unit for simultaneous tomogram method Med. Ultrason. 10 (1) 56.

Zernike F 1935 Das phasenkontrastverfahren bei der mikroskopischen Beobachtung Z. Tech. Phys. 16 454.

Ziedses des Plantes BG 1932 A new method of differentiation in roentgenography (planigraphy) Acta Radiol. 13 182-191.

Ziedses des Plantes BG 1971 Body-section radiography: History, image formation, various techniques and results Australasian Radiology 15 57-64.